ECC-SMART PROJECT

Joint European Canadian Chinese development of Small Modular Reactor Technology

Grant Agreement Number: 945234
H2020 – NFRP-2019-2020

Start Date of the Project: 1/09/2020
Duration: 54 Months

Deliverable Title:	**D3.3 Report on the preconceptual studies on the core layout and passive safety concept of the SCW-SMR**
Lead party:	UNIPI – University of Pisa
Author(s):	Ivan Otic (KIT), Thomas Schulenberg (KIT), Walter Ambrosini (UNIPI), Andrea Pucciarelli (UNIPI), Omar Chaaraoui (UNIPI), Tamás Varju (BME), Attila Kiss (BME), Boglárka Babcsány (BME), Csenge Antók (BME), Péter Mészáros (BME), Zeno Bertesina (BME), Szabolcs Czifrus (BME), Vladislav Filonov (IPP), Dmitriy Fedorov (IPP), Yuliia Filonova (IPP), Yaroslav Dubyk (IPP), Armando Nava-Dominguez (CNL), Xuebin Zhao (NPIC)
Participant(s):	UNIPI, BME, IPP, KIT, CNL, NPIC
Due Date:	31/08/2024

Version Number: 2.0

Approved by: Monika Šípová

Date: 31.8.2024

Dissemination level		
PU	Public	**X**
CO	Confidential: only for ECC-SMART Partners (including the Commission Services)	
EU-RES	Classified Information: RESTREINT UE*	
EU-CON	Classified Information: CONFIDENTIEL UE*	
EU-SEC	Classified Information: SECRET UE*	

**Commission Decision 2005/444/EC*

Document History – Version Control

Version	Issue Date	Stage	Description of Changes	Contributor
0.0	19.08.2024	Draft Version	First integrated version	Walter Ambrosini
1.0	31.8.2024	Final Version	Final integrated version	Watler Ambrosini

Project information

Project acronym:	ECC-SMART
Project title:	Joint European Canadian Chinese development of Small Modular Reactor Technology
Grant Agreement n°	945234
Start date:	1.9.2020
Duration	54 months
Programme:	Framework Programme for Research and Innovation (2019-2020) under the call NFRP-2019-2020
Coordinator:	Centrum Výzkumu Řež, s.r.o. (Czech Republic)

Document information

Work package:	WP3 Thermal Hydraulics and Safety of the SCW-SMR
Contractual Date of Delivery:	31.08.2024
Actual Date of Delivery to the EC:	31.08.2024
Document type:	Report
Dissemination level:	Public (PU)
Number of pages:	194

Abstract:
This report summarises the results obtained in the frame of the work performed for the tasks 3.4.2, 3.4.3 and 3.4.4 of the ECC-SMART Project, related to the study of the pre-conceptual core layout and passive safety concept for a SCW-SMR, respectively by the Limited Liability Company “IPP-Centre” (IPP), by the Budapest University of Technology and Economics (BME) and by the University of Pisa (UNIPI). The material presented herein is aimed mostly at assessing the suitability of the existing and further developed models for representing the phenomena envisaged in the postulated scenarios that may affect the proposed reactor concept. As in the general objectives of the ECC-SMART project, these represent pre-licensing studies aimed to propose guidelines for the future demonstration of the SCW-SMR concept addressed in the project, to be considered as a workbench to refine methodologies and tools necessary for nuclear reactor analysis and proposing a strategy for the future licensing.

Copyright / Disclaimer

The document is property of the ECC-SMART consortium members. This document reflects only the author's view. It does not represent the view of the European Commission and the European Commission is not responsible for any use that may be made of the information it contains. This deliverable contains original unpublished work except where clearly indicated otherwise. Acknowledgement of previously published material and of the work of others has been made through appropriate citation, quotation or both. Reproduction is authorized provided the source is acknowledged. (OR) No copying or distributing, in any form or by any means, is allowed without the prior written agreement of the owner of the property rights

The ECC-SMART project has received funding from the Euratom research and training programme 2019-2020 under grant agreement No 945234.

Executive Summary

This report summarises the results obtained in the frame of the work performed for the tasks 3.4.2, 3.4.3 and 3.4.4 of the ECC-SMART Project, related to the study of the pre-conceptual core layout and passive safety concept for a SCW-SMR, respectively by the Limited Liability Company "IPP-Centre" (IPP), by the Budapest University of Technology and Economics (BME) and by the University of Pisa (UNIPI). The material presented herein aims to mostly assess the suitability of the existing and further developed models for representing the phenomena envisaged in the postulated scenarios that may affect the proposed reactor concept. As in the general objectives of the ECC-SMART project, these represent pre-licensing studies aimed to propose guidelines for the future demonstration of the SCW-SMR concept addressed in the project, to be considered as a workbench to refine methodologies and tools necessary for nuclear reactor analysis and proposing a strategy for the future licensing.

In particular, Chapter 2 is devoted to general considerations about the Canadian and Chinese reactor concepts. Chapter 3 reports in greater detail the features of the reactor concept proposed by Schulenberg and Otic (2021); Chapter 4 summarises the early work performed by the University of Pisa for model development and code improvement and application for the analysis of passive safety aspects, with particular attention to natural circulation phenomena; Chapter 5 presents a further work performed by BME in an in-depth analysis of the pre-conceptual core layout and passive safety concept; Chapter 6 reports the additional work performed by IPP in the safety and design analysis of the SCW-SMR concept. Finally, Chapter 7 concludes the overall work performed in this frame.

The novel reactor concept proposed by Schulenberg and Otic (2021) features a seven passage core whose conception is driven by the attempt to minimise peaking factors often observed in SCWR reactor concepts owing to the large enthalpy jump across the core and to the uneven distribution of reactor power. The multiple passages through the core are in fact intended to allow mixing of the core at the outlet of each one of them, in order to equalise the fluid temperature entering the next stage. With respect to a previous three-pass core configuration proposed in previous projects (Schulenberg and Starflinger, 2012), the idea is here pursued to increase the number of passages to improve mixing and to use horizontal channels in order to allow for natural circulation conditions to be established in the medium- and long-term phases of postulated accidents. Safety systems are then proposed, mainly suggesting the use of passive devices. The combination of the concept of a SCWR, being the only Generation IV LWR concept, with a Small Modular Reactor structure, in line with the present tendencies in nuclear reactor research and development, makes the present proposal a quite promising one, also in consideration of the similar features exhibited by the Canadian and Chinese proposals.

The early work performed by the University of Pisa in modelling this reactor concept with system codes of the RELAP family immediately encountered a classical problem in the transition between supercritical and subcritical pressures. At such a threshold, in fact, numerical codes have to integrate solutions across the substantially troublesome difficulty represented by the critical point of water, characterised by vanishing or infinite property derivatives. This difficulty was overcome by simply acquiring a version of the RELAP/SCDAPSIM code maintained by an international Company, with which it was possible to activate a cooperation that led to the customisation of the code for the purposes of the analyses to be performed in the frame of the ECC-SMART project. This allowed to perform meaningful steady state and transient analyses providing for the first time insight into the dynamic behaviour of the proposed SCW SMR concept, thus paving the way for further and more refined studies. Among the several lessons learned from the work, the result that a minimal configuration of passive systems may be sufficient to assure

adequate natural circulation and core cooling during a postulated long-term station black-out (LTSBO) represented an interesting preview of the safety characteristics of the proposed concept.

The work performed in parallel by BME and carried on with greater refinement of the adopted tools reached similar conclusions, notwithstanding the different adopted programs. The Apros code, in particular, was already sufficiently flexible to cope with SCWR conditions, though ordinary problems had to be solved for performing the intended analyses. Among the several differences of the model adopted by BME with respect to the one by the University of Pisa, the use of a set of three representative channels at each heating stage in the core (cold, average and hot) instead of the two adopted by the University of Pisa (average and hot) allowed for better accuracy in the coupling with neutronic analyses, made also in the case of the University of Pisa. Moreover, the splitting of the downcomer model into two regions prepared for more realistic future analyses of LOCAs happening because of the break of one of the two feed-water or steam lines. With the adopted model, BME performed a series of detailed analyses of the LTSBO sequence and of steady state conditions with neutronic coupling with different core compositions. The conclusions about the LTSBO were anyway quite similar from a phenomenological point of view as those already mentioned for the work by the University of Pisa, though they were supported by a vaster amount of data.

For both the analyses performed by the University of Pisa and by BME, it must be mentioned that in the future a greater refinement in the vertical discretisation of the core could be needed, e.g, in representing each one of the 20 levels of fuel channels proposed in the concept. While this complication was not considered necessary at the present stage of preliminary analyses, such a more detailed description might be needed to assure that the present common feature of the RELAP and Apros models of using only seven levels of discretisation (one per each stage) may not hide some relevant phenomena occurring during postulated accidents, e.g., related to the creation of water levels feeding only part of the stacked fuel channels facing common inlet and outlet plena.

BME also performed a work in cooperation with CNL using the ASSERT-PV and the STAFAS subchannel codes, providing additional information on the maximum cladding temperature reached during steady-state conditions.

Finally, IPP tackled the tough problem of studying severe accident conditions for this novel configuration having horizontal channels in the reactor core, for which the classical MELCOR code models are not directly applicable. The problem was circumvented by a skilled use of MELCOR itself and of a CFD code; with the latter it was possible to evaluate the loads on the internal vessel structures caused by the depressurization from supercritical pressure of the system owing to a LB-LOCA, while the MELCOR code was adopted to consider the phases of core degradation and corium progression towards the bottom of the vessel and the final vessel attack and failure. The study was conducted in three stages, with the first one devoted to the mentioned fast depressurisation analysis, the second related to the corium degradation progression and the third to the vessel shell attack. The conclusions reached by this study suggest care in revising the proposed core configuration for the effects that the travelling depressurization wave may have on the reactor internals and warn about the need to avoid the possible unavailability of emergency core cooling systems after a LB-LOCA, something that seems to unavoidably lead to the collapse of the bottom head of the vessel, calling for a possible use of core catchers. While note is taken of both these warnings for future developments, it must be also mentioned that the use of passivity in the protection systems should be the key to avoid dangerous severe accident sequences in which the core is not sufficiently protected, making events like those described very unlikely or even ruling them out.

It must be mentioned that a remarkable product of the work performed is the nice cooperation established among the participants in Task 3.4, favoured by the innumerable weekly or bi-weekly meetings held online to monitor the progress of the work and to exchange useful data and ideas. Indeed, this strict cooperation will be a key asset for the continuation of the work in the frame of a future European project aimed at providing a new step in the proposal of feasible reactor concepts based on the supercritical pressure light water technology.

Table of contents

List of acronyms and abbreviations 11
List of tables 12
List of figures 12
Related documents 20
1 Introduction 21
2 Passive systems in Canadian and Chinese SCW reactor concepts 23
2.1 Canadian SCWR concept 23
2.1.1 General features of the Canadian SCW-SMR 23
2.1.2 Safety Systems 24
2.2 Chinese SCWR concept 25
2.2.1 CSR150 25
2.2.2 Core Conceptual Design 25
2.2.3 Safety Systems 27
3 General considerations on passive system identification for the SCW SMR 28
3.1 The first barrier of a SCWR 28
3.2 The second barrier of a SCWR 28
3.3 Control under normal operation 29
3.4 Safety systems 30
3.5 Core design concept 32
3.6 Structures around the reactor core 34
4 Early analyses of passive safety aspects by the University of Pisa 41
4.1 Focus of the work 41
4.2 Adopted RELAP Code Versions 41
4.3 Developed SCW SMR nodalisation 45
4.3.1 Vessel Flow Paths Nodalisation 45
4.3.2 Nodalisation refinement and extension for passive system 48
4.4 Steady-state calculation procedure 49
4.5 Transient analyses for the LTSBO 56
4.5.1 Base Calculation Case 56
4.5.2 Lowered IC units 63
4.5.3 Singular pressure drops at fuel channel inlet 65
4.5.4 Sequence without the accumulator system 71
4.5.5 Sequence without the accumulator system and with lowered IC units 74

4.5.6 Effect of operating pressure ... 77
4.6 Significance of the work and final remarks ... 80
5 Analysis of pre-conceptual core layout and passive safety concept for SCW-SMR by BME ... 82
5.1 Focus of the work ... 82
5.2 Developed Apros model of the SCW-SMR ... 82
5.2.1 Vessel Flow Paths Nodalisation ... 82
5.2.2 Primary loop model ... 85
5.2.3 Passive heat removal and accumulator models ... 87
5.3 Steady-state calculations with the Apros – Serpent 2 code system ... 89
5.3.1 Calculation procedure ... 89
5.3.2 Calculation results of the original concept (MOX core) ... 90
5.3.3 Calculation results of the concept with orifices (MOX core) ... 92
5.3.4 Calculation results of the concept with orifices and modified layout (MOX core) ... 96
5.3.5 Calculation results of the original concept (UO_2 core) ... 98
5.3.6 Calculation results of the concept with orifices (UO_2 core) ... 100
5.3.7 Calculation results of the concept with orifices and modified layout (UO_2 core) ... 101
5.3.8 Calculation results of further sensitivity analyses ... 103
5.3.9 Discussion about the steady-state results ... 108
5.4 Transient analyses for the LTSBO event with Apros ... 109
5.4.1 Base calculation case ... 110
5.4.2 Lowered IC units ... 119
5.4.3 Sequence without the accumulator system ... 121
5.4.4 Sequence without the accumulator system and with lowered IC units ... 125
5.4.5 Effect of the operating pressure ... 126
5.4.6 Effect of the orifices ... 127
5.4.7 Effect of the heat transfer correlation ... 129
5.4.8 Effect of the loading map ... 130
5.5 Steady-state calculations with the Apros – SPNDYN code system ... 131
5.5.1 The Gmsh model ... 131
5.5.2 Group constant database generation with Serpent 2 and group constant parametrisation 132
5.5.3 Corresponding Apros and SPNDYN regions ... 133
5.5.4 Coupling methodology of the models ... 133
5.5.5 Coupled, steady-state simulations ... 134

5.6 Steady-state calculations with adapted subchannel codes 137
5.6.1 Thermalhydraulic Modelling 138
5.6.2 Subchannel Analysis and Codes 139
5.6.3 Subchannel models 141
5.6.4 Results 143
5.7 Significance of the work and final remarks 146
6 Safety and design analysis of the SCW-SMR concept (by IPP) 148
6.1 Applicability of the severe accident analysis codes for the SCW-SMR concept 148
6.2 Stage 1. CFD modelling of the LB LOCA initial dynamics 150
6.2.1 The concept of representative CFD modelling 151
6.2.2 Generalization of heterogeneous two-phase formulation for supercritical coolant state 153
6.2.3 Representative CFD model of the SCW-SMR concept 156
6.2.4 CFD calculations of the decompression wave propagation during LB LOCA initial dynamics and assessment of corresponding dynamic loads 159
6.3 Stage 2. MELCOR code application for SCW-SMR core degradation analysis 163
6.3.1 SCW-SMR core input general description for MELCOR code 164
6.3.2 Molten materials characteristics and core state assessment during SA 166
6.4 Stage 3. Analysis of the late phase of severe accident in SCW-SMR 174
6.5 Significance of the work and final remarks 186
7 Conclusions 188
8 References 190

List of acronyms and abbreviations

BC	Boundary Condition
BME	Budapest University of Technology and Economics
BOC	Beginning of cycle
BWR	Boiling water reactor
CAD	Computer-aided design
CFD	Computational fluid dynamics
CL	Cold Leg
DC	Downcomer of the reactor vessel
ECC-SMART	(Joint) European Canadian Chinese development of Small Modular Reactor Technology
EOC	End of cycle
FA	Fuel Assembly
FE	Fuel Element (Fuel Rod)
FW	Feedwater
GDCS	Gravity driven coolant injection system
GIF	Generation IV International Forum
HP	High pressure (pre-heater)
HPLWR	High performance light water reactor
HR	Heat of vaporisation
HT	Heat transfer
IAEA	International Atomic Energy Agency
IC	Isolation condenser
IVMR	In-vessel melt retention
LBLOCA	Large break loos of coolant accident
LOCA	Loss of coolant accident
LP	Lower plenum of the reactor vessel OR low pressure (pre-heater)
LTSBO	Long-term station blackout
LWR	Light water reactor
PCM	Phase change model
PHRS	Passive heat removal system
PLF	Pressure loss factor
PWR	Pressurised water reactor
RPV	Reactor pressure vessel
SA	Severe accident
SBO	Station blackout
SC	Supercritical
SCL	Simantics Constraint Language (script language used in Apros)
SCRAM	Emergency shutdown of the nuclear reactor
SCWR	Supercritical water-cooled reactor
SCW-SMR	Supercritical water-cooled small modular reactor
TCP/IP	Transmission Control Protocol/Internet Protocol
UNIPI	University of Pisa
UP	Upper plenum of the reactor vessel
VVER	Russian design of PWR
WP	Working package

List of tables

Table 1: Flow rates in various flow paths for a nominal feed water flow of 145 kg/s and different values of the roughness parameter assumed to simulate the wire wraps 52
Table 2: Flow rates in various flow paths for a nominal feed water flow of 150 kg/s and different values of the roughness parameter assumed to simulate the wire wraps 53
Table 3: Flow rates at the various stages in the hot and average channels with optimised orifices and comparison of the hot-to-average flow and power ratios per bundle 55
Table 4: Number of assemblies per stage 84
Table 5: Flow rates at various part of the RPV model for a nominal feed water flow of 145 kg/s92
Table 6: Optimised orifice sizes 93
Table 7: Flow rates at the various stages in the three channels with optimised orifices and comparison of the cold-to-average and hot-to-average flow and power ratios per bundle 95
Table 8: Number of assemblies per stage in the alternative layout 96
Table 9: Optimised orifice sizes 96
Table 10: Optimised orifice sizes 100
Table 11: Optimised orifice sizes 102
Table 12: Effective multiplication factor result of the Serpent 2 calculations 109
Table 13: The proposed operating conditions of European and Canadian SCW-SMR 138
Table 14: Model options, correlations and operating conditions used in ASSERT-PV SC code 139
Table 15: Model options, correlations and operating conditions used in STAFAS code 139
Table 16: Subchannel dimensional data for the models of both codes 142
Table 17: Applied boundary conditions for ASSERT-PV SC model 142
Table 18: Applied boundary conditions for STAFAS model 142
Table 19. MELCOR initial conditions for the SCW-SMR SA progression analysis 167
Table 20. Main events and calculation output summary from MELCOR runs 173

List of figures

Figure 1: Canadian SCWR and Canadian SCW-SMR core and fuel channel 23
Figure 2: (left) Cross-sectional view of the Canadian SCWR and Canadian SCW-SMR fuel bundle, and (right) Canadian SCWR and Canadian SCW-SMR fuel channel 24
Figure 3: Isolation Condenser System layout for (left) Canadian SCWR, (right) Canadian SCW-SMR 24
Figure 4. CSR150 fuel rod design. 25
Figure 5. Mix Moderator Fuel Assembly Design. 26
Figure 6. CSR150 fuel loading patterns. 27
Figure 7. The new Coolant Flow Scheme of CSR150. 27
Figure 8: Once-through steam cycle of a SCWR 29
Figure 9: Generic differences between a BWR and a SCWR 30
Figure 10: Minimum set of safety systems for a SCWR. 31
Figure 11: Core design with horizontal fuel assemblies and with 7 heat up stages with intermediate mixing. 32
Figure 12: Rod bundle (wires removed) 33

Figure 13: Assembly and moderator boxes made of Zircalloy-4 with a thermal insulation of Zirconia and a thin stainless steel liner on the hotter side each. 33
Figure 14: Head end (top) and foot end (bottom) of the fuel assembly. 34
Figure 15: Principle sketch of the moderator flow path. 35
Figure 16: Sketch of the reactor pressure vessel, empty (left) and with core drum and core box inserted (right). Reactor closure head removed. 36
Figure 17: Design of the core drum with double bottom. 37
Figure 18: Flow path from the outlet plenum of moderator tubes to the core inlet header inside the double bottom of the core drum. 37
Figure 19:Top view of the total arrangement of RPV, core drum and core box. 38
Figure 20: Vertical cross sections through the reactor. 38
Figure 21: Horizontal cross section above the reactor core, looking downwards. 39
Figure 22: Horizontal cross section D-D through the double bottom of the core drum, looking downwards. 40
Figure 23: Sample results of the application of RELAP/SCDAPSIM to selected NTUU data 43
Figure 24. Prediction of a sample case by the Bishop et al. correlation: chart and contour plot 44
Figure 25. Prediction of a sample case by the Mokry et al. correlation: chart and contour plot.. 44
Figure 26. Sketches representing the subdivision into hydraulic components of the moderator flow path (left) and of the fuel coolant flow path (right) 45
Figure 27. Representation of the whole reactor system including feed-water and steam-line, as well the Isolation Condenser(s), the Accumulator(s) and the Gravity Driven injection system (not represented to scale) 48
Figure 28. Power distribution along the 20 node elements at each stage and per each fuel assembly 49
Figure 29. Cladding temperature in the middle of the cooling channels obtained during steady-state initialisation by the standard correlation in RELAP/SCSAPSIM and by the Bishop et al. correlation 50
Figure 30: Steady-state distribution of core temperatures with even core singular pressure drop distribution 50
Figure 31: Pressure trends along the reactor core average and hot channels at different values of surface roughness 51
Figure 32: Behaviour of flow rates during steady-state initialisation 52
Figure 33: Steady-state distribution of core temperatures with optimised core orificing 54
Figure 34: Inner moderator channels and plena temperature with optimized orificing 54
Figure 35: Pressure distribution across the average and hot channels with optimised orificing. 54
Figure 36: Fluid temperature along the upward moderator flow passing through the fuel boxes 55
Figure 37: Power exchanged with the fluid during the whole transient 56
Figure 38: Pressure at various locations in the vessel 57
Figure 39: Relevant flow rates in the vessel 58
Figure 40: Natural circulation flow paths established during the SBO sequence: the orange path is related to the 1st loop mentioned in the text, the yellow one is related to the 2nd, while the red arrow point outs a backward circulation observed at the 7th stage of the moderator channels . 59
Figure 41: Moderator flows in the vessel 59
Figure 42: Moderator flows in inner fuel channels 59
Figure 43: Coolant flows in fuel channels 60

Figure 44: Void fraction in coolant channels 60
Figure 45: Accumulator and isolation condenser flow rates 61
Figure 46: Fluid temperatures in the vessel moderator regions 61
Figure 47: Fluid temperatures at the inlet and at the outlet of the fuel channels 61
Figure 48: Cladding temperature at different levels in at middle length in fuel rods 62
Figure 49: IC and accumulator flow rates in the base case and with lowered IC 63
Figure 50: Temperatures in the vessel in the base case and with lowered IC 64
Figure 51: Moderator flows in average channels in the base case and with lowered IC 64
Figure 52: Hot fuel channel flows in the base case and with lowered IC 64
Figure 53: Cladding temperatures at mid hot fuel channels in the base case and with lowered IC 65
Figure 54: Fluid temperatures at inlet and outlet of fuel channels with lowered IC 65
Figure 55: Pressure in the vessel in the base case and with K = 5 66
Figure 56: IC and accumulator flow rates in the base case and with K = 5 66
Figure 57: Moderator flow rates in the vessel in the base case and with K = 5 66
Figure 58: Main temperatures in the vessel in the base case and with K = 5 67
Figure 59: Average moderator channel flows in the base case and with K = 5 67
Figure 60: Hot fuel channel flows in the base case and with K = 5 67
Figure 61: Average fuel channel flows in the base case and with K = 5 67
Figure 62: Cladding temperature in mid hot channels in the base case and with K = 5 68
Figure 63: Cladding temperature in mid average channels in the base case and with K = 5 68
Figure 64: Pressure in the vessel in the base case and without orifices 68
Figure 65: IC and accumulator flow rates in the base case and without orifices 69
Figure 66: Moderator flow rates in the vessel in the base case and without orifices 69
Figure 67: Main temperatures in the vessel in the base case and and without orifices 69
Figure 68: Average moderator channel flows in the base case and and without orifices 70
Figure 69: Hot fuel channel flows in the base case and and without orifices 70
Figure 70: Average fuel channel flows in the base case and and without orifices 70
Figure 71: Cladding temperature in mid hot channels in the base case and and without orifices 70
Figure 72: Cladding temperature in mid average channels in the base case and without orifices 71
Figure 73: Pressure trend 72
Figure 74: Overall vessel flows 72
Figure 75: Void fractions at fuel channel inlet and outlet 72
Figure 76: Gravity driven injection flow rate 72
Figure 77: IC flow rate 72
Figure 78: Overall moderator flow rates 73
Figure 79: Main fluid temperatures in vessel 73
Figure 80: Hot inner moderator channel flows 73
Figure 81: Avg inner moderator channel flows 73
Figure 82: Hot fuel channel flows 73
Figure 83: Avg fuel channel flows 73
Figure 84: Fluid inlet and outlet fuel channel temperatures (Levels 1 to 3) 74
Figure 85: Fluid inlet and outlet fuel channel temperatures (Levels 6 to 7) 74

Figure 86: Cladding temperature in mid hot and average channels 74
Figure 87: Pressure in the vessel 75
Figure 88: GDCS and IC flow rates 75
Figure 89: Sequence of pressure, void fraction and temperatures along the IC path at three different times in the transient 75
Figure 90: Overall moderator flows and temperatures in the vessel 76
Figure 91: Inner moderator channel flows 76
Figure 92: Fuel channel flows 76
Figure 93: Cladding temperatures in mid hot and average channels 76
Figure 94: Steady-state distribution of core temperatures for the base case 77
Figure 95: Steady-state distribution of core fluid density for the base case 77
Figure 96: Steady-state distribution of inner moderator fluid density for the base case 78
Figure 97: Steady-state distribution of moderator fluid density for the base case 78
Figure 98: Steady-state distribution of fuel channel pressures in the base case 78
Figure 99: Transient trend of pressure in the vessel for the base case 79
Figure 100: Accumulator system flow rate in the base case 79
Figure 101: Transient trend of IC flow rate in the base case 79
Figure 102: Transient trend of flows in the vessel for the base case 79
Figure 103: Transient trend of cladding temperature for the base case 80
Figure 104: RPV diagram of the Apros model 83
Figure 105: User Component model of the fuel and moderator box channels 84
Figure 106: Primary loop model of Apros 86
Figure 107: One loop of the passive heat removal system of Apros 88
Figure 108: One accumulator model of Apros 88
Figure 109: The MOX and the pure UO_2 loading maps of the Serpent 2 model 89
Figure 110: Nodal power distribution per assembly 90
Figure 111: Pressure profile along the coolant channels 90
Figure 112: Temperature profile of the moderator boxes 91
Figure 113: Density profile of the moderator boxes 91
Figure 114: Temperature profile of the coolant channels 91
Figure 115: Density profile of the coolant channels 91
Figure 116: Cladding temperature profiles 91
Figure 117: Central fuel temperature profiles 91
Figure 118: Nodal power distribution per assembly 94
Figure 119: Pressure profile along the coolant channels 94
Figure 120: Temperature profile of the moderator boxes 94
Figure 121: Density profile of the moderator boxes 94
Figure 122: Temperature profile of the coolant channels 95
Figure 123: Density profile of the coolant channels 95
Figure 124: Cladding temperature profiles 95
Figure 125: Central fuel temperature profiles 95
Figure 126: Nodal power distribution per assembly 97
Figure 127: Pressure profile along the coolant channels 97
Figure 128: Temperature profile of the moderator boxes 97
Figure 129: Density profile of the moderator boxes 97

Figure 130: Temperature profile of the coolant channels 97
Figure 131: Density profile of the coolant channels 97
Figure 132: Cladding temperature profiles 98
Figure 133: Central fuel temperature profiles 98
Figure 134: Nodal power distribution per assembly 98
Figure 135: Pressure profile along the coolant channels 98
Figure 136: Temperature profile of the coolant channels 99
Figure 137: Density profile of the coolant channels 99
Figure 138: Cladding temperature profiles 99
Figure 139: Central fuel temperature profiles 99
Figure 140: Nodal power distribution per assembly 100
Figure 141: Pressure profile along the coolant channels 100
Figure 142: Temperature profile of the coolant channels 100
Figure 143: Density profile of the coolant channels 100
Figure 144: Cladding temperature profiles 101
Figure 145: Central fuel temperature profiles 101
Figure 146: Nodal power distribution per assembly 102
Figure 147: Pressure profile along the coolant channels 102
Figure 148: Temperature profile of the coolant channels 102
Figure 149: Density profile of the coolant channels 102
Figure 150: Cladding temperature profiles 102
Figure 151: Central fuel temperature profiles 102
Figure 152: Temperature profile of the average coolant channels 104
Figure 153: Pressure profile along the average coolant channels 104
Figure 154: Hot channel cladding temperature profiles 104
Figure 155: Hot channel central fuel temperature profiles 104
Figure 156: Temperature profile of the average coolant channels 105
Figure 157: Pressure profile along the average coolant channels 105
Figure 158: Hot channel cladding temperature profiles 105
Figure 159: Hot channel central fuel temperature profiles 105
Figure 160: Temperature profile of the average coolant channels 106
Figure 161: Pressure profile along the average coolant channels 106
Figure 162: Hot channel cladding temperature profiles 106
Figure 163: Hot channel central fuel temperature profiles 106
Figure 164: Temperature profile of the average coolant channels 107
Figure 165: Pressure profile along the average coolant channels 107
Figure 166: Hot channel cladding temperature profiles 107
Figure 167: Hot channel central fuel temperature profiles 107
Figure 168: Average channel cladding temperature profiles 107
Figure 169: Hot channel cladding temperature profiles 107
Figure 170: Comparison of the optimised orifice sizes in the investigated cases 108
Figure 171: Pressure at various locations in the vessel 111
Figure 172: Moderator flow rates at various locations in the vessel 111
Figure 173: Flow rates at various locations of the primary system 111
Figure 174: Moderator flows in the boxes 112

Figure 175: Mass flow rates in the coolant channels 112
Figure 176: Void fraction in the coolant channels 113
Figure 177: Total mass flow rates of the accumulators 114
Figure 178: Water level of the accumulators 114
Figure 179: Collapsed water level in the IC tubes 114
Figure 180: Total mass flow rates of the Isolation Condensers 115
Figure 181: Thermal powers of the reactor and the IC system 115
Figure 182: PHRS tank average temperature 115
Figure 183: PHRS tank water level 115
Figure 184: Fluid temperatures at various locations in the vessel 116
Figure 185: Moderator box fluid temperatures 116
Figure 186: Coolant channel fluid temperatures 117
Figure 187: Cladding temperatures 118
Figure 188: Maximum coolant, cladding and central fuel temperatures of the stages 118
Figure 189: Total mass flow rates of the Isolation Condensers 120
Figure 190: Thermal powers of the reactor and the IC system 120
Figure 191: Moderator flows in the average boxes (Left – Base Case; Right – Lower IC) 120
Figure 192: Mass flow rates in the hot coolant channels (Left – Base Case; Right – Lower IC) 120
Figure 193: Total mass flow rates of the accumulators 121
Figure 194: Maximum cladding and coolant temperatures at stage 7 121
Figure 195: Void fraction in the 7th stage coolant channels (Left - Base Case; Right - Lower IC) 121
Figure 196: Steam line pressures 122
Figure 197: Maximum cladding and coolant temperatures at stage 7 122
Figure 198 Total mass flow rates of the Isolation Condensers 123
Figure 199 Thermal powers of the reactor and the IC system 123
Figure 200: Moderator flows in the average boxes 123
Figure 201: Mass flow rates in the hot coolant channels 123
Figure 202: Flow rates at various locations of the primary system 123
Figure 203: Main fluid temperatures in vessel 123
Figure 204: Void fraction in the 7th stage coolant channels 124
Figure 205: Collapsed water level in the IC tubes 124
Figure 206: Steam line pressures 125
Figure 207: Maximum cladding and coolant temperatures at stage 7 125
Figure 208: Total mass flow rates of the Isolation Condensers 126
Figure 209: Thermal powers of the reactor and the IC system 126
Figure 210: Void fraction in the 7th stage coolant channels 126
Figure 211: Collapsed water level in the IC tubes 126
Figure 212: Steam line pressures 126
Figure 213: Total mass flow rates of the Isolation Condensers 127
Figure 214: Total mass flow rates of the accumulators 127
Figure 215: Maximum cladding and coolant temperatures at stage 7 127
Figure 216: Void fraction in the 7th stage coolant channels 127
Figure 217: Feddwater line pressures 128

Figure 218: Maximum cladding and coolant temperatures at stage 7 128
Figure 219: Total mass flow rates of the Isolation Condensers 128
Figure 220: Thermal powers of the reactor and the IC system 128
Figure 221: Total mass flow rates of the accumulators 128
Figure 222: Void fraction in the 7th stage coolant channels 128
Figure 223: Mass flow rates in the coolant channels 129
Figure 224: Total mass flow rates of the Isolation Condensers 130
Figure 225: Total mass flow rates of the accumulators 130
Figure 226: Maximum cladding and coolant temperatures at stage 7 130
Figure 227: Void fraction in the 7th stage coolant channels 130
Figure 228: Total mass flow rates of the Isolation Condensers 131
Figure 229: Total mass flow rates of the accumulators 131
Figure 230: Maximum cladding and coolant temperatures at stage 7 131
Figure 231: Void fraction in the 7th stage coolant channels 131
Figure 232: The Gmsh model of the core (left), the assembly power distribution (centre) and the positioning of the hot (yellow), cold (dark blue) and average (aquamarine) fuel assemblies (right) in the SCW-SMR SPNDYN model. The symmetry plane is on the right side of the model. (Bertesina et al., 2023; Varju et al., 2024) 132
Figure 233: Nodal power distribution 135
Figure 234: Differences of the nodal power distribution 135
Figure 235: Temperature profile of the coolant channels 136
Figure 236: Density profile of the coolant channels 136
Figure 237: Temperature profile of the moderator boxes 137
Figure 238: Temperature profile in theupward moderator channel 137
Figure 239: Radially averaged fuel temperature profiles 137
Figure 240: Cladding temperature profiles 137
Figure 241: Disciplines involved in the design of a fuel rod and fuel assembly (Rao et al., 2014) 138
Figure 242: ASSERT-PV SC (“full“) discretization for the SCW-SMR fuel assembly 141
Figure 243: STAFAS (“1/8“) discretization for the SCW-SMR fuel assembly with the numbering of modelled subchannels (SC 1-9) and fuel rods (FR 1-7) 141
Figure 244: The cold, average and hot power levels for STAFAS subchannel analysis. 143
Figure 245: Comparison of MCTs calculated with ASSERT-PV SC and STAFAS v01 cold/ave/hot subchannel models 144
Figure 246: Comparison of MCTs calculated with ASSERT-PV SC and STAFAS v02 cold/ave/hot subchannel models 144
Figure 247: Comparison of MCTs calculated with ASSERT-PV SC and STAFAS v03 cold/ave/hot subchannel models 145
Figure 248: Comparison of MCTs calculated with ASSERT-PV SC and STAFAS (averaged v01, v02 and v03 calculation series) subchannel models 145
Figure 249: Dependence of the sound velocity of the mixture on the vapor content 151
Figure 250: Calculation models of the reactor primary circuit of a VVER type (a – sub-channel, system code, b – representative approach, c – detailed CFD model). 152
Figure 251: Saturation line with the consideration of supercritical region 153
Figure 252: Analogy of boiling and pseudo-phase transition 154
Figure 253: Determination of the specific heat of phase transition 155

Figure 254: Results of depressurization assessment from supercritical pressure depending on the initial temperature of the vapor phase 155
Figure 255: The SCW-SMR concept (a) and the core cross-section (b) general view 156
Figure 256: Cross section of the FAs model 156
Figure 257: General view of the calculation mesh constructed for the flow part and metal structures of the core 157
Figure 258: General view of the calculation model and boundary conditions specification applied for the steady state regime 157
Figure 259: Steady state conditions for operation at the nominal power (a – pressure drop, b – coolant temperature, c – velocity) 158
Figure 260: Dynamics of the pressure field change (a – Option #1, b – Option #2, c – Option #3) 160
Figure 261: Dynamics of changes in the maximum total pressure difference along the length of the assembly and stairs for each of the levels (a – Option #1, b – Option #2, c – Option #3) .. 161
Figure 262: Dynamics of changes in the maximum total pressure difference between FAs and the reflector/moderator for each of the levels (a – Option #1, b – Option #2, c – Option #3) 162
Figure 263: Maximum equivalent von Mises stress (a – Option #1, b – Option #2) 162
Figure 264: Maximum equivalent von Mises stress (left – Option #1, right – Option #2) non-linear case, level #7 163
Figure 265: Representation of the modelled SCW SMR internal region in MELCOR 164
Figure 266: SCW SMR core nodalization scheme in MELCOR 165
Figure 267: General approach to mass distribution of core structural components 165
Figure 268: Core internal radial boundary structures 166
Figure 269: Heat generation sources rates in the core 166
Figure 270: Reactor in-vessel TH scheme and cavity schematic view 167
Figure 271: Case #1. SA chronology 169
Figure 272: Case #2. SA chronology 170
Figure 273: Case #3. SA chronology 171
Figure 274: Case #4. SA chronology 172
Figure 275: Mass characteristics of the molten materials in lower plenum 173
Figure 276: Molten materials distribution in LP 174
Figure 277: Calculation model general view, boundary conditions and melt configuration 176
Figure 278: Functional dependence of ultimate strength on temperature (Holmström et al. (re-edition), 2017) 177
Figure 279: Comparative analysis of the reactor vessel initial temperature influence (a - initialization at minimum temperature, b - initialization at average temperature) 178
Figure 280: Comparative analysis of the influence of the method of determining the corium thermal conductivity (a - ideal mixture, b - assumption of additivity of the heat flux of i-fraction) 178
Figure 281: Effect of the choice of boiling correlation for the reactor vessel outer surface (HTC#1 - eq. 3a, HTC#1 - eq. 3b, HTC#3 - eq. 3c) 179
Figure 282: Temperature and dimensionless velocity fields at the reactor vessel failure time for Case#1 as a function of corium configuration 181
Figure 283: Dynamics of thickness and temperature change and shape at the reactor vessel failure time for Case#1 181

Figure 284: Temperature and dimensionless velocity fields at the reactor vessel failure time for Case#2 as a function of corium configuration 182
Figure 285: Dynamics of thickness and temperature change and shape at the reactor vessel failure time for Case#2 182
Figure 286: Temperature and dimensionless velocity fields at the reactor vessel failure time for Case#3 as a function of corium configuration 183
Figure 287: Dynamics of thickness and temperature change and shape at the reactor vessel failure time for Case#3 183
Figure 288: Temperature and dimensionless velocity fields at the reactor vessel failure time for Case#4 as a function of corium configuration 184
Figure 289: Dynamics of thickness and temperature change and shape at the reactor vessel failure time for Case#4 184
Figure 290: Change in the concentration field of the “light” component under dynamic stratification 185
Figure 291: Summary results of parametric analysis for the calculated cases 186

Related documents

- None

1 Introduction

The ECC-SMART project has as one of its main objectives the definition of the design requirements for Small Modular Reactors (SMRs) based on the Supercritical Water Reactor (SCWR) technology. The SCWR represents an innovative reactor concept, included in the six Generation IV designs (see the Page of SCWR on the GIF website), which has been developed in past decades mainly by proposing a number of large-scale reactors. Reviews of the different SCWR concepts proposed in past times are reported in textbooks appeared in literature, also as a result of national projects and general literature reviews (see Pioro and Duffey, 2007; Oka et al., 2010; Schulenberg and Starflinger, 2012), and in technical documents by IAEA resulting from Coordinated Research Projects aimed to gather results from the institutions contributing to the analyses of the scientific and technical issues to be solved to propose future prototype reactors (IAEA 2014; IAEA 2019a; IAEA 2020a).

Recently, Small Modular Reactors (SMRs) have gathered the attention of the nuclear scientific community for their potential advantages under several respects (IAEA 2020b). In particular, their low power level may reduce the consequences of severe accidents, possibly also decreasing their probability. Moreover, the possibility that the reactors can be at least in part manufactured in workshops and then installed in several modules on a site may considerably reduce the economic exposure encountered in the construction of large plants and may enhance the flexibility in responding to the needs of future electrical networks dominated by intermittent renewable energy sources.

These promising features may be combined with the inherently favourable characteristics of supercritical water reactor concepts, e.g., in terms of higher core outlet temperature with respect to current light water reactors (LWRs) and hence higher energy conversion efficiencies (in the range of 44%, see e.g., Pioro and Duffey, 2007; Schulenberg and Starflinger, 2012). Moreover, the more compact layout due to the use of a direct cycle is promising for reducing costs of the overall plant.

The above considerations justify the interest that triggered the proposal of the ECC-SMART project for the pre-conceptual analysis of a SCW-SMR. A possible SMR configuration with supercritical pressure water has been recently proposed by Schulenberg and Otic (2021) in the early phases of the project, exploiting and furthering previous experience gained in the design of the High Performance Light Water Reactor (Schulenberg and Starflinger, 2012) Unlike the previous proposal that involved a vertical core with three coolant passages, aiming to homogenise the bulk fluid temperature at each stage, the present concept features a seven-stage horizontal core made of short fuel elements, arranged in a 20x20 square matrix, with a total power of 290 MWth. At the exit of each stage, composed by a variable number of rows of fuel elements to account for the different density of the fluid, the coolant is fed to the inlet plena by returning channels arranged in a stair-like structure.

This novel concept was firstly examined by single channel analyses (Schulenberg and Otic, 2021) that proposed a preliminary characterisation of the fluid and the cladding behaviour that could be envisaged in the seven stages of the reactor core concept. Models of the reactor have been then developed by the RELAP code (RELAP5 Code Development Team, 2001; SCDAP/RELAP5 Development Team, 1998) at the University of Pisa and by the Apros code (Kurki, 2008) at the Budapest University of Technology and Economics (BME). Modelling assumptions were made on the basis of the data proposed in the documentation distributed in the frame of the project in electronic format, including CAD files.

This report summarises the results obtained in the frame of the work performed for the tasks 3.4.2, 3.4.3 and 3.4.4, related to the study of the pre-conceptual core layout and passive

safety concept for SCW-SMR respectively by the Limited Liability Company “IPP-Centre” (IPP), by the Budapest University of Technology and Economics (BME) and by the University of Pisa (UNIPI). The material presented herein is aimed mostly at assessing the suitability of the existing and further developed models for representing the phenomena envisaged in the postulated scenarios that may affect the proposed reactor concept. As in the general objectives of the ECC-SMART project, these represent pre-licensing studies aimed to propose guidelines for the future demonstration of the SCW-SMR concept considered in the project, to be considered as a workbench to refine methodologies and tools necessary for nuclear reactor analysis and proposing a strategy for the future licensing.

In particular, Chapter 2 is devoted to general considerations about the Canadian and Chinese reactor concepts. Chapter 3 reports in greater detail about the features of the concept proposed by Schulenberg and Otic (2021); Chapter 4 summarises the early work performed by the University of Pisa for model development and code improvement and application for the analysis of passive safety aspects, with particular attention to natural circulation phenomena; Chapter 5 presents a further work performed by BME in an in-depth analysis of the pre-conceptual core layout and passive safety concept; Chapter 6 reports the additional work performed by IPP in the safety and design analysis of the SCW-SMR concept. Finally, Chapter 7 draws conclusions about the overall work performed in this frame.

2 Passive systems in Canadian and Chinese SCW reactor concepts

In order to pave the way to the following discussion on passive system preliminarily identified for the studies reported in the present report, information on the systems identified in the Canadian and Chinese designs is reported below.

2.1 Canadian SCWR concept

2.1.1 General features of the Canadian SCW-SMR

Several options for the Canadian SCW-SMR core, fuel assembly and fuel channel were explored and discussed. To leverage the knowledge gained through the development of the Canadian SCWR (Yetisir et al., 2012), it was decided to scale down the Canadian SCWR to develop a supercritical water-cooled small modular reactor (SMR), hereafter referred to as Canadian SCW-SMR (Figure 1). The reference core concept consists of a pressure-vessel type inlet plenum linked to a low-pressure calandria vessel, which houses 188 fuel channels in a 250-mm lattice pitch. The operating pressure of the reactor is 25 MPa with a core outlet temperature of 450-500°C. An outlet header is installed inside the inlet plenum to reduce the pressure and temperature gradients over the header wall. A direct thermodynamic cycle has been adopted, eliminating the need for steam generators, and the single-phase coolant eliminates the need for a moisture separator (required in boiling water reactors).

The fuel assembly (Figure 2 (left)) consists of 64 fuel elements distributed into two rings around a central flow tube (Nava-Dominguez et al. 2016). All fuel elements are contained inside a double-wall structure with an insulator between the two walls. Coolant from the inlet plenum is distributed into the fuel channel through openings acting as orifices to control the mass flow rate and dampen instability. The coolant flows through four nozzles into the central flow tube and downward to the bottom of the fuel assembly. The coolant then reverses flow direction and travels upward through the fuel elements to the outlet header. Under accident conditions, the fuel cladding temperature may increase. Heat is then transferred through natural convection and radiation from the fuel cladding to the liner and subsequently to the moderator through the insulator. This would maintain the coolability of the fuel cladding and maintain its integrity under accident conditions.

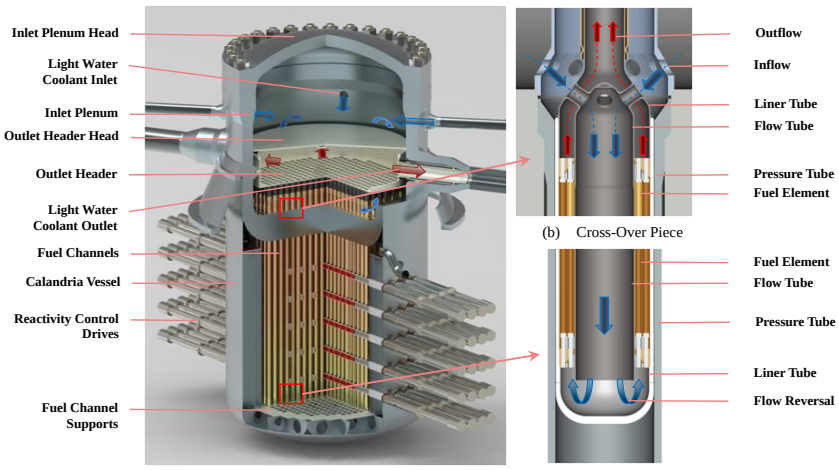

(a) Reactor Core (b) Cross-Over Piece (c) Bottom of Fuel Channel

Figure 1: Canadian SCWR and Canadian SCW-SMR core and fuel channel

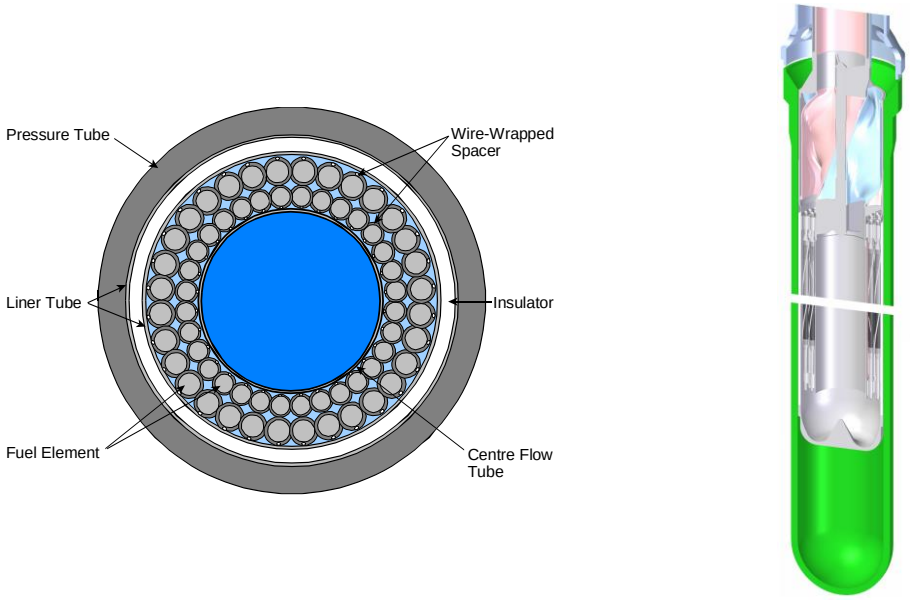

Figure 2: (left) Cross-sectional view of the Canadian SCWR and Canadian SCW-SMR fuel bundle, and (right) Canadian SCWR and Canadian SCW-SMR fuel channel

2.1.2 Safety Systems

Similarly to the Canadian SCWR, the Canadian SCW-SMR uses an Isolation Containment System (ICS) as a long-term heat removal system (Figure 3). Three heat exchangers are submerged in a cooling pool as shown in Figure 3(right). The dimensions of these heat exchangers are based on the BWRX-300 concept developed by GE-HITACHI (Pomogaev, 2022) as starting point, as the power produced is similar to the Canadian SCW-SMR.

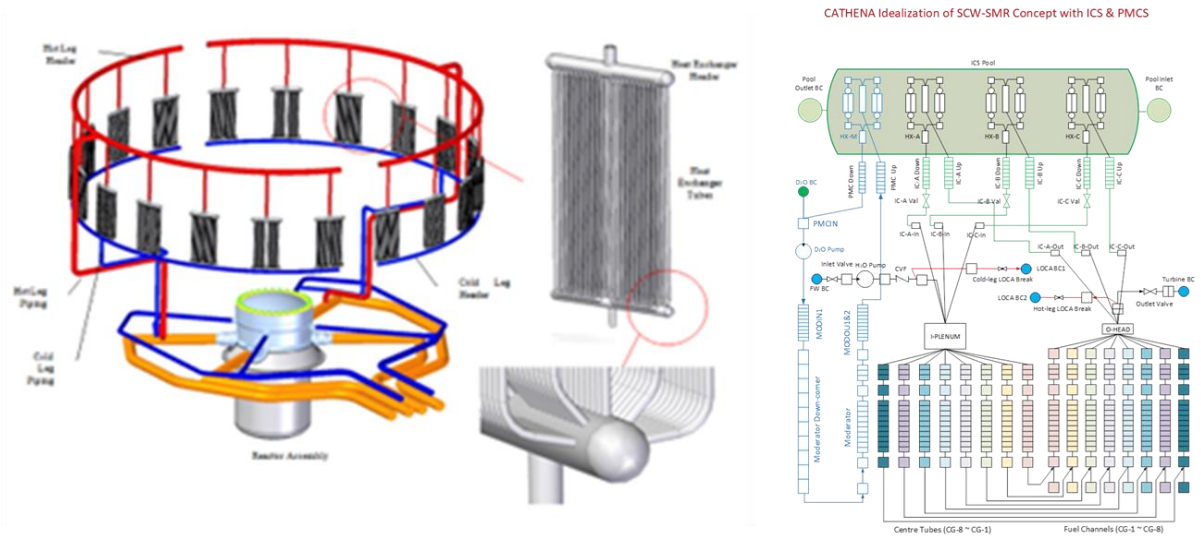

Figure 3: Isolation Condenser System layout for (left) Canadian SCWR, (right) Canadian SCW-SMR

The moderator system in the Canadian SCW-SMR is similar to the one of the CANDU type reactors, where the moderator is independent of the coolant and both systems are physically separated. All fuel channels are located inside a calandria vessel housing the low-pressure, low-temperature heavy-water moderator, which is cooled with a passive and active cooling systems.

Safety analyses were performed to quantify the safety performance and demonstrate the effectiveness of the safety system for four postulated accident events in the Canadian SCW-SMR concept. The events of interest include the following:

- Loss-of-coolant accident (LOCA), Cold-leg and Hot-Leg.
- Loss-of-flow accident (LOFA), which is also referred to as the loss-of-feedwater accident (LOFA) for the direct thermodynamic cycle.
- Station Black Out (SBO).

The results from these analyses showed that it is possible to have a natural circulation on the reactor core and the ICS. However, further analyses are needed to dimension properly the equipment used in the simulations.

2.2 Chinese SCWR concept

2.2.1 CSR150

The improved core conceptual design of CSR150 includes fuel design, assembly design and core fuel management design. The fuel design of CSR150 is based on CSR1000. The fuel rod consists of enriched UO_2 pellets with 310s cladding. In order to accommodate more fission gas and reduce the temperature in the centre of pellet, the centre hole design is adopted. The assembly design of CSR150 is different from the CSR1000; instead of water rod, the mixed moderators is adopted in the design. The core consists of 45 fuel assemblies. Two different enrichments of fuel assemblies are adopted to obtain flat power distribution. The two-pass coolant flow scheme is also adopted in the core design to get the high outlet coolant temperature.

2.2.2 Core Conceptual Design

2.2.2.1 Core design criteria

Referring to CSR1000, the core design criteria are as follows: ① Under normal condition, MCST (maximum cladding surface temperature) ≤650 °C; ② MLHGR (maximum linear heat generation rate) ≤39 kW/m.

2.2.2.2 Fuel assembly design

The Fuel Assembly design of CSR150 is based on CSR1000. The fuel rod structure is shown in Figure 4. As already mentioned, the fuel rod consists of enriched UO_2 pellets with 310s cladding; the fuel rod has a diameter of 9.5 mm and the cladding thickness is 0.57 mm. In order to accommodate more fission gas and reduce the temperature in the center of pellet, the center hole design is adopted.

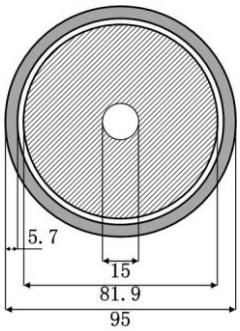

Figure 4. CSR150 fuel rod design.

Since supercritical water is used as the coolant, the moderating capacity of the assembly is insufficient. The concept of “water rod” is often applied for the assembly; although this design can improve the moderating capacity, it makes the system too complex and difficult to achieve in the industry. Different from the CSR1000, in order to simplify the design and improve safety, instead of the water rod, a new fuel assembly with mixed moderators is devised. The square fuel assembly shows good neutronics and thermal-hydraulics performance and structural implementation ability and is chosen as the fuel assembly of CSR150 conceptual design.

The square fuel assembly structure is shown in Figure 5. The square fuel assembly with solid moderator rod consists of 4 sub-assemblies. The gap between subassemblies is filled with coolant and the channel between subassemblies is liquid moderator. There are 56 fuel rods and a centre solid moderator rod (4×4 lattice cells) per subassembly. The edge distance of fuel assembly is 119.5 mm and the centre distance is 239.0 mm. The fuel assembly wall thickness is 2.0 mm and the solid moderator rod wall thickness is 0.8 mm. A cruciform-shaped control rod is adopted in the centre of assembly and the material is B_4C. The solid moderator is made of zirconium hydride material and is surrounded by an air chamber and cladding to contain the released hydrogen under the accident condition.

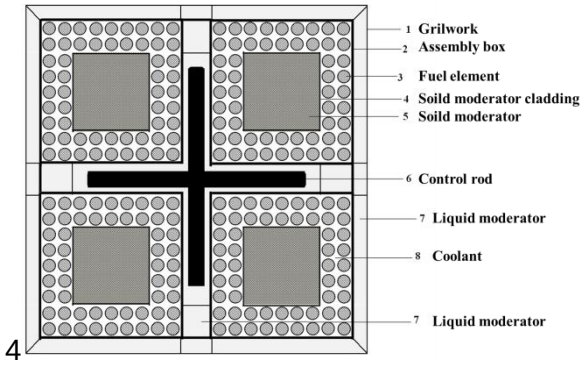

4

Figure 5. Mix Moderator Fuel Assembly Design.

2.2.2.3 Core design

Referring to the design of CSR1000, the following core design parameters have been determined from the viewpiont of the core performance and scale requirements. The average coolant core outlet temperature has been increased from 500 °C of the CSR1000 design to 520 °C.

- Core pressure: 25 MPa;
- Core thermal power: 150 MW;
- Core average inlet/outlet temperatures: 280/520 °C;
- Average linear heat generation rate(ALHGR) : 14.9 kW/m;
- Number of fuel rods per assembly: 224;
- The active core height: 2.5m;
- Average ^{235}U fuel enrichment: high enrichment: 7.2 wt%. low enrichment:5.6 wt%.

The fuel loading patterns are shown in Figure 6.

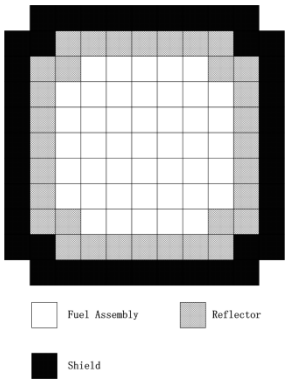

Figure 6. CSR150 fuel loading patterns.

2.2.2.4 Coolant flow scheme

A new flow scheme has been devised. The 24 fuel assemblies in periphery are the first flow path assemblies, in which the coolant flows from top to bottom. The other 21 fuel assemblies in centre are the second flow path assemblies, in which the coolant flows from bottom to top. the new coolant flow scheme in Figure 7.

	I	I	I	I	I	
I	I	II	II	II	I	I
I	II	II	II	II	II	I
I	II	II	II	II	II	I
I	II	II	II	II	II	I
I	I	II	II	II	I	I
	I	I	I	I	I	

Figure 7. The new Coolant Flow Scheme of CSR150.

About 10% of the inlet coolant flows down the downcomer, and the rest is guided to the top dome and distributed to: ① 70% flows as the first flow pass coolant, ② 10% flows as the first flow pass moderator, ③ 10% flows as the second flow pass moderator. ④ the peripheral mixed coolant finally rises in the core through the fuel channels of second flow pass.
On the one hand, the new flow scheme can reduce the cladding temperature of the peripheral assembles, on the other hand, it can increase the core outlet temperature and improve the power generation efficiency.

2.2.3 Safety Systems

Similar to CSR 1000, a passive safety system is proposed for CSR 150 to increase the safety reliability at abnormal conditions. The passive safety system of CSR 150 is mainly made of the high pressure reactor make-up tank (RMT), the isolation condenser system (ICS), the automatic depressurization system (ADS), the gravity driven core cooling system (GDCS), the passive containment cooling system (PCCS) and the direct vessel injection (DVI).
The accidents of ‘‘pump seizure’’, ‘‘loss of coolant flow accidents (LOFA)’’, ‘‘core depressurization’’, as well as some typical transients are analysed with code SCTRAN, which is a one-dimensional safety analysis code for SCWRs. Further analyses are needed to dimension properly the equipment used in the simulations.

3 General considerations on passive system identification for the SCW SMR

When talking about innovative reactors, we should also remind about the safety requirements applicable in general to nuclear reactors: The safety systems shall be designed such that nobody shall be exposed to any serious radiation damage, neither during normal operation nor during any conceivable accident. For this purpose, neutron and gamma radiation must be shielded by providing sufficient lead, steel, or concrete structures or by water layers. Furthermore, radioactive material must be confined inside three leak-tight barriers, which are the fuel cladding, the primary system and the containment. These barriers are defended in depth like walls in medieval castles. Should any of these barriers fail, the other barriers shall take over the confinement. On a closer look, however, these basic principles are anything but well defined. According to the ALARA principle, the dose rate shall be as low as reasonably achievable, for which a clear definition is often missing and some accidents, e.g., an airplane crash, seem to be conceivable only in certain countries. Therefore, a nuclear design project for innovative reactors is well advised to specify the safety requirements precisely before starting the design process.

3.1 The first barrier of a SCWR

Like in a pressurized water reactor (PWR), in SCWRs the fuel claddings are exposed to an outer pressure, which is around 25 MPa instead of around 15 MPa under operating conditions. The inner pressure increases by about 10 MPa during burn-up, depending on the size of the fission gas plenum. If the fuel rods are filled with fuel pellets at a pressure of about 5 MPa under cold conditions, we expect an inner pressure around 15 MPa under hot conditions at the beginning of a burn-up cycle (BOC) due to thermal expansion of the helium inside. The inside pressure is increasing then to around 25 MPa at the end of a burn-up cycle (EOC). Thus, the pressure difference between outside and inside is around 10 MPa at BOC, decreasing to almost zero at EOC. Therefore, though having a higher pressure in a SCWR, the mechanical loads of the fuel claddings can be similar to those of PWRs. A major difference is rather due to the higher cladding temperatures, requiring stainless steels instead of Zircalloy. In any case, however, venting of fuel claddings is not allowed to avoid stresses.

3.2 The second barrier of a SCWR

A basic principle of SCWRs considered here is a once-through steam cycle as sketched in Figure 8. Feedwater, which is preheated to 280 °C is supplied to a reactor pressure vessel (RPV) at a pressure of around 25 MPa. It passes through the core without any recirculation and leaves the pressure vessel as superheated steam at a pressure of about 24 MPa with a temperature of about 500 °C. This steam is supplied directly to a high-pressure turbine and, after being reheated, to an intermediate pressure turbine and a low pressure turbine. The reheater and the latter turbines are not shown in Figure *8* for simplicity. The entire steam cycle is forming the primary system, which shall be leak-tight confining its radioactive inventory.

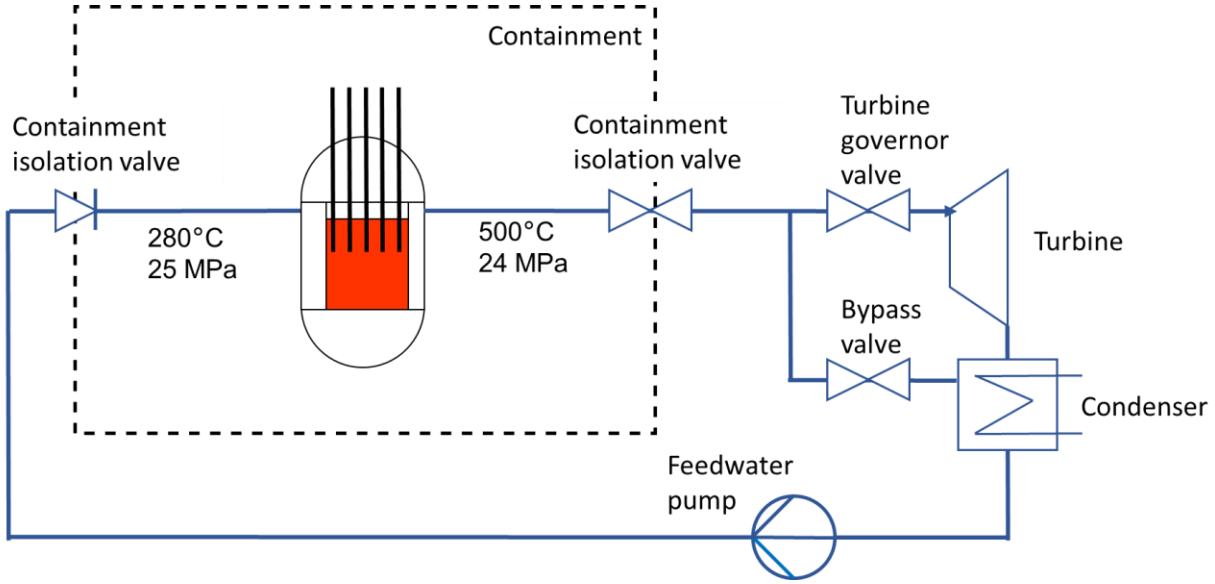

Figure 8: Once-through steam cycle of a SCWR

If the turbines, condensers and feedwater pumps are outside the containment, however, the second barrier is penetrating the third barrier during normal operation. Consequently, radioactive material, in particular N-16 which is produced from O-16 inside the reactor core, is transported to the steam turbine under normal operation. Therefore, the turbine building may only be entered with protective measures and the turbine parts become low-active radioactive waste at the end of their life. Close to the high-pressure turbine, a worker could receive a higher gamma dose rate when standing there during operation. With a half-life of 7 s, however, N-16, decays rapidly before reaching the condenser and the feedwater system. In case of leakage from the steam cycle, containment isolation valves need to be closed passively at the feedwater inlets to the containment, usually designed as check valves, and at the steam outlets. Such penetration of the second and third barrier is well-known from boiling water reactors and has been accepted there in several countries. We cannot claim *per se*, however, that such penetration of barriers will be accepted also for future reactors or in Countries which have never operated BWRs. It might be argued instead that this is violating the ALARA principle. Again, the safety system requirements of a SCWR should be specified precisely before starting the design process to clarify this issue.

3.3 Control under normal operation

Even though a SCWR has much in common with a BWR, it is controlled differently even under normal operation. As we see in Figure 9, a BWR has an internal coolant recirculation, usually driven by reactor internal coolant pumps. The coolant is partly evaporated in the core and steam and liquid are separated above the core. The saturated steam is dried and supplied to the turbine, while the liquid part is recirculated through a downcomer to the core inlet. In the upper load range, the core power can be controlled by the pump speed. The feedwater pump or its downstream valve is controlling the liquid level inside the reactor pressure vessel.

A SCWR, instead, does not have internal coolant recirculation as steam and liquid cannot be separated at supercritical pressure. The liquid coolant at core inlet is heated up until it becomes superheated steam at the core outlet. Now the feedwater pump or its downstream valve is controlling the core outlet temperature. The core power must be controlled by the control rods. In

both cases, the turbine governor valve is controlling the pressure inside the reactor pressure vessel. In case of a turbine trip, the turbine bypass valve is taking over this control function.

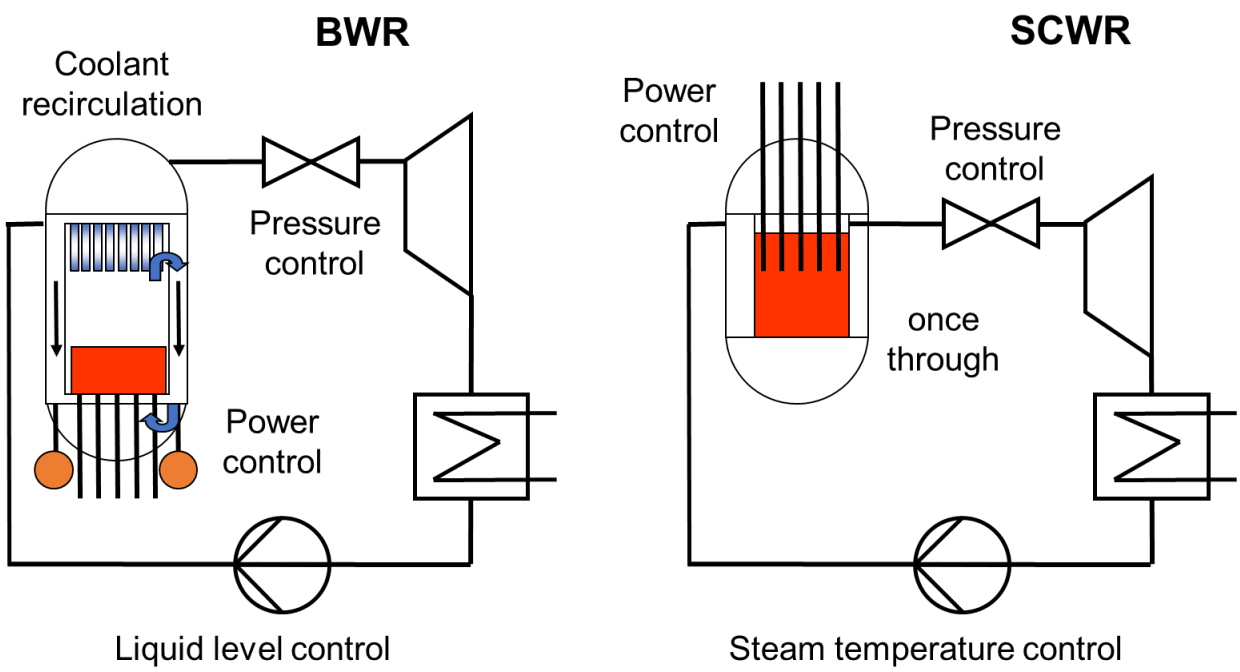

Figure 9: Generic differences between a BWR and a SCWR

This generic difference is causing also a different strategy for residual heat removal. Once a BWR has been shut down, the reactor internal pumps may be stopped and the residual heat may be removed from the core by natural convection, driven by the density difference between liquid water in the downcomer and steam inside the core. The residual heat removal system needs just to maintain sufficient coolant inventory inside the RPV. In a SCWR instead, the residual heat must be removed by forced convection through the core unless a natural convection loop is established outside the RPV after shut-down.

3.4 Safety systems

Besides these differences, however, there are several safety systems which are common for both reactor types. Shut-down rods are driven into the core causing reactor SCRAM. Boron can be injected as a second, independent shut-down system in case that these control rods were lost, e.g. during a core melt accident. Boric acid is not used in both cases for compensation of excess reactivity. Both reactor types need containment isolation valves (CIV) to close the third barrier in case of an accident. Then, pressure relief valves (PRV) must open, discharging steam into a cooled pool inside the containment and an active or passive system must refill the lost condensate into the RPV again. In case of steam release into the containment, the increase of containment pressure is limited by vent pipes running into a pressure suppression pool (PSP).

The minimum set of safety systems required for a SCWR is sketched in Figure 10. Systems which are used under normal operation are shown in blue. In case of a reactor SCRAM, the turbine is tripped by the emergency stop valve at the turbine inlet and the turbine bypass valve opens, both passively by a spring, keeping a high pressure inside the RPV. The containment isolation valves stay open. The feedwater pump is providing sufficient mass flow rate to cool the fuel rods as needed.

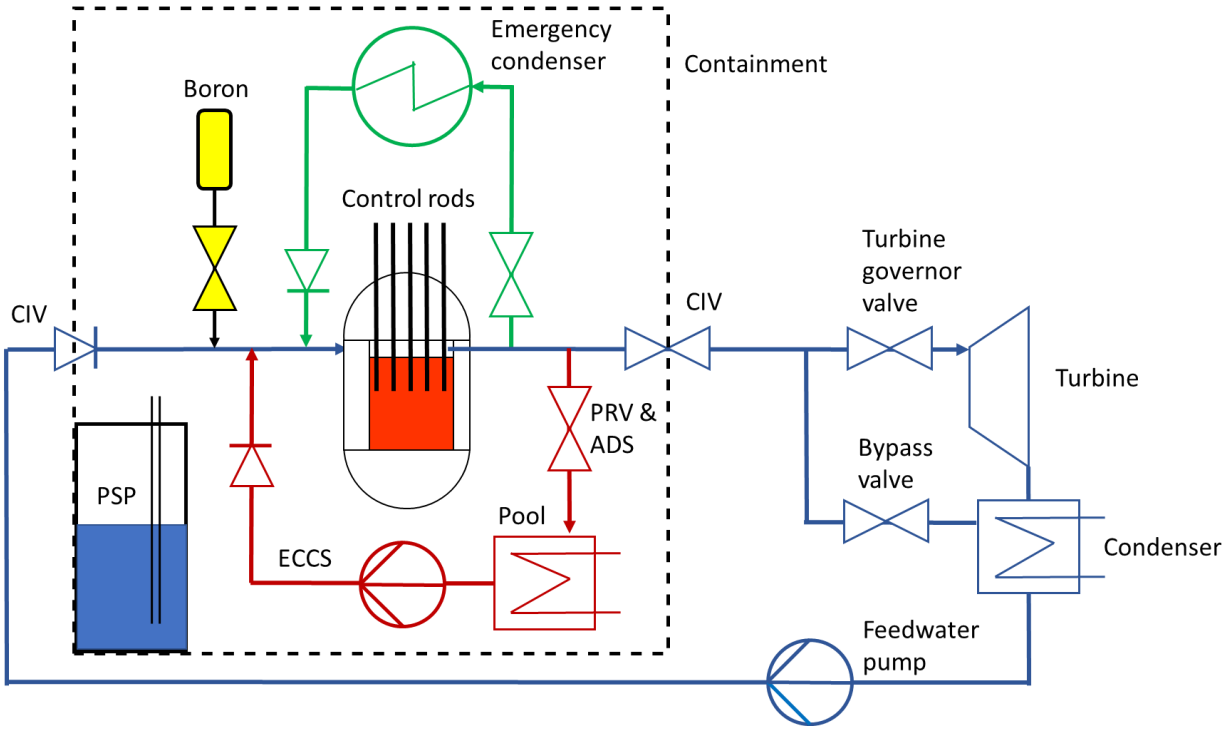

Figure 10: Minimum set of safety systems for a SCWR.

In case that the containment isolation valves were closed, the pressure relief valves must open to avoid a pressure increase inside the RPV. Without any coolant pump, however, they may not close again, but the core must be depressurized, at least slowly, by an automatic depressurization system (ADS) to maintain sufficient mass flow rate through the core. The released steam condenses in a cooled pool inside the containment, from where it can be pumped back into the RPV by an active emergency core cooling system (ECCS), shown in red in Figure 10.

How fast does this ECCS needs to be activated now? The feedwater temperature inside the RPV is less than 310 °C and this water stays liquid until a pressure of 10 MPa is reached. If the emergency core cooling pump can be activated within this time frame, the coolant injection system will drive the coolant flow through the core and the core stays well-cooled for long term. Once the saturation pressure has been reached, the feedwater inside the RPV starts boiling. The RPV acts now like a pressurizer. The produced steam keeps the pressure high enough to drive a coolant flow through the core until the water level drops down to the core inlet. Once the emergency core cooling pump starts injecting cold water into the RPV, however, the pressure inside drops rapidly, the core flow stops and the core overheats. It is necessary therefore to inject coolant immediately, e.g. within less than 20 s, which is quite a challenge for the diesel generators and for the pumps in case of loss of offsite power.

More grace time can be reached with a passive residual heat removal system, shown in green in Figure 10, which is favoured for a small modular reactor. In case of loss of offsite power, the reactor SCRAM causes a turbine trip and the containment isolation valves close. The pressure relief valves open and they stay open to depressurize the RPV, maintaining a minimum mass flow rate through the core. Then a riser to an emergency condenser opens and condensate from the emergency condenser returns, driven by gravity, replacing the evaporated coolant. Once this passive heat removal system is working, the pressure relief valves close again.

The emergency condenser may be placed outside the containment, releasing the residual heat to the atmosphere, which provides an unlimited heat sink. If an airplane crash has to be considered, however, a kerosene fire around this condenser would turn the heat sink into a heat source. In such cases, an emergency condenser inside the containment would be safer, heating up some internal water pools, which can provide a heat sink for at least 3 days. This will lead, of course, to a completely different containment design, demonstrating again that the safety system requirements should be well defined before starting the design work.

Residual heat removal by natural convection will work only if the reactor core is designed with horizontal or upward flow only. If superheated steam is produced at the core outlet, however, it has only a small specific heat and small local differences in core power or mass flow rate will result in large differences in coolant temperature, overheating some fuel rods. This problem is minimized by heating up the coolant step-wise, with an intensive coolant mixing between these steps to get rid of hot streaks. Therefore, the coolant inside the High Performance Light Water Reactor (Schulenberg and Starflinger, 2012) was intended to heat up in 3 upwards or downwards steps, with mixing plenums above and underneath the core. This design, however, did not allow a natural convection flow as siphons were formed by the plenums. An innovative design with horizontal fuel assemblies, as shown in Figure 11, might solve this problem (Schulenberg and Otic, 2021). The coolant is heated up inside the fuel assemblies with a horizontal flow, from left to right as shown in the side view, Figure 11 right, and is mixed between these steps when returning around the core, as shown in the front view in Figure 11, left. The coolant enters the internal flow path as liquid at stage 1 through an inlet header from below, and leaves the core as steam when exiting from stage 7.

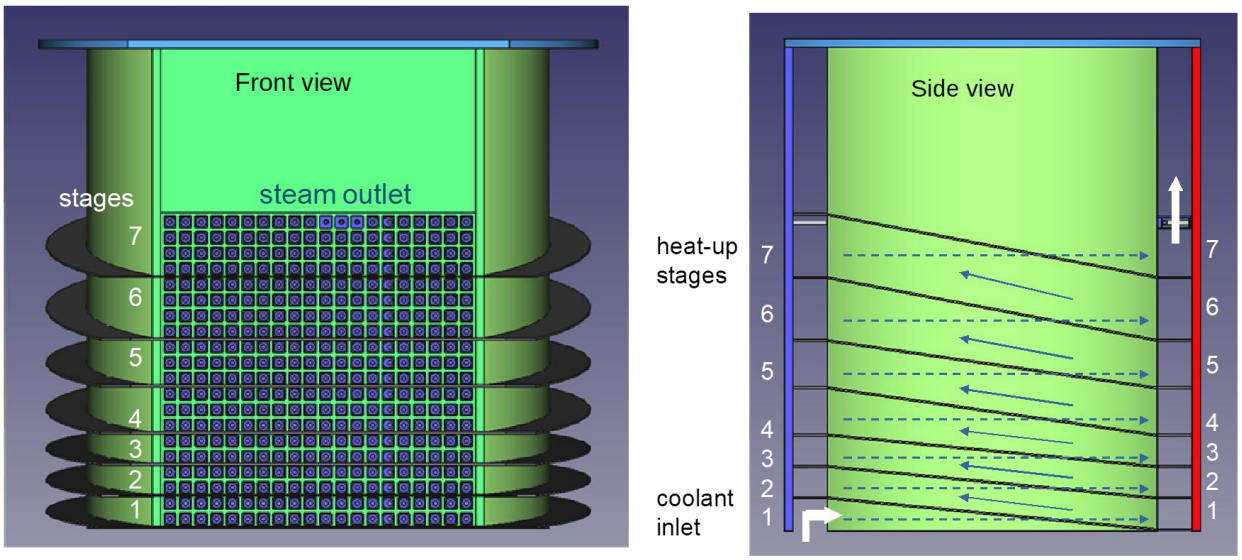

Figure 11: Core design with horizontal fuel assemblies and with 7 heat up stages with intermediate mixing.

3.5 Core design concept

A concept for such a core design has been described by Schulenberg and Otic (2012). The fuel assembly design is taken, in principle, from the HPLWR. Forty fuel rods with 8 mm outer diameter, but with 1680 mm active length only, are placed inside a square assembly box of 67.5 mm inner width. The fuel rods are wrapped by a wire of 1.34 mm diameter and 200 mm pitch as a spacer, which showed to provide good mixing inside the assemblies during the HPLWR project. In the

centre of the rod bundle is a square space for a moderator box with 26.9 mm outer width, as we can see in Figure 12.

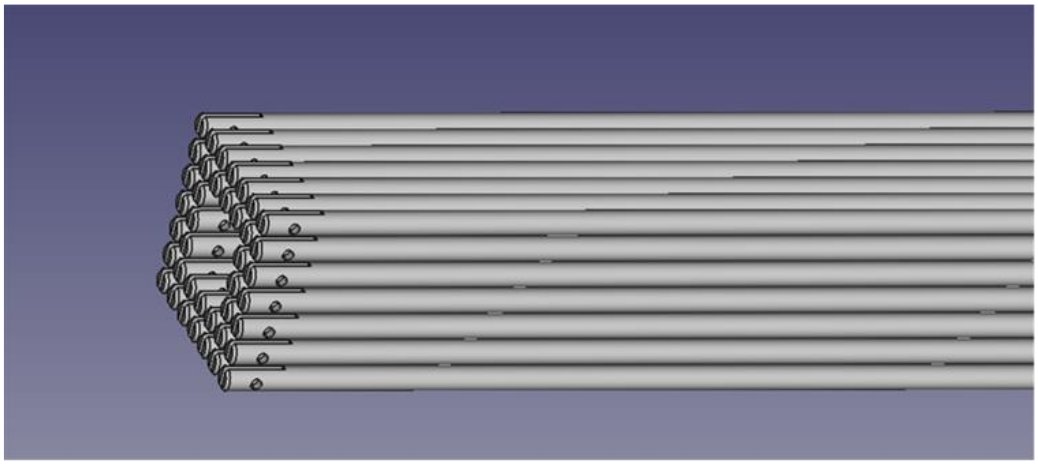

Figure 12: Rod bundle (wires removed)

The outer assembly box (Figure 13) is designed as a sandwich with a stainless steel liner of 0.4 mm thickness on the inside, facing the hot steam, a zircalloy structure with 2.5 mm thickness on the outside, facing the moderator, and a thermal insulation of yttria stabilized zirconia (7% YO_2 in ZrO_2) with a thickness of 4 mm and a thermal conductivity of around 2 W/mK in between. The inner moderator box is designed similarly, with a stainless steel liner of 0.4 mm thickness on the outside, a zircalloy structure with 0.8 mm thickness on the inside, and a thermal insulation of 2 mm thickness in between.

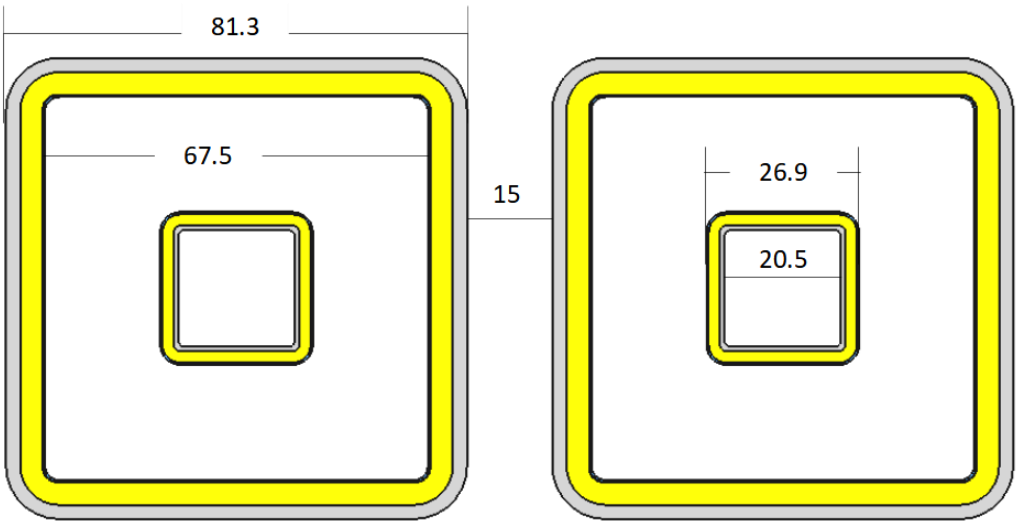

Figure 13: Assembly and moderator boxes made of Zircalloy-4 with a thermal insulation of Zirconia and a thin stainless steel liner on the hotter side each.

The moderator box (shown in pink colour in Figure 14) has cylindrical extensions on both ends, which shall penetrate the end plates after installation. The assembly box, shown in yellow, shall be welded with its square end into the head end tube sheet of the reactor core. A cylindrical extension at the opposite foot end will allow a sealing element such that the assembly box can freely expand when it warms up.

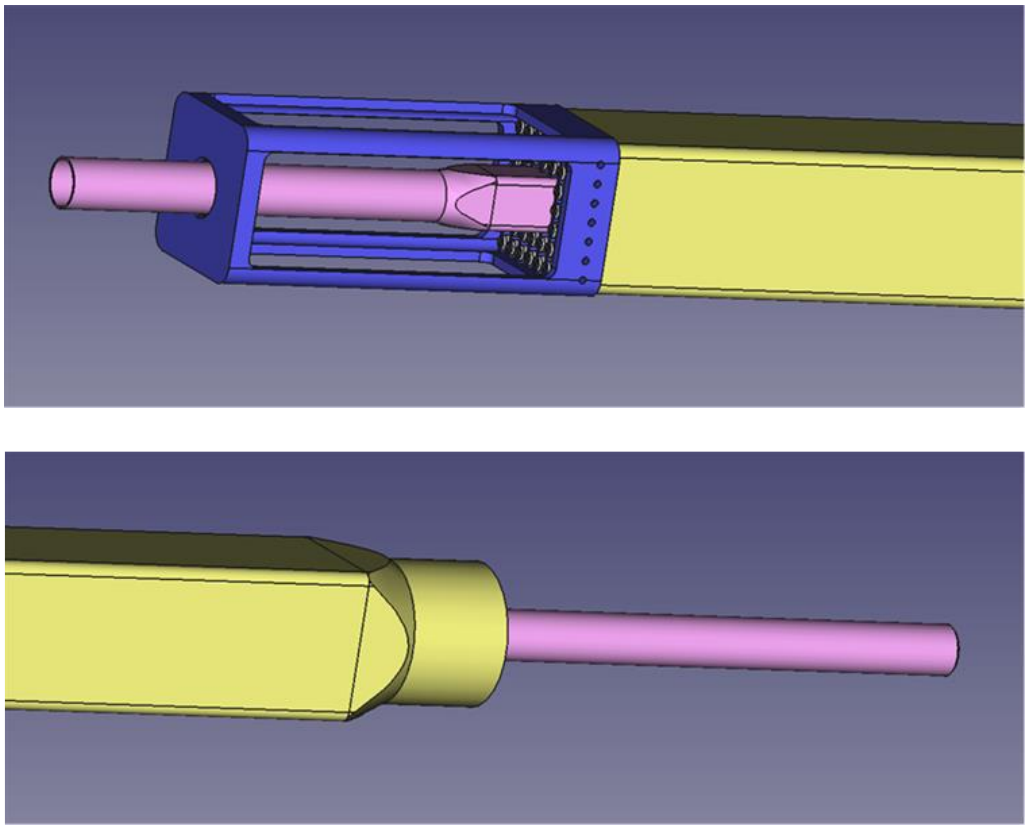

Figure 14: Head end (top) and foot end (bottom) of the fuel assembly.

The fuel rods are fixed in the head piece, shown in blue colour in Figure 14. Vertical grid plates and horizontal bolts are keeping the fuel rods in place. The rods can freely expand towards the foot end when getting hot. Headpiece and assembly box are not connected. Instead, the assembly box is assumed to be welded into the tube sheet, where it remains during fuel shuffling. During refuelling, the rod bundle can be pulled out by the head piece. The headpiece will need a spring element (not shown here yet) to be pressed by the end plate against the tube sheet.

3.6 Structures around the reactor core

A conceptual design of the structures around this core box shall fulfil the following general design requirements.

1. After the feedwater, considered here with 280 °C and 25 MPa, was entering the reactor pressure vessel, it needs to purge the entire pressure vessel from inside to keep it at a uniform temperature of about 280 °C. This requirement is important, in particular, for the large O-ring in the reactor flange, which does not allow much thermal deformations of the reactor pressure vessel to remain leak tight.
2. Following this task, the feedwater serves as moderator water in the gap volume between the assembly boxes, inside the moderator boxes and inside the reflectors. Therefore, its temperature must be kept well below the pseudo-critical temperature.
3. Temporary temperature changes of this moderator water might change the local power distribution inside the fuel assemblies. Therefore, the moderator water shall have a stable temperature distribution, in particular also in the large gap volume between the assembly

boxes. Otherwise, roaming hot spots due to natural convection phenomena could cause instabilities of the core power distribution.

4. Like between the heat-up steps of the reactor core, the coolant should be well mixed before entering the first heat-up step.
5. Last but not least, the moderator flow path should be kept simple to enable a natural convection loop for residual heat removal.

These design requirements can be met, in principle, with a moderator flow path as indicated in Figure 15. After entering the reactor pressure vessel, most of the feedwater shall be directed downwards to the lower plenum and only a small fraction, e.g. 20 kg/s, to the upper plenum. Orifices on the way upwards can optimize the flow split as needed. The moderator water through the fuel assembly gaps and through the reflector shall rise upwards from the lower plenum to yield a stable temperature distribution inside the gap volume: cold on bottom and warm on top. With 11.3 MW of heat transferred over the assembly box walls, the moderator water will not exceed 300 °C in average. After being mixed with the feedwater given to the upper plenum, the moderator water shall run horizontally through the 400 parallel moderator tubes. The heat-up there may differ significantly and mixing of the moderator water shall be foreseen before entering the reactor core at the bottom.

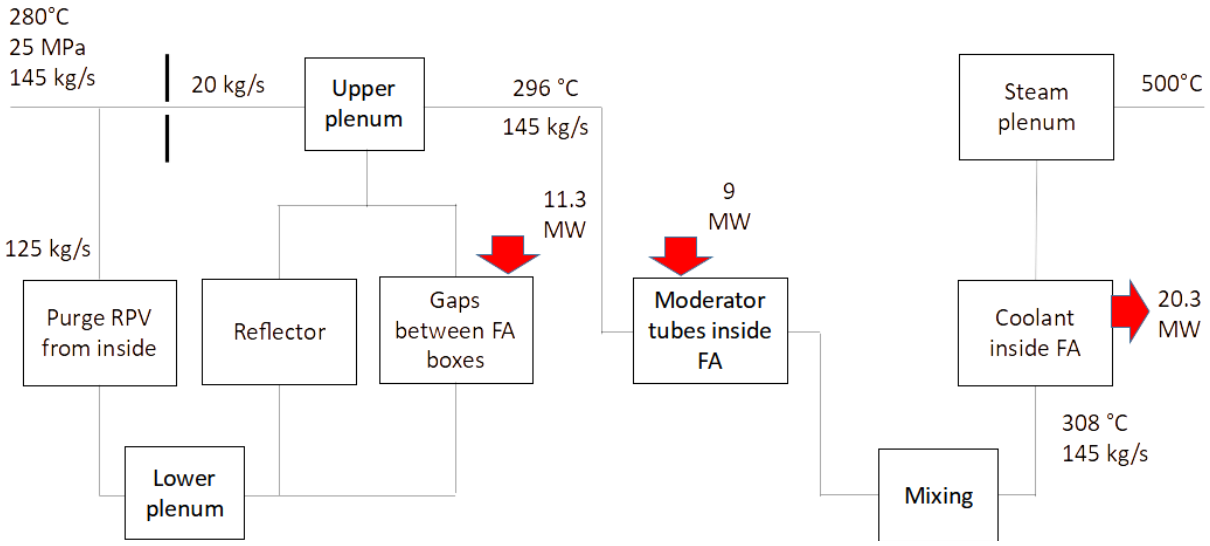

Figure 15: Principle sketch of the moderator flow path.

The following figures shall give a first impression of how such a flow path can be realized. Please note, however, that these are only sketches to illustrate some basic design features. They should not be considered as drawings.

A sketch of the reactor pressure vessel (RPV) is shown in Figure 16. The reactor closure head has been removed. In this example, two feedwater lines and two steam lines are foreseen, but the design could be modified as well to more or less feedwater and steam flanges, if needed. Like with the HPLWR, a core drum, shown in grey, is suspended in the reactor flange. Four fins, acting as a radial alignment of the core drum, are foreseen in the lower plenum of the RPV. Orifices in the suspension ring, of which just four ones are shown as examples here, determine the mass flow of feedwater penetrating to the upper plenum. The hot steam lines must be shielded from the RPV by coaxial steam pipes, shown in red, like with the HPLWR design. The core box, including the reactor core, may be inserted into the core drum from above. Four rails on the inside of the core drum shall help to align the core box precisely.

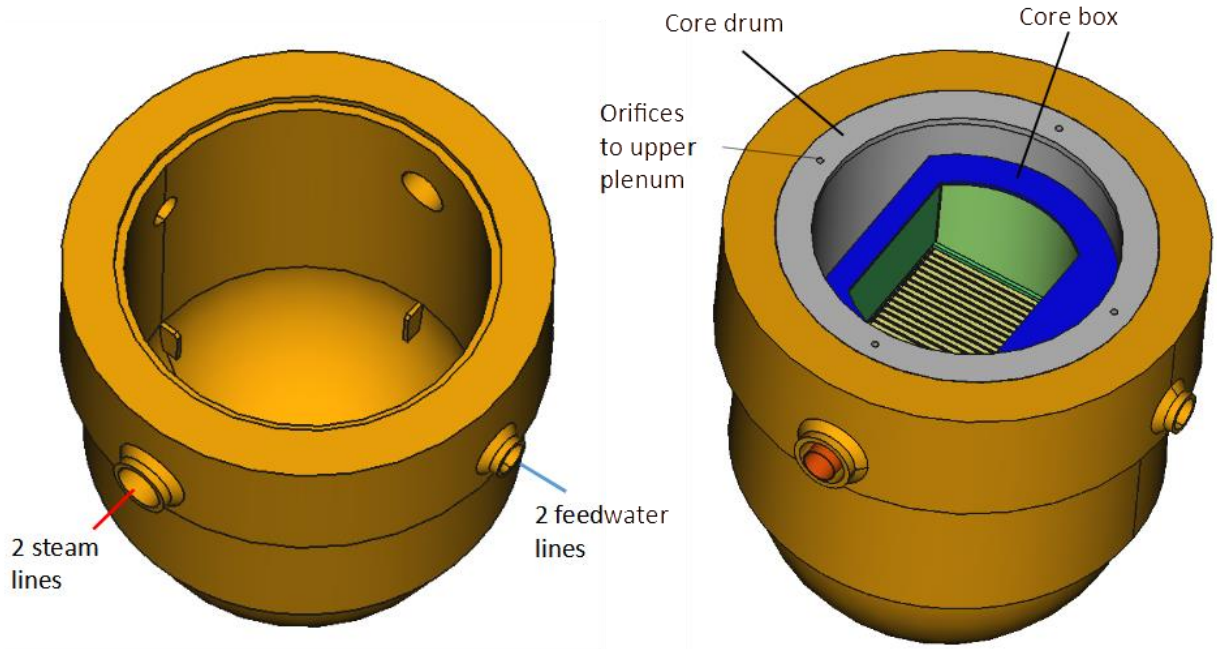

Figure 16: Sketch of the reactor pressure vessel, empty (left) and with core drum and core box inserted (right). Reactor closure head removed.

The core drum is designed with a double bottom with penetrations as shown in Figure 17. A large square window in the bottom allows the moderator water from the lower plenum to reach the gap volume between the assembly boxes. Additional orifices on both sides adjust the mass flow of moderator water given to the reflector. Their number and diameters can be modified as required for each specific reflector design.

The lower plate of the core bottom has been colored in green to differ it from the upper plate. In a top view, Figure 17 and Figure 18, left, we see that the upper plate has two additional large openings: One for the moderator water coming from the outlet plenum of the horizontal moderator tubes, and another one leading to the inlet header of the core, shown in Figure 11. If the green bottom plate is removed, we see in Figure 18 (right) from below that moderator water is guided through two mixing channels from the outlet plenum of moderator tubes, around the square window and around the reflector water supply channel, to the core inlet.

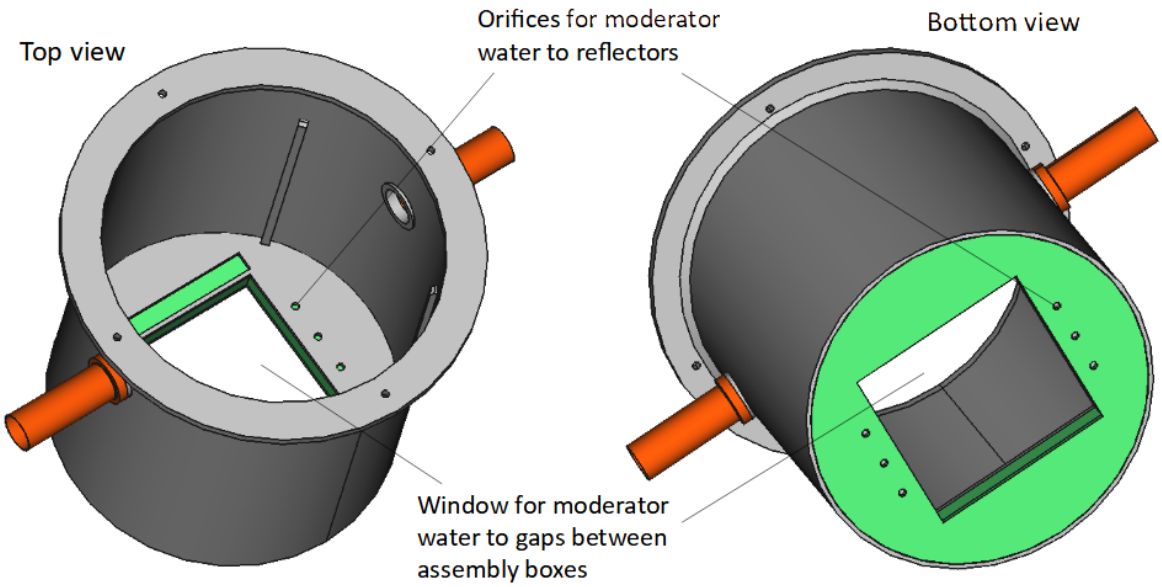

Figure 17: Design of the core drum with double bottom.

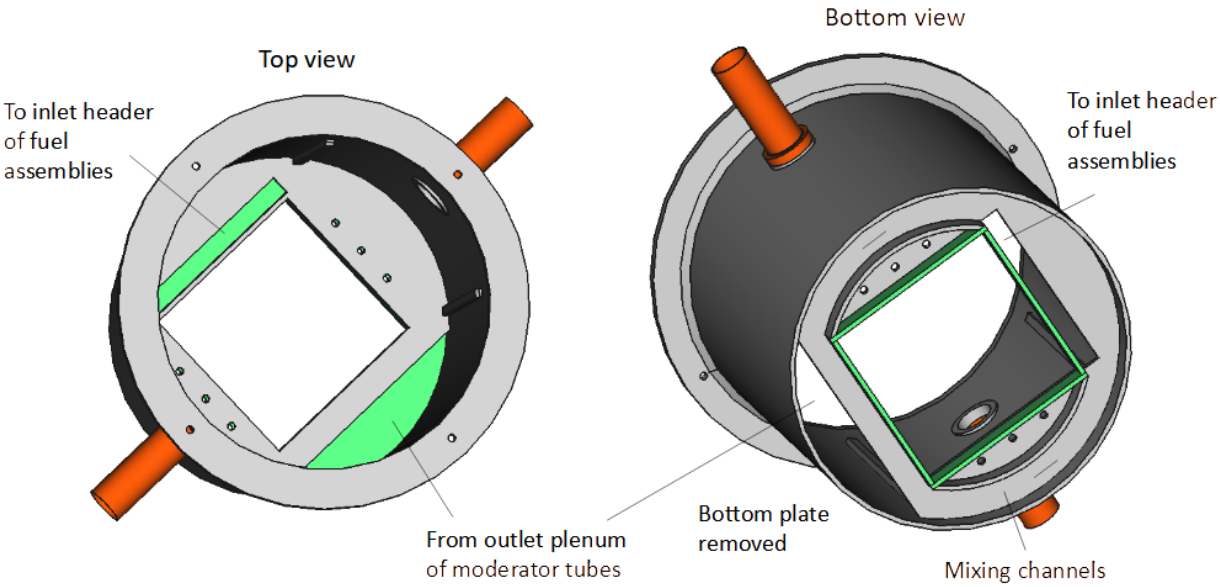

Figure 18: Flow path from the outlet plenum of moderator tubes to the core inlet header inside the double bottom of the core drum.

A top view of the total arrangement of RPV, core drum and core box (Figure 19), is showing now how the moderator water rising upwards between the assembly boxes is first merged above the core with water from the two reflectors and released downwards then to the inlet plenum of moderator tubes on the left side. The outlet plenum of moderator tubes, on the right side, is closed by the top plate of the core box, but open to the bottom instead. Consequently, the moderator water is driven from left to right through the moderator tubes, i.e. from foot piece to head piece like the coolant.

The reflector volume is shown here just as an empty space, filled with moderator water, but it may as well be filled with a solid reflector material instead, e.g. with beryllium pebbles. In

this case, cover plates with penetrations will be needed the on top and bottom of the reflector to keep the pebbles inside.

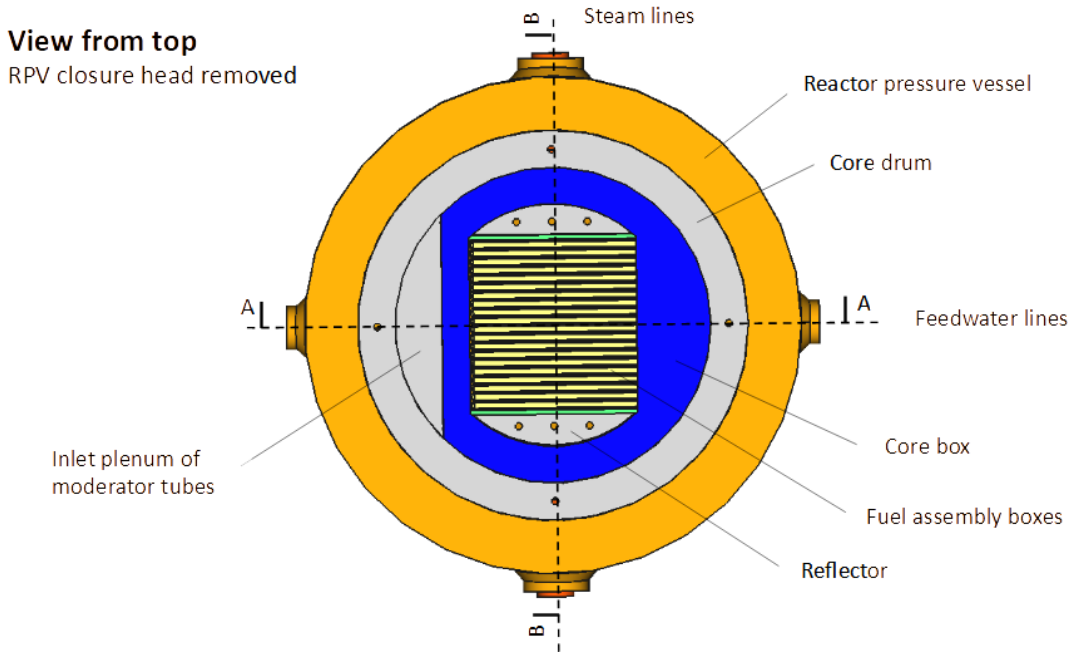

Figure 19:Top view of the total arrangement of RPV, core drum and core box.

Two vertical cross sections, of which one is taken through the feedwater lines (A-A) and another one through the steam lines (B-B), shall illustrate this flow path from a different view, shown in Figure 20.

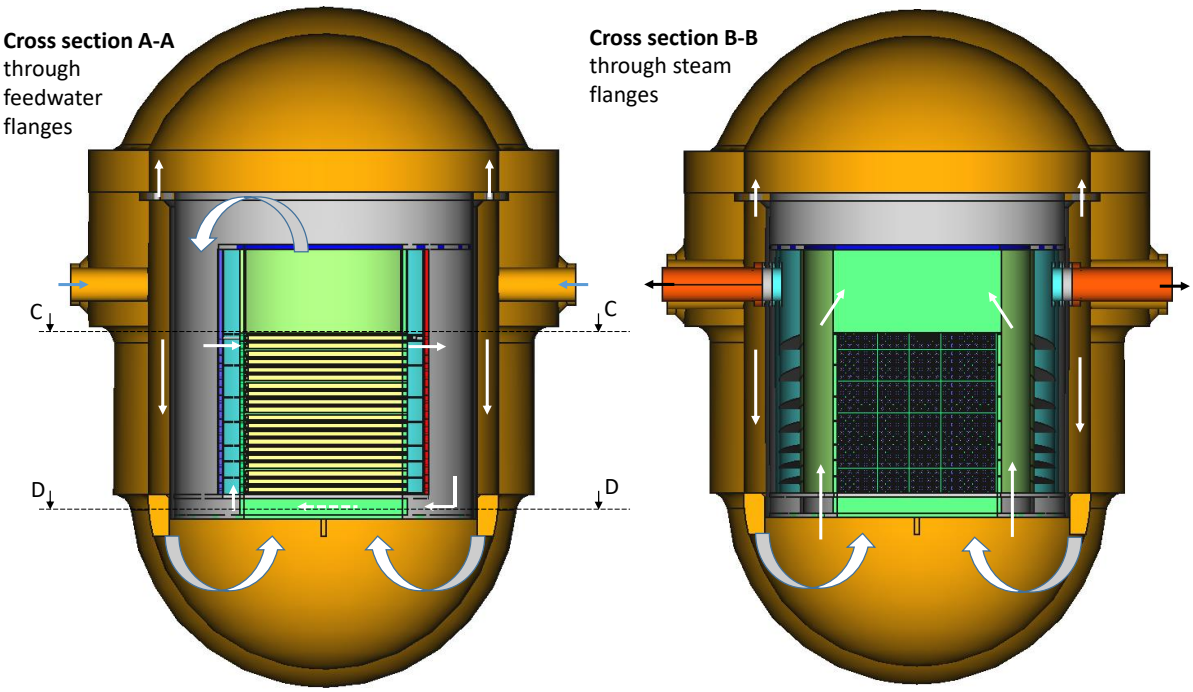

Figure 20: Vertical cross sections through the reactor.

Most of the feedwater supplied through the two feedwater flanges is supplied through the downcomer to the lower plenum, and only a small part is entering the upper plenum through the orifices of the core drum. Control rods, theirs drives and their guide tube assembly above the reactor core are not shown yet in this sketch. From the lower plenum, the moderator water is rising through the square window of the bottom of the core drum, and through the gaps between the assembly boxes. Both parts are merged above the reactor core, as shown in Figure 20, right. Figure 20, left, shows that the water running through the horizontal moderator tubes can enter from above on the left side and can be released to the bottom on the right side. From there, it flows around the bottom window of the core drum to the core inlet header on the left.

Two horizontal cross sections, of which Figure 21 is taken at the core top (C-C) and Figure 22 through the double bottom of the core drum (D-D), are illustrating this flow path again. The inlet plenum of the moderator tubes appears in gray in Figure 21, because it is closed at the bottom, and the outlet plenum appears in green, because it is open at the bottom, giving view onto the green bottom plate of the core drum.

Three rod bundles and their moderator tubes are installed exemplarily to illustrate how the moderator tubes are connected with the inlet and outlet plenums. The three orifices at the bottom of each reflector appear in brown color, as we are looking down there to the RPV bottom. Figure 21 can show as well that the four rails of the core drum are not only needed to align the core box, but also to minimize a bypass flow from the inlet to the outlet plenum.

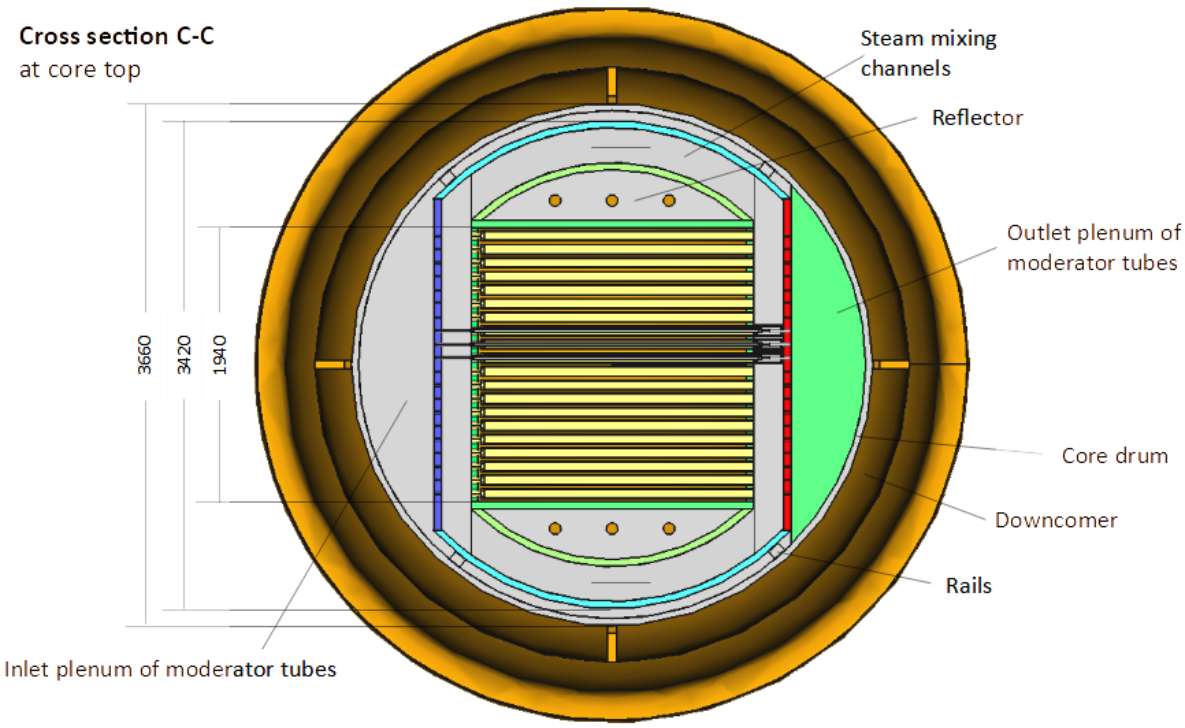

Figure 21: Horizontal cross section above the reactor core, looking downwards.

With 20x20 fuel assemblies, the core has a width and a height of 1940 mm each. Depending on the size of the steam mixing channels, the core box may have a diameter of around 3420 mm. The diameter of the core drum may by around 3660 mm then. The size of the downcomer may be somewhat smaller than indicated here, resulting in an inner diameter of the RPV of around 4 m.

The cross section D-D through the double bottom of the core drum in Figure 22 is illustrating its internal welded structures, the open window for the moderator water to the assembly gaps and the orifices for the two reflectors.

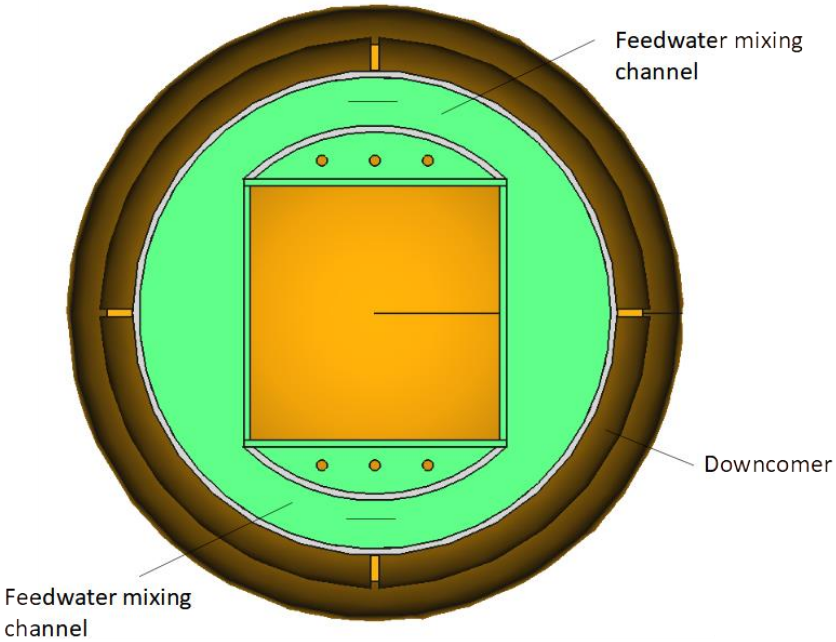

Figure 22: Horizontal cross section D-D through the double bottom of the core drum, looking downwards.

This design concept has been analysed with system codes within this project to check if the envisaged passive safety features can indeed be achieved.

4 Early analyses of passive safety aspects by the University of Pisa

4.1 Focus of the work

The analysis of the proposed SCW SMR in charge to the University of Pisa concerned the conceptual investigation of passive safety aspects such as natural circulation in the event of accidents like a long-term station blackout. Considering the complex flow paths involved in the novel proposed plant configuration, the attention was focused on the modelling of the behaviour of the flows in the vessel, given tentative choices for the passive systems to be included in the reactor plant. Indeed, the relatively small thermal power of the reactor core (290 MWth), in the range of one tenth of current, even passive reactor systems, leaves no reasonable doubt about the possibility to provide a sufficient heat sink for releasing the decay heat to the outer environment, e.g., by the use of the mentioned isolation condenser or by any suitable passive residual heat removal system of sufficient size.

Therefore, the main attention in the performed work was put on the analysis of the flow paths established by natural circulation in the reactor vessel whenever a sufficient sink for the decay heat is assured. Components of the passive systems have been identified by reasonable estimates of their characteristics, just checking that the assumed features could be sufficient for assuring a reasonable thermal behaviour of the reactor in the long term. A detailed optimisation and design of the passive systems is deferred to a further phase, once additional details of the reactor system will be defined (e.g., presence and location of control rods with their drive mechanisms, specific choices for the flow distribution, etc.).

The analyses here reported have therefore the worth of targeted calculations suggesting the forced and natural circulation behaviour of a new reactor configuration that departs from those of currently operating reactors, e.g., for the presence of the multiple passages with horizontal channels in the core of a vessel type configuration.

4.2 Adopted RELAP Code Versions

The reactor proposed by Schulenberg and Otic (2021) was firstly modelled by the use of the NRC version of the RELAP5 code (SCIENTECH Inc., 1999; RELAP5 Code Development Team, 2001). By this version of the code also first analyses of NTUU experimental data about 1-rod, 3-rod and 7-rod bundle mock-ups (Razumovskiy et al. 2009; Razumovskiy et al. 2016), kindly provided by IPP, were performed as reported in Ambrosini et al. (2022).

The NRC version of the code was also used for coupled neutronic and thermal-hydraulic analyses performed in the distance with the cooperation of researchers of BME involved in WP4 (Boglárka Babcsány), using the Serpent 2 code (see, e.g., Leppänen et al., 2015) with the thermal-hydraulic parameters calculated by RELAP5, in order to obtain the reference power distribution along the different core stages that was used for the calculations since that time on. In this respect, though it is clear that the later use of a slightly different version of the code as well the changes in the boundary conditions for the different analyses and/or consideration of beginning- or end-of-cycle conditions should suggest repeating these coupled analyses for each particular case, this was considered of lesser importance for the objectives of the work presented herein and the obtained power distribution was considered sufficiently representative of reference reactor core conditions.

After repeated trials to perform depressurisation transients from supercritical pressures to subcritical ones by the NRC version of the code, including the use of more refined property tables, it became clear that it was impossible to perform the intended analyses of the long-term station

black-out with this code version. Depressurising below the critical pressure from supercritical ones represents a well-known problem for system codes, since the critical point of any fluid exhibits singularities, especially in the derivatives of thermodynamic properties, that play a deleterious role in time advancement algorithms of the pressure-velocity coupling type, needing to predict the pressure field on the basis of coupled momentum, energy and mass balance equations. This problem represented a clear challenge for the initially adopted version of the RELAP5 code that could not be overcome at user level, having neither access nor the requested knowledge and authorisation to make changes to the source code. Efforts were repeatedly spent in trying to circumvent the issue by the selection of the limited available user options, but this finally resulted ineffective.

Therefore, a specific cooperation agreement was established with Innovative Systems Software, L.L.C. (ISS) in USA, in order to be allowed to make use of the RELAP/SCDAPSIM code (SCDAP/RELAP5 Development Team, 1998; Allison and Hohorst, 2010), still under maintenance and development, thus also benefitting of the cooperation of developers to receive support in solving numerical problems. This decision to revert to RELAP/SCDAPSIM allowed to fulfil the contractual commitment of making use of RELAP5 in the planned analyses, while also allowing the promised improvement of existing modelling tools to be performed in the frame of the ECC-SMART project.

In fact, the cooperation with ISS gave rise to a specific version of the code that could solve the problems encountered during the analysis of the station black-out transient and also to provide the user with a generalised heat transfer correlation, to be used only at supercritical pressure, encompassing the form of many existing correlations for supercritical fluids, based on the modification of the Dittus-Boelter (1930) relationship by the correction with several property ratios. The implemented correlation has the form:

$$Nu = \frac{HTC \times D}{k_b} = \left[1 + \frac{C}{(x/D_h)^n}\right] a_1 \, Re_b^{a_2} \, Pr_b^{a_3} \left(\frac{\rho_w}{\rho_b}\right)^{a_4} \left(\frac{\mu_w}{\mu_b}\right)^{a_5} \left(\frac{k_w}{k_b}\right)^{a_6} \left(\frac{C_{p,w}}{C_{p,b}}\right)^{a_7} \left(\frac{\overline{C_p}}{C_{p,b}}\right)^{a_8} \quad (1)$$

where the coefficients and exponents a_i, C and n can be specified by the user via the input deck for each heating structure. In particular, the implementation of correlations by Bishop et al. (1965) and Mokry et al. (2011) can be performed in the form shown hereafter:

- <u>Bishop et al.</u>

$$Nu = 0.0069 \cdot Re_b^{0.9} \cdot \overline{Pr}_b^{0.66} \cdot \left(\frac{\rho_w}{\rho_b}\right)^{0.43}$$

$$Nu = \frac{HTC \times D}{k_b} = \left[1 + \frac{C}{(x/D_h)^n}\right] a_1 \, Re_b^{a_2} \, Pr_b^{a_3} \left(\frac{\rho_w}{\rho_b}\right)^{a_4} \left(\frac{\mu_w}{\mu_b}\right)^{a_5} \left(\frac{k_w}{k_b}\right)^{a_6} \left(\frac{C_{p,w}}{C_{p,b}}\right)^{a_7} \left(\frac{\overline{C_p}}{C_{p,b}}\right)^{a_8}$$

- <u>Mokry et al.</u>

$$Nu = 0.0061 \cdot Re_b^{0.904} \cdot \overline{Pr}_b^{0.684} \cdot \left(\frac{\rho_w}{\rho_b}\right)^{0.564}$$

$$Nu = \frac{HTC \times D}{k_b} = \left[1 + \frac{C}{(x/D_h)^n}\right] a_1 \, Re_b^{a_2} \, Pr_b^{a_3} \left(\frac{\rho_w}{\rho_b}\right)^{a_4} \left(\frac{\mu_w}{\mu_b}\right)^{a_5} \left(\frac{k_w}{k_b}\right)^{a_6} \left(\frac{C_{p,w}}{C_{p,b}}\right)^{a_7} \left(\frac{\overline{C_p}}{C_{p,b}}\right)^{a_8}$$

It must be noted that the features to operate over critical pressure were introduced in RELAP5 long ago by code developers. While the code was mostly prepared for simulating depressurization across the critical point, it did anyway require some fine-tuning. The recent

actions to improve convergence across that discontinuity primarily consisted of introducing fixes to the pre-existing code, without adding any specific mechanisms or techniques. These fixes were related to some exceptions in evaluating the internal energy of supercritical water, with some specific time-step control options that could lead to unphysical values and to some exception in the calculation of heat transfer to the gas phase that had to be treated in a specific way in the case of supercritical pressures, where a gas phase basically does not exist. Moreover, the event of crossing of the supercritical pressure had to be dealt with better care, to avoid excessive time consumption in the time steps where this event occurred.

Owing to the continuous cooperation with ISS, the version of the RELAP/SCDAPSIM code used for the present analysis is evolving, further customising and improving its characteristics. The results presented herein are those obtained by the version released to the University of Pisa in July 2023 and adopted for the present sensitivity analyses.

While a more detailed description of the improvements that the code underwent to is planned to be proposed in deliverable D3.4, to be released by month 51 in the project, hereafter an example of its new capabilities is reported in relation to a few of the cases of the mentioned NTUU experiments which were analysed by the Mokry et al. (2010) and Bishop et al. (1965) correlations.

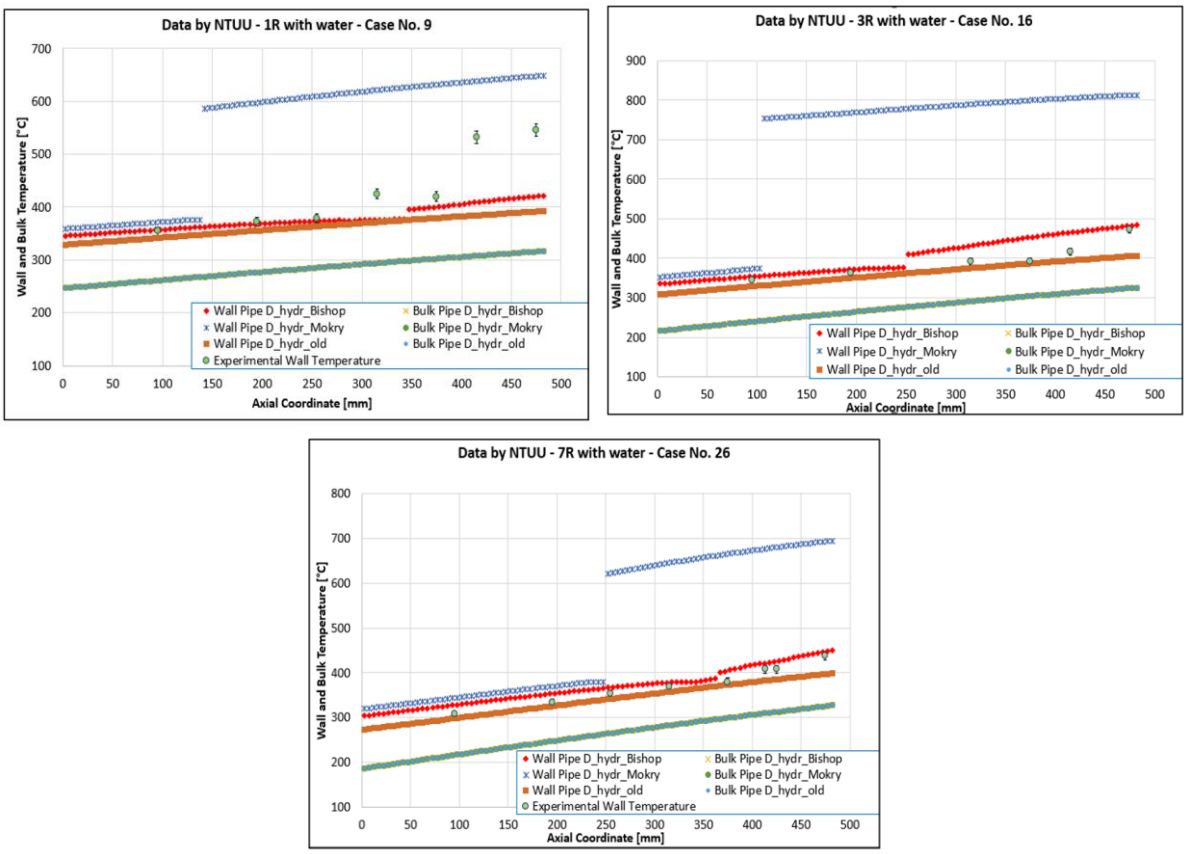

Figure 23: Sample results of the application of RELAP/SCDAPSIM to selected NTUU data

Figure 23 shows the results obtained for some of the cases identified in Ambrosini et al. (2022) suggesting that the Bishop et al. correlation has sometimes the possibility to catch mild deterioration trends, while the Mokry et al. one tends to provide highly deteriorated behaviour, with jumps also observed by IPP and BME in the application of their 1D codes to the same data. These results, which have been partly reported in Deliverable D3.2 (Zhao et al., 2023) only for the ones obtained with the NRC version of RELAP5, show the mentioned jumps which were explained in a recently published joint paper (Varju et al., 2024) as a consequence of the presence

of multiple solutions identified by searching for the zeros of correlations in which thermodynamic property ratios appear as a function of wall temperature. While the reader is referred to the published paper to consider the exact characteristics of the sample problem referred to in Figure 24 and Figure 25, it is here remarked that the contour plots in the two figures identify the actual loci of the zeroes of the correlation (i.e., the actual predicted wall temperature), while the charts represent what a 1D model, as the applied system codes are, would likely to predict in the presence of multiple solutions (see the case with the Mokry et al. correlation), i.e., a jump to the one of the admissible manifolds that results more stable for the combination of conductive (if any) and convective heat transfer models. In the analysis of the full set of data, it became apparent that the Bishop et al. correlation is less prone to this phenomenon and generally represents a more realistic trend of wall temperature.

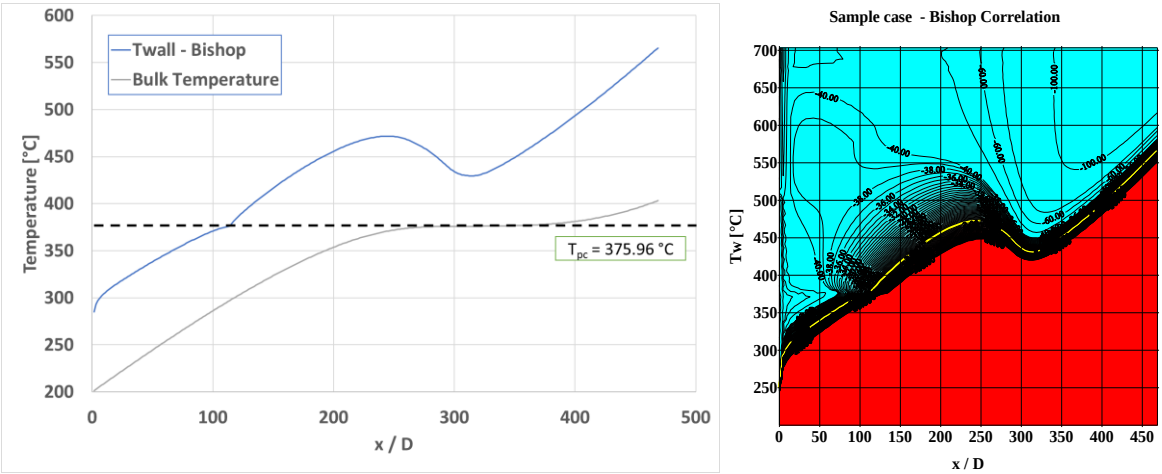

Figure 24. Prediction of a sample case by the Bishop et al. correlation: chart and contour plot

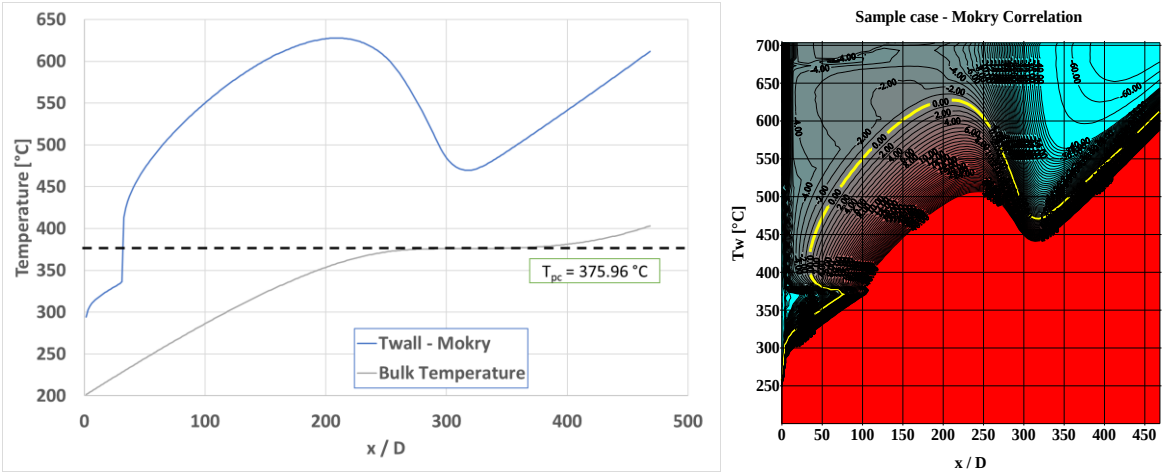

Figure 25. Prediction of a sample case by the Mokry et al. correlation: chart and contour plot

The above considerations suggested to BME, which together with IPP conducted a very extensive analysis of correlations, and later to the University of Pisa as well to make use of the Bishop et al. correlation in the application of their system codes for plant analyses, though the horizontal bundle configuration would certainly need the use of a specific correlation for bundles with that particular geometrical orientation. In this regard, the capability of both Apros and RELAP/SCDAPSIM to apply user defined correlations represents a useful feature in view of future studies.

4.3 Developed SCW SMR nodalisation

4.3.1 Vessel Flow Paths Nodalisation

Modelling the vessel flow paths as described in Chapter 3 was started at the University of Pisa in January 2022, even before the release of CAD data and then was made more precise of the basis of this updated information. Indeed, the topology of the system is by far more complex than the one of usual nuclear reactors, owing to the presence of the multiple core passages. Given this complexity and the requirement to define channels at properly matching heights at the seven stages for both the moderator channels and the fuel cooling ones, the nodalisation of the latter was started first, assuming the cooling system separated from the moderator one. This justifies the use of lower numbers adopted as labels for identifying the fuel coolant hydraulic components, at the right of Figure 26, with respect to those used to label the moderator flow paths at the left of the same figure. The two nodalisations are actually composing a single fluid system, as the "branch" 480, representing the last volume of the moderator flow path, is joined by a "single junction" to the "branch" 8 that with the 10 represents a vertically split inlet plenum for the lower stage of the fuel channels. It must be mentioned that the strategy for modelling the system was discussed in several steps with BME though, owing to the adoption of different codes and specific choices in modelling features, the two models are somehow different.

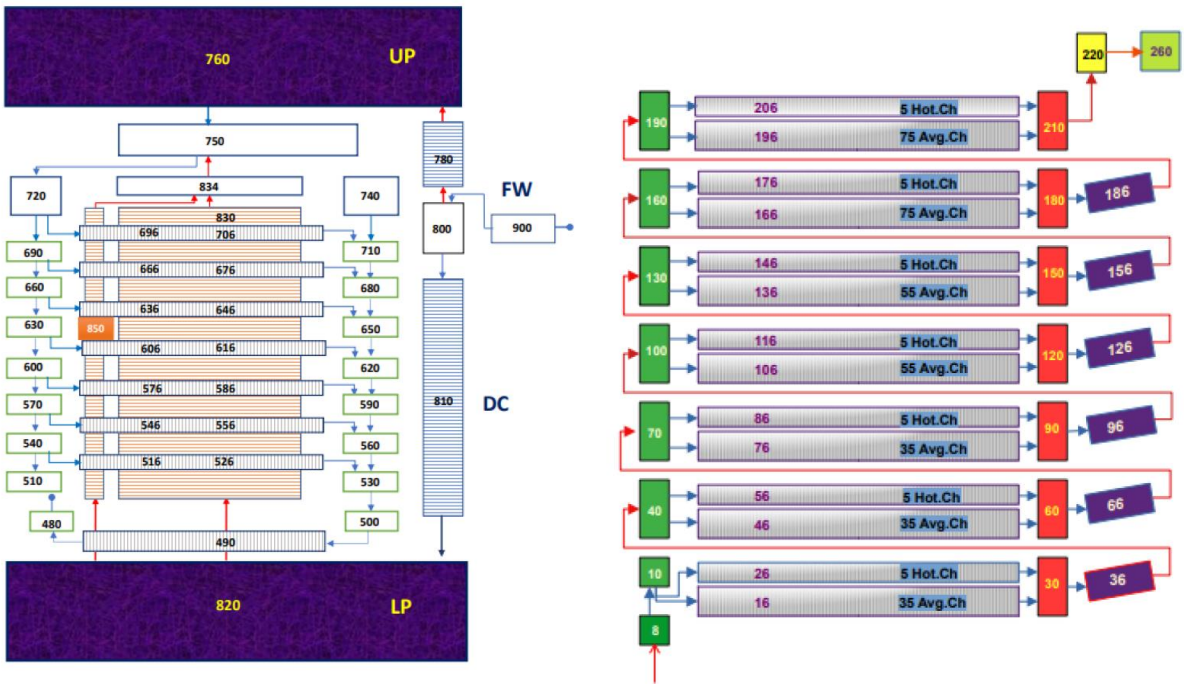

Figure 26. Sketches representing the subdivision into hydraulic components of the moderator flow path (left) and of the fuel coolant flow path (right)

For making easier to understand the model, we start here from the moderator flow path sketch reported at the left of Figure 26. The "time dependent volume" 900, later replaced by a more complex system simulating the feedwater pipe with the injections coming from the outlet of the Isolation Condenser and the Accumulator system (see below) is connected via a "time dependent junction" assigning the flow rate to the volume 800, representing the "tee" necessary to split the feedwater flow into the two streams intended to be directed to the upper and lower downcomer. The upper downcomer is represented by the "pipe" 780, while the lower downcomer by the "pipe" 810. The "single junction" connecting the pipe 780 to the "branch" 760, representing the vessel

upper plenum, is sized to represent 12 orifices having a diameter of 0.1 m. This choice was made early in the steady state analyses to obtain the specified flow rate of 20 kg/s initially intended to keep the upper shell of the vessel dome at the same temperature of the FW line, though it was later noted that this flow rate could not be achieved so easily owing to buoyancy phenomena that superpose to the pressure driving forces, making the flow through the orifices even to invert under some specific conditions. This aspect will be matter for discussion later on.

Following the path of the flow along the lower downcomer (pipe 810), the fluid reaches the lower plenum (branch 820), where two single junctions split the flow rate into the stream directed through the upward moderator flow path (pipe 830), simulating the flow streaming through the outer boxes of the fuel elements, and the one passing through the two reflector volumes, simulated by a single hydraulic component (pipe 850). The junction connecting the lower plenum (820) to the bottom of the reflector (850) was sized to represent 6 orifices having a diameter of 0.08 m each, assumed to be three on one side of the reflector and three on the other. The flows exiting from both the upward moderator flow paths through the outer boxes of the fuel elements (830) and the reflectors (850) join in the branch 834, connected by a single junction to the branch 750 which receives (or supplies) flow from (to) the upper plenum branch 760. The net flow rate from these flow paths is then directed by a single junction to the branch 720 that represents the first of a stack of branches (from top to bottom, numbered as 720, 690, 660, 630, 600, 570, 540, 510) that represent the inlet plenum for the seven stage moderator channels located in the centre of the fuel elements. Each one of these branches is connected by a single junction to the lower one (except for the 510, being the last one and then a blind volume); two single junctions depart from each one of the upper branches to feed flow into the inner moderator channels that, in similarity with the fuel cooling channels, have been subdivided into the two groups of “average” and “hot” channels. This splitting deserves some further clarification provided hereafter.

Since the very beginning, the need was felt to consider “average” channels and “hot” channels in order to consider the different “horizontal” power distributions, in addition to the vertical one. This is the usual way in which vertical bundle reactor cores are treated in modelling, in order to represent both the average conditions and the peaking ones. Here the concept was combined with the one of the seven-stage core, resulting in average and hot channels at each of the seven stages. Needless to say, this represented a considerable difference with the usual description of reactor cores, resulting in the need to have 14 inner moderator channels and 14 fuel coolant flow channels in the nodalisation.

As it can be noted in the right part of Figure 26, considering that the first three stages from the core bottom (1 to 3) are composed by two rows of fuel elements (i.e., 40 fuel elements), the average and the hot fuel coolant and moderator channels represent 35 and 5 fuel elements respectively; stage 4 and 5, instead, having there rows (i.e., 60 fuel elements) are split into 55 and 5 average and hot channels; finally, the stages 6 and 7, having four rows (i.e., 80 fuel elements) are split into 75 and 5 average and hot channels. In other words, five fuel elements have been assigned to the representation of the hot channels at all the stages and the rest are used to represent the average ones. As mentioned, this complexity applies to both fuel coolant and the inner moderator channels and to all the multilayer interfacing structures, resulting in a great number of hydraulic components and heating structures to be represented. A greater complexity was chosen by BME in their Apros nodalisation, since a further subdivision into “hot”, “average” and “cold” channels was chosen for reasons of better interpolation of fluid properties in thermal-hydraulic and neutronic coupling; such a choice was not considered feasible with RELAP5 after the effort made to have a rational numbering of components also for the difficulty to assign the proper numbering to the additional “cold” channels.

Resuming the description of the moderator flow path, the above-mentioned junctions from the branches representing the inlet plenum lead to the “pipes” numbered in decreasing order of stage as 696 and 706 (“average” and “hot”), 666 and 676 (idem), 636 and 646 (idem), 606 and 616 (idem), 576 and 586 (idem), 546 and 556 (idem), 516 and 526 (idem). As it can be noted, it was necessary to use a very well-established rationale for the numbering, in order to avoid as far as possible errors and to number the heating structures shared by moderator and fuel coolant channels in accordance.

In similarity with the inlet moderator plena, the outlet moderator ones were represented by a stack of “branches” connected by junctions with the inner moderator channels and with each other. In particular, from top to bottom, the branch 740 (which is blind at the upper end) and the branches 710, 680, 650, 620, 590, 560 and 530 receive the flows coming from the inner moderator channels (“average” and “hot”) and convey them downwards towards the branch 500, representing a plenum at the inlet of the double bottom, routing the resulting flow to the pipe 490, which actually represents the two curved flow paths embracing the window of the upward moderator channel, ending in the mentioned branch 480, finally connected to the inlet plenum of the first stage of the fuel channels (branches 8 and 10).

The connections between branch 8 and 10 and to the “average” and “hot” fuel channels at the first stage (pipes 16 and 26) have been made in such a way as to avoid that volume 10 is idle, i.e., not washed by the fluid coming from the moderator flow path; therefore, branch 8 is connected to branch 10, from which two junctions depart for the pipes 16 and 26. Then, the fluid is heated by the “average” and “hot” fuel and is then mixed in the branch 30, being then routed back to the inlet plenum 40 at the next stage by the returning channel 36, and so on for the other stages. In other words, the sequence of hydrodynamic components describing the seven stages of the fuel coolant channels is as follows:

- First stage: inlet plena 8 and 10, average and hot channels 16 and 26, outlet plenum 30, returning channel 36;
- Second stage: inlet plenum 40, average and hot channels 46 and 56, outlet plenum 60, returning channel 66;
- Third stage: inlet plenum 70, average and hot channels 76 and 86, outlet plenum 90, returning channel 96;
- Fourth stage: inlet plenum 100, average and hot channels 106 and 116, outlet plenum 120, returning channel 126;
- Fifth stage: inlet plenum 130, average and hot channels 136 and 146, outlet plenum 150, returning channel 156;
- Sixth stage: inlet plenum 160, average and hot channels 166 and 176, outlet plenum 180, returning channel 186;
- Seventh stage: inlet plenum 190, average and hot channels 196 and 206, outlet plenum 210.

Out from the seventh stage, the provisional nodalisation involved a steam plenum (220) and a time dependent volume (260) for assigning the outlet pressure condition, assumed for reference at 25 MPa. This part of the nodalisation had to be changed later to introduce an actual steam line with the tee junction for the Isolation Condenser inlet and the “motor valves” needed to close the steam line and open the “bypass” (or automatic depressurisation system).

Likewise, also the feed water system, here represented only by the time dependent volume 900 and by the related time dependent junction for assigning the 145 kg/s of nominal flow rate, had to be substituted by a more realistic feedwater line, with the tee junctions for representing the return of fluid from the Isolation Condenser and the injection from the

Accumulator system, introduced in order to have a passive injection suitable to cope with station blackout conditions.

4.3.2 Nodalisation refinement and extension for passive system

Once completed the description of the most important flow paths via the topology described in the previous section, it was then necessary to check the geometry of the components, introduce heating structures to more accurately represent the heat transfer connections between adjoining volumes separated by plates (this reactor concept has a lot of such features) and to represent the feedwater and the steam line with the previously mentioned passive systems. The latter were namely an Isolation Condenser, an Accumulator and a Gravity Driven Injection system. The work was made in two steps, in the frame of a grant assigned to a young engineer (Hassan et al., 2022) and of a MSc thesis in Nuclear Engineering (Chaaraoui, 2024).

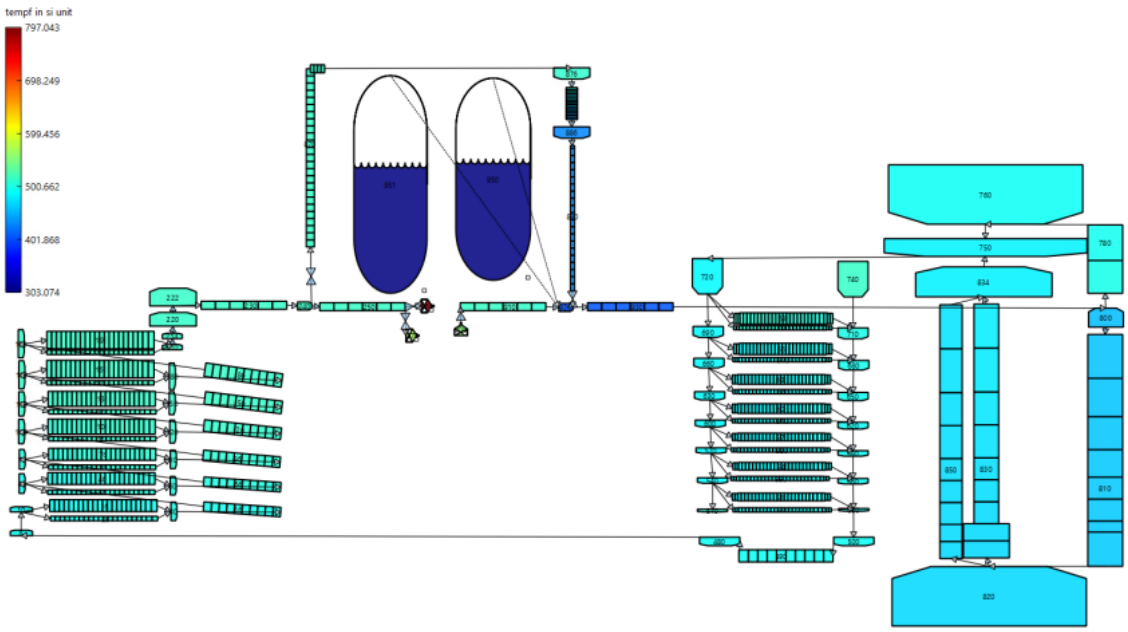

Figure 27. Representation of the whole reactor system including feed-water and steam-line, as well the Isolation Condenser(s), the Accumulator(s) and the Gravity Driven injection system (not represented to scale)

Figure 27, obtained with the RHYS software from ISS, represents a complete view of the reactor system equipped with a more complete feedwater line, a steam line, the Isolation Condenser and the Accumulator. The Gravity driven injection system is not represented to the real scale.

Actually, the feed water and the steam line represent with single hydrodynamic components two real components, something obtained by specifying the actual hydraulic diameter and length with a doubled area and doubled heat structures for modelling their shells. The same applies to the Isolation Condenser and the Accumulator system, obtained with single components with doubled flow areas.

In particular:

- the steam line is obtained with a first 3 m long (double) pipe (230), a 0.5 m long (double) branch (240) and another 3 m long (double) pipe (250) leading to two motor valves representing the Main Steam Isolation Valve, connected to a downstream time dependent

volume, and the Depressurisation Valve, connected to another downstream time dependent volume; the diameter of the pipes is 0.2 m;

- the feedwater line is modelled in a similar way (time dependent volume 900, time dependent junction 905 for injecting flow rate, pipe 910, branch 920, pipe 930) and with a diameter of 0.1 m;
- the Isolation Condenser (IC) is also modelled as a double unit with a pipe (870) departing from branch 240, having a diameter of 0.2 m, a vertical length of 12.5 m and a horizontal 1 m length leading to the IC collector branch (876); IC pipes (880) (2 cm in diameter with a 2 mm wall thickness) have a length of 1.5 m and are in number of 200 for 2 units (i.e., 400), terminating with the outlet collector (886), from which a downward vertical pipe (890), having a length of 10.2 m and a diameter of 0.1 m is finally connected to the branch in the feed water line (920); the isolation condenser pipes have a thickness of 2 mm and on the external side it is assumed to exchange heat with a fluid at 30 °C with a parametrically defined heat transfer coefficient equal to 10,000 W/(m^{2}K);
- the accumulator is assumed to be spherical and also to represent two units; it is loaded with nitrogen at 4.8 MPa and has an overall initial liquid volume of 44.2 m^3, filled with water at 30 °C.

It must be mentioned that the above modelling assumptions may result slightly different from the ones assumed by BME, though they are very similar.

The nodalisation as a whole totals 937 control volumes, 959 junctions, 1337 heating strcutures and 26740 heat conduction mesh points.

4.4 Steady-state calculation procedure

The steady-state analysis with the code is initiated by first starting the feed water flow rate and then increasing the power to the rated value. In particular:

- the flow rate is increased from zero to 145 kg/s in 10 s from the calculation start;
- then the power is increased to the rated value of 290 MWth from 100 to 200 s, leaving the system to stabilise up to 2000 s.

The power distribution adopted for the seven average and hot channels, obtained by the mentioned interaction with the neutronics group of BME, is reported in Figure 28 where it appears assigned in each one of the 20 axial nodes in which the fuel element is horizontally subdivided at each stage.

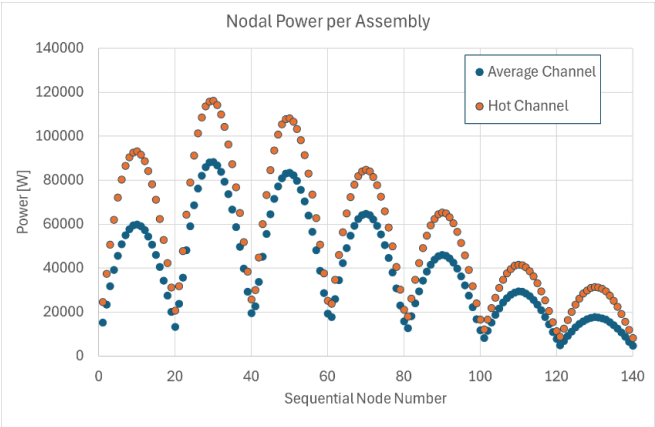

Figure 28. Power distribution along the 20 node elements at each stage and per each fuel assembly

Since the stages are ordered from bottom to top of the reactor core (from 1 to 7), the figure provides at the same time a representation of the power distribution in the horizontal and in the

vertical directions. Though this power distribution may further change owing to details of the flows, requiring a coupled thermal-hydraulic and neutronic analysis at each different configuration, it was considered a reasonable reference for the purposes of the present thermal-hydraulic analyses.

After using for some initial calculation tests the standard correlations embedded in the code for supercritical pressures (Mode 1 of heat transfer), it was then adopted the Bishop et al. (1965) correlation that, though conceived for vertical flow, tends to provide more conservative values of cladding temperatures, exploiting the development achieved in the RELAP/SCDAPSIM code purposely for the work to be done in the frame of ECC-SMART. As an example of the consequences obtained by this change, Figure 29 provides a comparison of the temperature levels reached during the 2000 s of steady state analyses:

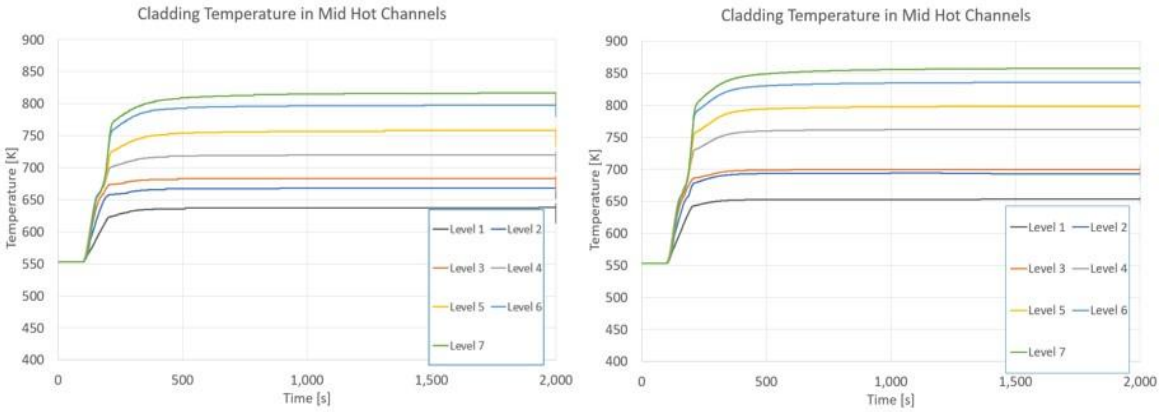

a) standard correlation b) Bishop et al. correlation

Figure 29. Cladding temperature in the middle of the cooling channels obtained during steady-state initialisation by the standard correlation in RELAP/SCSAPSIM and by the Bishop et al. correlation

First calculations were also run with uniform inlet pressure drop distributions in average and hot channels, providing an uneven power-to-flow ratio partitioning in cooling fuel elements characterised by different average linear powers. This gives rise to different fluid and cladding temperature levels, as shown in Figure 30.

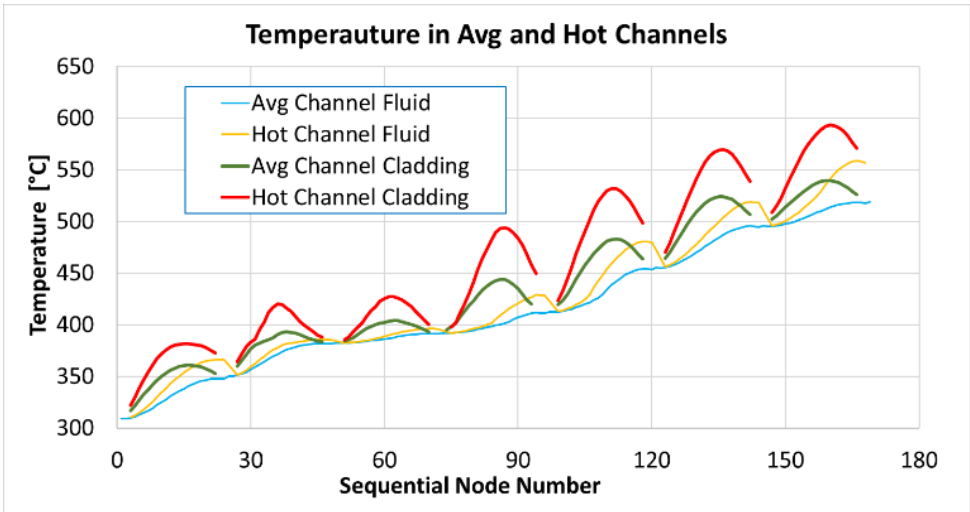

Figure 30: Steady-state distribution of core temperatures with even core singular pressure drop distribution

Figure 30, in which it must be noted that the number of sequential nodes is larger than 140, owing to the presence of unheated nodes (corresponding to the fuel gas plena) and to the inlet and outlet plena, is helpful in highlighting some features that are consequence of the specific arrangement of the reactor core in seven heating stages:

- without optimisation of inlet orifices, the bulk fluid temperatures are different along average and hot channels, though, owing to the mixing provided by the presence of common plena and returning channels, the values of the temperatures of the two streams are homogenised at each step: this is the main reason for pursuing a seven-passage structure of the reactor core, trying to reduce peaking factors;
- the evolution of cladding temperature along the average and hot channels is consequently different; in the figure, the reaching of the pseudo-critical temperature at the cladding surface appears to occur at the second stage for both average and hot channels; this effect is highlighted by an apparent discontinuity in the slope of the wall temperature, close to the value of the pseudocritical temperature at the local pressure (being around 385 °C);
- the bulk fluid temperatures, instead, reach the pseudocritical point somehow later, between the second and the third stage, where the classical flattening of the bulk fluid curve is observed, owing the maximum reached by the specific heat.

Concerning the pressure drops along the reactor core channels, the presence of wire wraps had to be taken into account. In the lack of a specific correlation for such kind of spacers available in the code, it was considered reasonable to make use of the definition of surface roughness in order to approximately account for them. Figure 31 reports the results of a sensitivity analysis aimed to highlight the effect of this parameter, showing the consequences it has on the pressure distribution. On the basis of early considerations, also made in comparison with the single channel data proposed by Schulenberg and Otic (2021), it appeared reasonable to choose the value of 30 μm as an approximate value representing the expected effect of the wire spacers, to be adopted in subsequent analyses.

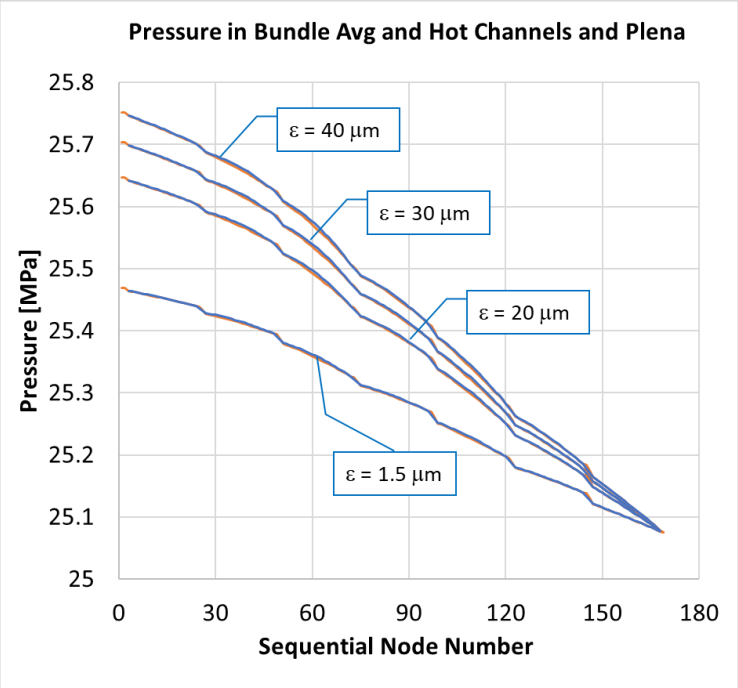

Figure 31: Pressure trends along the reactor core average and hot channels at different values of surface roughness

The discussion of the effect of roughness on pressure drops gives the opportunity to introduce the flow distribution observed in the reactor vessel during steady-state analyses. As shown in Table 1, in the presently adopted code model the nominal feed water flow of 145 kg/s could not be split, contrary to what suggested in the preliminary proposals, into 20 kg/s routed to the upper downcomer (DC) and then to the upper plenum via the orifices placed between them and 125 kg/s flowing downwards to the lower plenum via the lower DC. Instead in the present configuration the flow through the upper DC orifices is negative, i.e. from the upper plenum to the downcomer, thus joining the feed water flow on its way to the lower plenum.

Flow rates [kg/s]	1.5 μm	20 μm	30 μm	40 μm
Upper DC	-1.3915	-1.4209	-1.4268	-1.4378
Lower DC	146.4	146.43	146.43	146.44
UModCh	126.79	126.83	126.83	126.84
Wat-Refl	19.603	19.601	19.6	19.599

Table 1: Flow rates in various flow paths for a nominal feed water flow of 145 kg/s and different values of the roughness parameter assumed to simulate the wire wraps

This effect, was noted in early calculations and is due to the establishment of buoyancy effects when the moderator flowing through the fuel boxes in the upward motion from the lower plenum to the upper plenum is heated up, so decreasing its density.

Figure 32 illustrates this behaviour, shown in the early phases of calculation initialisation. In particular, remembering that the calculation is started by initiating the FW flow at zero power conditions and then starting the heating with a ramp up to the rated power of 290 MWth, the initial flow rate through the orifices nearing 50 kg/s decreases becoming negative though small in magnitude. In repeated analyses, it was noted that the phenomenon is quite sensitive to the pressure drops encountered by the moderator through the fuel boxes and, in some analyses conducted with an incomplete description of the heating of the moderator, the flow though the upper DC orifices could become positive, though small.

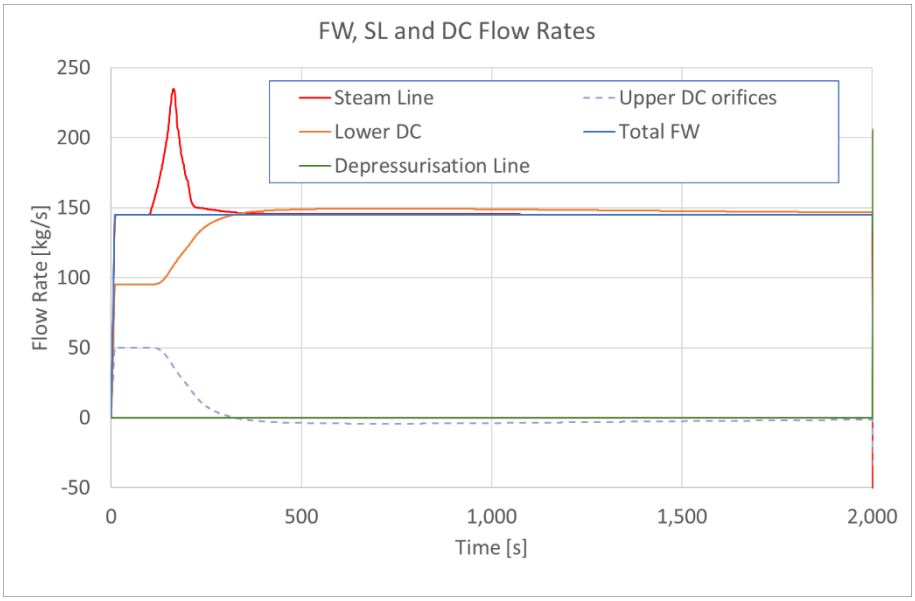

Figure 32: Behaviour of flow rates during steady-state initialisation

In relation to this aspect, the present understanding suggests the following considerations:

- per se the fact that flow rate from the downcomer to the upper plenum is positive or negative is not too important, because the moderator temperature that possibly will be in contact with the upper vessel shell in case of negative flow will be only 10 or 20 °C hotter than the feed water one, creating little problems from the structural point of view, e.g. in terms of distortions and/or leak tightness of the flange surfaces;
- little details in the actual configuration of the system, not considered at the moment, may strongly influence the repartition of flows in the downcomer;
- increasing either the pressure drops in the lower downcomer or in the one guessed in the upward moderator channel, e.g., by the presence of obstructions for the placement of control rods, or the inlet flow rate may definitely change the situation.

As an example of the effect of the latter provision, Table 2 shows that increasing the feedwater flow rate to 150 kg/s is effective in reversing the sign of the flow rate in the upper downcomer, resulting in a situation closer to the one initially envisaged.

Flow rates [kg/s]	1.5 μm	20 μm	30 μm	40 μm
Upper DC	3.6134	3.5469	3.5263	3.5093
Lower DC	146.39	146.45	146.47	146.49
UModCh	126.56	126.62	126.64	126.66
Wat-Refl	19.826	19.832	19.834	19.835

Table 2: Flow rates in various flow paths for a nominal feed water flow of 150 kg/s and different values of the roughness parameter assumed to simulate the wire wraps

In front of the previous considerations and of the sensitivity to details of the boundary conditions to be defined in a more advanced phase of the pre-conceptual design, it was not considered necessary to artificially modify the pressure drops at the bottom of the dowcomer or in the upward moderator flow path though the fuel boxes, accepting the slight deviation from the initial planned flow path distribution obtained with a feedwater flow of 145 kg/s.

As above anticipated, it was then considered useful to explore the effect of the use of an uneven orifice distribution at the hot and average channel inlet. As known, it is a quite widespread practice for Boiling Water Reactors (BWRs), but also in some SCWR design (Oka et al. 2010), to recur to channel inlet throttling in relatively low power regions of the reactor core in order to make more even the distribution of the power-to-flow ratio, thus avoiding reaching high power peaking. Indeed, the choice of throttling should be based on a better detailed regional description of the reactor core than possible with only “average” and “hot” channels, also considering the evolution of the neutron flux distribution during fuel depletion. However, the present attempt has the value to provide an estimate of the advantage that can be achieved by the application of such well-known technique.

Figure 33 shows the results obtained by adjusting the singular pressure drop coefficients at the inlet of the average fuel channels, in order to let more flow rate be directed into the hot channels. As it can be noted by comparing with Figure 30, this provision is effective in decreasing the maximum cladding temperature obtained during steady state conditions. Figure 34 shows the corresponding fluid temperature distribution in the inner moderator channels at the different stages, while Figure 35 reports the corresponding pressure distribution obtained by applying the optimised orificing; indeed, the optimised flow distribution is obtained at the price of a higher pressure drop across the core, at least in the case of such a rough description of the subdivision between hot and average channels, making the moderator region of the reactor to operate at a

pressure greater than 26 MPa, in the case in which a pressure of 25 MPa must be assured at the turbine inlet, as it was assumed in our analyses.

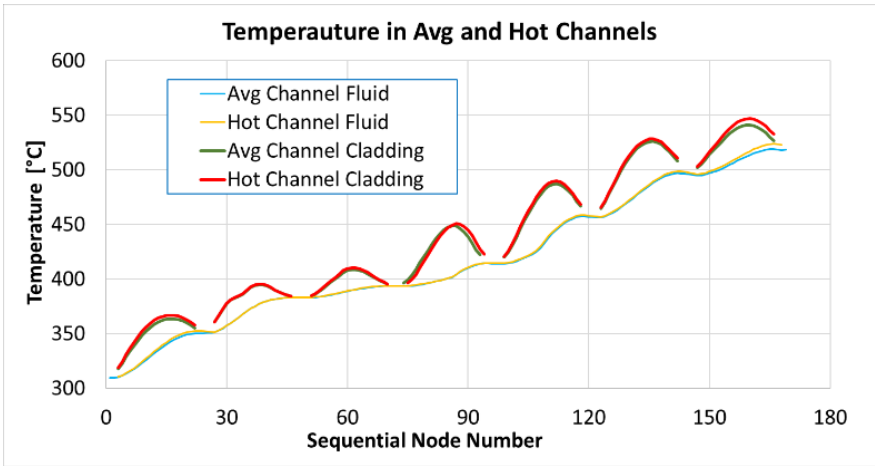

Figure 33: Steady-state distribution of core temperatures with optimised core orificing

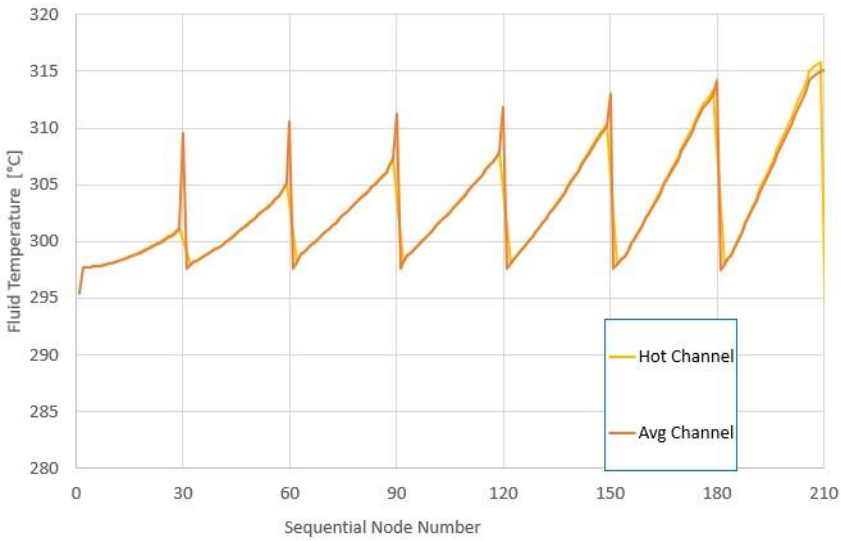

Figure 34: Inner moderator channels and plena temperature with optimized orificing

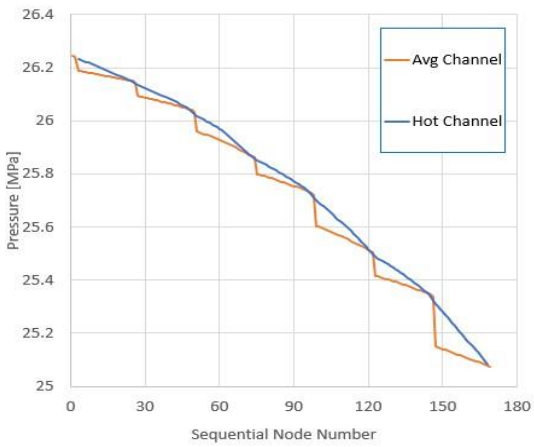

Figure 35: Pressure distribution across the average and hot channels with optimised orificing

Being aware of the limitations of the analysis performed for the optimisation of the flows by inlet orifices, it was tried to check the results obtained by the code by considering the resulting flow rates in the average and hot channels in view of obtaining nearly the same power-to-flow

ratio in both. The manual iterative procedure consisting in changing the pressure drop coefficients at the inlet of the average channels was in fact performed just by considering at each step the obtained fluid and cladding temperatures, aiming to reach a more uniform distribution as presented in Figure 33; ideally, this should have led to the same hot to average power ratio per bundle. As it can be noted from Table 3, this is approximately the case, with a slightly larger deviation at the first stage, thus confirming that, within the limitations of the present analysis, the adopted procedure to optimise inlet orifice coefficients achieved the intended results. Indeed, how much such a procedure may be translated into a sound engineering practice in shaping the foot of fuel elements in different ways to obtain similar results is a matter of further investigation.

		Average [kg/s]	Hot [kg/s]	Flow Ratio	Power Ratio
Stage 7	**Total**	129.700	15.362		
	Per bundle	1.729	3.072	1.78	1.78
Stage 6	**Total**	132.440	12.617		
	Per bundle	1.766	2.523	1.43	1.42
Stage 5	**Total**	128.420	16.643		
	Per bundle	2.335	3.329	1.43	1.42
Stage 4	**Total**	129.530	15.527		
	Per bundle	2.355	3.105	1.32	1.32
Stage 3	**Total**	122.480	22.578		
	Per bundle	3.499	4.516	1.29	1.31
Stage 2	**Total**	121.850	23.203		
	Per bundle	3.481	4.641	1.33	1.32
Stage 1	**Total**	119.810	25.244		
	Per bundle	3.423	5.049	1.47	1.56

Table 3: Flow rates at the various stages in the hot and average channels with optimised orifices and comparison of the hot-to-average flow and power ratios per bundle

In order to complete the picture obtained by the results of steady-state analyses, Figure 36 shows the distribution of the moderator temperature along the height of pipe 830, representing the flow path among the fuel boxes. As it can be noted, the heat transfer from the insulated boxes pre-heats the moderator temperature of nearly 20 °C while moving towards the upper plenum.

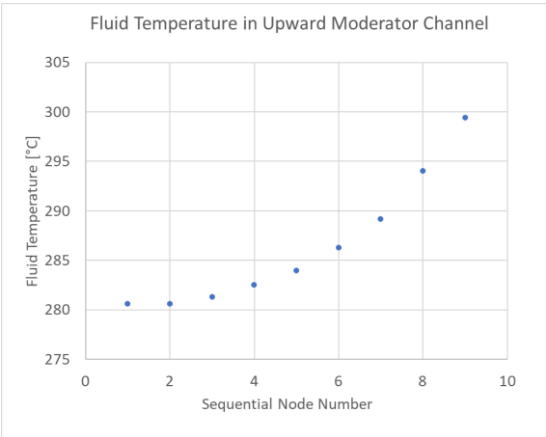

Figure 36: Fluid temperature along the upward moderator flow passing through the fuel boxes

4.5 Transient analyses for the LTSBO

4.5.1 Base Calculation Case

The basic sequence of the transient to be simulated was discussed in the frame of technical meetings of Work Package 3 of the ECC-SMART project and was implemented in RELAP/SCDAPSIM code as described below.

- After reaching the steady-state conditions, at 2000 s the transient is initiated with coolant pumps running down in 10 s and the steam line being closed in 3 s.
- Reactor SCRAM then follows with a 2 s delay with respect to the start of the transient and a decay heat curve is applied from that time on. The decay heat curve follows the trend specified in Attachment 1 – Decay heat Standards of Appendix K to 10 CFR 50 (3a. ANS94 proposal w/ U235 only @ 2 sigma), integrated beyond 10,000 s with data reported by a well-known textbook (Todreas and Kazimi, 2012).
- Short term depressurization of the primary system, via a bypass line or an automatic depressurization line inside the containment depending on the sequence of containment closure, is assumed to take place with a parametrically imposed depressurization curve, leading the system to subcritical pressure; the depressurization line is then closed when the feedwater line pressure reaches 11 MPa (other values were anyway tried, e.g. 10 MPa, with no significant difference in the resulting scenario).
- An isolation condenser system, initially in cold low-pressure conditions, is assumed to be open simultaneously to the closure of the depressurisation line, with 50 s of relaxation time to account for the whole transient inertia and for possible delays in actuation.
- The accumulator system starts the discharge of fluid at the rated pressure of 4.8 MPa, aiming to compensate for the loss of coolant inventory due to the previous actuation of the depressurisation line and, later, in response to the slow depressurisation caused by the operation of the Isolation Condenser and to the related shrinkage of the cooled fluid.

Different calculations were run in order to simulate the behaviour of the system as a consequence of this transient. A base case was run making use of the optimised orifices. Runs were made up to different durations, with 12 hours being the most investigated period (reaching 45,200 s after the transient start). Figure 37 reports the power computed by considering the exchanges with the fluid through the various heating structures that refer to the fuel channel (fuel rods, boxes, etc.). This computation was made in order to check that the power input was actually received by the fluid, considering the complex flow paths present in the vessel and the several heat structures.

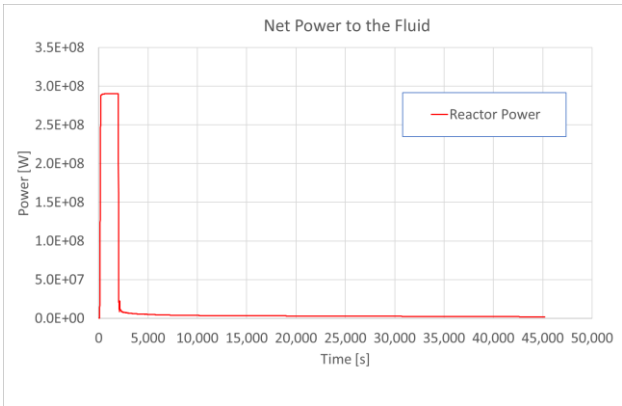

Figure 37: Power exchanged with the fluid during the whole transient

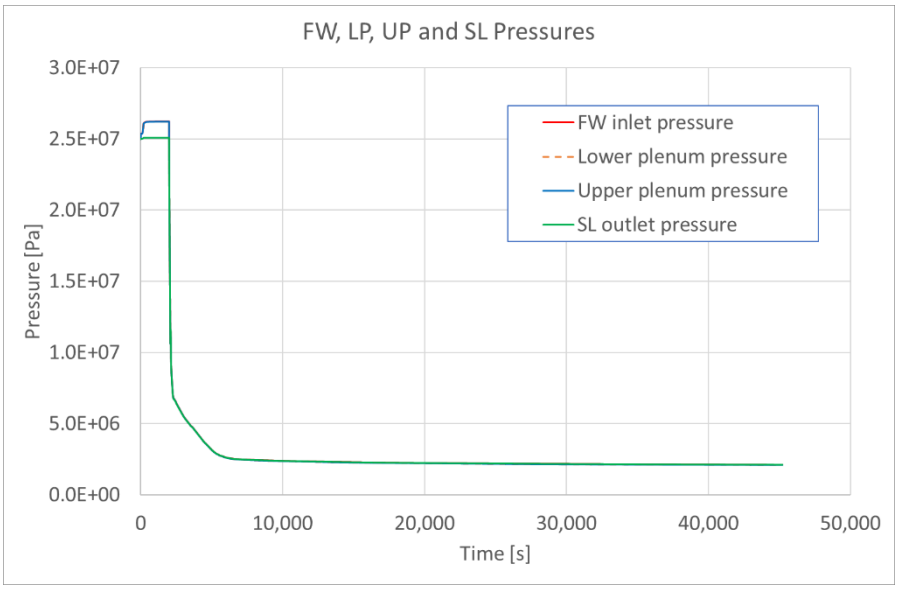

Figure 38: Pressure at various locations in the vessel

Figure 38 shows the trend of pressure in various regions of the vessel as obtained in the computations. The actuation of the depressurization line, closed after about 90 s from its opening due to reaching the pressure setpoint, is effective in bringing the reactor at subcritical pressure. The subsequent opening of the Isolation Condenser inlet and outlet valves could be done only when the depressurisation line, departing from the steam line, is closed; in fact, as it can be seen in Figure 27, the isolation condenser bridges the steam line with the feedwater line and a depressurisation line opened on the former would result in a reverse flow in it. Contrary to what happens in the ESBWR reactor, in which the steam side connection of IC is always open and the condensate side is closed (GE Hitachi Nuclear Energy, 2011), it was necessary in this case to keep closed both valves, opening them slowly at the signal of reaching the pressure threshold. In addition, in the model a very large reverse flow pressure drop coefficient was adopted at the inlet of the piping (e.g., representing a check valve), in order to avoid backward flow in the transient related to the closure of the bypass valve and the opening of both the upstream and downstream valves of the IC. One of the reasons for isolating the IC from the rest of the plant and opening it when the pressure was sufficiently low was in particular to avoid exposing the condenser unit to high pressures; especially in the case (implicitly assumed here) in which the IC is located in a pool outside the containment, this would avoid possible mechanical failure due to overpressure ([1]).

Figure 39a shows that the depressurisation line is open for a very short period of time after the start of the transient, while the steam line is being promptly closed. The behaviour of the flow rate in the lower downcomer and the negative flow rate through the upper downcomer orifices contributing to it are interesting features of the whole simulated transient. In practice, two main flow loops are simulated, as it will be confirmed later, being: 1) a natural circulation loop including the upper downcomer, the lower plenum and the upward moderator flow path through the fuel channel boxes and the upper plenum; 2) the loop that from the previous one detaches towards

([1]) Since the mechanical design of the system was out of the scope of the work, the sizing of the condenser unit is admittedly parametrical, supported by the confidence that the selection of appropriate tube thicknesses and heat transfer surfaces should not pose any problem for a reactor having 1/10 of the power normally encountered for 1 GW electric units. Again, the main aim of the work was to explore the natural circulation features of the reactor during the postulated LTSBO transient.

the moderator channel inlet plena, passes through the inner moderator channel to the outlet plena, flows down to the double bottom structure and finally enters the sequence of the seven stages of the fuel coolant channels and is finally captured through the steam line by the Isolation Condenser to be returned together with the Accumulator flow to the downcomer.

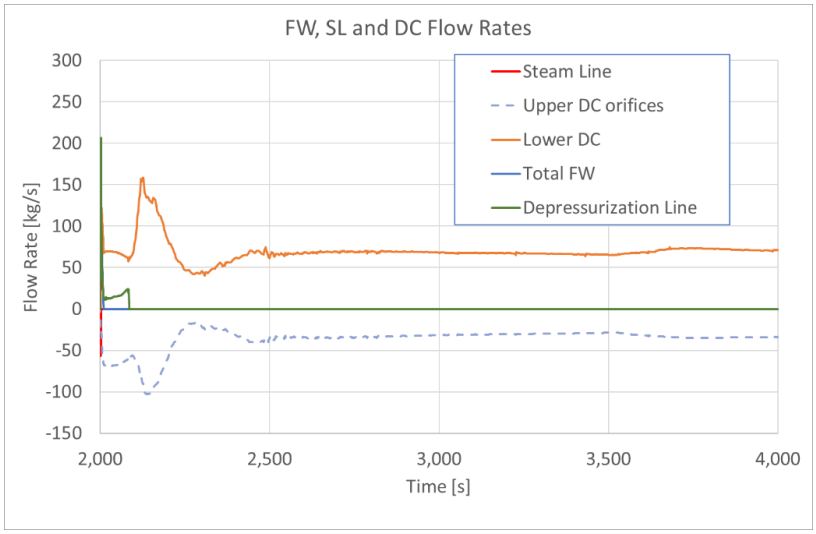

a) short term

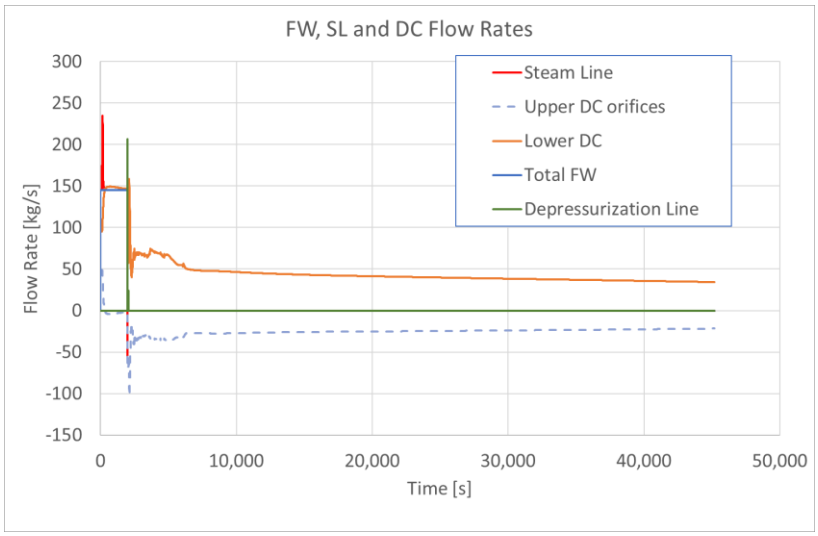

b) whole transient

Figure 39: Relevant flow rates in the vessel

Figure 40 helps understanding the pattern of these two main flow paths. As it can be noted**, the orange arrows indicate the 1st main flow path** described above, involving the moderator recirculation through the upper downcomer orifices, while **the yellow ones point out the 2nd flow path** detaching from the previous one and involving the fuel channels. It is noteworthy to consider that at the 7th stage of the inner moderator channels, both hot and average, the flow is reversed, something that can be explained by the little value of the downward flow rate at that height (zero at the top owing to the blind node 740 and increasing with the contribution of each channel moving downwards) combined with an opposing density distribution in the inlet and the outlet plena of the moderator channels, since the inlet plena have a lower temperature than the outlet ones.

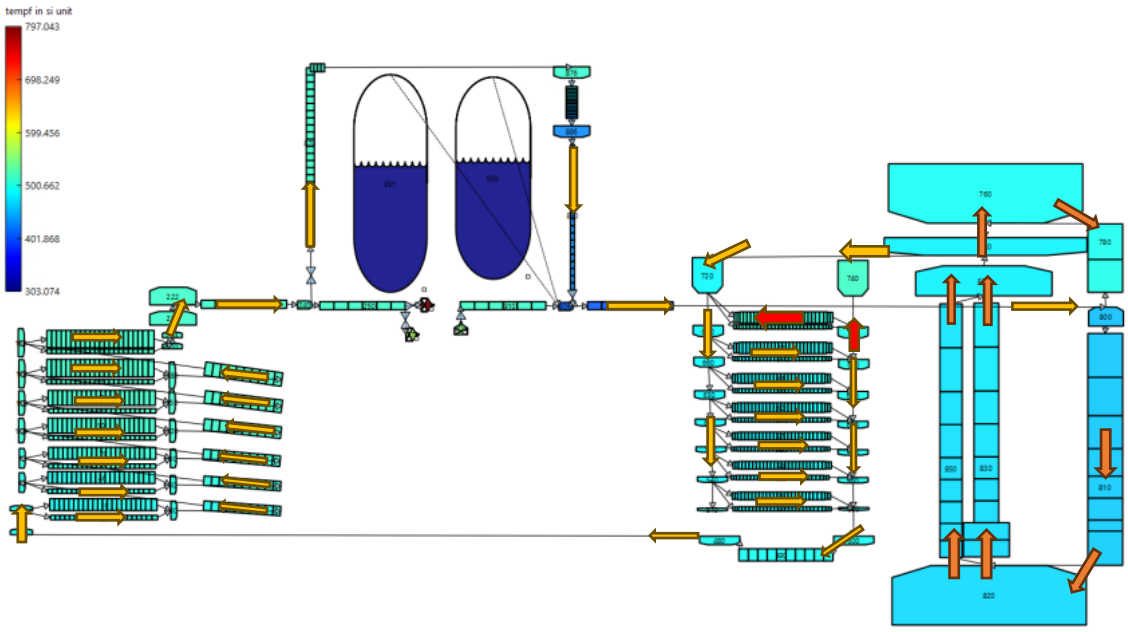

Figure 40: Natural circulation flow paths established during the SBO sequence: the orange path is related to the 1st loop mentioned in the text, the yellow one is related to the 2nd, while the red arrow point outs a backward circulation observed at the 7th stage of the moderator channels

Figure 41 and Figure 42 help in confirming the above described patterns. In particular, the reversal of flows at the 7th level of the inner moderator channels can be noted.

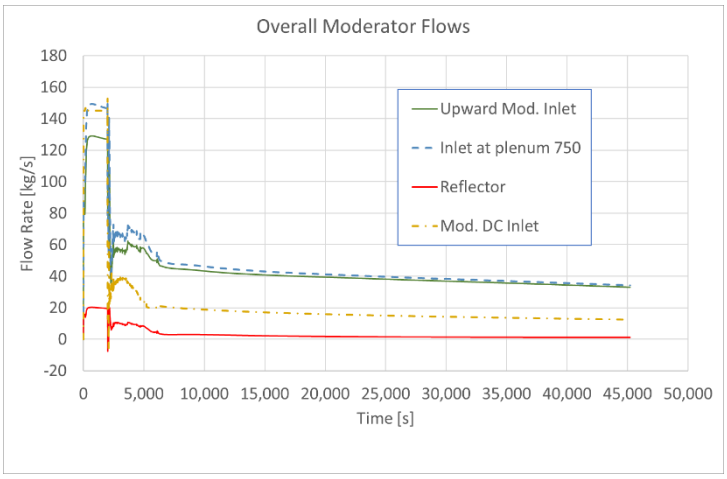

Figure 41: Moderator flows in the vessel

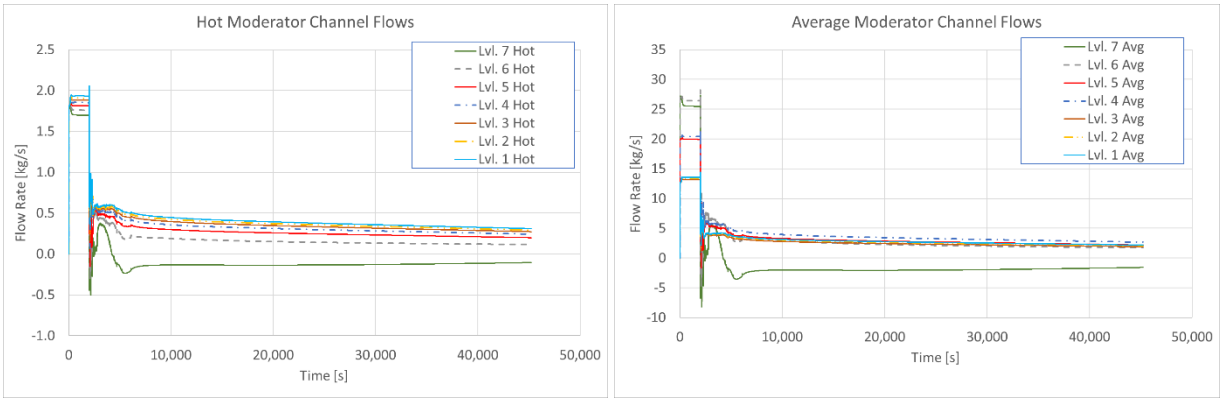

Figure 42: Moderator flows in inner fuel channels

On the other hand, the flow distribution in hot and average fuel channels is shown in Figure 43, showing a rather uniform distribution in average channels and a limited spread in hot ones.

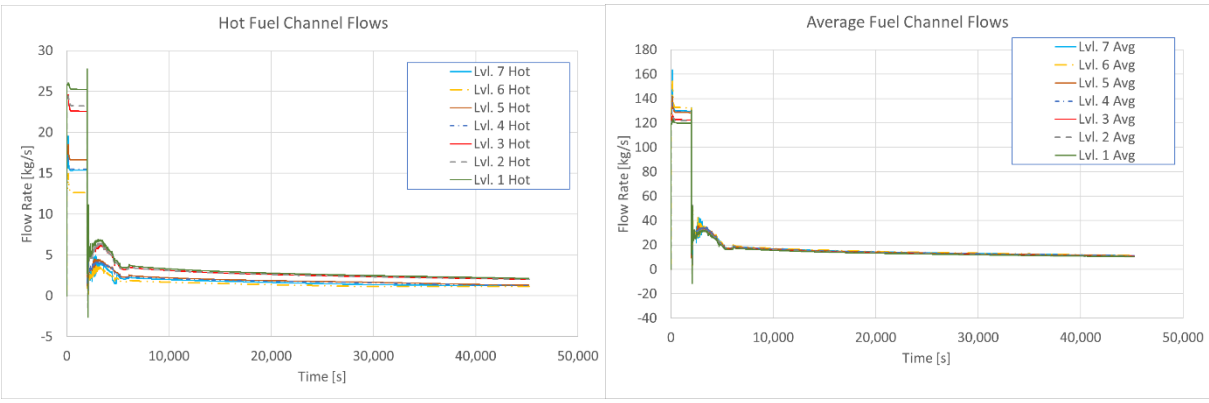

Figure 43: Coolant flows in fuel channels

The time history of void fraction during the transient shows the sudden flashing of flow in the hotter channels at the transition from the supercritical to the subcritical pressure. Observation of such trends explains why this passage is really difficult for codes to be coped with.

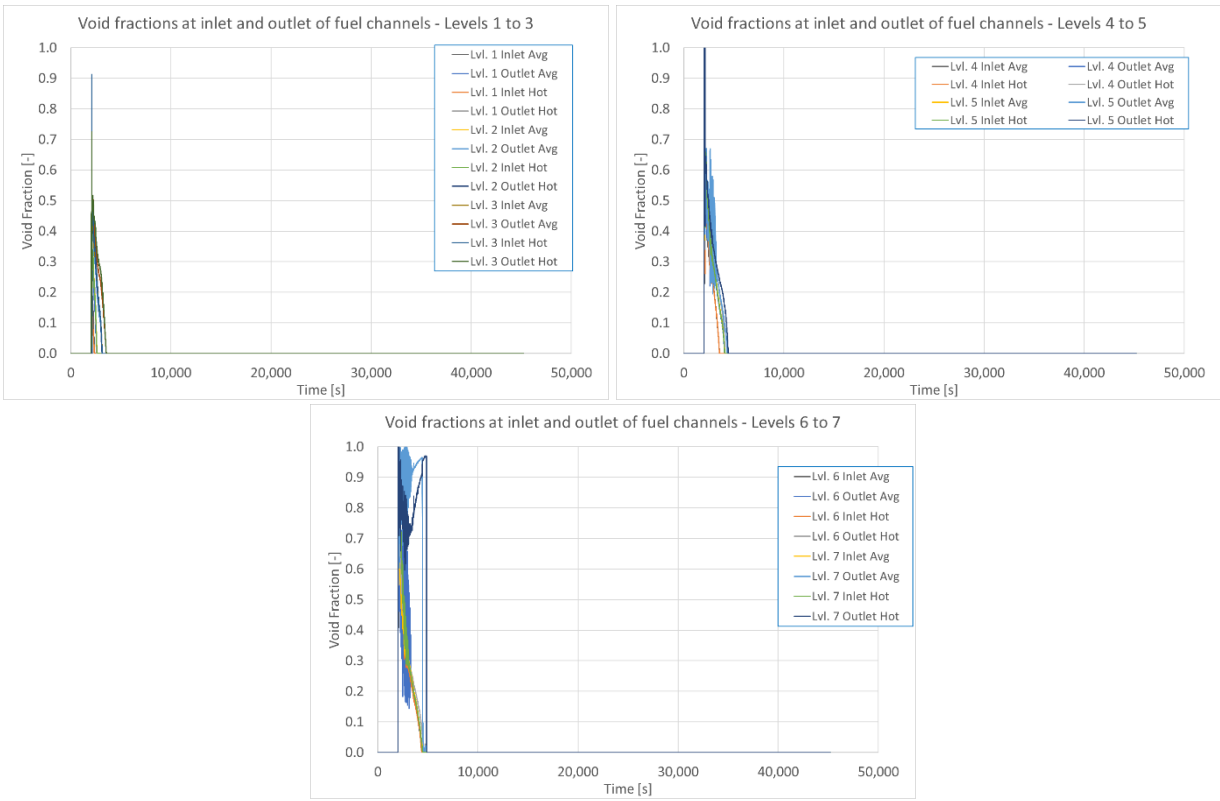

Figure 44: Void fraction in coolant channels

Figure 45, presenting the accumulator and isolation condenser system flow rates, show why the void fraction is disappearing with the vessel being cooled by the isolation condenser and flooded by the accumulator systems. As it can be noted, the discharge of the accumulator is mainly concentrated during the fast depressurisation phase of the transient, while the isolation condenser provides a long lasting flow, rejecting the decay heat to the related pool. It was seen that this intervention of the accumulator system is progressively filling the reactor with water.

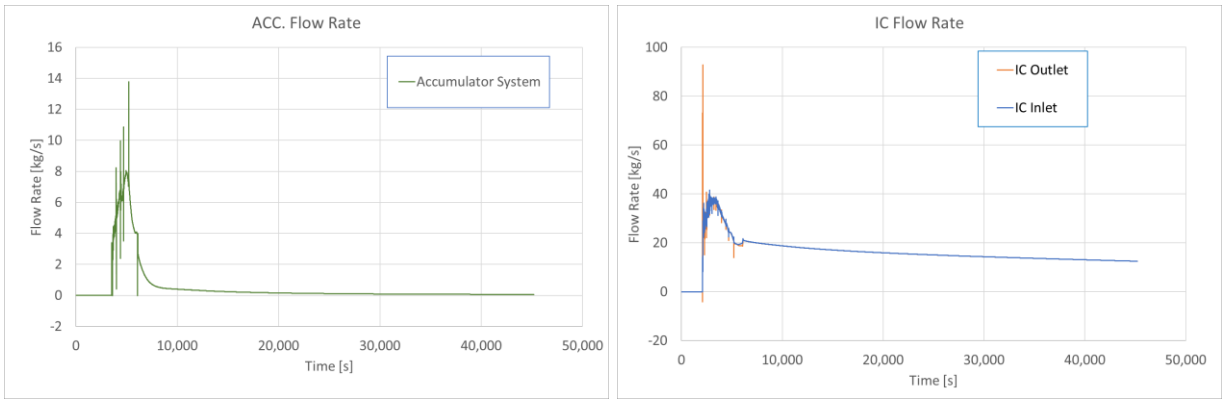

Figure 45: Accumulator and isolation condenser flow rates

As it can be noted, in Figure 46 and Figure 47, the fluid temperatures in the most important moderator and fuel channel region steadily decrease with time, sign of the cooling process.

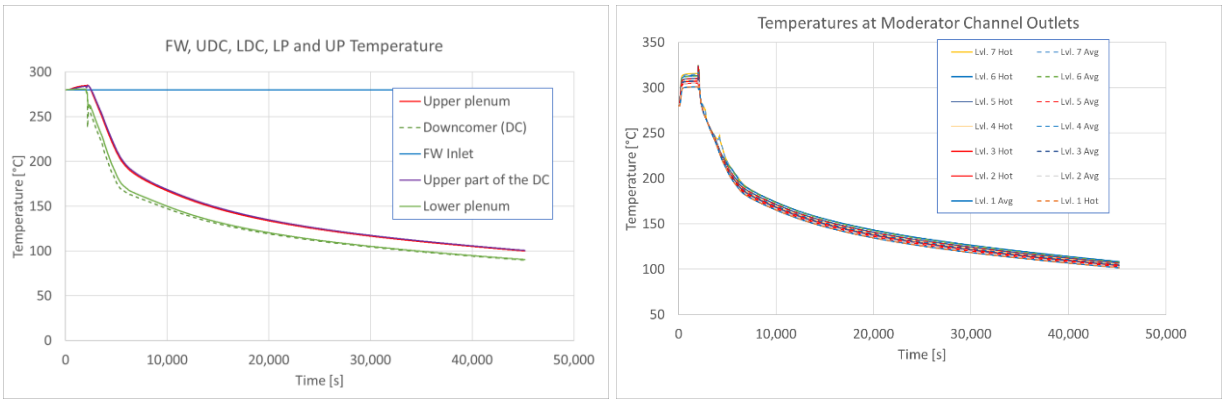

Figure 46: Fluid temperatures in the vessel moderator regions

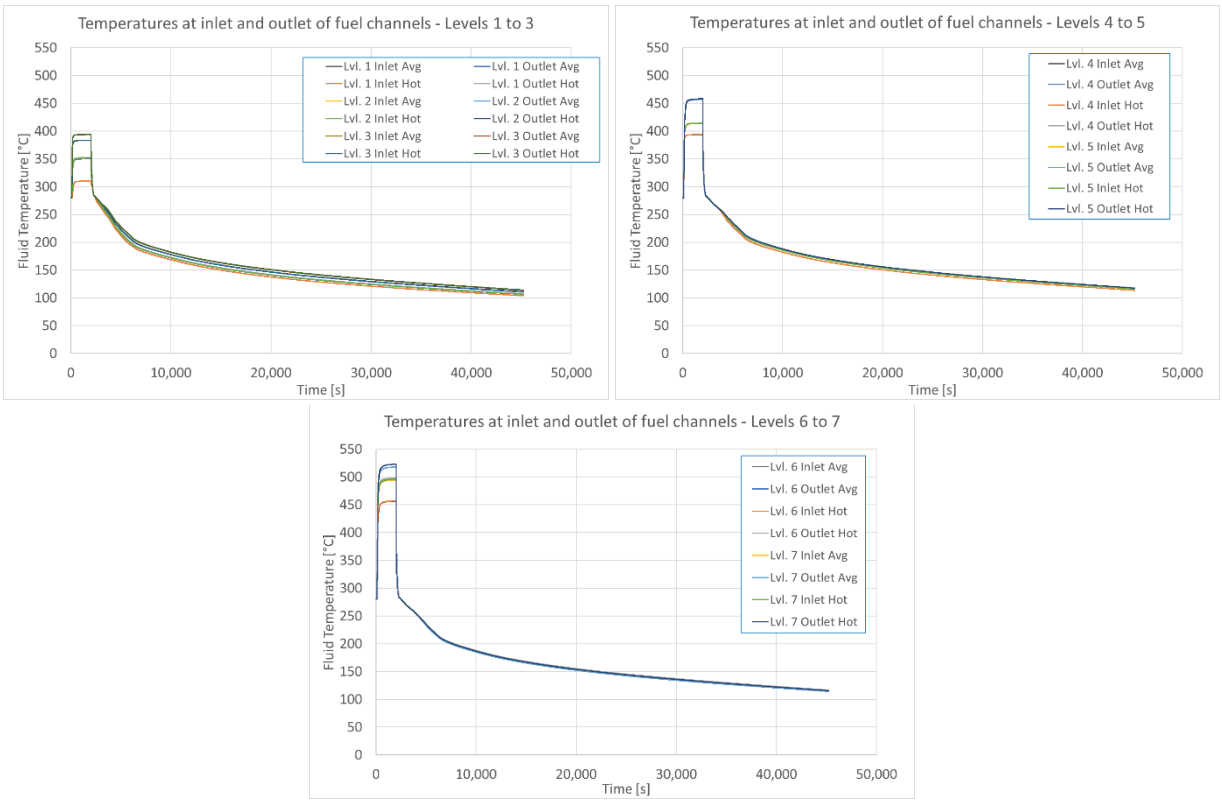

Figure 47: Fluid temperatures at the inlet and at the outlet of the fuel channels

More importantly, the cladding temperatures show no sign of deterioration or dry-out owing to the level of cooling being maintained by the introduced passive system. In particular, it can be noted that after 12 hours the temperatures of the fluid and of the cladding is nearing 100 °C, so that, notwithstanding the possible further depressurisation of the system down to atmospheric pressure, soon no flashing will be possible.

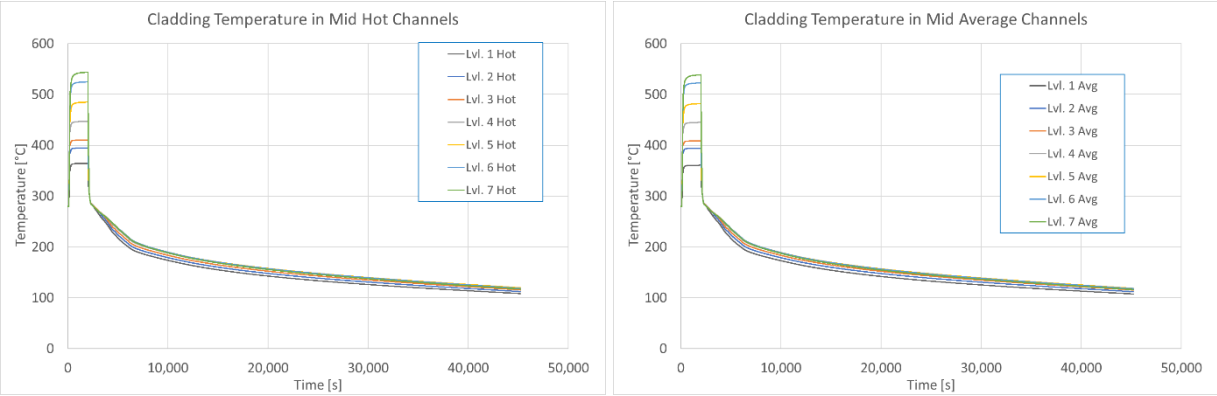

Figure 48: Cladding temperature at different levels in at middle length in fuel rods

Though the transient calculation has been stopped at 12 hours in the transient, it can be expected that the scenario can likely continue unchanged with progressive cooling and depressurization for a sufficiently long grace period. In fact, the residual mass of water in the accumulator at the end of the transient is still around 21800 kg, with a flow rate of some tens of grams per second (50-80 g/s), by the way in continuous decrease; this suggests that the accumulator system will have enough water to continue supplying the little rate of volume requested by fluid densification due to cooling in the reactor for more than the requested grace period (72 hours).

In summary:

- the modelling assumptions and the approximate sizing of the isolation condenser and of the accumulator systems appear to be sufficient to keep the reactor cooled for a long period of time, even exceeding the target grace period;
- within the limitations of the present study, no dangerous levels of cladding temperature is observed during the station black-out transient;
- the discharge of the accumulator tends to keep the reactor full of water, with pressure that decreases very slowly (it is still above 2 MPa at the end of the 12 hours);
- during the grace period there is no need for a gravity driven injection system to intervene, so that it seems that, once recovered the on-site and/or off-site powers, it will be possible to bring the reactor to cold shutdown conditions by active means.

Nevertheless, there are motivations for performing sensitivity analyses. In particular:

- the isolation condenser system is actually transformed into a passive residual heat removal system, with only liquid inside, due to the discharge of the accumulator system; a possibly worrying aspect is that its height (12.5 m) does not allow to keep the siphon at atmospheric pressure, so that during further depressurisation the system may undergo to an emptying of the “isolation condenser”, leading to a partial stop of its effectiveness in removing heat, up to the point that the reactor system may tend to boil and vapour may be condensed by the IC again; using a lower height isolation condenser (definitely much below the theoretical limit of nearly 10 m) this could be possibly avoided;
- during the transient, the accumulator remains the only relatively compressible part of the plant, working as a sort of nitrogen loaded pressuriser: this justifies the very slow pressure decrease, that keeps the reactor at sufficiently high pressure with liquid; it could be possible to avoid its

intervention, keeping part of the voiding generated by the depressurisation, so that the isolation condenser could actually work as a condenser, possibly with sufficient efficiency; this would possibly depict a more “compressible” situation, in which liquid and vapour are present in the vessel, so that there is no fear that the system may become “solid” owing to liquid expansion in the accumulator;

- the optimised orifice pattern introduced considerable pressure drop in the reactor core, as it was shown in a previous section; this is because achieving in “hot” channels a same power-to-flow ratio as in average ones forced to increase their flow rate by an average factor around 1.4; since pressure drop increase roughly with the square of flow rate, a doubling of the pressure drop was observed (1.4 x 1.4 = 1.96); the analysis of the transient without orifice optimisation will tell if in view of the envisaged SBO sequence the orifice optimisation can actually bring any advantage;
- finally, since no real attempt was made in order to study the actual shape of the foot of the fuel element in terms of inlet throttling to be used in the analyses, an arbitrary uniform increase of the singular pressure drop coefficient at the inlet of fuel elements could be experimented to assess the predicted behaviour of this change.

4.5.2 Lowered IC units

The only difference in the assumed plant configuration adopted for this calculation with respect to the base case has been the lowering of the IC unit of 6.5 m, a length that was subtracted to both the rising and the return piping. This analysis, stimulated by the considerations about the possible breaking of a liquid siphon in the tall IC unit at low pressure, is therefore useful also to assess a more general condition in which the postulated efficiency in natural circulation is reduced.

Figure 49 shows the differences obtained in the two cases for the IC and accumulator discharge flow rates. As it can be noted, the IC flow rate is correspondingly lower in the lower IC case, as a consequence of the reduced driving force developed by the fluid. This reduction is expectedly depending on the interplay between the smaller buoyancy force and the smaller friction along the riser and return pipes. The accumulator flow rate is also influenced by the slightly different behaviour of pressure, driven by a less efficient residual heat removal system.

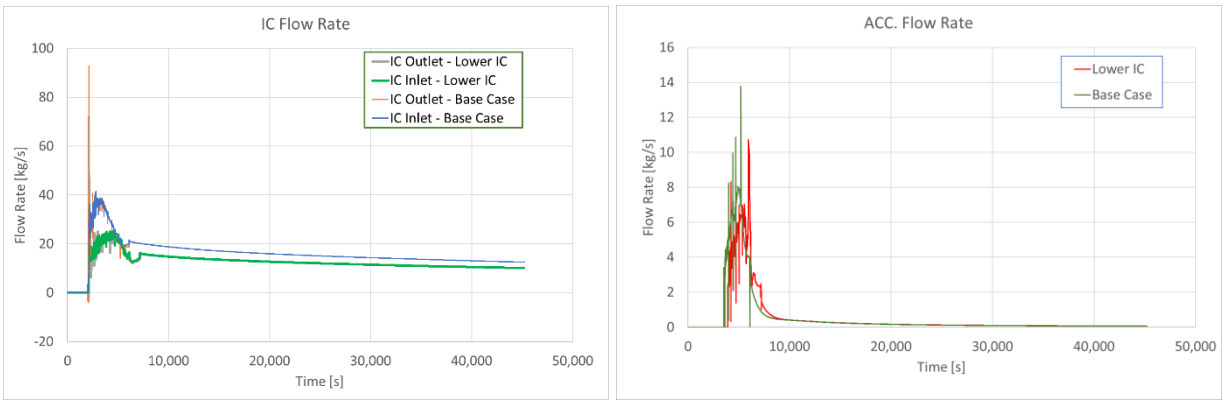

Figure 49: IC and accumulator flow rates in the base case and with lowered IC

Correspondingly, the temperatures of the fluid in the vessel are slightly higher, though they anyway reach the neighbourhood of 100 °C at the end of the 12 hrs transient, as shown in Figure 50.

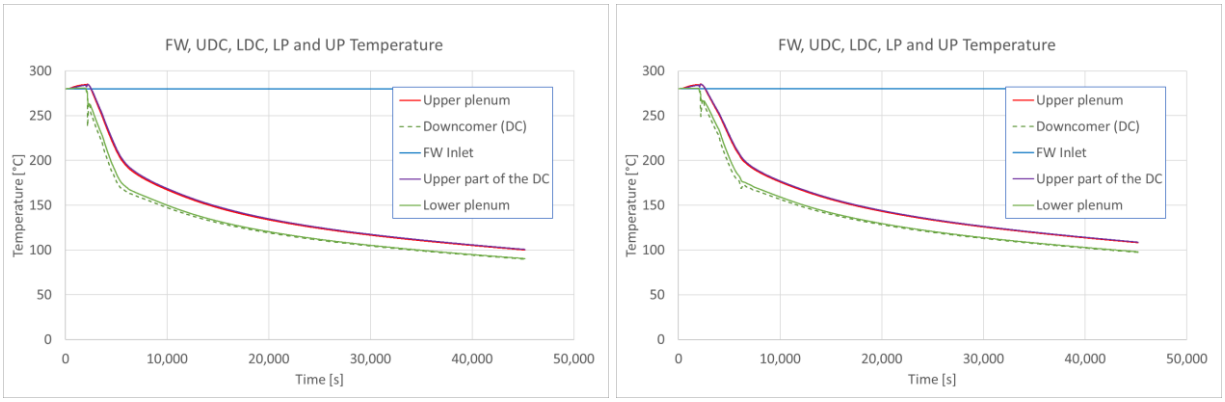

a) Base case b) Lower IC

Figure 50: Temperatures in the vessel in the base case and with lowered IC

The behaviour of flows in the natural circulation flow paths is similar, as shown by Figure 51 and Figure 52. The inversion of flows in the inner moderator channels at the 7th level appears enhanced, probably due to higher temperature differences and then buoyancy forces driving the involved natural circulation flow paths (see Figure 51). The flows in the cooling channels remain comparable, as shown in Figure 52, leading to comparable cooling conditions, as shown in Figure 53; slight irregularities observed in the temperature trends around 6500 s have a counterpart in the inlet and outlet fluid temperatures (Figure 54) and are not supposed to be due to thermal crisis phenomena.

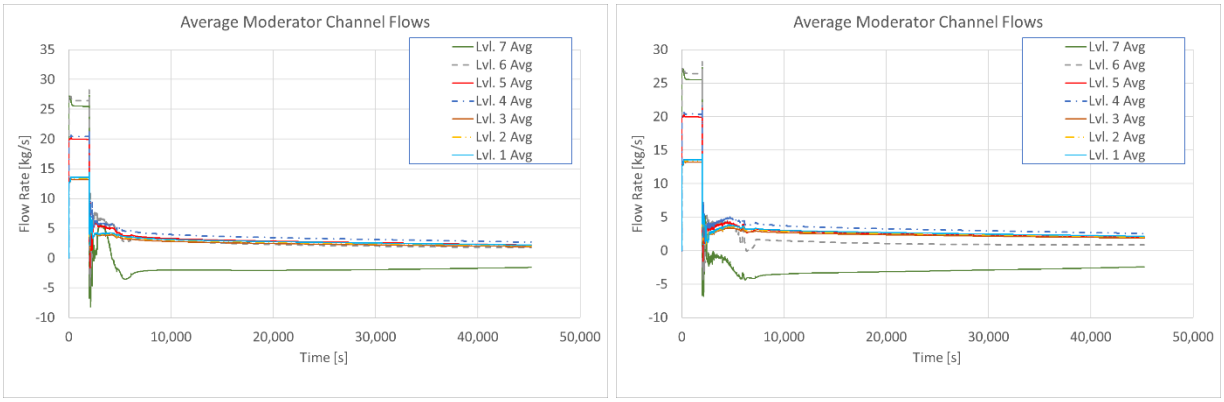

a) Base case b) Lower IC

Figure 51: Moderator flows in average channels in the base case and with lowered IC

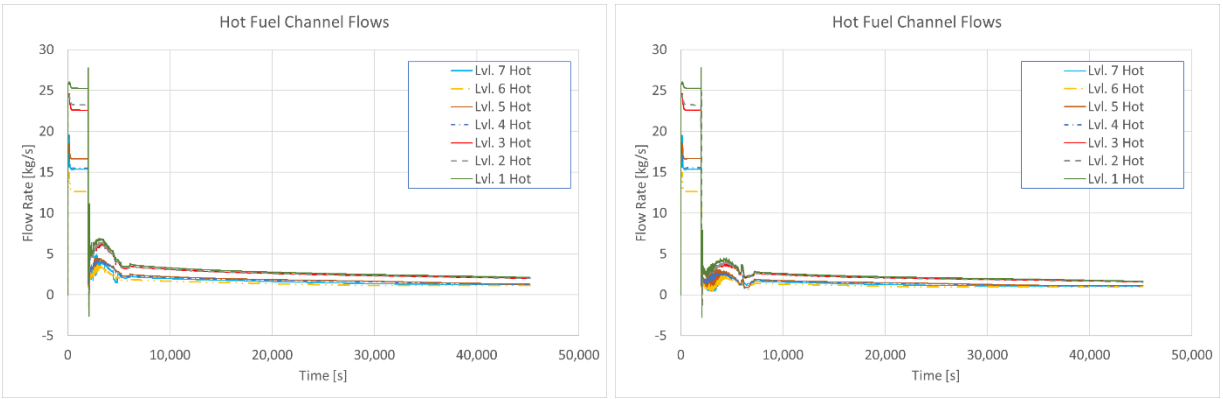

a) Base case b) Lower IC

Figure 52: Hot fuel channel flows in the base case and with lowered IC

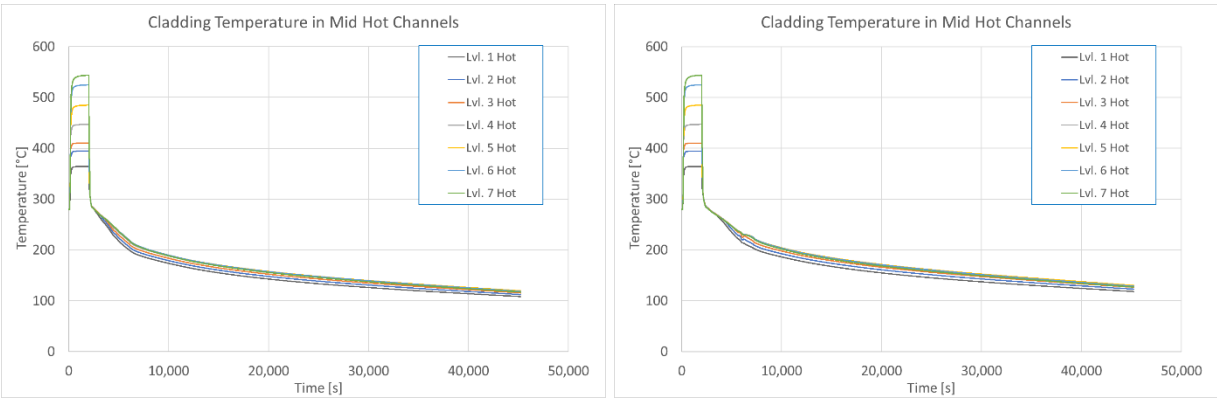

a) Base case b) Lower IC

Figure 53: Cladding temperatures at mid hot fuel channels in the base case and with lowered IC

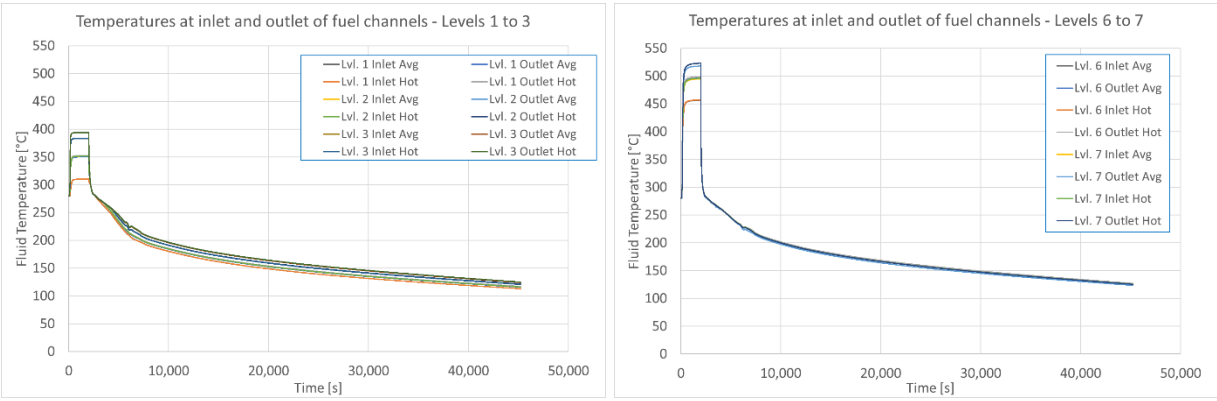

Figure 54: Fluid temperatures at inlet and outlet of fuel channels with lowered IC

In summary, the lowering of the IC unit in height changes the observed transient behaviour quantitatively in a somehow expected way, without introducing qualitative changes in the observed phenomena. Also in this case, the residual mass of water in the accumulator system at the end of the 12 hrs is sufficiently large (more than 22,000 kg) and the residual discharge flow rate sufficiently low to suggest that the presented scenario will remain qualitatively unchanged during the depressurization of the system for a sufficiently long grace period.

4.5.3 Singular pressure drops at fuel channel inlet

A calculation case was run by assigning the entrance singular pressure drop coefficients at the foot of the fuel elements uniformly to the value of K = 5, aiming to assess the effect of a possible inlet throttling which was not evaluated in detail in present analyses. As it will be clear from the plots to be shown later, the main effect of this action is to suppress the orifice optimisation that allowed to decrease steady-state coolant and cladding temperatures in hot channels, leaving the rest of the transient nearly unchanged.

Figure 55 shows the trends of pressure in the system, highlighting little differences between the base case and the one with K=5 singular pressure drop coefficients, except for the fact that the latter case gives rise to a lower pressure in the moderator zone in steady-state, owing to the reduced pressure drop in the whole core with respect to the case with optimised inlet throttling. Figure 56, in addition, shows the little effects observed on the Isolation Condenser and the accumulator system flow rates, consequent to the little changes in the overall scenario in qualitative and quantitative terms.

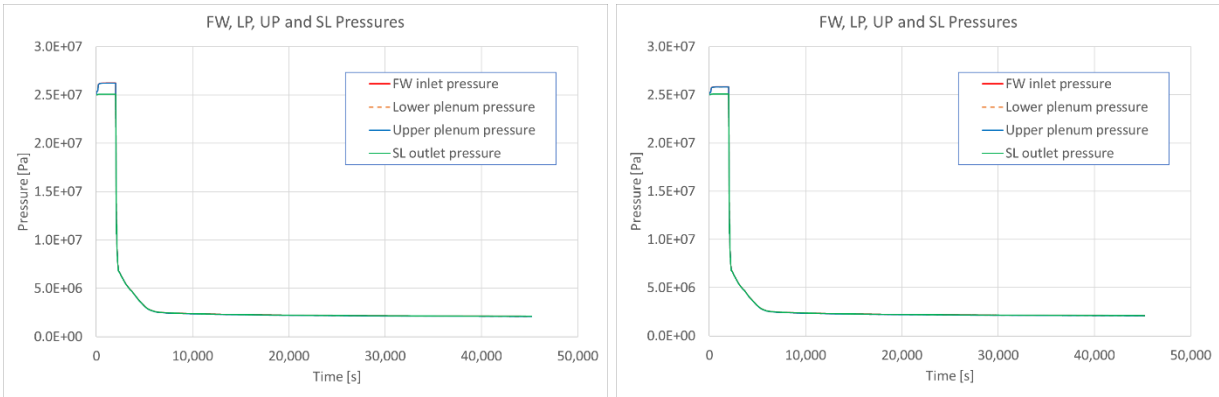

a) Base case b) K = 5

Figure 55: Pressure in the vessel in the base case and with K = 5

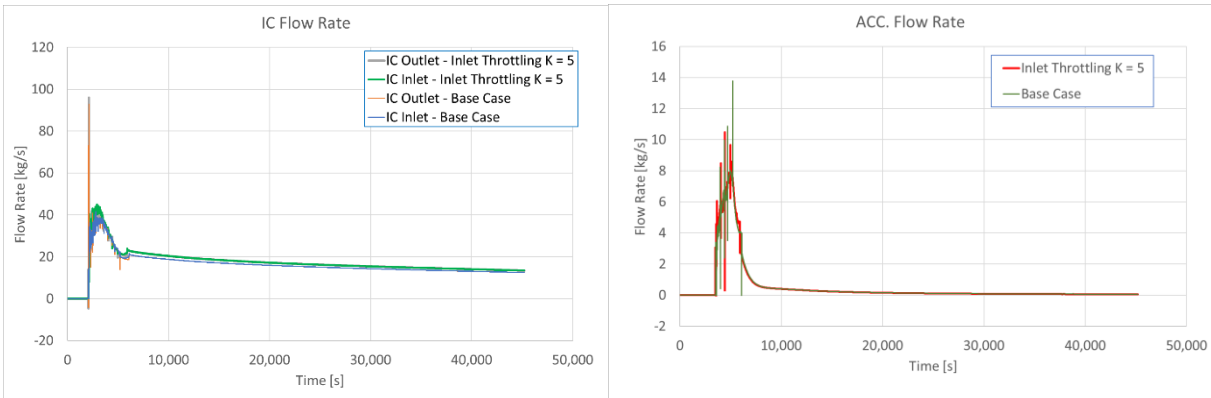

Figure 56: IC and accumulator flow rates in the base case and with K = 5

In particular, Figure 57 and Figure 58 show very limited changes in the flow and temperature distributions in different zones of the reactor vessel, while Figure 59 to Figure 61 show quantitative differences mostly in the flow rates of the hot fuel channels in steady state conditions and, at a more limited extent, during the SBO transient.

Finally, Figure 62 and Figure 63 show that the main changes in the cladding behaviour are related to the steady-state values of the cladding in the hot channels, while the differences in the average channel cladding are much more limited.

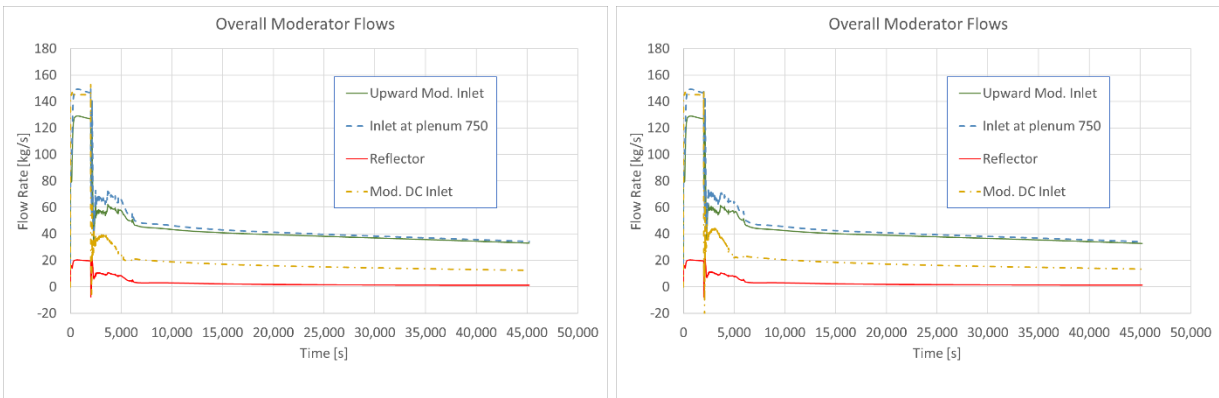

b) Base case b) K = 5

Figure 57: Moderator flow rates in the vessel in the base case and with K = 5

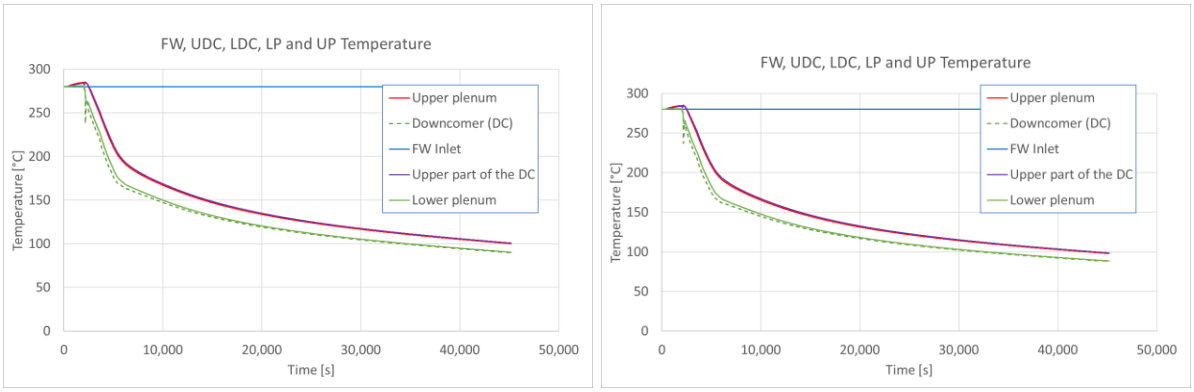

a) Base case b) K = 5

Figure 58: Main temperatures in the vessel in the base case and with K = 5

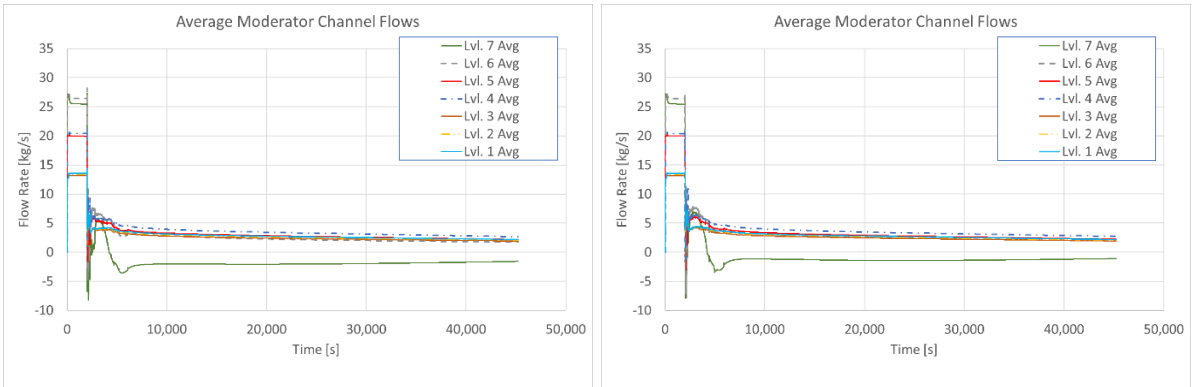

a) Base case b) K = 5

Figure 59: Average moderator channel flows in the base case and with K = 5

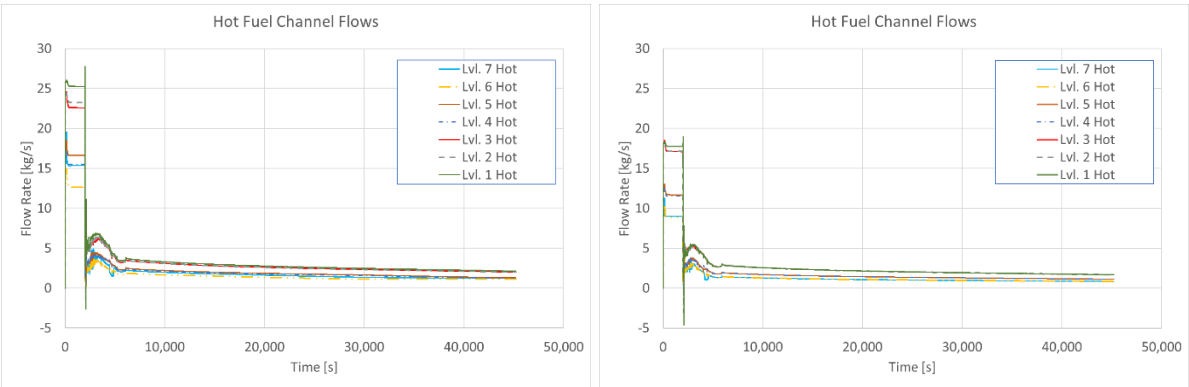

a) Base case b) K = 5

Figure 60: Hot fuel channel flows in the base case and with K = 5

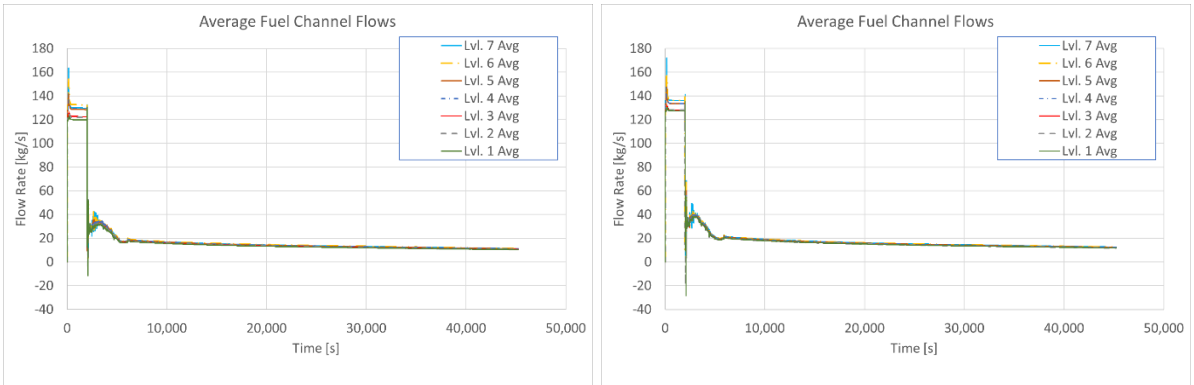

a) Base case b) K = 5

Figure 61: Average fuel channel flows in the base case and with K = 5

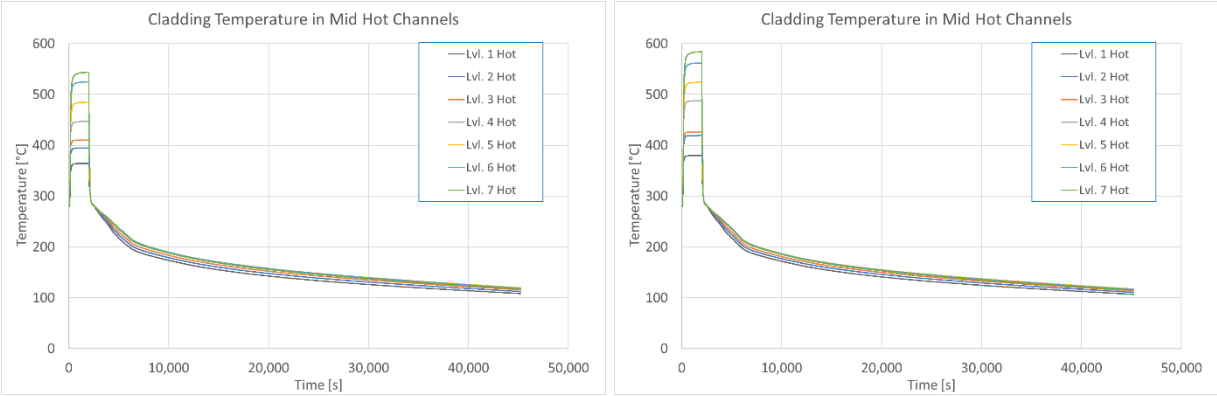

a) Base case b) K = 5

Figure 62: Cladding temperature in mid hot channels in the base case and with K = 5

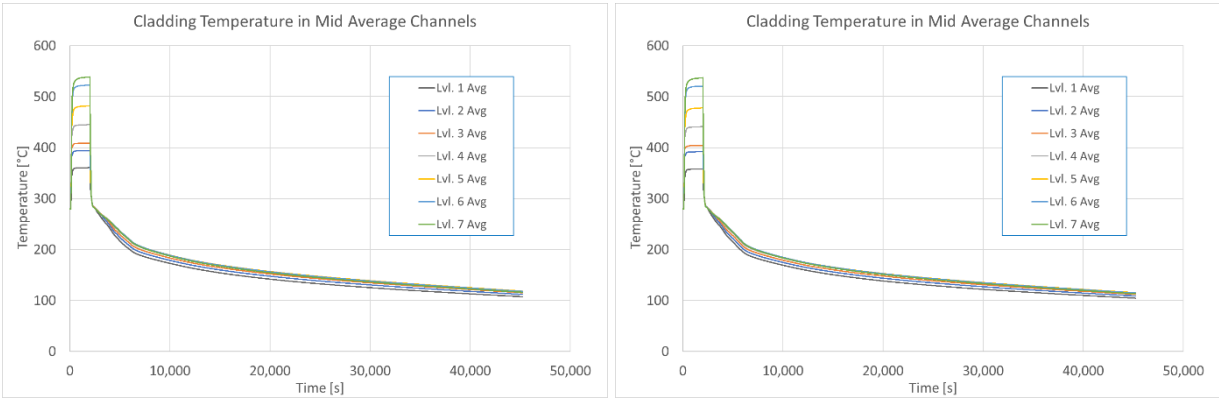

a) Base case b) K = 5

Figure 63: Cladding temperature in mid average channels in the base case and with K = 5

In summary, the uniform increase of the inlet throttling in fuel elements has little effect on the predicted SBO scenario in the postulated conditions. This leaves open the opportunity to conceive the fuel inlet throttling trying to optimise it only on the basis of considerations driven by the optimisation of pressure drop and flow distributions, confident that, at least within the limits of the conditions explored in this analysis, there is little consequence in the response of the system to the postulated station-blackout scenario.

Similarly a calculation case with basic choices for the singular pressure losses at the inlet and outlet of fuel channels (labelled as No Orifices) showed minimal changes with respect to the base case. Again the most important change is related to the fact that the flow rates in the hot and average channels are not optimised for obtaining a similar power-to-flow ratio in steady-state conditions and the pressure drop in steady-state is lower (see Figure 64).

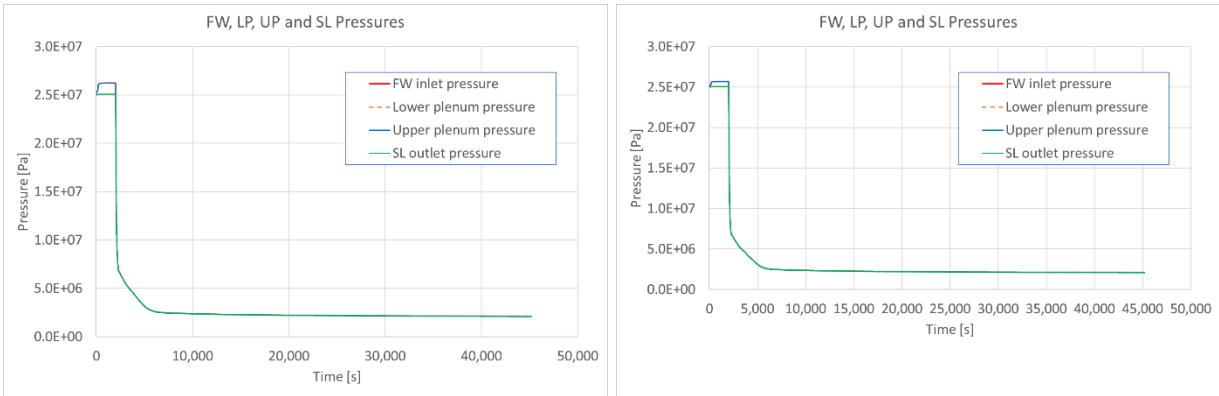

a) Base case b) No orifices

Figure 64: Pressure in the vessel in the base case and without orifices

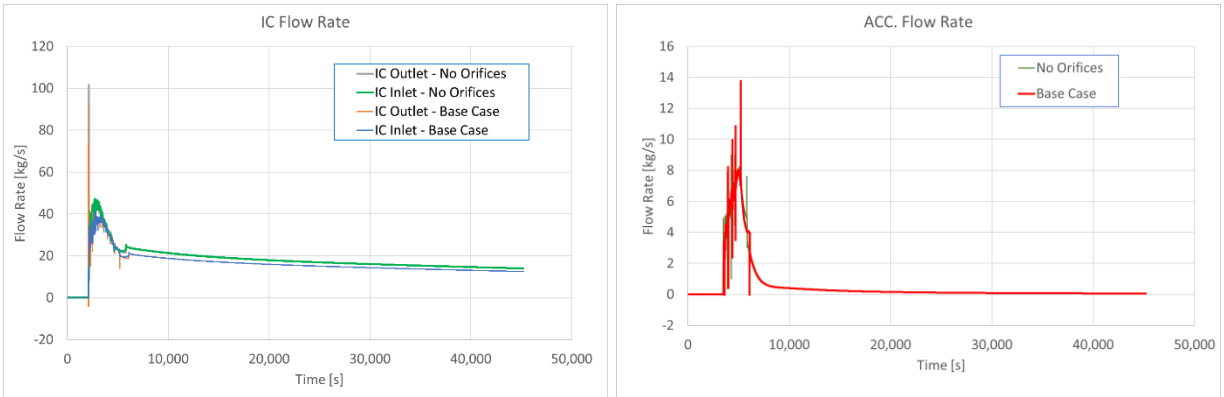

Figure 65: IC and accumulator flow rates in the base case and without orifices

While the accumulator flow rate is practically not affected by the change, as in the case K=5 a globally lower pressure drop across the core makes the flow rate in the IC system slightly larger (see Figure 65).

The rest of the information obtained by the analyses is shown in Figure 66 to Figure 72, where it can be noted a different level of steady state moderator flow rates (Figure 66), similar trends of fluid temperatures in the vessel (Figure 67), similar behaviour of the average moderator channel flows (Figure 68), different hot fuel channel flow rates in steady-state that do not reflect into too remarkable changes in transient behaviour (Figure 69), very similar average fuel channel flows (Figure 70) and changes in fuel cladding temperatures mostly in hot channels and in steady state (Figure 71 and Figure 72).

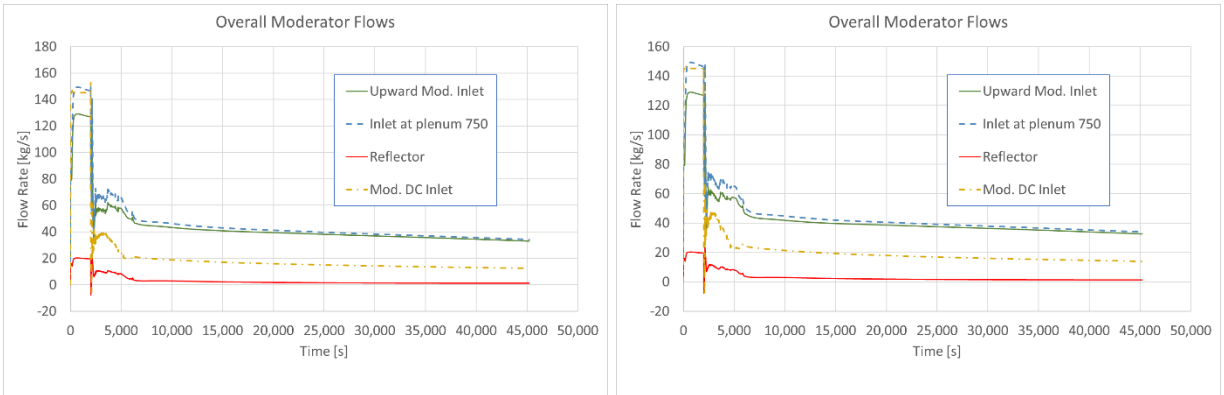

c) Base case b) No orifices

Figure 66: Moderator flow rates in the vessel in the base case and without orifices

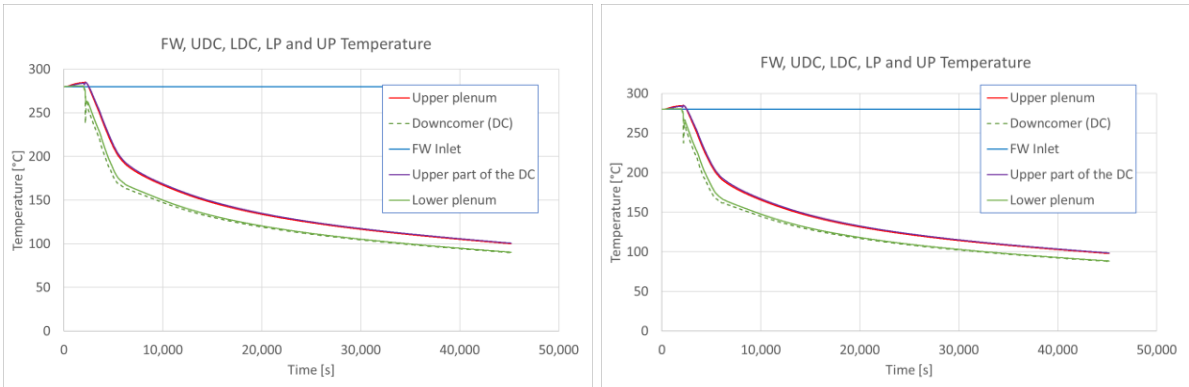

b) Base case b) No orifices

Figure 67: Main temperatures in the vessel in the base case and and without orifices

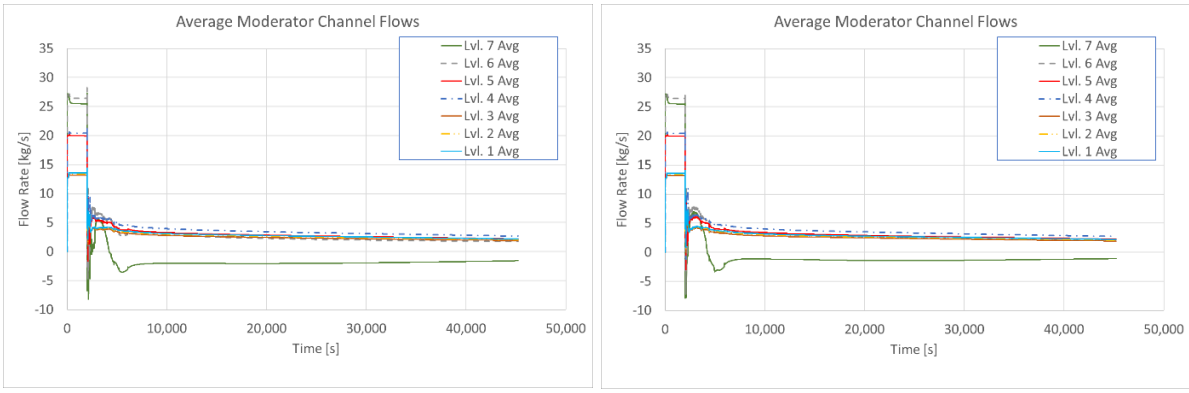

b) Base case b) No orifices

Figure 68: Average moderator channel flows in the base case and and without orifices

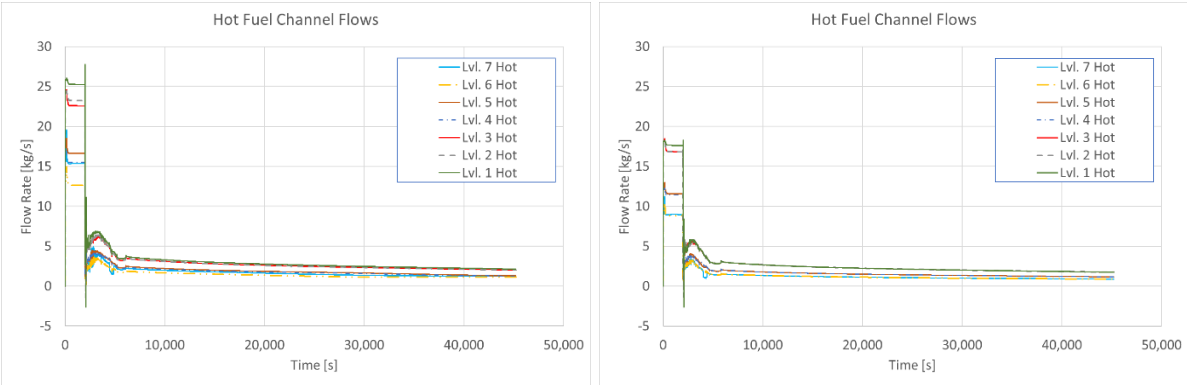

b) Base case b) No orifices

Figure 69: Hot fuel channel flows in the base case and and without orifices

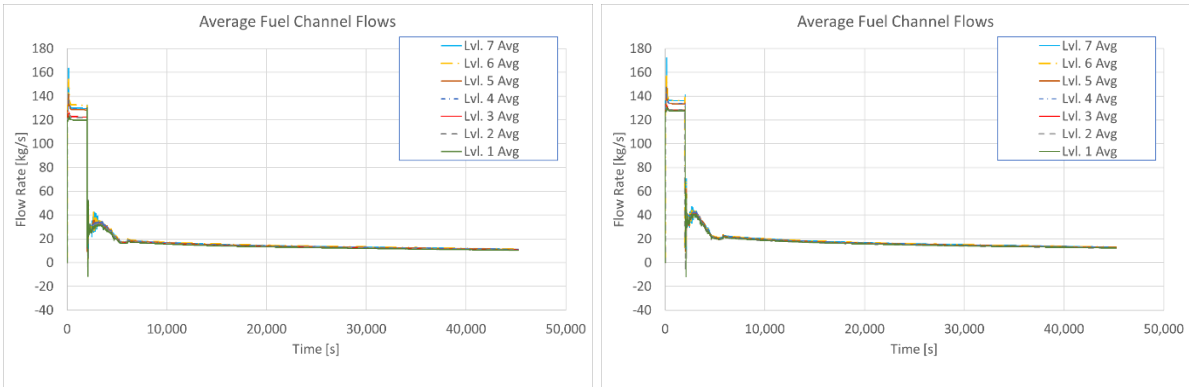

b) Base case b) No orifices

Figure 70: Average fuel channel flows in the base case and and without orifices

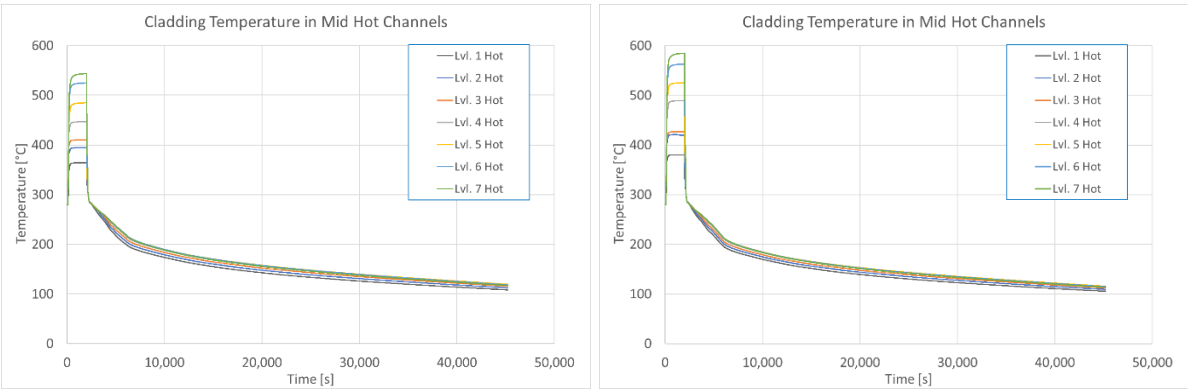

b) Base case b) No orifices

Figure 71: Cladding temperature in mid hot channels in the base case and and without orifices

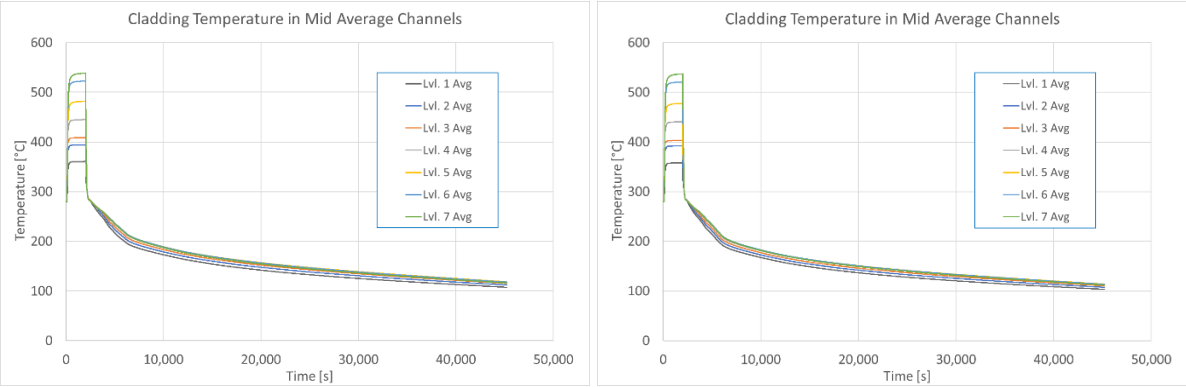

b) Base case b) No orifices

Figure 72: Cladding temperature in mid average channels in the base case and without orifices

4.5.4 Sequence without the accumulator system

This transient was run for assessing the consequences of the introduction of the accumulator system discharge in the sequence of events, more than to postulate a possible failure to activate such a well-assessed passive system. In previous analyses, in fact, it was noted that the final level of pressure in the coolant system is mainly driven by the partial discharge of the accumulators, filling with liquid all the vessel and thus becoming a sort of gas-filled pressuriser for the rest of the transient. In the base calculation case, in particular, at the end of the considered 12 hrs of transient pressure is still at a level of 2.1 MPa, mainly due to the pressurization action of nitrogen in the accumulators. While this situation does not represent a real problem for a system to be probably designed for a maximum pressure equal to or exceeding 30 MPa, depressurising further the system would need to exclude the accumulator and possibly opening again a depressurisation valve, something that could be made also manually after a so long transient as a final provision to bring the reactor in depressurized and relatively cold conditions.

So, the scenario presented here differs from the one of the base calculation case for the absence of the accumulator system, while a Gravity Driven Coolant injection System (GDCS) is assumed to be available. For the purposes of this calculation and without pretence to properly define its sizing, the GDCS system has been considered to have a 1200 m^3 volume, with a liquid pool of 600 m^3, placed at an elevation of 3 m above the legs of the reactor with a discharge line of 0.1 m in diameter and kept at a pressure of 0.12 MPa to account for a mild containment pressurisation. Needless to say, a proper sizing of the pool should be made on the basis of considerations related to a spectrum of accidents, especially of the Loss of Coolant (LOCA) type; the main purpose here is again to characterise the natural circulation characteristics of the system in the considered sequence.

Figure 73 and Figure 74 present the pressure trend and the overall vessel flows. It can be noted that, in the absence of the accumulator, pressure is reaching nearly atmospheric levels at a sufficient time after the initial depressurisation and the actuation of the Isolation Condenser. Flow rates have actually an initial behaviour similar to the one of the base case, with a subsequent phase of huge oscillations, having probably a mixed physical and numerical origin, which exceed also the limits of the vertical axis scale, chosen to have a reasonable range of representation of the obtained results.

These oscillations have to be put into perspective considering the trend of void fraction in the fuel channels, reported in Figure 75. As it can be noted, an initial voiding phase is terminated even without any accumulator intervention, in the period of system cooling down and

depressurisation, well before the intervention of the GDCS (Figure 76), only owing to the action of the Isolation Condenser system (Figure 77).

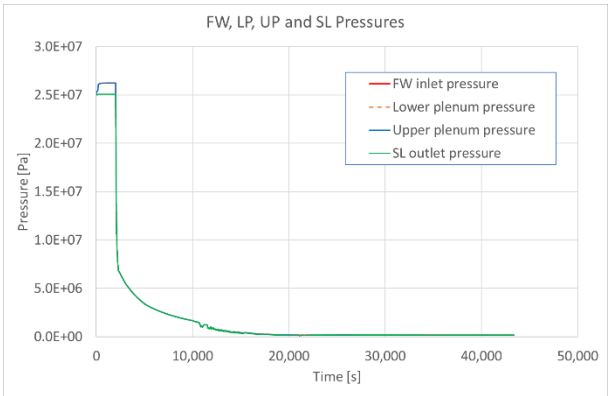

Figure 73: Pressure trend

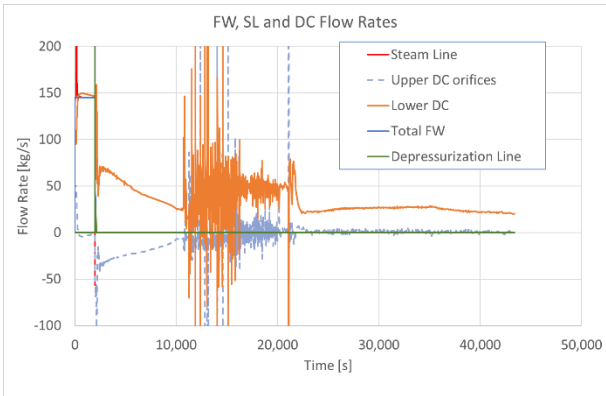

Figure 74: Overall vessel flows

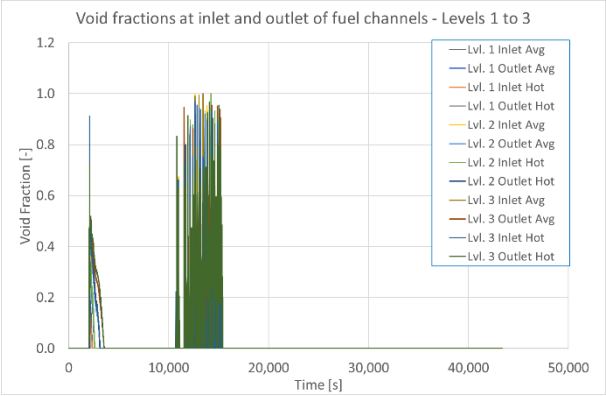

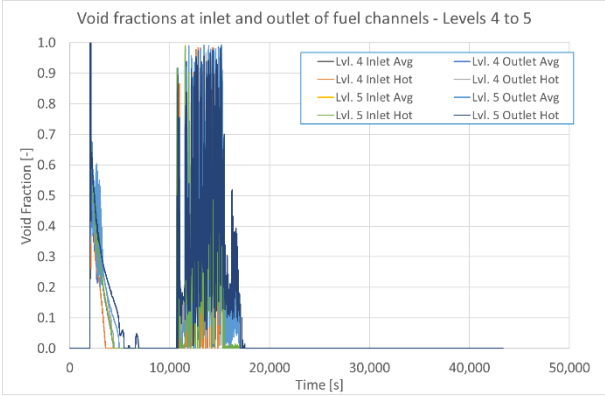

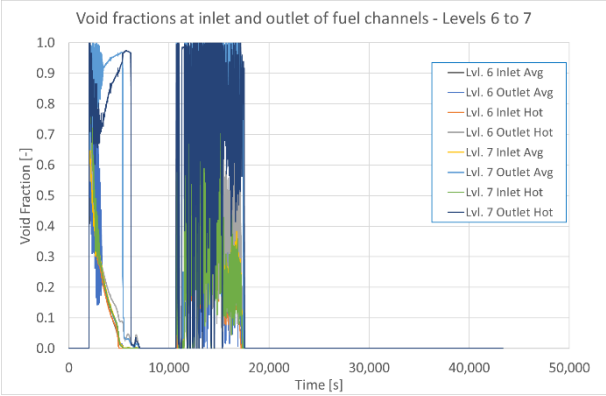

Figure 75: Void fractions at fuel channel inlet and outlet

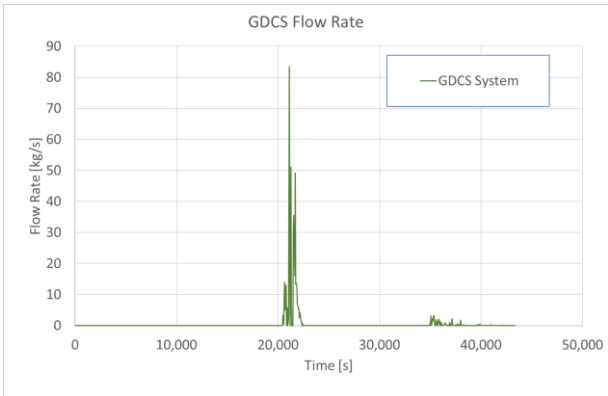

Figure 76: Gravity driven injection flow rate

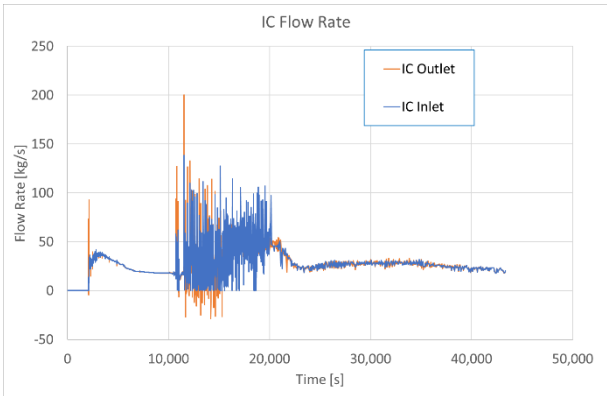

Figure 77: IC flow rate

Then, a second period of voiding occurs later and is terminated by the GDCS injection. This period of voiding is causing the wild oscillations predicted by the computation that have consequences on both the moderator flows (Figure 78) and on the trends of temperatures at different locations in the vessel (Figure 79) that, though steadily decreasing, show oscillations due to the corresponding ones observed in flow rates. Consequent oscillations are observed also in inner moderator channel flows and in coolant fuel channel flows (Figure 80 to Figure 83).

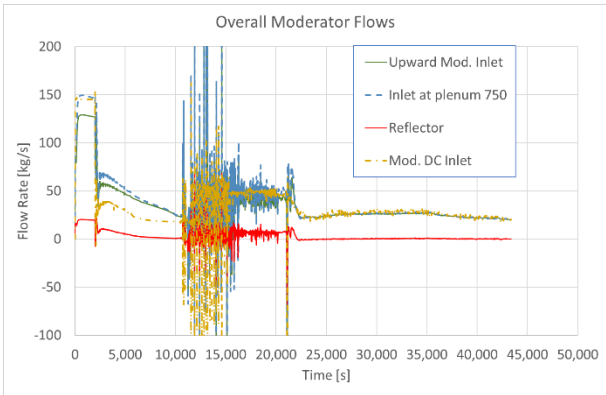

Figure 78: Overall moderator flow rates

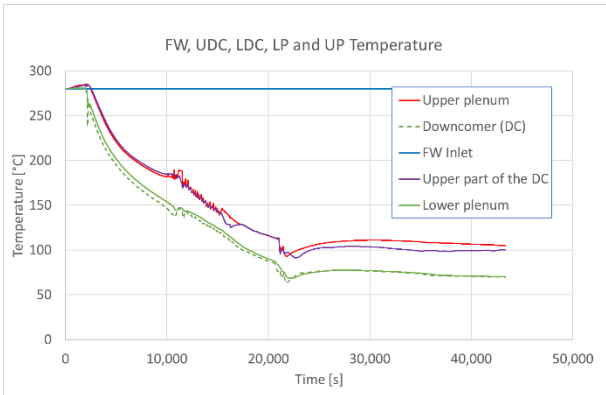

Figure 79: Main fluid temperatures in vessel

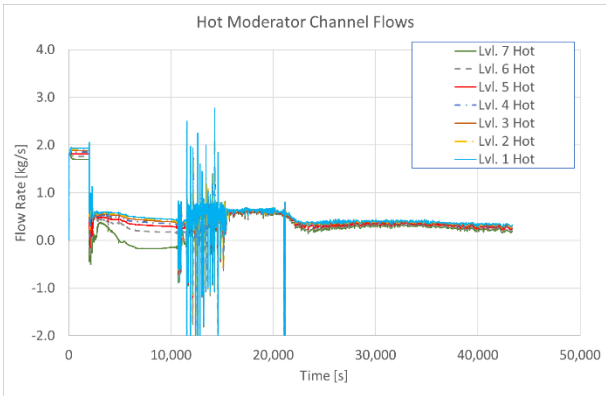

Figure 80: Hot inner moderator channel flows

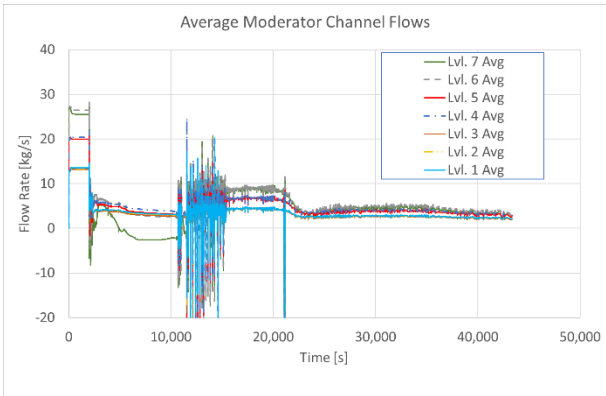

Figure 81: Avg inner moderator channel flows

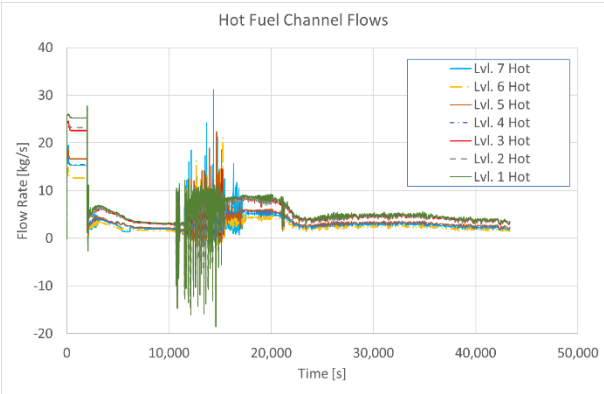

Figure 82: Hot fuel channel flows

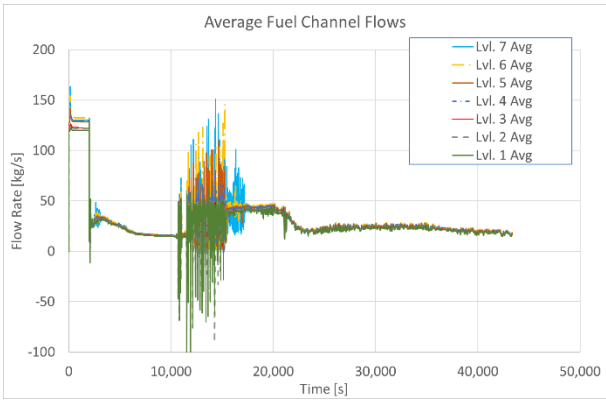

Figure 83: Avg fuel channel flows

Concerning the fluid temperatures, Figure 79, Figure 84 and Figure 85 show that, once depressurised to slightly less than 0.2 MPa (owing to the head of the liquid level in the pool, nearly 3 m and to the 3 m elevation drop assumed for the discharge line), the fluid keeps at a temperature around 100 °C, with the system that is full of liquid. It must be noted that, owing to its height (12.5 m at its top) the Isolation Condenser unit operates at subatmospheric pressure, determining a

two phase mixture being present in the pipes; this may again suggest the opportunity that the rising and condensate returning legs are shortened to keep the IC unit at a pressure greater than the atmospheric one even when the system is completely filled with water and depressurised.

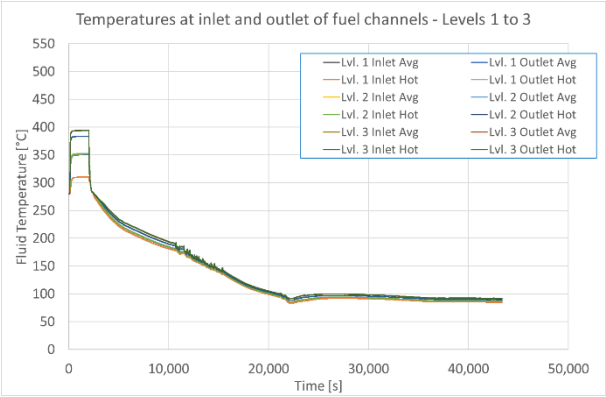

Figure 84: Fluid inlet and outlet fuel channel temperatures (Levels 1 to 3)

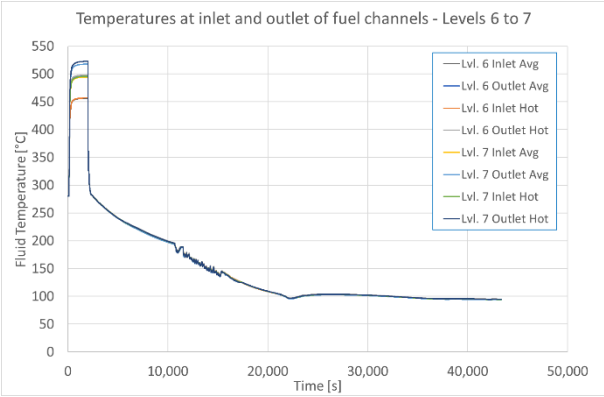

Figure 85: Fluid inlet and outlet fuel channel temperatures (Levels 6 to 7)

Finally, even in this scenario cladding temperatures appear not to suggest any particular threat to the integrity of the core (Figure 86).

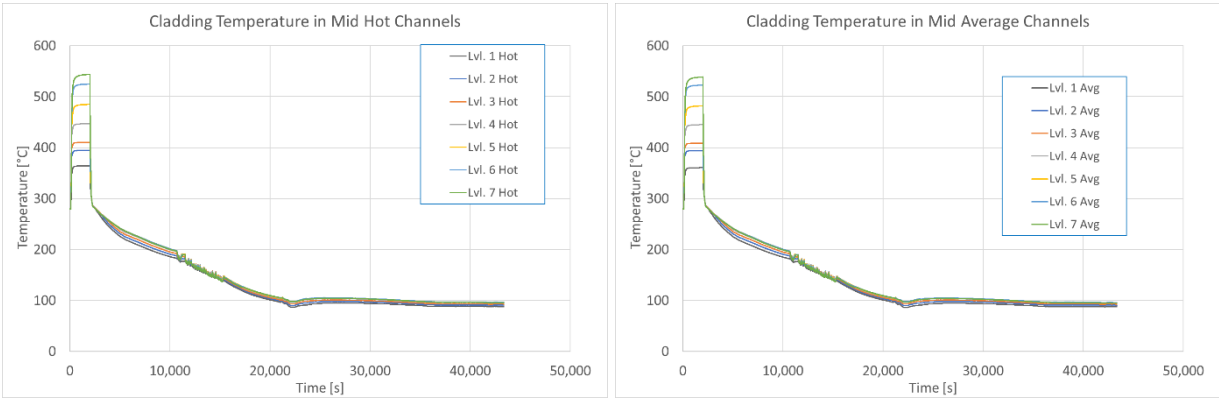

Figure 86: Cladding temperature in mid hot and average channels

4.5.5 Sequence without the accumulator system and with lowered IC units

As a variant of the above described sequence, a further case was run by inhibiting the accumulator system and using the lowered version of the IC unit as in a previous instance. As it it will be noted in the following figures, the differences with respect to the previous sequence is limited, except for a change in the regime of the isolation condenser unit that, slightly earlier than at the end of the first 12 hours undergoes to a change in the distribution of void fraction that causes a momentary decrease in heat removal efficiency.

This effect is observed between 40,000 and 50,000 s in the plot of system pressure (Figure 87), where a momentary increase is observed. This behaviour can be considered in relation to the release of an additional discharge from the GDSC system that may be a cause or an effect of a global system behaviour, leading to a momentary decrease or stop in the isolation condenser flow rate (Figure 88). The sequence of distributions of pressure, void fraction and fluid and saturation temperatures occurring before, during and after this event along the modelled component is reported in Figure 89, showing a decrease in buoyancy effects during the event.

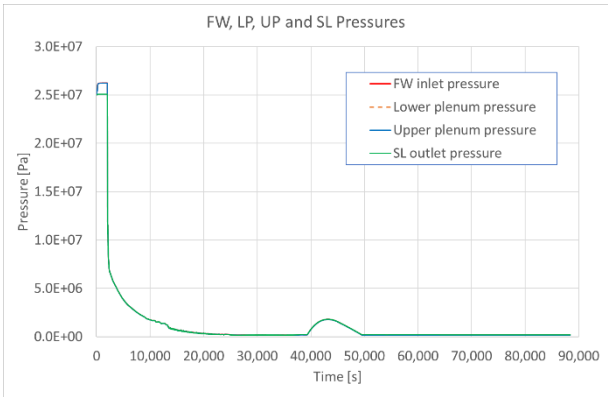

Figure 87: Pressure in the vessel

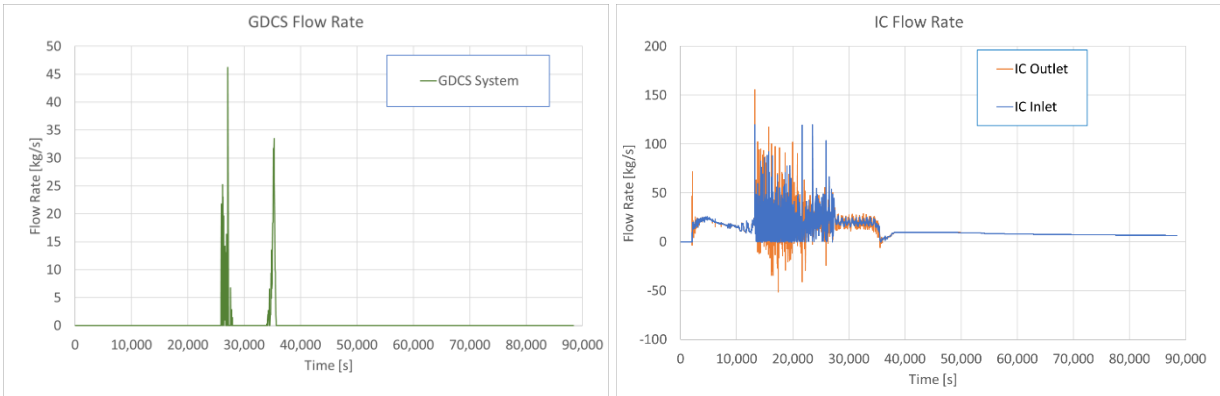

Figure 88: GDCS and IC flow rates

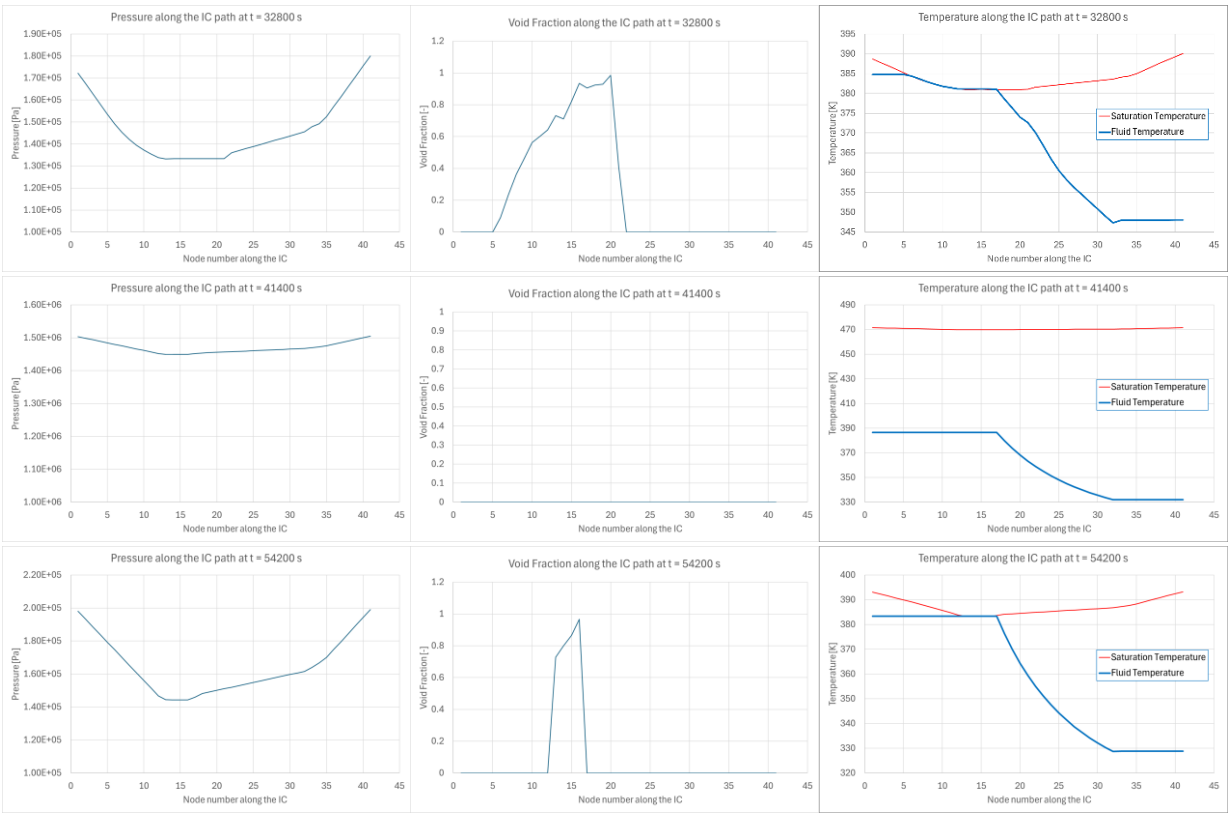

Figure 89: Sequence of pressure, void fraction and temperatures along the IC path at three different times in the transient

However, the effect of this momentary occurrence is minimal on the evolution of the transient as it can be noted from Figure 90 to Figure 93, showing the settling of the fluid and cladding temperature around 100 °C in the longer term, evaluated up to 24 hours.

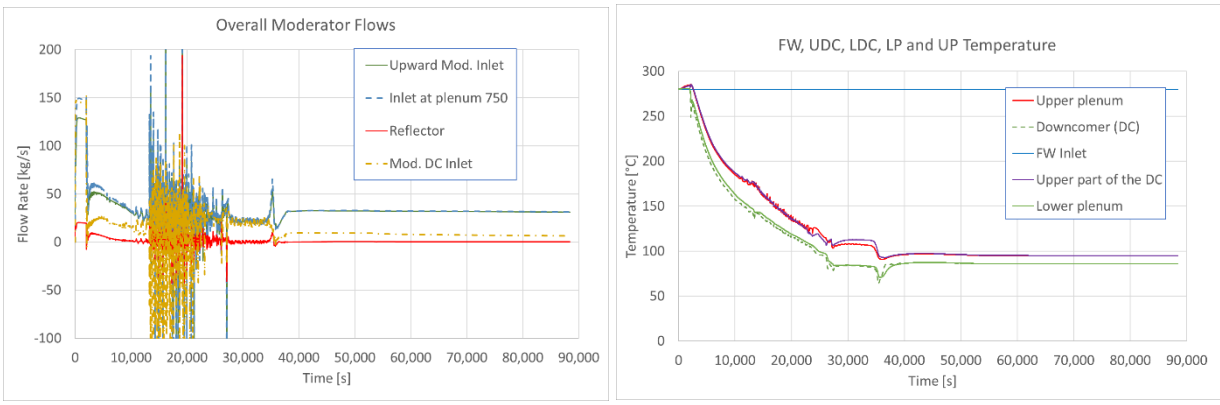

Figure 90: Overall moderator flows and temperatures in the vessel

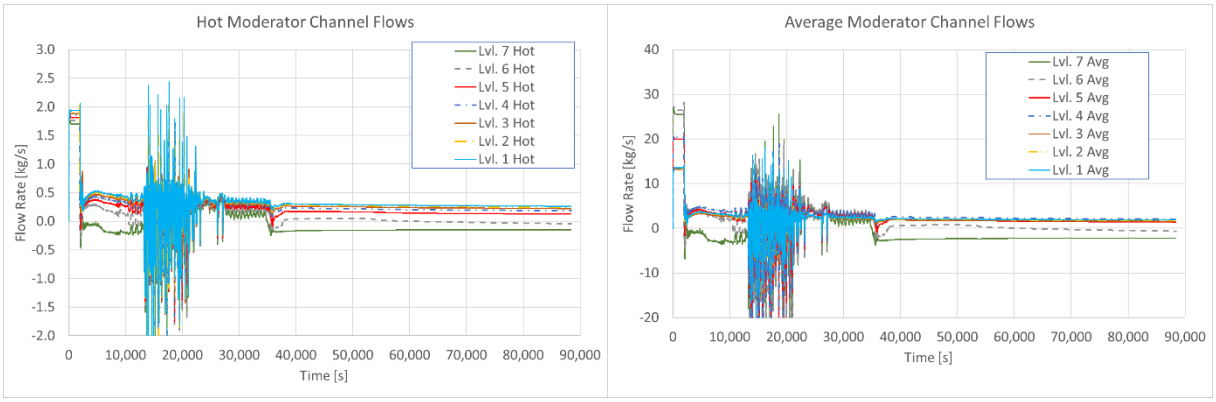

Figure 91: Inner moderator channel flows

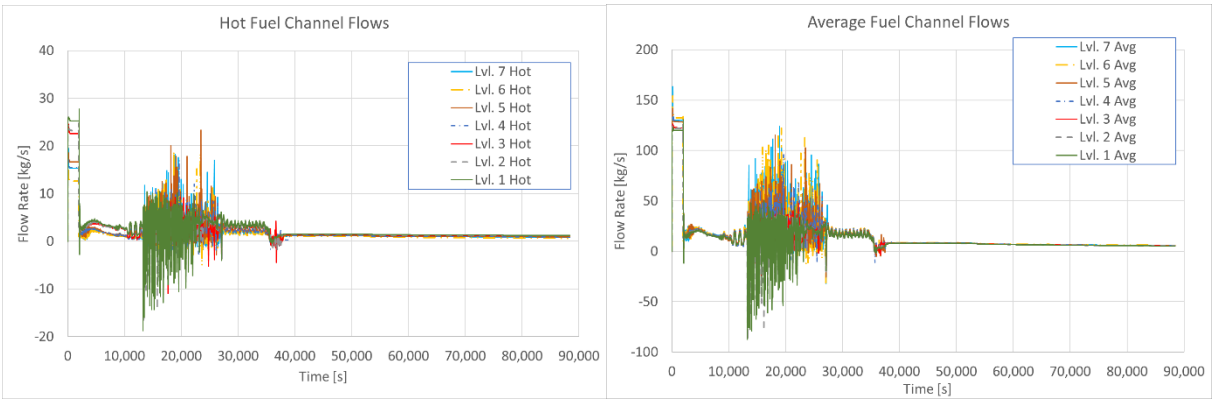

Figure 92: Fuel channel flows

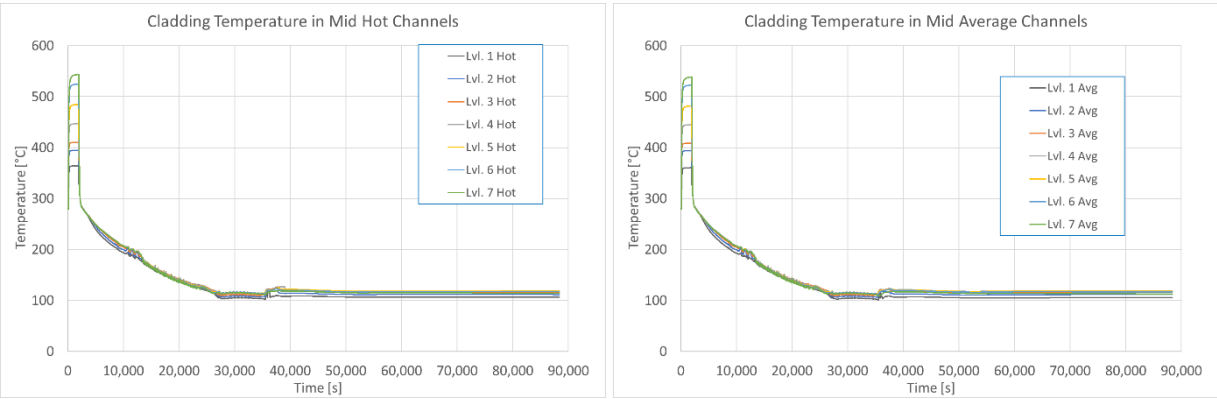

Figure 93: Cladding temperatures in mid hot and average channels

4.5.6 Effect of operating pressure

The previous analyses have been conducted imposing a pressure of 25 MPa (the operating pressure of most SCWR reactors) downstream the steam line. This indeed results in a higher pressure in the reactor, also depending on the core pressure drops providing an additional burden for reactor vessel design.

In order to assess the validity of the previously reached conclusions with a lower operating pressure, an analysis was run assuming a pressure of 24 MPa assigned in the time-dependent volume located downstream the steam line. As it will be shown, though quantitative changes occur as expected, they look quite limited in steady-state conditions with respect to previous evaluations with 25 MPa and, for obvious reasons, they are even smaller during the LTSBO transients, mainly involving depressurised conditions.

As shown in Figure 94, the core temperatures are very similar in steady-state conditions; similarly the densities of the coolant and moderator fluids are very close to each other (Figure 95 to Figure 97), suggesting a limited effect also on neutronic feedback behaviour. It is interesting to note that this occurs with a large difference in the distribution of pressure in the fuel channels and in the reactor in general (Figure 99).

Transient phenomena are also very little different (see Figure 99 to Figure 103), since the long term SBO is mostly encompassing conditions at subcritical pressures that are weakly influenced by the difference in the initial steady-state conditions. In summary, previous conclusions can be assumed to hold also in the present case.

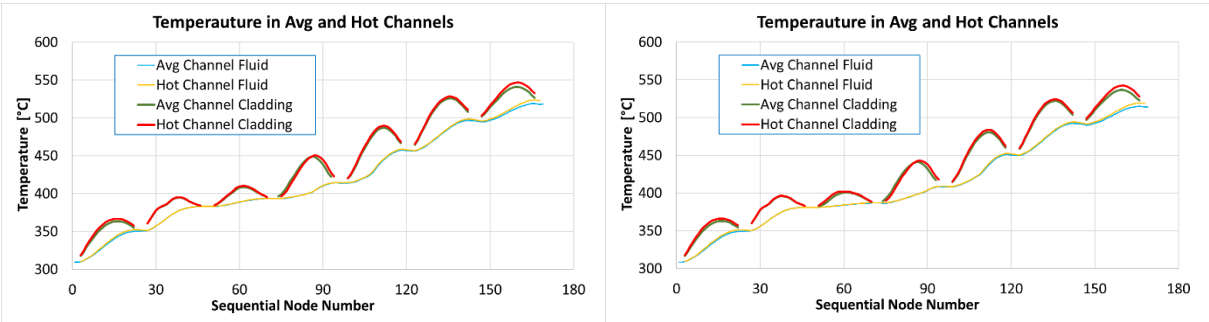

a) 25 MPa downstream the SL b) 24 MPa downstream the SL

Figure 94: Steady-state distribution of core temperatures for the base case

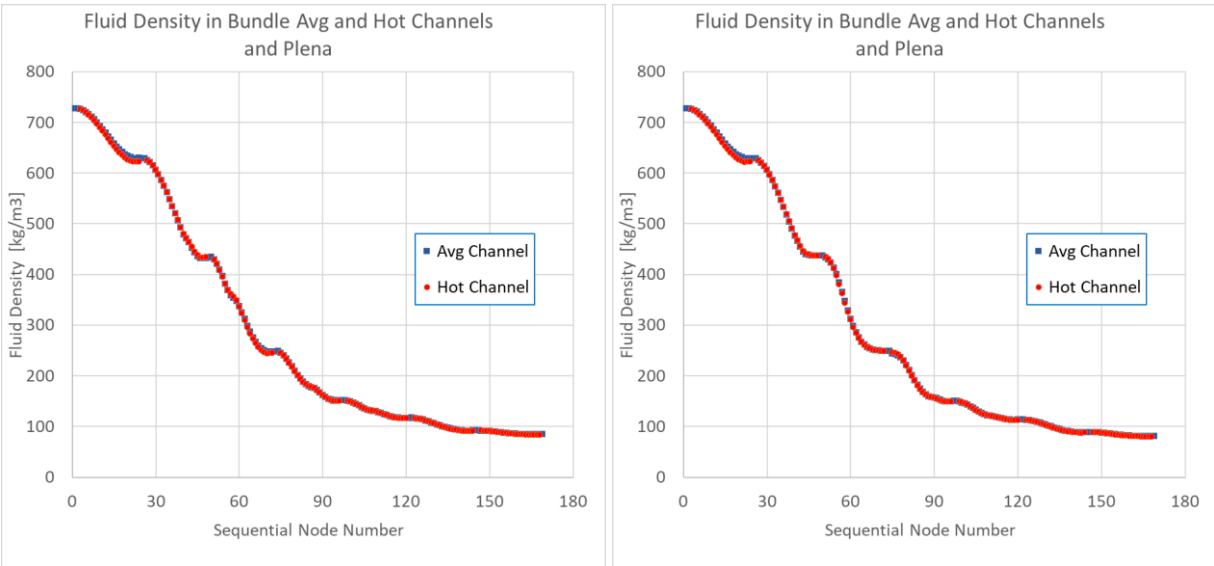

a) 25 MPa downstream the SL b) 24 MPa downstream the SL

Figure 95: Steady-state distribution of core fluid density for the base case

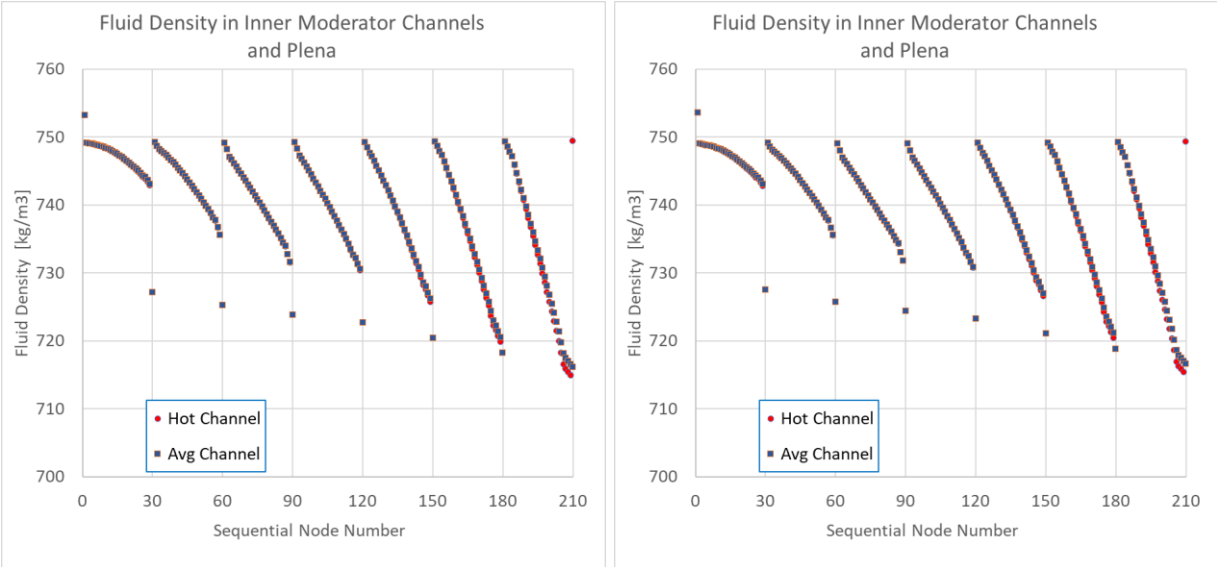

a) 25 MPa downstream the SL b) 24 MPa downstream the SL

Figure 96: Steady-state distribution of inner moderator fluid density for the base case

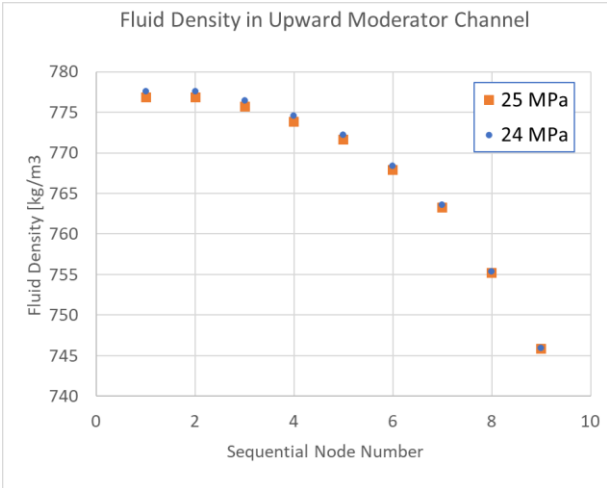

Figure 97: Steady-state distribution of moderator fluid density for the base case

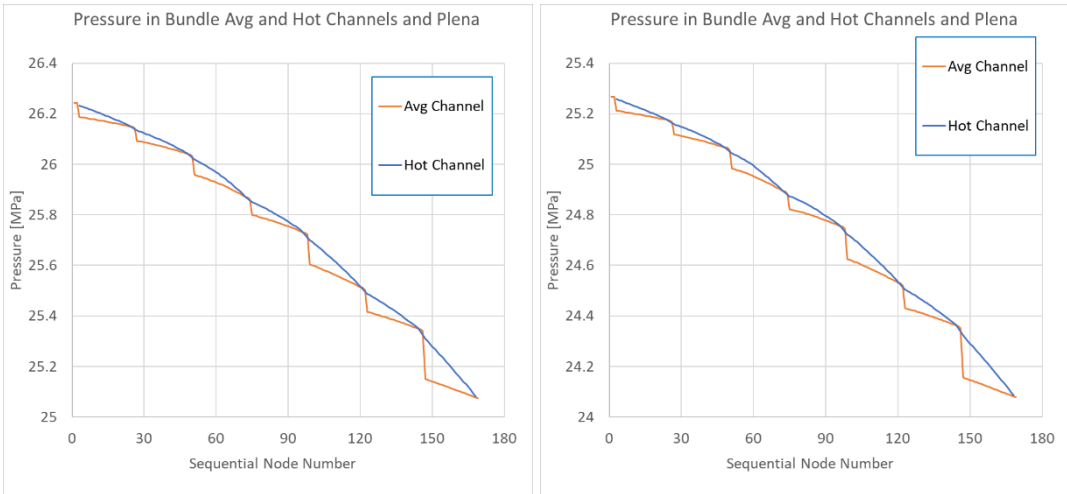

a) 25 MPa downstream the SL b) 24 MPa downstream the SL

Figure 98: Steady-state distribution of fuel channel pressures in the base case

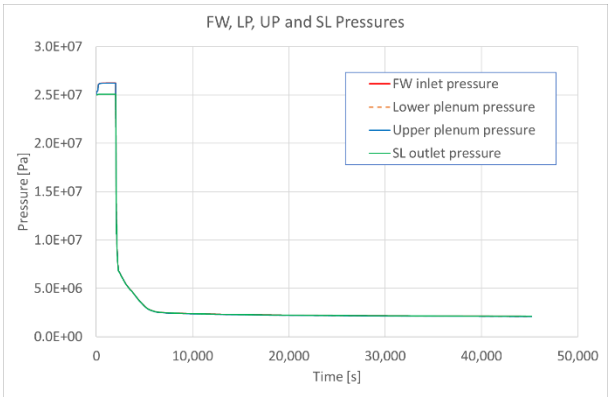

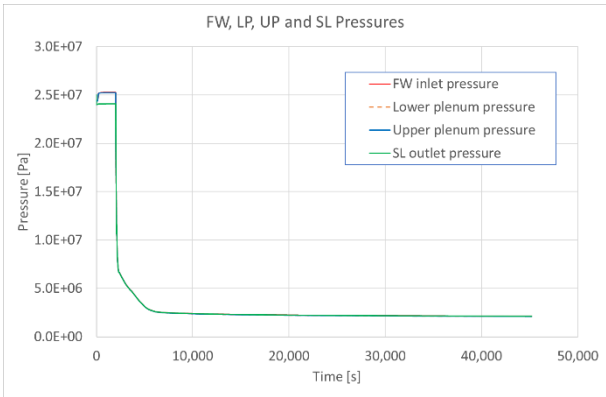

a) 25 MPa downstream the SL b) 24 MPa downstream the SL

Figure 99: Transient trend of pressure in the vessel for the base case

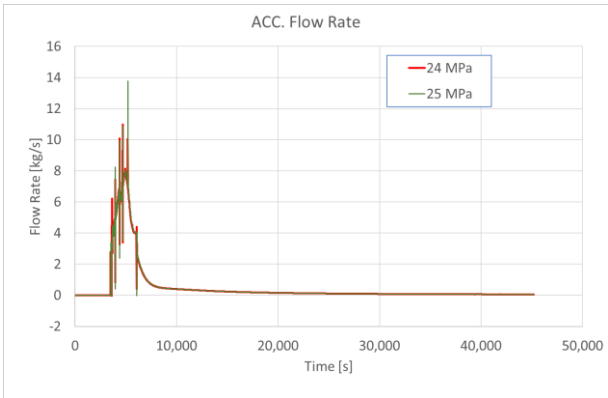

Figure 100: Accumulator system flow rate in the base case

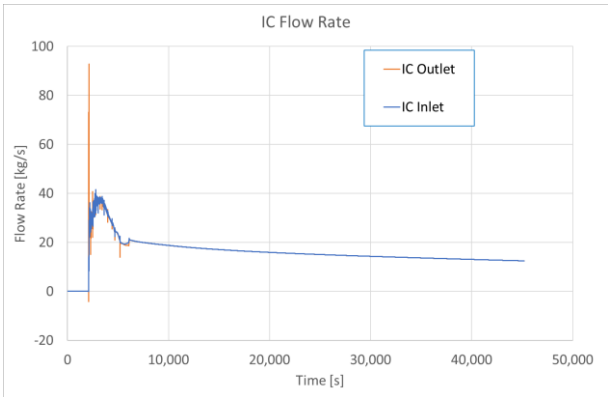

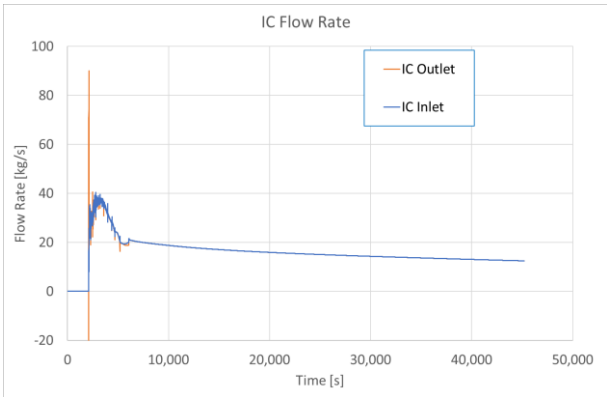

a) 25 MPa downstream the SL b) 24 MPa downstream the SL

Figure 101: Transient trend of IC flow rate in the base case

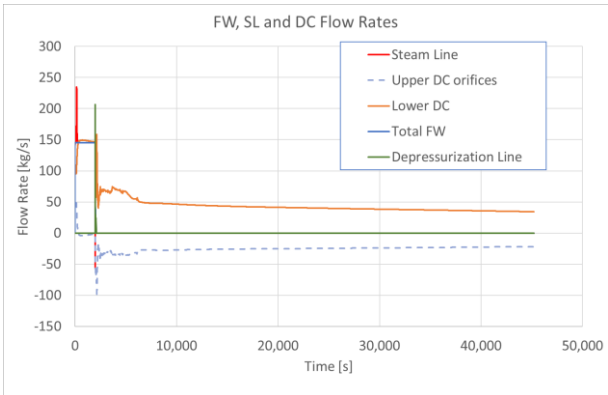

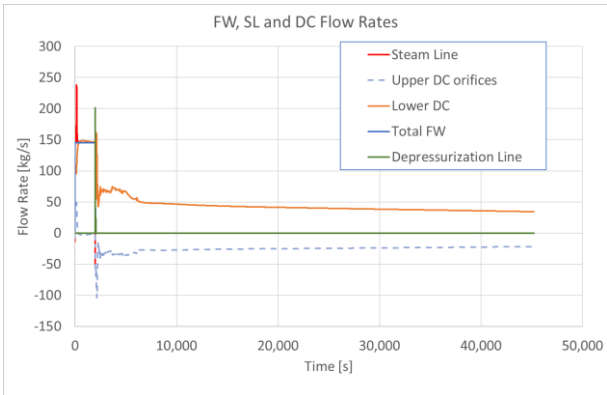

a) 25 MPa downstream the SL b) 24 MPa downstream the SL

Figure 102: Transient trend of flows in the vessel for the base case

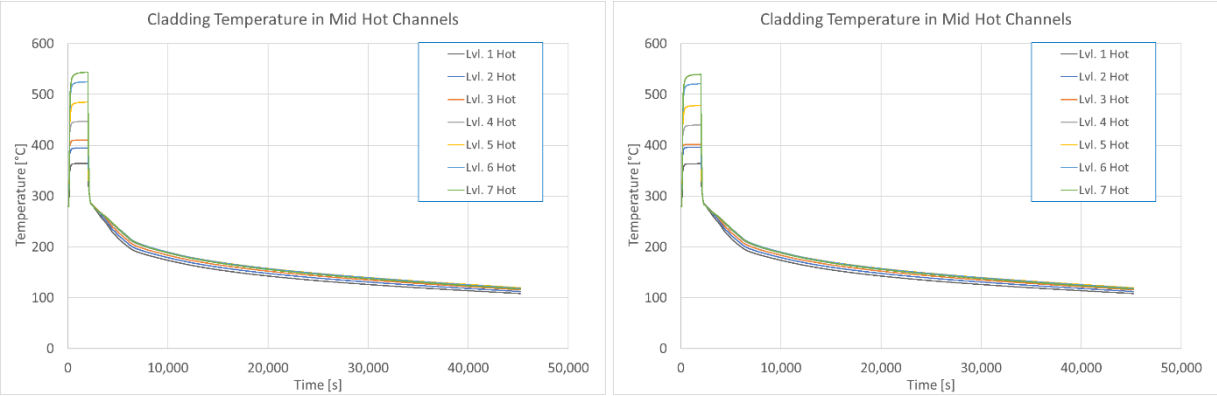

a) 25 MPa downstream the SL b) 24 MPa downstream the SL

Figure 103: Transient trend of cladding temperature for the base case

4.6 Significance of the work and final remarks

Since the very beginning, the focus of the performed work has been mainly on the assessment of the natural circulation behaviour inside the reactor, assuming that sufficient cooling could be achieved for such a low power system by appropriate passive systems during the postulated sequence of events. A considerable effort was spent at the beginning of this work in setting up the nodalisation for such a complex system and in trying to overcome the problems related to the simulation of the depressurisation below the critical pressure, in order to allow for the considered transient to be simulated. Some parametric choices were proposed for the passive systems which were introduced at a later stage to assess the overall plant behaviour; these choices have not to be taken as an accurate design, but just as exemplary system configurations that may prove to be sufficient and should be revised and improved at a possible later stage in the design of the proposed reactor. The sequence of events including an initial short term limited depressurisation of the system was conceived after discussions in the several technical meetings held for carrying on the work and was mainly dictated by the choice to avoid exposing the IC unit to the full reactor pressure or 25 MPa, thus limiting its requirements in terms of mechanical resistance.

The adopted RELAP5 plant model started to be set up with a topology and a first sizing proposed at the beginning of 2022 when CAD data about the dimensions of the proposed reactor were not yet distributed. The topology and dimensions of the nodalisation were anyway repeatedly updated by subsequent work in front of the released information (Hassan et al., 2022; Chaaraoui, 2024), mostly leaving the overall layout of the first modelling approach unchanged, though improving the quantitative detail in description. The description of the passive systems was included later and the choice to make a single system representing double trains was introduced. In making this development, it was chosen not to focus on the behaviour of the pool of the IC assuming a temperature of 30 °C for its water during the postulated transient and assigning parametric heat transfer conditions. This assumption, retained in the present analyses, may be removed in further studies by including the model for an in-containment or an external pool of appropriate size, whenever a decision on this aspect will be taken.

A number of sequences has been investigated in the presented analyses, starting with a base case that included nominal conditions for the passive systems and considering variants in some of the retained modelling choices, aiming to assess their consequence on the predicted behaviour. All the analysed sequences show the presence of a pattern of natural circulation within the reactor that represents one of the main outcomes of this study. This pattern, that is being shown for the first time for the novel reactor configuration proposed by Schulenberg and Otic (2021), is critically dependent on some of the adopted modelling choices in terms of number and

size of orifices placed at the top of the reactor downcomer and at the bottom of the reflector, as well as of introduced modelling assumptions. It is expected that further refinements or changes in the adopted choices may change the quantitative features of this pattern in terms of partitioning of the flow rates among the different flow loops due to natural circulation, also as a consequence of future design developments in the reference configuration or inclusion of lacking components as, for example, the control rods and their drive mechanisms. Better guesses of the local pressure drops in complex parts of the reactor, as the region in which the moderator crosses the outer fuel boxes (to be obtained, e.g., by CFD studies), or the inclusion of an increased pressure drop at the bottom of the lower downcomer could also contribute to change the quantitative results obtained by these analyses. A larger number of fuel channels introduced to represent the multiple core stages and different subdivisions of the inlet and outlet plena of both the moderator and the coolant channels may also provide further details.

The overall message from the obtained results is related to the characteristics of natural circulation established in the reactor core and shown for the first time for this new plant configuration. Though the specific values of flow rates may change owing to different modelling assumptions, as partly shown in the reported analyses, it is confirmed that natural circulation involving the seven stage reactor core can be established at a level that appears sufficient to cool the fuel in long term conditions as those addressed in the analysed scenarios. In the examined transients, fluid pressures and temperatures in the system reach sufficiently low values that a further depressurisation, also by manual means, may represent the final outcome of the transients whenever considered necessary.

Further studies on a spectrum of postulated accidents may say if the level at which the considered reactor configuration is allowing natural circulation to be established may be considered sufficient to propose the present reactor as a safe one for further exploitation.

5 Analysis of pre-conceptual core layout and passive safety concept for SCW-SMR by BME

5.1 Focus of the work

The analysis of the proposed SCW-SMR in charge to the Budapest University of Technology and Economics (BME) concerned the conceptual investigation of the steady-state behaviour and the passive safety aspects such as natural circulation in the event of accidents like a long-term station blackout (LTSBO). Several types of codes were required to achieve these objectives, so the first step was to select the right codes for the given tasks.

For the system code analyses, the Apros code (Kurki, 2008) was selected, with which BME has decades of experience and which has been suitable for handling supercritical media for more than 15 years, as also shown by previous applications. For example, VTT Research Centre has successfully performed several analyses related to the HPLWR concept in the frame of previous projects (Kurki and Seppälä, 2009; Schlagenhaufer et. al, 2010; Andreani et. al, 2012). For subchannel analyses, the STAFAS code system was selected.

A large part of the analysis has been performed with various coupled code systems, which required a strong cooperation of Work Package 3 and 4 members. For the neutronics calculations, WP4 colleagues selected the Serpent 2 Monte-Carlo code and the in-house SPNDYN code, which is a finite-element-method-based reactor physics code developed at BME as part of a PhD work (Babcsány, 2021).

Using the above codes, the analyses focused on the following main areas:

- Detailed steady-state analysis with the weakly coupled Apros - Serpent 2 code system;
- Steady-state analysis with the coupled Apros - SPNDYN code system;
- Steady-state analysis with the STAFAS code system;
- Detailed investigation of the long-term station blackout event using the Apros code.

The development of the Apros model and the analysis of the SBO event have been carried out in close collaboration with colleagues from the University of Pisa (see chapter 4), with the aim of applying similar modelling approaches and considerations. The selection of the cases studied, as well as the way in which the results are presented, have been done so that it supports comparability between RELAP and Apros codes as well.

5.2 Developed Apros model of the SCW-SMR

5.2.1 Vessel Flow Paths Nodalisation

Modelling the vessel flow paths, as described in chapter 3, was started at the BME in spring 2022 in Apros version 6.11SR1, right after the release of the CAD data.

The main diagram of the Apros model for the RPV pre-conceptual design is shown in Figure 104. It models the entire moderator and coolant flow path through the vessel, including the reflector and bypass flows. It takes into account all passive and active, inner and outer heat structures and is therefore able to describe the heat transfer between the internal volumes separated by walls. This is a key phenomenon in the proposed concept, as a complex flow path has been designed, in which the water passes through the core 2+7 times, while heating up by more than 200 °C. Therefore, a wide range of temperatures and states of media are in contact through the walls.

To model the individual stages, a so-called User Component has been set up (Figure 105), seven instances of which are used in the RPV model (indicated by boxes with 'SC Stage' label in Figure 104). They have the same internal structure but are parametrized individually for each stage. These components include the coolant and moderator channels of the assemblies (active and non-active parts), their inlet and outlet plenums, the inter assembly space, and all associated heat structures. The rest of the vessel (downcomer, lower and upper plenum, reflector space and the outlet steam dome) is modelled separately as shown in Figure 104. The built-in DESIGN_REACTOR, DESIGN_REACTOR_HS, NODE, BRANCH and HEAT_STRUCTURE_X components of Apros have been used to set up the whole model.

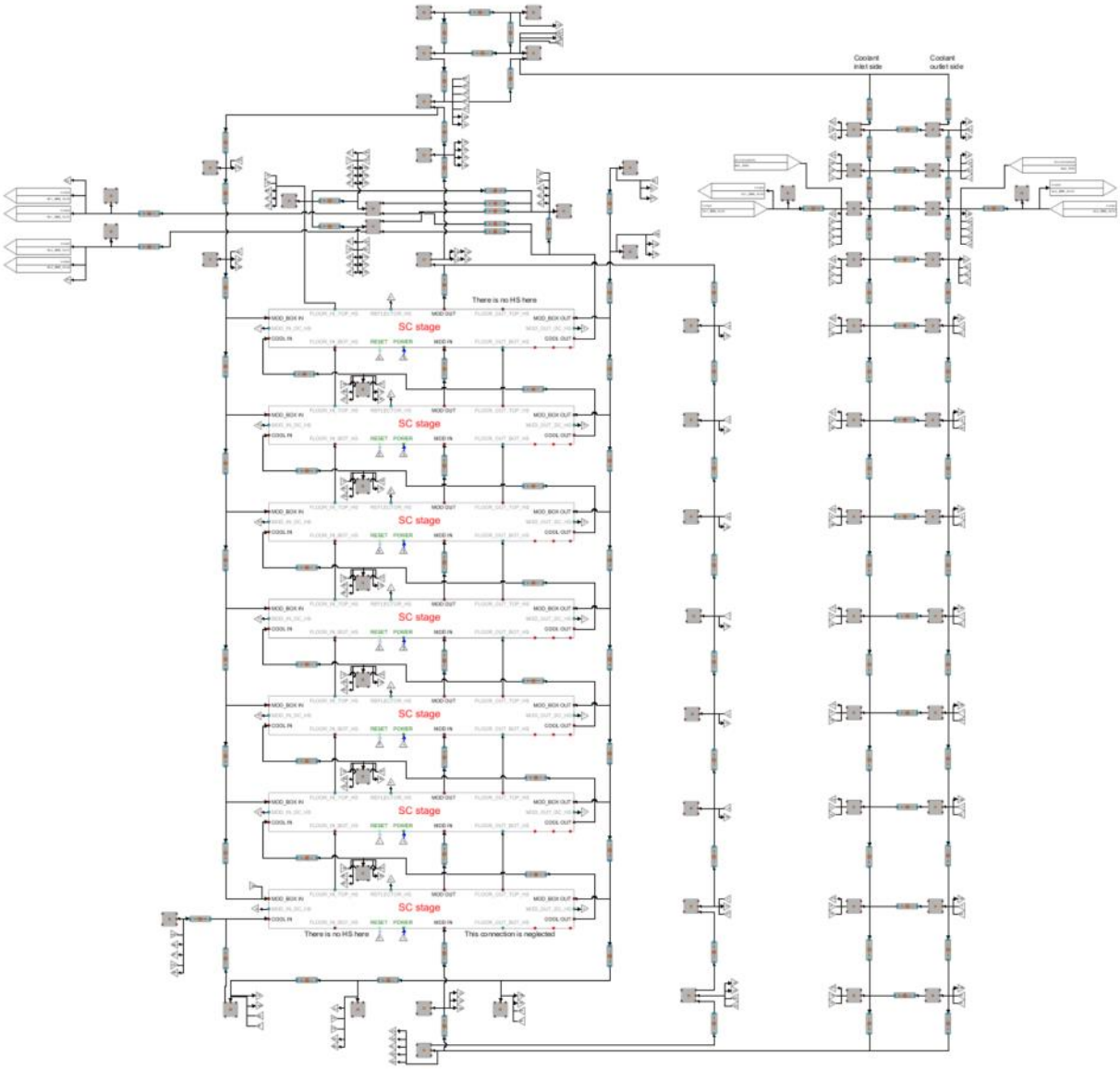

Figure 104: RPV diagram of the Apros model

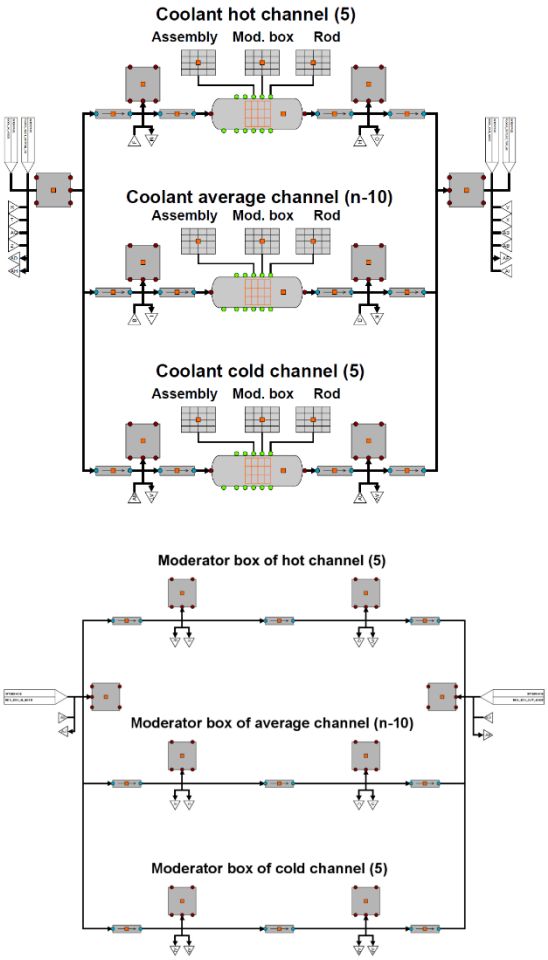

Figure 105: User Component model of the fuel and moderator box channels

Within the heat-up stages, the assemblies and their components are classified based on their heating power. There are 3+3 parallel coolant and moderator channels representing the five coldest, five hottest and (N-10) average assemblies for each stage (see Figure 105), where N is the total number of assemblies in that stage (see Table 4). This approach is one of the main differences between the developed RELAP and Apros models, as the RELAP model has only two channels, a hot and an average one, per stage. With the introduction of the third, cold channel, the main objective was to enable better interpolation of the transferred parameter profiles when the Apros model is coupled with a reactor physics model.

Stages	Total number of assemblies in the stage (N)
1	40
2	40
3	40
4	60
5	60
6	80
7	80

Table 4: Number of assemblies per stage

The coolant channels include 1+1 non-active inlet and outlet nodes, while their heated section is divided into 20 axial nodes whose axial power profiles can be set independently for the three channels. The total of 21 (7 x 3) power profiles are provided by the coupled reactor physics calculation. The steady-state temperature and density profiles, calculated with the received power profiles, are the primary outputs of the Apros steady-state calculations, required by the neutronics simulation. The form loss coefficients of the coolant channels, which also take into account the effects of the wrapped wire, are based on the detailed CFD analyses also performed at BME.

To make it easier to understand the flow path of the Apros RPV model, a brief description is given below. The feedwater enters the vessel through two, opposite side nozzles shown on the right side of Figure 104, where the flags represent the connections with the primary loop and the accumulator diagrams. The downcomer is modelled by two parallel channels (half rings) with vertical and cross connections. Most of the flow goes downwards, but small orifices provide a bypass flow directly to the upper plenum. From the lower plenum, the flow is again divided into two streams. The main stream passes through the core in the inter-assembly space, while a bypass is provided through the orifices and the reflector volume on the sides of the core. These two streams reunite above the core and flow towards the upper plenum, which is modelled by 4+1 nodes, and where the DC bypass also joins the main flow. From here, the entire flow turns downwards and enters the inlet plenum of the moderator boxes. The flow is parallel in all the 400 boxes and is collected in the outlet side plenum. Finally, the flow reaches the inlet of the Stage1 fuel channels through the channels formed below the core.

From now on, the main role of the flow is to provide adequate cooling to the fuel. It passes through the fuel channels of all the seven consecutive stages and the intermediate spiral return channels. These spiral channels are currently modelled by a single node per stage, which may be refined later. However, this will be a complex task as this volume has several thermal connections through the walls, while it is also inclined. From the outlet of the topmost stage, the supercritical steam is collected in the steam dome and directed towards the two outlet nozzles shown on the left side of Figure 104.

As can be seen above, another important difference compared to the RELAP model is that the two primary loops and the associated DC and steam dome regions are separated into two parts. This is mainly intended to facilitate a more accurate modelling of future LOCA transients. However, the analyses performed so far show that even in steady-state there is a significant temperature and hence mass flow rate difference between the two sides of the DC, since one half is in thermal contact with the inlet side moderator plenum, while the other half is in contact with the outlet side plenum. This can have a significant effect on the natural circulation and hence the transient behaviour during an SBO event.

In the frame of the project, a comprehensive benchmark activity has also been performed, mainly focusing on the heat transfer phenomenon under supercritical conditions, the result of which was summarized in Deliverable D3.2 and in (Varju et. al, 2024). Based on this experience, the SCW-SMR model uses the Bishop et al. (1965) correlation for the heat transfer calculations.

5.2.2 Primary loop model

The developed preliminary primary loop model of Apros is presented in Figure 106, where the flow goes from the left-hand side to the right. As can be seen, 2+2 steam and feedwater lines are installed inside the containment, but they join after the containment isolation valves, and share a common turbine and feedwater system. From left to right, the loop comprises the following main units:

- group of 3 valves for modelling a 200% LBLOCA event at the nozzle (hotleg, inside the containment, non-isolable break);
- connections towards the passive heat removal loops;
- connections towards the controlled depressurization valves;
- containment isolation valves;
- conjunction of the two steam lines;
- group of 3 valves for modelling a 200% LBLOCA event (hotleg, outside the containment, isolable break);
- connection towards the turbine bypass line (via a shut-off valve to the condenser);
- turbine isolation and check valves;
- boundary condition point at the turbine inlet;
- boundary condition point at the turbine outlet with a control valve;
- condenser with its own cooling circuit;
- condensate pump;
- low pressure preheater;
- feedwater tank with heating steam provided from a boundary condition point;
- feedwater pump;
- high pressure preheater;
- group of 3 valves for modelling a 200% LBLOCA event (cold leg, outside the containment, isolable break);
- separation of the two feedwater lines;
- containment isolation valves;
- connections of the passive heat removal loop returning lines;
- group of 3 valves for modelling a 200% LBLOCA event at the nozzle (cold leg, inside the containment, non-isolable break);

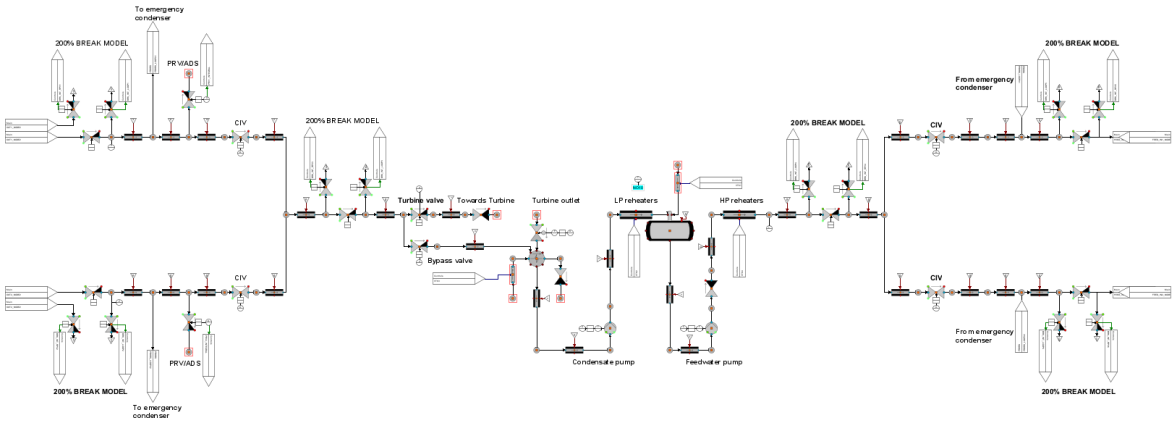

Figure 106: Primary loop model of Apros

The separated steam lines have an inside diameter of 200 mm each, while it is increased to 283 mm after the conjunction to provide the same total flow area. On the feedwater side, the inside diameters are 142 mm and 2x100 mm in the respective sections. The length of the lines are currently completely approximative. The passive heat removal loop connections and the containment isolation valves are 5.5 m and 12.5 m away from the nozzles in all four lines (both hot and cold).

The turbines are not directly modelled and boundary conditions are used instead. At the turbine inlet, a pressure boundary is applied to set the steady-state outlet pressure of the vessel

to 25.0 MPa. This boundary condition is not modified even during the SBO transient, but the line is closed with the turbine shut-off valve (3 s operation time). On the outlet side of the turbine, an enthalpy boundary condition in combination with a controlled valve provides the flow to the condenser. During the SBO analyses, controlled depressurization is provided through the turbine bypass line to the condenser. This line has an inside diameter of 150 mm, a length of 5.5 m, while the valve opens with a 3 s operation time.

The condensate is pumped to the feedwater tank through a low pressure preheater. The thermal equilibrium of the feedwater tank is set with the controlled preheater and the controlled heating steam provided with boundary conditions. The feedwater is then pumped through the high pressure preheater, which sets the inlet temperature of the RPV to 280.0 °C. Both the condensate and feedwater pumps have an own control system to set the mass flow rates. In case of the SBO event, the pumps are tripped (including the condenser cooling system) and the preheater heating is stopped.

The 3-valve groups provides the possibility to model the 200% LBLOCA event at various locations in future analyses. However, these are currently in pre-preparation phase only, as the general model would still require further developments to perform the analysis of such a complex event.

The above described model, with the help of various control systems, is able to set the required steady-state of the vessel and the primary loops. During the investigated SBO event, however, most of the primary loop model got separated by shut-off or check valves after a few seconds and no longer affects the main processes, so these might have significant effects only on the early transient phase. This is also the main reason behind the decision that the RELAP model does not take into account the primary loops in such detail; a more detailed Apros model has also been built only to facilitate the future developments.

5.2.3 Passive heat removal and accumulator models

The developed, preliminary Apros model of the passive heat removal system is presented in Figure 107. The model has two main part: an isolation condenser, with its riser and downcomer pipelines, and a pool, in which the isolation condenser is placed and which serves as the heat sink. The riser pipeline includes a shut-off valve and has a vertical section of 12.5 m and a horizontal section of 1 m with an inner diameter of 200 mm. The isolation condenser (IC) has a horizontal top hot and a bottom cold collector, both with an inner diameter of 0.4 m and a length of 1 m. There are 200 vertical heat transfer tubes between the collectors, with a length of 1.5 m, inner diameter of 20 mm and a wall thickness of 2 mm. The downcomer includes a pipe section, a check valve and a shut-off valve. The total length is 10.2 m and the inner diameter is 100 mm. The shut-off valves are closed in normal operation states and get an open signal, when the RPV outlet pressure drops under 11.0 MPa. The use of the check valve prevents the potential reversal of the flow.

The heat sink pool is simulated by a two-channel model with vertical and cross-connections. One channel represents the volume around the isolation condenser (heater part), while the other channel represents the more distant part of the tank (recirculation part). The volume above the heat exchanger is modelled by a single node, the top of which is connected to a boundary condition point keeping an atmospheric pressure and providing an outlet for the steam flow in long term phases of the transient. The initial pool temperature is 30 °C and the initial water volume is 300 m^3. This volume is however just a preliminary guess, and the exact requirements will have to be investigated later.

In the current model, it is assumed that two units of the above-described heat removal loop with own tanks is required, one connecting to each of the two primary loops.

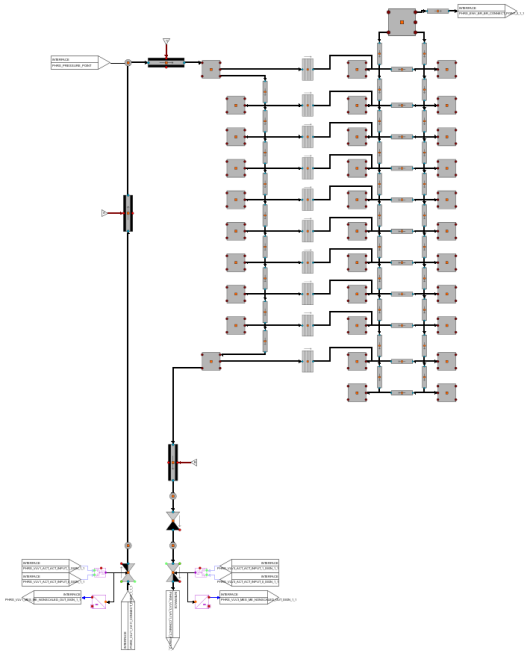

Figure 107: One loop of the passive heat removal system of Apros

The developed, preliminary Apros model of the passive emergency core cooling system is shown in Figure 108. This model includes an accumulator module with additional wall heat structures and an injection pipeline with a check valve and a shut-off valve. The shut-off valve is open during normal operation states and closes, if the accumulator water level drops under 0.2 m to avoid nitrogen injection to the RPV. The accumulator is cylindrical and it has a total volume of 30 m^3, from which 20 m^3 is water and 10 m^3 is nitrogen. In the initial state, it has a temperature of 30 °C and a pressure of 4.8 MPa. In nominal state, this system is separated by the check valve and starts to inject once the primary pressure drops below that of the accumulator. Currently, two units of the above described system is included in the Apros model, connecting to the RPV downcomer halves.

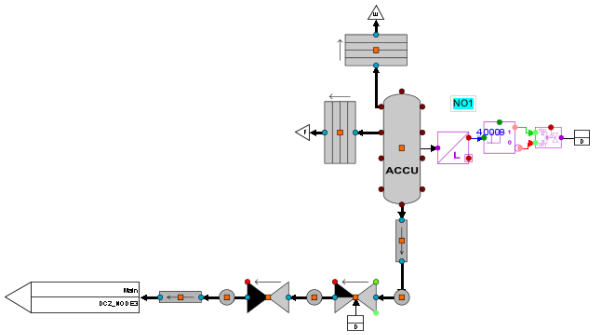

Figure 108: One accumulator model of Apros

The above presented models are quite similar to those of the RELAP model developed by the University of Pisa (UNIPI), but there are also some different approaches. For example, the passive heat removal pool and its changing state is currently modelled in greater detail by the Apros model.

5.3 Steady-state calculations with the Apros – Serpent 2 code system

5.3.1 Calculation procedure

Most of the coupled analyses for the SCW-SMR concept have been performed using the full-core Serpent 2 – Apros code system. The Serpent 2 model is described in detail in the Deliverable D4.3, while most of the coupled results are presented in this document. The calculation procedure has been established in cooperation by WP3 and WP4 participants of BME and a part of these calculations have been performed in the frame of an MSc thesis work (Mészáros et. al, 2023).

WP4 colleagues of BME have performed a thorough core optimization procedure and developed two main core loading maps, one using UO_2 fuels only and another one using MOX fuels. These two types of maps are shown in Figure 109. It must be mentioned that in the coupled RELAP – Serpent 2 calculations, presented in chapter 4.4, a preliminary MOX fuel map and an earlier version of the Serpent model was used. At first, the Apros model was also coupled with that earlier Serpent model and the results showed really good agreement with those of the RELAP (see Mészáros et. al, 2023). In the present document, however, the results of the calculations with the most recent Serpent and Apros models is presented.

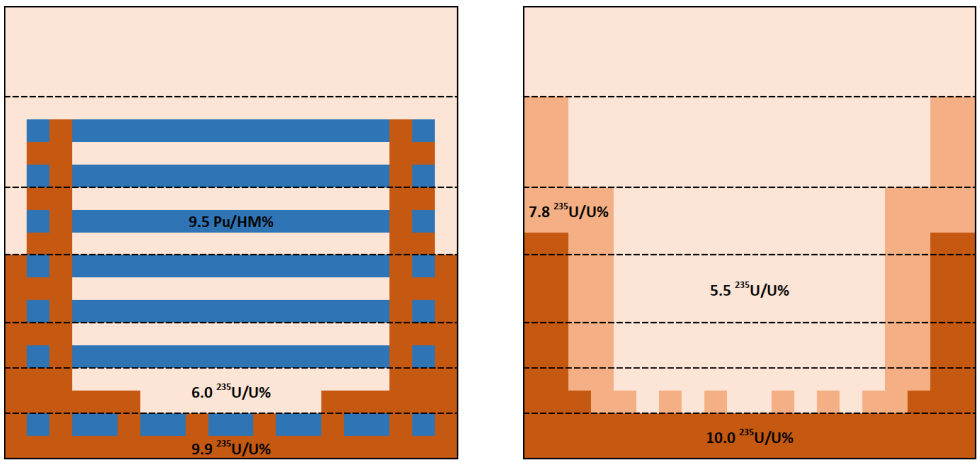

Figure 109: The MOX and the pure UO_2 loading maps of the Serpent 2 model

The calculations were carried out in an iterative manner, i.e., they were first started with a stand-alone Serpent 2 simulation and then a stand-alone Apros calculation was run using the resulting power distribution until a new thermal equilibrium was established in the entire reactor vessel. With the temperature and density profiles obtained, a subsequent Serpent 2 calculation could be performed. This iterative process was repeated until the convergence of the entire coupled system was achieved. In most cases, this required only 2-3 iteration steps. Nevertheless, usually at least 5 steps were performed to ensure that the system reached a stable state. The data transfer and the required data processing was carried out using various Matlab and Python scripts specifically developed for this purpose.

The Apros code itself has quite different running features compared to those of RELAP. One of them is that the start-up process from the cold state, described for RELAP in chapter 4.4, was required in Apros only in the very first run of the model. Once it has reached a nominal state, the model configuration with its state was saved and the simulation could be continued from that state after new model modifications, for example after the change of power profiles during the iteration procedure. Any later states could also be saved and used for the continuation of the

simulation. This is a great advantage of the code, because the new thermal equilibrium could be reached much faster and much of the computational resources could be saved.

In the following chapters, the results of the coupled calculations are presented for various alternative versions of the SCW-SMR concept. It should be emphasised that for each case presented here, a specific iteration has been performed with the code system and the results represent the final equilibrium state.

The power, moderator, coolant, cladding and fuel temperature profiles are plotted in a way that the consecutive stages are placed one after the other (even in the case of the moderator boxes, in which the flow is actually parallel), forming a total number of 7x24 = 168 nodes. These 24 nodes per stage include the inlet plenum (1), non-active inlet part of the channel (1), the active section (20), non-active outlet part of the channel (1) and the outlet plenum (1). In case of the power, cladding and fuel temperatures, the profiles are interpreted only for the active section, so these are plotted only in the intermediate 20 nodes. The three channels (cold, average and hot) share a common inlet and outlet plenum, in which perfect mixing is assumed. For the most appropriate representation, in case of the moderator and coolant parameters, the plenum values are included in the average curves, while these points have been left out in the cold and hot curves.

5.3.2 Calculation results of the original concept (MOX core)

The final results of the iterative coupled calculation performed with the original concept model, using the MOX fuel map and 145 kg/s system flow rate is presented in Figure 110 to Figure 117. This concept does not include specific orificing of the coolant channels, therefore the same form loss coefficients and flow areas per assembly were used in the cold, average and hot channels. This approach provided an uneven power-to-flow ratio partitioning in the coolant channels characterised by different average linear powers (Figure 110). This gives rise to different fluid, cladding and fuel temperature levels, as shown on the figures.

The usual cosine power profile is formed axially within each stage, but in the vertical direction the power density decreases continuously from stage 2 upwards. This is both a direct consequence of the enrichment map used in the Serpent 2 model (see Figure 109) and a design goal. The coolant temperature (Figure 114) rises continuously as it passes through the stages, while the mass flow rate per assembly decreases due to the increasing number of assemblies per stage (see Table 4) (to limit the pressure drop - Figure 111), so only with such a decreasing power profile can the formation of hot spots and the occurrence of heat transfer deterioration be avoided.

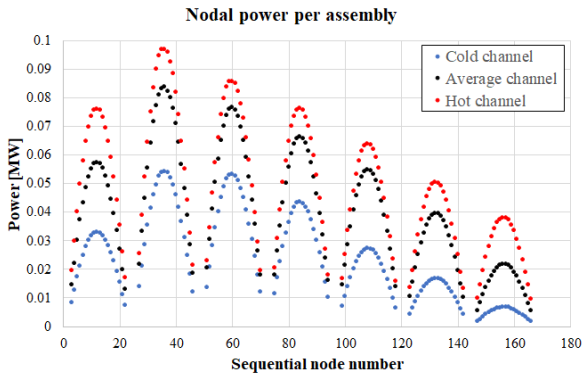

Figure 110: Nodal power distribution per assembly

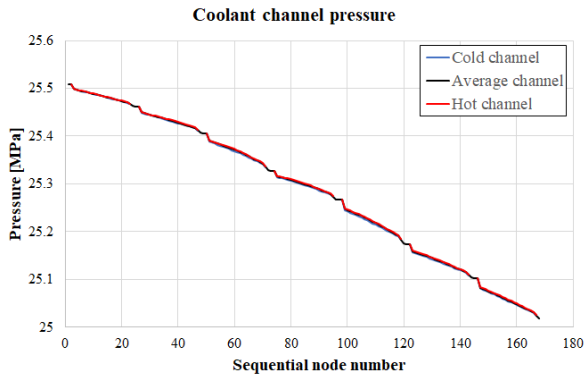

Figure 111: Pressure profile along the coolant channels

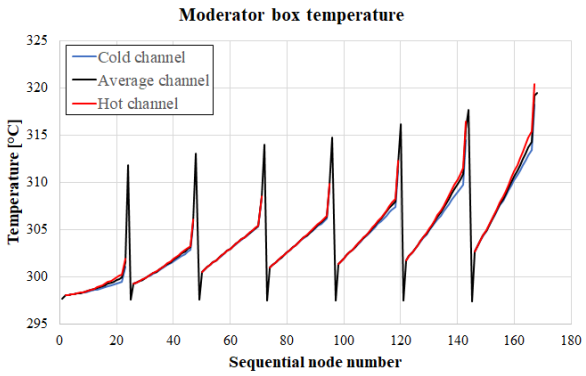

Figure 112: Temperature profile of the moderator boxes

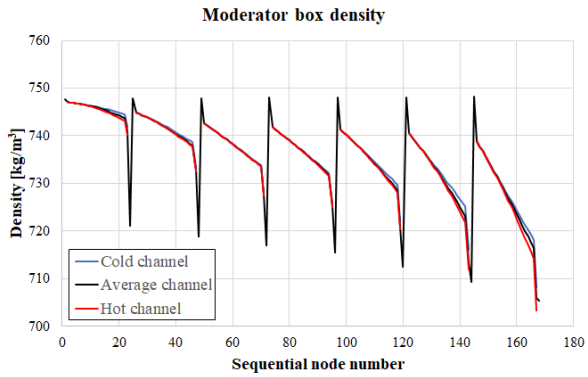

Figure 113: Density profile of the moderator boxes

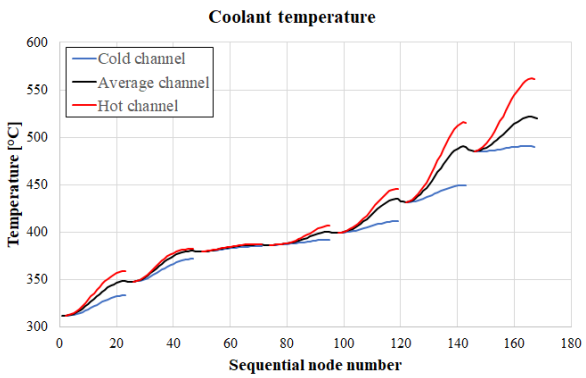

Figure 114: Temperature profile of the coolant channels

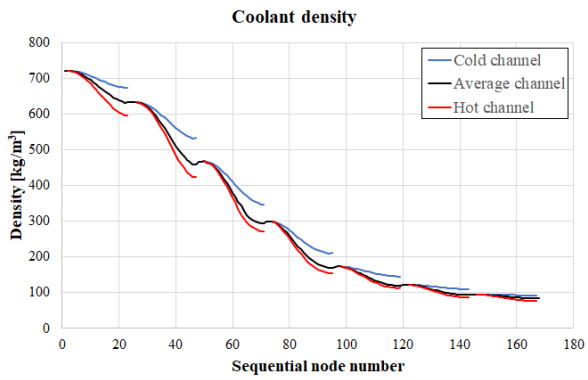

Figure 115: Density profile of the coolant channels

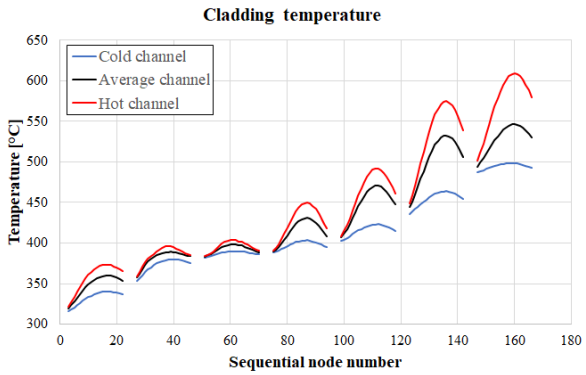

Figure 116: Cladding temperature profiles

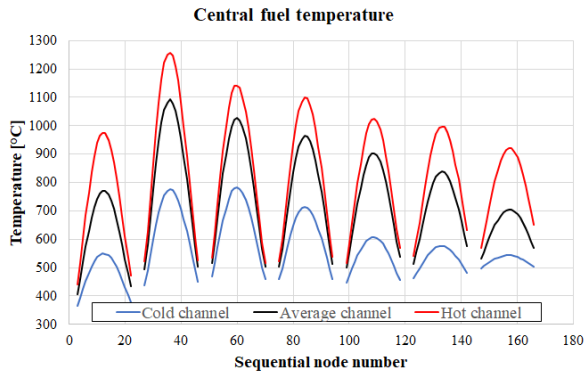

Figure 117: Central fuel temperature profiles

As a result of the axially cosinusoidal power distribution, the rise in the coolant temperature describes successive S-shaped curves, flattening out around stages 2 to 4, despite the relatively high local power. This apparent contradiction is caused by the occurrence of the pseudocritical transition (Figure 115), a second order phase transition that consumes a large amount of energy, similar to boiling at subcritical pressures. At the design power of 290 MW_{th} and inlet mass flow rate of 145 kg/s, an outlet temperature of about 518 °C was achieved, higher than the initial target of 500 °C, for which a mass flow rate of about 150 kg/s would be required. This higher temperature may provide higher system efficiency, but at the same time may compromise certain operating limits, so its acceptability must be further investigated later.

The combination of the continuously increasing coolant temperature and the shown power distribution results in a humped cladding temperature curve with maxima that are increasing along the stages and axially shifted forward within the stages. Based on the calculations, the global maximum is around 600 °C. However, this value corresponds to the average of the 5 hottest assemblies, which means that the maximum cladding temperature of the hottest fuel rod, the real peak cladding temperature, may significantly exceed this value.

The central fuel temperature profiles follow well that of the power, having a global maximum of around 1250 °C at the second stage. However, an additional peaking factor should also be considered as mentioned in the case of the cladding.

The above described results confirm the designer's idea that inequalities, and hence high temperatures, can be well reduced by using more heat-up stages, compared to the HPLWR concept. However, it can also be seen that even using 7 stages is not efficient enough, as the cladding temperatures of stage 7 show a deviation of about 70 °C. This issue has been addressed by further improvement of the concept, as shown in later chapters.

The mass flow rates along the available flow paths of the reactor vessel are summarised in Table 5. As noted already, there is a significant mass flow difference between the two half rings of the DC, which even increases as moving downwards. The outlet moderator plenum transfers more heat to its DC half through the wall and, as a result, its water temperature increases, causing its density to decrease and its pressure drop to be more significant. As a consequence, the mass flow of the outlet side DC half-ring is lower.

Location	Flow rates [kg/s]
DC bypass – inlet side	4.43
DC bypass – outlet side	4.44
DC below the nozzle – inlet side	70.56
DC below the nozzle – outlet side	65.57
Lower DC– inlet side	78.63
Lower DC – outlet side	57.50
Upward moderator	131.56
Reflector	4.57

Table 5: Flow rates at various part of the RPV model for a nominal feed water flow of 145 kg/s

A detailed discussion of the DC main and bypass mass flow is provided in chapter 4.4 based on the RELAP simulations. For Apros, quite similar experiences can be reported, i.e. the direction and rate of the DC bypass mass flow is extremely sensitive to various parameters like the pressure drop of the upward moderator channel, the rate of the internal wall heat transfers, the feedwater mass flow rate and other factors. In the version of the Apros model used for this case, the bypass mass flow rate was found to be positive (towards the UP; see Table 5) in contrast to RELAP, but given the many uncertainties and slightly different assumptions of the models (e.g. 1 or 2 channel downcomer, UP nodalisation), this difference was considered acceptable at this stage of the pre-conceptual development.

5.3.3 Calculation results of the concept with orifices (MOX core)

Based on the presented results of the original design concept, the University of Pisa suggested that an uneven inlet orifice distribution should be introduced, similar to BWR reactor and some

SCWR concept (Oka et al. 2010) practice, in order to achieve a more even distribution of the power-to-flow ratio, thus avoiding reaching high temperature peaking.

Based on this proposal, the cold and average coolant channels of the Apros model were supplemented with inlet orifices, while the hot channels remained unchanged. The exact orifice sizes (flow areas and the form loss coefficients, calculated using a specific formula from Idel'chik, 1960) were determined independently for each stage and for the cold and average channels. The target was a core state where the three channels have the same outlet coolant temperature in case of the first 5 stages and the same maximum cladding temperature in case of stages 6-7. This optimisation required an iterative process, but it was also combined with the Apros - Serpent code coupling iteration, resulting in a double iteration procedure. This combined iteration was continued until the code system was in equilibrium and the above objectives were achieved.

For a future final design, the orifice distribution will obviously need to be determined more precisely, using an assembly wise model; however, the approach used here is suitable for investigating the main qualitative effects. All calculations presented in this document have been performed for the BOC (Beginning Of Cycle) state of the reactor. During burn-up, the power distributions and the power peaking will change significantly and therefore their effect must also be taken into account, when selecting the optimal orifice sizes. Some efforts have already been made at BME to perform burn-up calculations with the Serpent model and also to investigate the EOC (End Of Cycle) state. However, some difficulties have been encountered, mainly related to the high memory requirements of such calculations; so, no results of these calculations can be reported yet, but research in this direction is ongoing.

In addition to the introduction of inlet orifices, an important parameter of the model was also changed in this version, namely the feedwater mass flow rate was increased from 145 kg/s to 150.12 kg/s in order to reduce the RPV outlet temperature to nearly 500 °C, which would also contribute to a further reduction of the maximum cladding temperature. The final results of the double iteration process performed with this model version using the MOX fuel map are shown in Figure 118 to Figure 125, while the orifice sizes are summarised in Table 6.

Orifice diameters [mm]	Stage 1	Stage 2	Stage 3	Stage 4	Stage 5	Stage 6	Stage 7
Average channel	40.5	45.0	42.0	42.5	43.0	41.0	35.5
Cold channel	32.5	35.5	34.0	34.5	32.0	29.4	24.0

Table 6: Optimised orifice sizes

The coolant (Figure 122) and cladding (Figure 124) temperature plots show that both the use of orifices and the higher feedwater mass flow achieved the desired effect, as the RPV outlet temperature dropped to 500 °C and the three channels show an even temperature distribution despite their significant power differences (Figure 118). The temperature feedback also slightly changed the power profiles themselves, mainly in the cold and hot channels, but this effect is nearly negligible. The modifications resulted in a reduction of the maximum cladding temperature to around 525 °C, which is almost 80 °C lower compared to the original design. Therefore, the use of orificing has proved to be a quite effective solution for the reduction of the temperature peaking and to reach a more even state of the reactor. However, it should also be emphasised that the applied method has some limitations and drawbacks:

- the received maximum temperature is the average of the five hottest assemblies and is therefore not the real peak cladding temperature;
- the consideration of only 3 channels and two orifice sizes per stage is only a rough approximation, which needs to be refined in the further phases of the development;
- in these analyses, the orifice sizes have been optimised specifically for the BOC state of the reactor; however, this optimum will continuously change during the burn-up cycle as the power profiles change, so that in the final design, a distribution of the orifices will have to be determined, which is optimal throughout the whole cycle; of course, that distribution will not be that perfect for the BOC state as the one specifically determined here for this single state;
- the use of orifices will of course significantly increase the overall pressure drop of the core: while the total pressure drop in the coolant channels was originally about 0.5 MPa (Figure 111), this is now increased to about 0.9 MPa (Figure 119); therefore, the moderator region is now at a pressure of almost 26 MPa, if a pressure of 25 MPa is required at the RPV outlet; the effects of such an increased pressure drop have also been investigated through the LTSBO transient analysis (see chapter 5.4).

Finally, the central fuel temperature has not changed significantly, as it is mainly determined by the power profiles. Its maximum is still around 1250 °C and located in the hot channel of Stage 2.

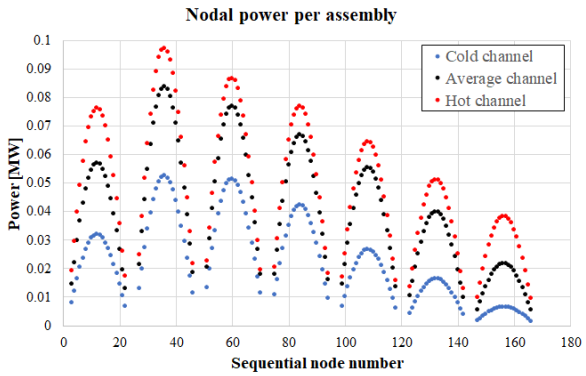

Figure 118: Nodal power distribution per assembly

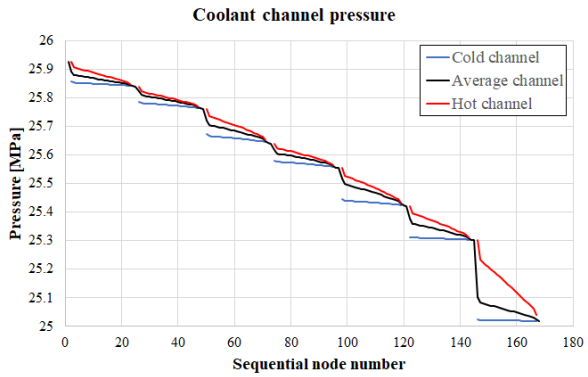

Figure 119: Pressure profile along the coolant channels

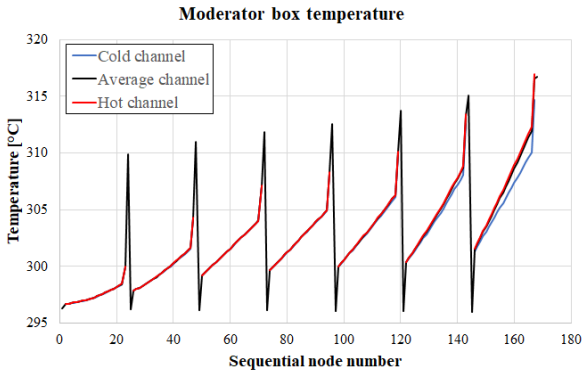

Figure 120: Temperature profile of the moderator boxes

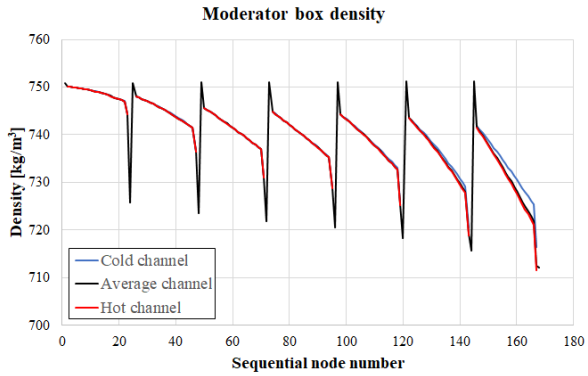

Figure 121: Density profile of the moderator boxes

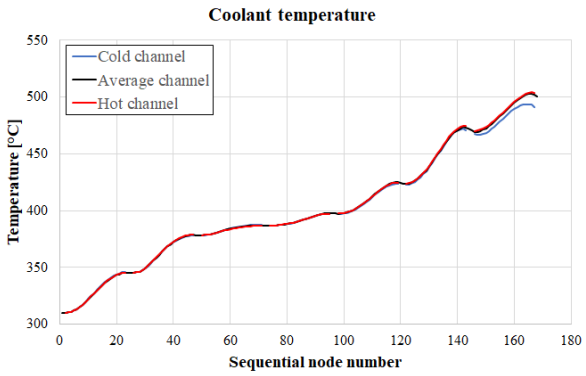

Figure 122: Temperature profile of the coolant channels

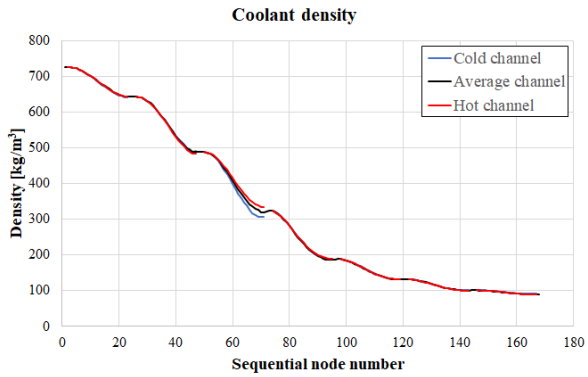

Figure 123: Density profile of the coolant channels

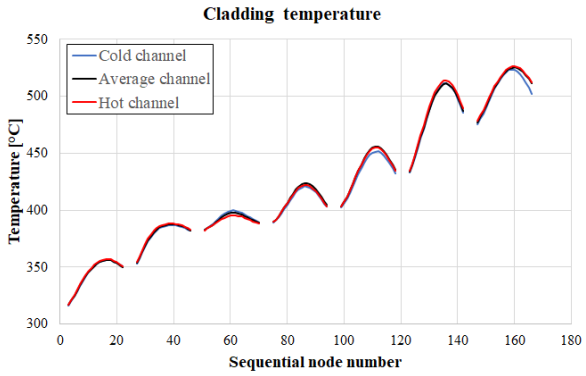

Figure 124: Cladding temperature profiles

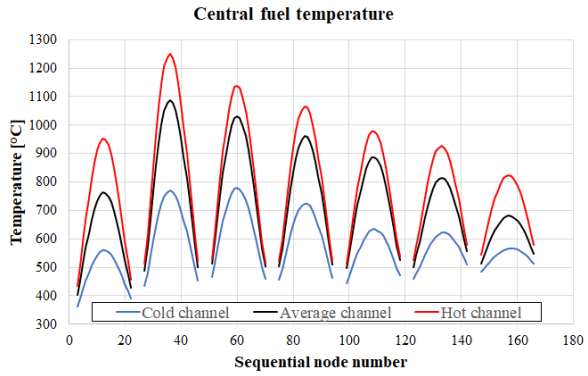

Figure 125: Central fuel temperature profiles

The power and flow ratios of both the cold and hot channels have been determined and collected in Table 7.

		Mass flow rates [kg/s]			Flow ratio		Power ratio	
		Cold channel	Average channel	Hot channel	Cold	Hot	Cold	Hot
Stage 7	Total	2.110	130.416	17.575				
	Per bundle	0.422	1.863	3.515	0.23	1.89	0.30	1.77
Stage 6	Total	3.505	134.273	12.323				
	Per bundle	0.701	1.918	2.465	0.37	1.28	0.41	1.29
Stage 5	Total	6.051	128.709	15.342				
	Per bundle	1.210	2.574	3.068	0.47	1.19	0.48	1.16
Stage 4	Total	8.013	126.931	15.158				
	Per bundle	1.603	2.539	3.032	0.63	1.19	0.62	1.15
Stage 3	Total	11.355	114.894	23.855				
	Per bundle	2.271	3.830	4.771	0.59	1.25	0.66	1.13
Stage 2	Total	12.000	116.147	21.956				
	Per bundle	2.400	3.872	4.391	0.62	1.13	0.62	1.16
Stage 1	Total	10.212	114.460	25.433				
	Per bundle	2.042	3.815	5.087	0.54	1.33	0.55	1.34

Table 7: Flow rates at the various stages in the three channels with optimised orifices and comparison of the cold-to-average and hot-to-average flow and power ratios per bundle

In case of stages 6 and 7, the objective of the optimisation procedure was to receive the same maximum cladding temperature, which however resulted in higher deviations of the outlet coolant temperature and therefore higher deviations of the power and flow ratios. In case of the first five stages, in line with the optimisation objective, the ratios show a fairly good agreement, except at the stage 3, where both the cold and hot ratios have a higher deviation. Stage 3 is the one where the pseudocritical phase transition mainly takes place; so, although the outlet temperatures have been set to be almost identical, the density curves (Figure 123) indicate that a more significant difference remained in the state of the channels compared to other stages. The optimisation could therefore be further refined here, as also indicated by the ratios.

5.3.4 Calculation results of the concept with orifices and modified layout (MOX core)

Possible modifications to the core layout have also been investigated to further reduce the maximum cladding temperature and optimise the design. The original implementation of dividing the 400 assemblies into 7 stages is shown in Table 4. An alternative Apros model version has been prepared, in which the top two stages have only 3+3 rows of assemblies, while the lowest one have 4. The new distribution is shown in Table 8.

Stages	Total number of assemblies in the stage (N)
1	80
2	40
3	40
4	60
5	60
6	60
7	60

Table 8: Number of assemblies per stage in the alternative layout

The double iteration process of the orifices and the coupled code system have also been performed with this alternative layout. The final results are presented in Figure 126 to Figure 133, while the specific orifice sizes are summarized in Table 9.

Orifice diameters [mm]	Stage 1	Stage 2	Stage 3	Stage 4	Stage 5	Stage 6	Stage 7
Average channel	38.7	45.0	43.9	42.1	41.5	39.6	35.5
Cold channel	28.6	34.5	34.2	31.1	30.1	28.4	24.5

Table 9: Optimised orifice sizes

The calculations carried out in this case used the original Serpent model and the MOX loading map optimised for the original layout (see Figure 109). However, minor modifications had to be made in the scripts used for the coupling to accommodate the different layout. When examining and comparing the presented profiles, it is important to keep in mind that the stage boundaries have been shifted, so that each cold/average/hot channel now represents a different group of assemblies.

In case of the power profiles (Figure 126), the most significant changes affect the first stage, as this now covers the first two stages of the original layout (bottom 4 rows of assemblies). The hot channel maximum is now shifted here and its peaking factor has also increased significantly (the hot channel power is more than three times that of the cold). Its effect is also reflected in the orifice dimensions required for the equalisation (Table 9). Partly as a result of these smaller orifices, but mainly due to the reduced total flow area of the upper two stages, the pressure drop of the core has increased from 0.9 MPa to over 1.3 MPa (Figure 127), which is a serious drawback of the alternative layout.

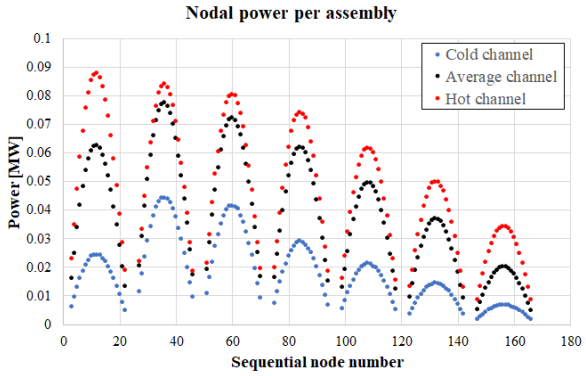

Figure 126: Nodal power distribution per assembly

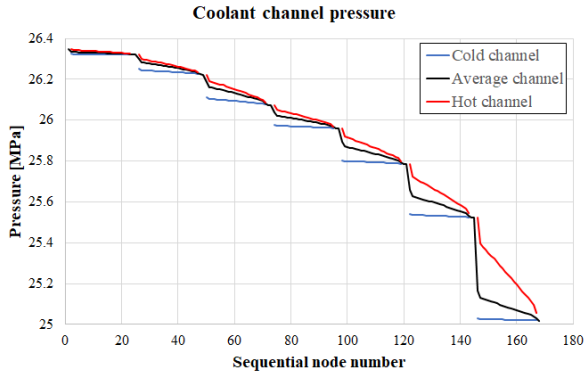

Figure 127: Pressure profile along the coolant channels

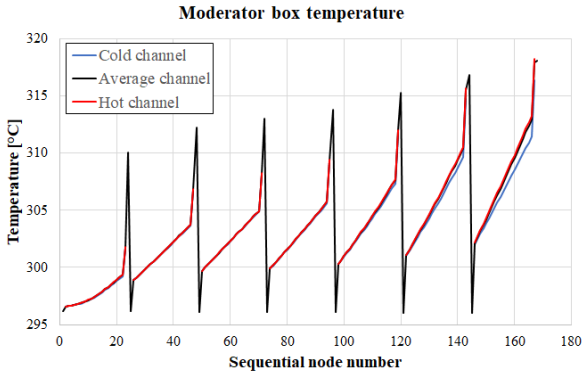

Figure 128: Temperature profile of the moderator boxes

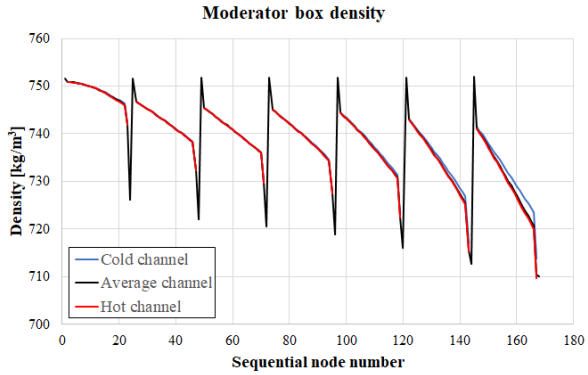

Figure 129: Density profile of the moderator boxes

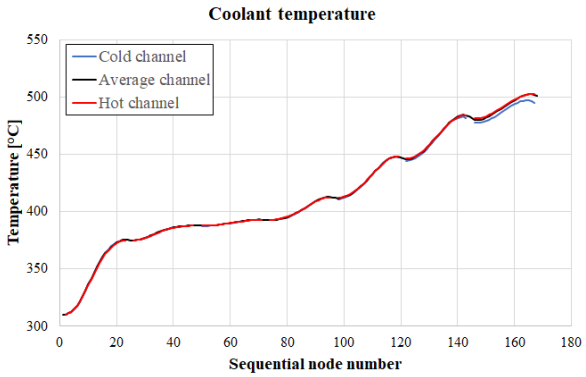

Figure 130: Temperature profile of the coolant channels

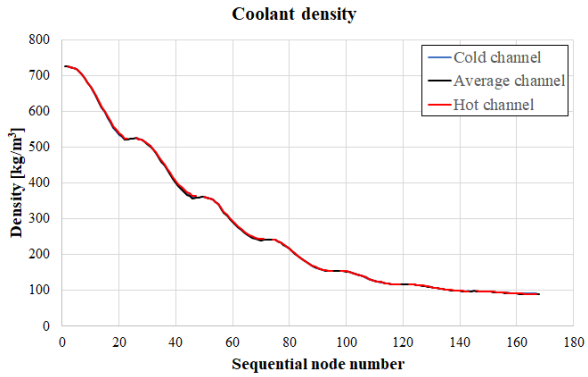

Figure 131: Density profile of the coolant channels

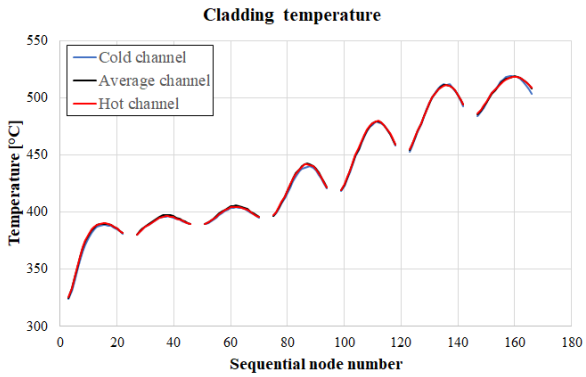

Figure 132: Cladding temperature profiles

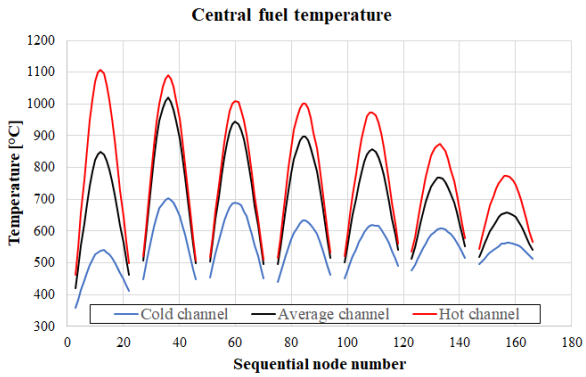

Figure 133: Central fuel temperature profiles

In accordance with the power profiles and the stage boundary shifts (total flow area of stage 1 has been duplicated, therefore its velocity is approximately halved), the coolant suffers a more significant heat up in the first stage and remains at a higher temperature all the way to the outlet (Figure 130). This is also an unfavourable change compared to the original case, as the system now operates at a higher average temperature and lower average density (Figure 131), with more heat stored, making it more difficult to deal with the potential accidents.

The modification has achieved the objective of reducing the cladding temperature maxima (Figure 132), but only by a few degrees. The central fuel temperature shows a more significant reduction and the maximum is now around 1100 °C (Figure 133).

Overall, it can be concluded that the alternative layout considered has more negative effects on the system behaviour than benefits; so, it does not seem advisable to proceed with this approach. However, it is recommended that further alternatives be explored and investigated in the future.

5.3.5 Calculation results of the original concept (UO_2 core)

All three calculation cases presented so far have been performed using the MOX loading map. However, these calculations have been repeated using the pure UO_2 map as well (see Figure 109). For the Apros model, this did not entail any modifications, only the dimensions of the orifices had to be revised in the relevant cases (see chapter 5.3.6 and 5.3.7). The results for the original design are presented in Figure 134 - Figure 139.

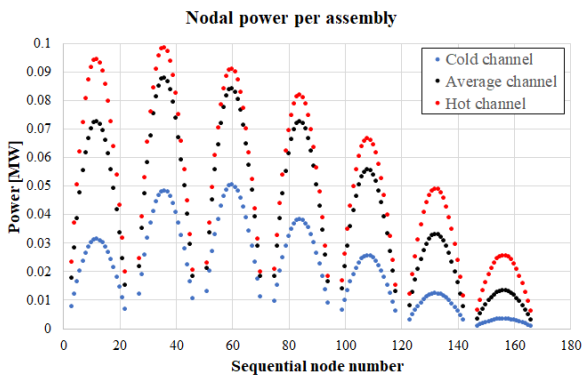

Figure 134: Nodal power distribution per assembly

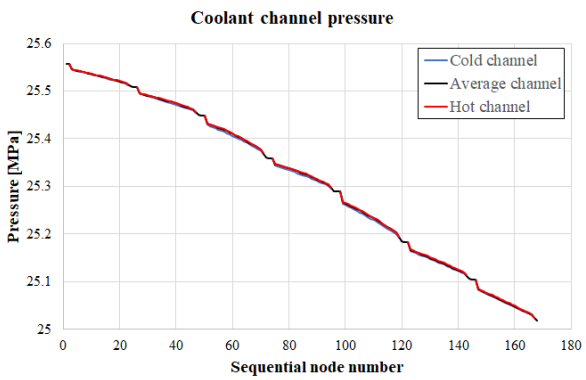

Figure 135: Pressure profile along the coolant channels

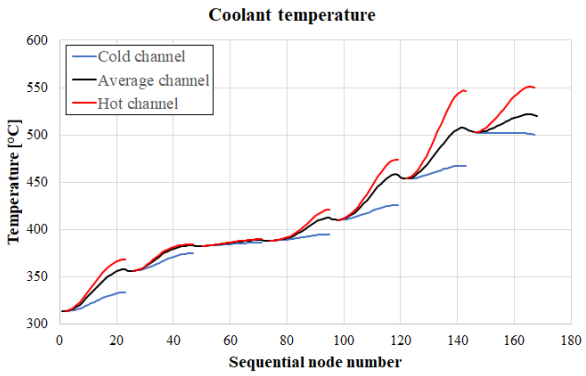

Figure 136: Temperature profile of the coolant channels

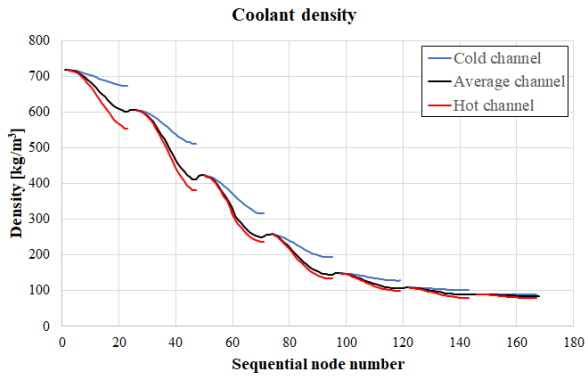

Figure 137: Density profile of the coolant channels

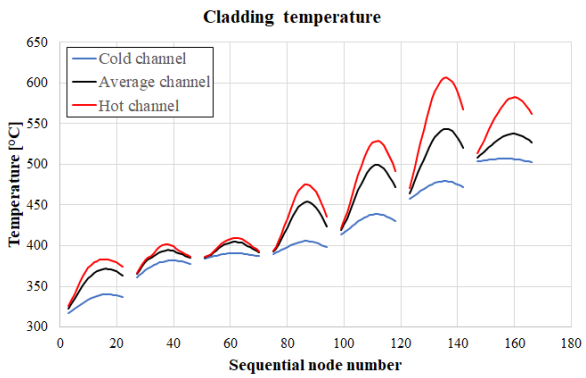

Figure 138: Cladding temperature profiles

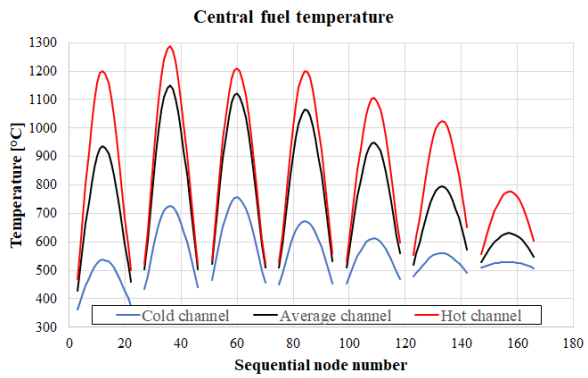

Figure 139: Central fuel temperature profiles

By comparing these results with those obtained using the MOX map (chapter 5.3.2), it can be seen that the power (Figure 134) has decreased in all cold channels and in the average and hot channels of the top two stages, while the average and hot powers have increased in the bottom 5 stages. The most significant changes are observed in the average and hot channels of the first (increase) and seventh (decrease) stage. As a result of these power profile changes, the coolant undergoes a faster and earlier warm-up (Figure 136), resulting in a slight increase in the average core temperature, similar to the case of the alternative layout discussed in the previous chapter. However, the magnitude of the change is much less pronounced here, because the total flow area of the first stage follows the original layout. The higher average temperature means a lower average density (Figure 137), which in turn means a higher pressure drop across the core (Figure 135). The latter is about 0.5 bar higher compared to the MOX map.

An interesting consequence of the significantly reduced power of stage 7 is that the maximum coolant temperatures of stage 6 and 7 are almost the same, while the maximum cladding temperature occurs at stage 6 (Figure 138) and is practically the same as in the MOX core at the seventh stage (Figure 116). From an accident management point of view, it is typically advantageous to have a maximum at a lower stage. The central fuel temperatures are shifted slightly upwards (Figure 139), with the exception of the uppermost stage. The maximum of around 1300 °C is observed at stage 2.

On the basis of the parameters examined above, it can be concluded that the use of a pure UO_2 loading map, although having some positive effects, has overall a rather negative effect on the behaviour of the system. However, this does not mean that the use of pure UO_2 maps should be discarded, since the negative effects observed are not so great, the optimisation of the loading

maps can be further refined on the basis of the experience gained and in the future development phases the changes during burn-up and its effects should also be taken into account in order to be able to take such a decision. In addition, there are many other considerations to be taken into account when deciding whether or not to use MOX core in a reactor design.

5.3.6 Calculation results of the concept with orifices (UO_2 core)

As a continuation of the previous cases, those Apros and Serpent model versions were also coupled, which use the inlet orifices and the UO_2 loading map. A double iteration procedure, including re-optimisation of the orifices, has also been performed here. The final results of this iteration are shown in Figure 140 to Figure 145, while the orifice sizes are summarised in Table 10.

Orifice diameters [mm]	Stage 1	Stage 2	Stage 3	Stage 4	Stage 5	Stage 6	Stage 7
Average channel	40.5	45.0	46.0	43.5	42.7	37.7	33.9
Cold channel	30.3	33.8	34.8	32.5	31.1	27.2	*27.2*

Table 10: Optimised orifice sizes

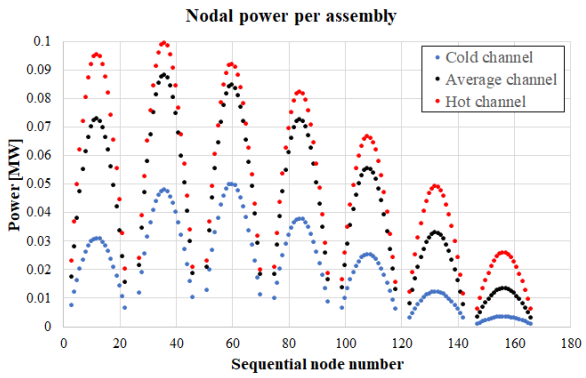

Figure 140: Nodal power distribution per assembly

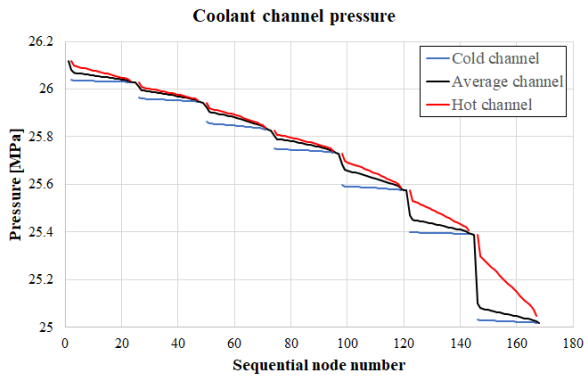

Figure 141: Pressure profile along the coolant channels

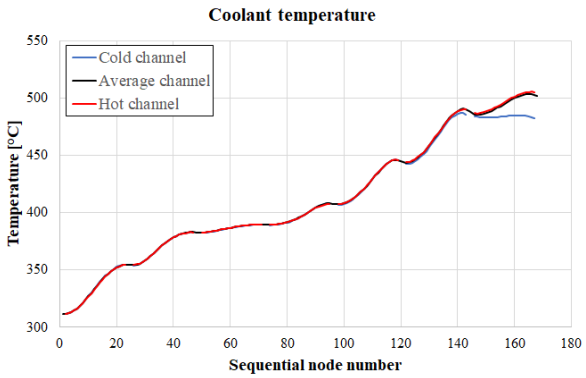

Figure 142: Temperature profile of the coolant channels

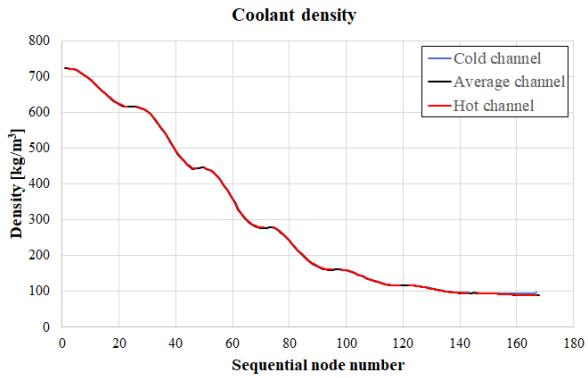

Figure 143: Density profile of the coolant channels

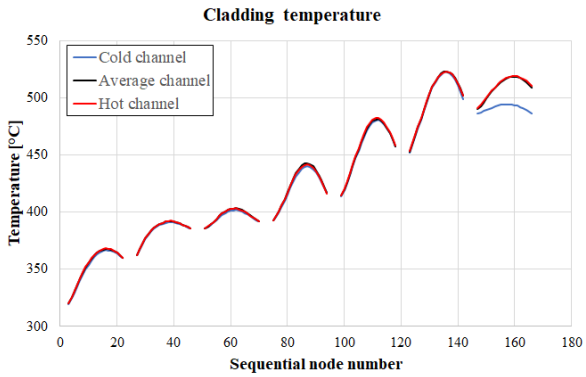

Figure 144: Cladding temperature profiles

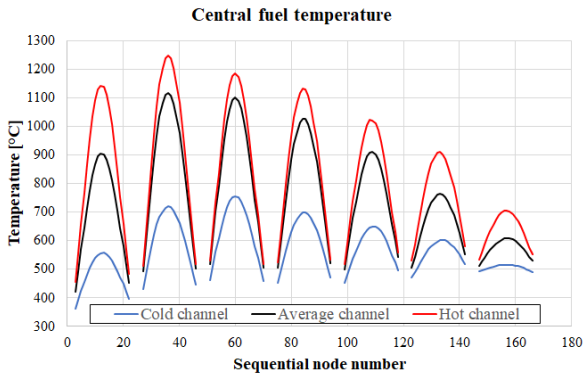

Figure 145: Central fuel temperature profiles

The results reveal an important difference compared to the previous cases. The optimisation of the orifices in the seventh stage is only partial, resulting in lower cold channel coolant (Figure 142) and cladding (Figure 144) temperatures. The reason for this is as follows. When using the UO_2 loading map, the power of the topmost stage, and in particular of its cold channel (Figure 140), is very low (the hot channel power is 8 times greater than the cold); so, to achieve the same maximum cladding temperature (Figure 144), the cold assemblies would have to be extremely restricted, which would result in dangerously low flow rates. Based on these considerations, it was decided to set the cold channel orifice size of stage 7 to be the same as that of the 6th stage (i.e., 27.2 mm, see Table 10). It can be seen that, although this is also a very small orifice size, the cold temperatures are still significantly lower than in the other two channels, the coolant temperature is practically constant (Figure 142), which means that the heating power is approximately equal to the loss through the walls. This behaviour, although different from that of the MOX core, is not necessarily worse. Further investigation is required, as also suggested above.

In general, when comparing the MOX and UO_2 map results for the orifice case, similar observations can be made as for the non-orifice case in the previous chapter:

- the most significant differences in the power profiles are observed at the two boundary stages, increasing at stage 1 and decreasing at stage 7 (Figure 140);
- the average coolant temperature is slightly increased (Figure 142), while the average density is decreased (Figure 143);
- the total pressure drop of the coolant region is increased by about 0.2 MPa (Figure 141);
- the maximum cladding temperature is observed at stage 6 and is a few degrees lower than in the MOX core (Figure 144);
- the maximum central fuel temperature occurs at stage 2 and its value of about 1250 °C is practically the same as in the case of the MOX map (Figure 145).

5.3.7 Calculation results of the concept with orifices and modified layout (UO_2 core)

The final case presented here considered the pure UO_2 loading map and the Apros model with optimised orifices and alternative core layout described in chapter 5.3.4. The double iteration procedure has been performed just as before, the results of which are shown in Figure 146 to Figure 151, while the orifice sizes are summarised in Table 11.

For similar reasons as in the previous case, a complete orifice optimisation for the stage 7 cold channel has not been performed, but the orifice size of the stage 6 cold channels was used instead (see Table 11).

Orifice diameters [mm]	Stage 1	Stage 2	Stage 3	Stage 4	Stage 5	Stage 6	Stage 7
Average channel	40.5	45.0	45.5	43.5	40.5	37.7	34.6
Cold channel	29.2	34.6	34.8	31.9	29.5	26.8	*26.8*

Table 11: Optimised orifice sizes

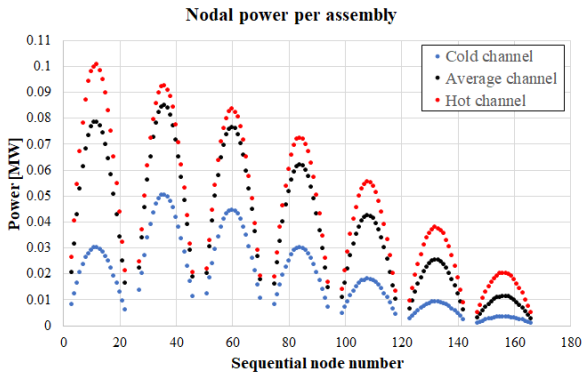

Figure 146: Nodal power distribution per assembly

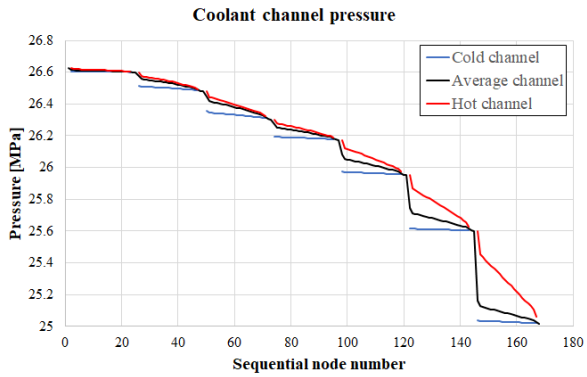

Figure 147: Pressure profile along the coolant channels

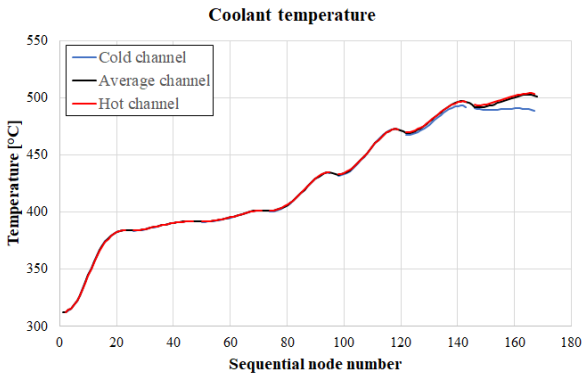

Figure 148: Temperature profile of the coolant channels

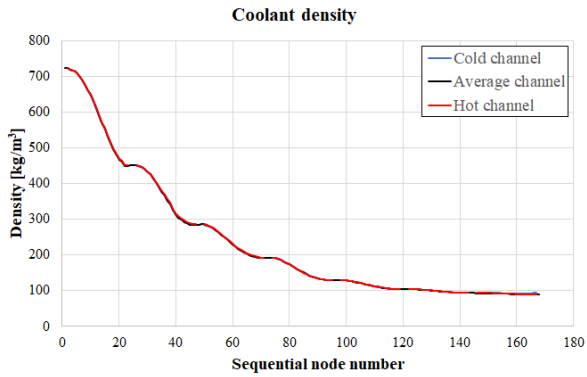

Figure 149: Density profile of the coolant channels

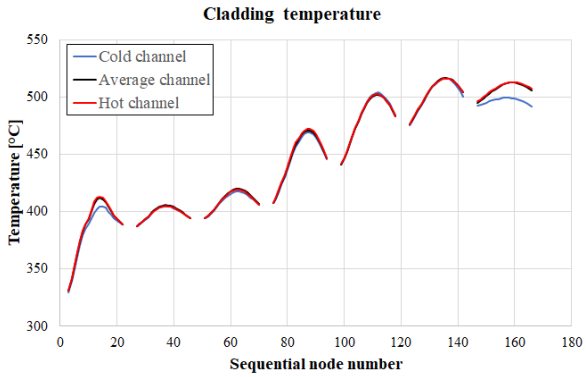

Figure 150: Cladding temperature profiles

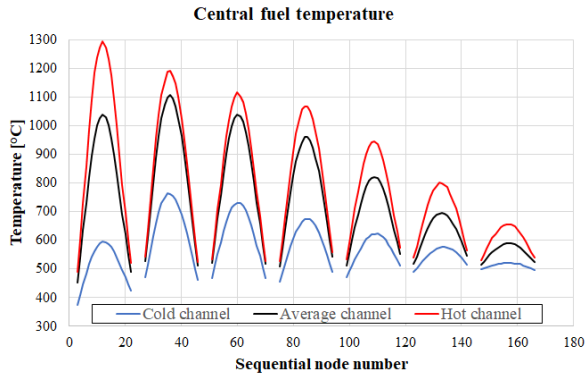

Figure 151: Central fuel temperature profiles

In the case of the power profiles (Figure 146), it can be seen that the effects of using the UO_2 loading map and the alternative layout are practically combined here, resulting in a really high power in the first stage, while it drops significantly in the upper stages. The combination of these

changes with the duplicated flow area of stage 1 results in a reactor state where the coolant starts the pseudocritical phase transition already at the end of stage 1 (Figure 148). The average coolant temperature therefore increases and the density (Figure 149) decreases significantly. The total pressure drop of the coolant channels reaches 1.6 MPa (Figure 147), which means a further increase of 0.2 MPa compared to the case of the MOX map.

For the cladding temperatures (Figure 150), a previously unseen phenomenon is also observed, namely a slight heat transfer deterioration develops at around 2/3 axial position of the assemblies in stage 1 as a result of the rather high power rates and low flow velocities. This corresponds to an additional temperature peak of approximately 20 °C in case of the hot and average channels. Such a condition should be avoided as far as possible during normal operation: so, the use of the combination considered here is not recommended.

Finally, the maximum fuel temperature of about 1300 °C is also observed in the first stage in accordance with the above (Figure 151).

5.3.8 Calculation results of further sensitivity analyses

In the previous chapters, the results of 6 different conceptual variations were presented and examined in detail. Based on their experience and the best comparability with UNIPI's RELAP model, the version of chapter 5.3.3 was selected as the BASE version, with which a number of additional sensitivity analyses have been performed. It is important to emphasise that no further Serpent-Apros iterations or further orifice optimisation were performed during these analyses: the orifice sizes of Table 6 and the power profiles of Figure 118 were used throughout these calculations. The sensitivity analysis included the variation of the inlet temperature, mass flow rate, system pressure, total reactor power and the HT correlation used. For each case investigated, the Apros model was run to the new equilibrium state after the parameter modification and the equilibrium results are presented in the following subsections.

When comparing the results, it was found that the three (cold, average, hot) channels undergo similar changes, with no significant detuning of the orifices. Therefore, for the sake of clarity, it was decided not to plot the results for all three channels, but rather to plot the curves for the most important, typically average or hot, channels for a given parameter.

5.3.8.1 Variation of the inlet temperature

In the first investigated case, the inlet fluid temperature of 280 °C was varied by ± 5 °C, the results of which are shown in Figure 152 - Figure 155.

The variation of the coolant (Figure 152) and cladding (Figure 154) temperatures corresponds well to the variation of the inlet temperature, with smaller differences in the region of the pseudocritical phase transition (stage 2-4), and a slightly higher variation of about ±7 °C in the uppermost stage, where the maximum cladding temperature is also observed. The maximum central fuel temperature (Figure 155), as having a maximum in stage 2, has a variation of only ±2 °C. In the states with higher average coolant temperatures, the average density is lower and therefore the pressure drop is higher, showing a variation of about ±0.02 MPa at the stage 1 inlet. The observations are consistent and in accordance with the expectations, with no strange behaviour or states to be avoided.

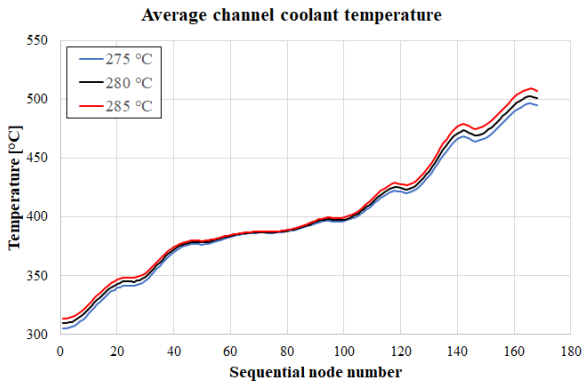

Figure 152: Temperature profile of the average coolant channels

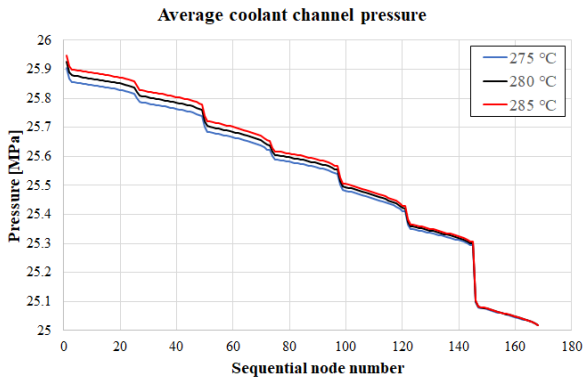

Figure 153: Pressure profile along the average coolant channels

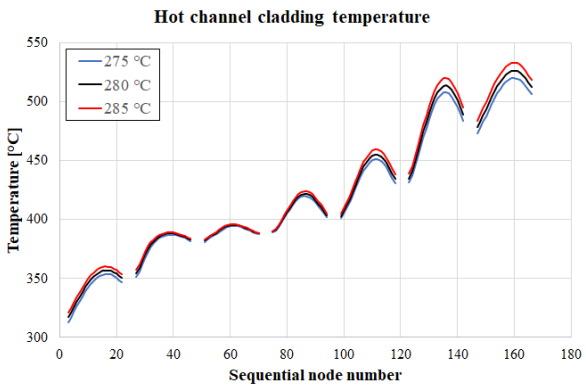

Figure 154: Hot channel cladding temperature profiles

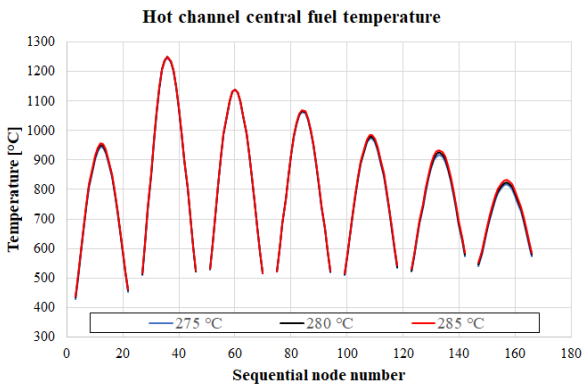

Figure 155: Hot channel central fuel temperature profiles

5.3.8.2 Variation of the mass flow rate

In the second investigated case, the mass flow rate of 150.12 kg/s was varied by ±5 %, the results of which are shown in Figure 156 - Figure 159.

The variation of the coolant (Figure 156) and cladding (Figure 158) temperatures, with the exception of the pseudocritical transition zone, increases continuously in accordance with the series connection of the stages and the varying mass flow rates, and therefore velocities. The outlet coolant and maximum cladding temperatures have a variation of (-23) - (+28) °C, and (-27) - (+32) °C, respectively. On one hand, this can be considered as a significant variation for a change in mass flow of only 5%. On the other hand, the observed sensitivity can be attributed to and explained by the very low heat capacity of the fluid at the core outlet. Based on these results, it is extremely important to maintain an adequate and stable mass flow rate in the system under normal operating conditions, and also to try to maintain a sufficiently high mass flow rate in the first phase of an accident using appropriate, automatic actions, when required.

The increasing variance of the coolant temperature is also reflected in the density, which in turn has a significant effect on the pressure drop (Figure 157), reducing it as the mass flow increases. However, a counter effect is produced by the variation of the mass flow itself, since a higher mass flow means higher velocities and higher pressure drops. These two effects almost cancel each other out, resulting in a pressure drop variation of only ±0.02 MPa at the stage 1 inlet (higher mass flow rate causes higher pressure drop). The maximum central fuel temperature (Figure 159) at stage 2 varies by only ±4 °C, while at the seventh stage the variation is around (-34) - (+40), but still well below the lower stages.

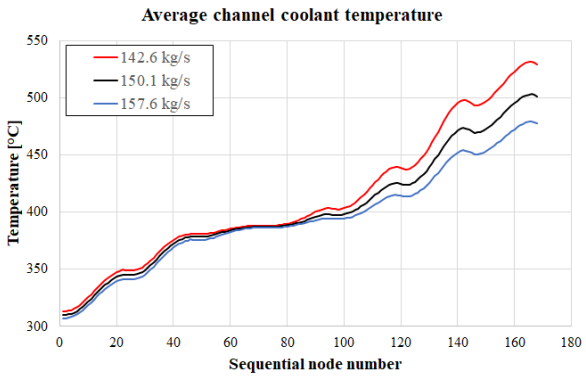

Figure 156: Temperature profile of the average coolant channels

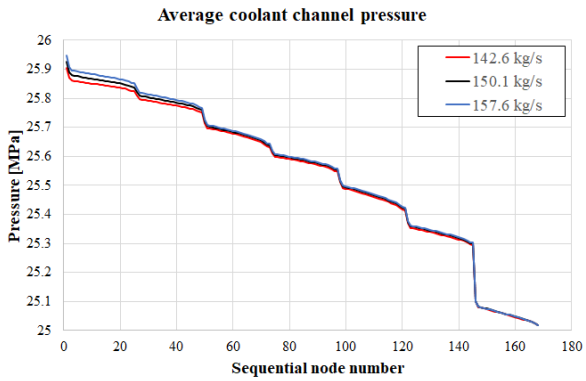

Figure 157: Pressure profile along the average coolant channels

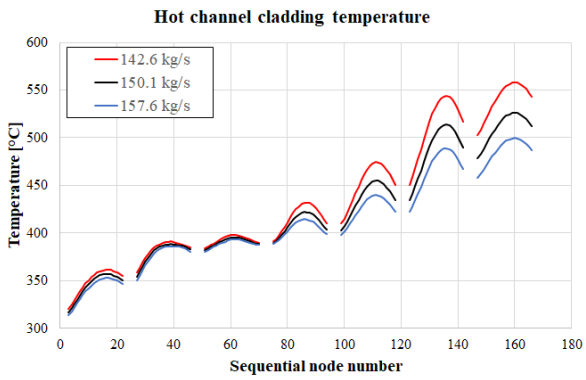

Figure 158: Hot channel cladding temperature profiles

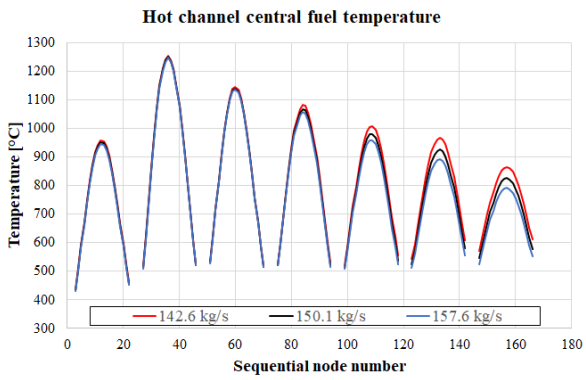

Figure 159: Hot channel central fuel temperature profiles

5.3.8.3 Variation of the system pressure

In the third investigated case, the RPV outlet pressure of 25.0 MPa was varied by ±1 MPa, the results of which are shown in Figure 160 - Figure 163.

In this case, the observed small coolant temperature variation is caused by the pressure dependence of the water properties. At higher pressures, the coolant (Figure 160), cladding (Figure 162) and central fuel (Figure 163) temperatures also increase slightly, and they have a variation of ±4 °C (outlet), ±4 °C (maximum at stage 7) and ±4 °C (maximum at stage 2), respectively. As a result of the change in system pressure, the pressure drop curves (Figure 161) are shifted, but they also have a variation of around ±0.02 MPa caused by the change in the coolant temperature.

Overall, it can be concluded that the pressure variation does not have a significant effect on the temperatures and the system behaviour, so the exact operating pressure should be chosen based on other aspects (turbine demand, design pressure, efficiency, etc.).

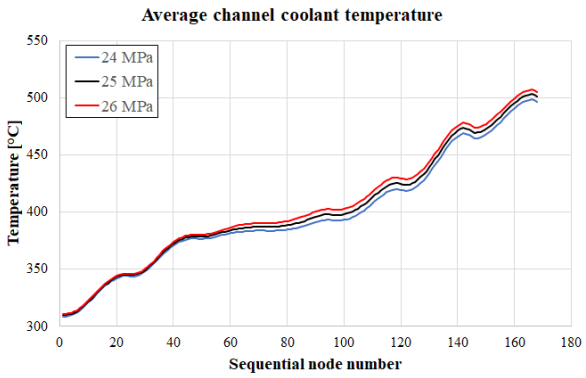

Figure 160: Temperature profile of the average coolant channels

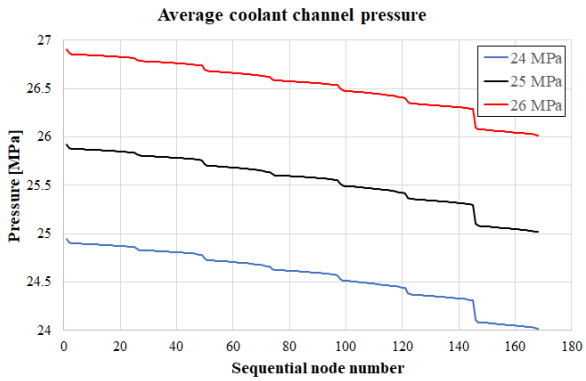

Figure 161: Pressure profile along the average coolant channels

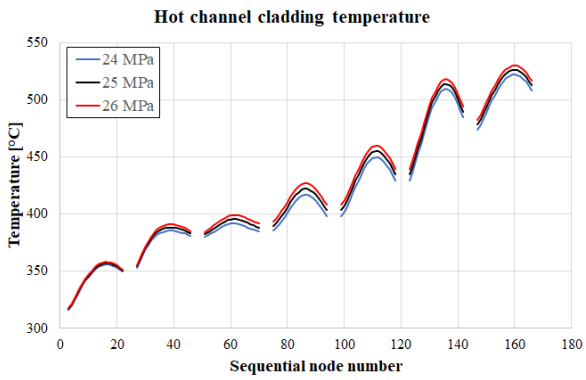

Figure 162: Hot channel cladding temperature profiles

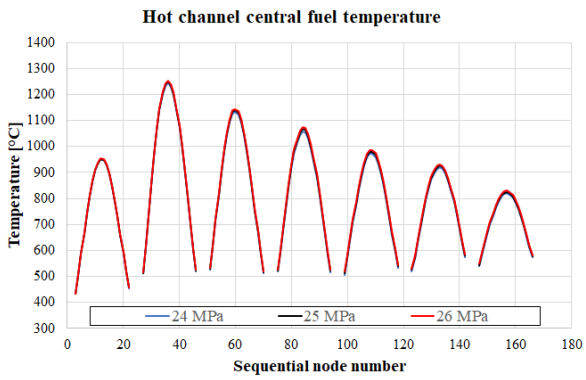

Figure 163: Hot channel central fuel temperature profiles

5.3.8.4 Variation of the reactor power

In the fourth investigated case, the relative power profiles of Figure 118 were retained, but the total power was varied by ±5 % using a single multiplication factor. The results are shown in Figure 164 - Figure 167.

The variation of the coolant (Figure 164) and cladding (Figure 166) temperatures are almost identical to those observed in chapter 5.3.8.2 for the mass flow variation. This is not surprising, since in both cases it is the power-to-flow ratio that is actually being varied by 5%, with the difference that the increase in power has a similar effect to the decrease in mass flow and vice versa.

In case of the pressure drop (Figure 165), only one of the two opposite effects described in chapter 5.3.8.2 is present here, since the mass flow rate is constant. As a result, the variation is much greater and reaches up to ±0.065 MPa. Finally, as a combined effect of the power changes and the varying coolant temperatures, the central fuel temperatures (Figure 167) are shifted by less than ±5% on the lower stages and by about ±6-7% at the upper ones.

Overall, the variation of the power has the strongest effects on the system behaviour of all the parameters studied so far, so keeping it stable and constant is of great importance, similar to the mass flow rate.

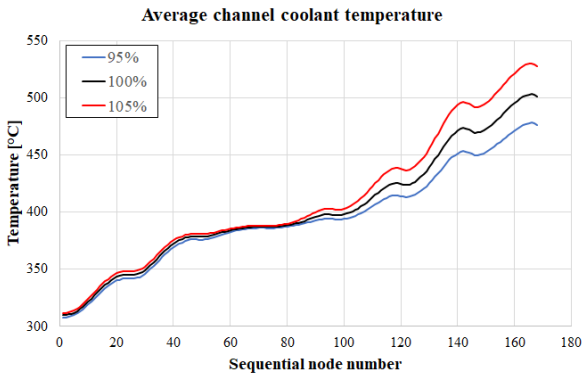

Figure 164: Temperature profile of the average coolant channels

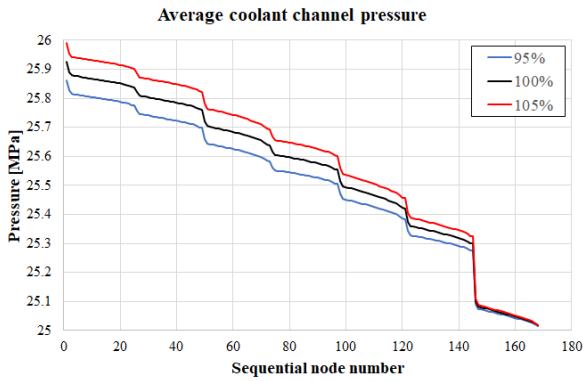

Figure 165: Pressure profile along the average coolant channels

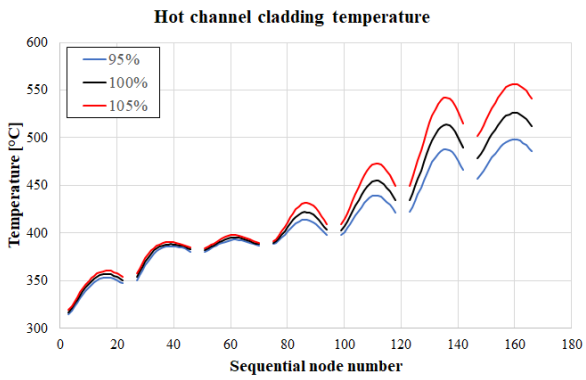

Figure 166: Hot channel cladding temperature profiles

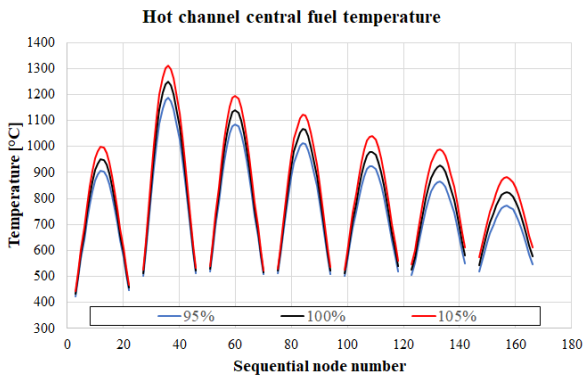

Figure 167: Hot channel central fuel temperature profiles

5.3.8.5 Variation of the HT correlation

In the fifth, and final, investigated case, the used heat transfer correlation was varied. All the calculations presented so far have been performed using the Bishop et al. (1965) correlation, so here the Mokry et al. (2011), and the Jackson and Hall (1979) correlations were tested. This modification did not affect the coolant parameters, the pressure drops and most other parameters, so only the cladding temperatures are compared in Figure 168 - Figure 169.

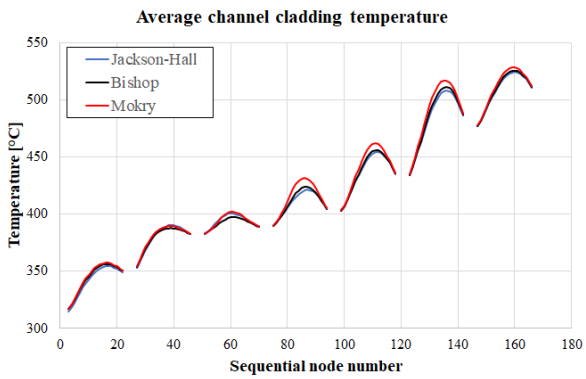

Figure 168: Average channel cladding temperature profiles

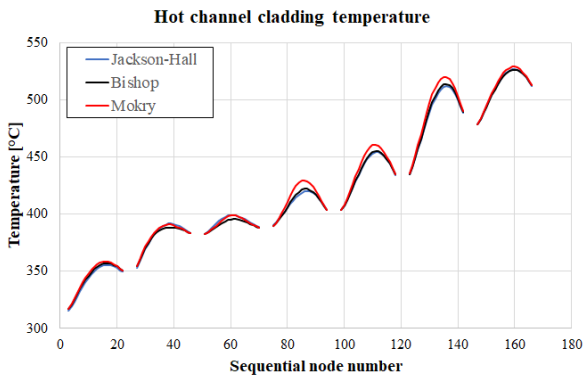

Figure 169: Hot channel cladding temperature profiles

As can be seen, the deviation between the Bishop and Jackson-Hall correlations is almost negligible, while the Mokry correlation shows slightly higher temperatures, with a maximum deviation of around 6-8 °C at the stages 4-6. No heat transfer deterioration is indicated by either correlation. Based on these results, the previous decision to use primarily the Bishop correlation has not been changed.

5.3.9 Discussion about the steady-state results

On the basis of the coupled calculations and further sensitivity analyses performed, it can be concluded that the design concept shows a fairly robust and predictable behaviour. The lower, liquid-like coolant region is quite stable and, based on the observations in chapter 5.3.7 and 5.3.8, the main model versions introduced in chapter 5.3.3 (MOX) and 5.3.6 (UO2) have a sufficiently high safety margin to avoid heat transfer deterioration in the nominal operating conditions. No deterioration was observed during the sensitivity analyses and only a slight deterioration occurred in chapter 5.3.7, which however required a high local power and a doubled total flow area (i.e. halved mass flux) in stage 1. The sensitivity of the gas-like region is much more significant, mainly due to its low heat capacity and the cumulated effects of the lower stages, which means that the coolant and hence the cladding temperature can undergo significant changes in case of fluctuations of some main system parameters.

In four investigated cases, the orifice sizes were specifically optimised and collected in Table 6, Table 9, Table 10 and Table 11. These have also been compared in Figure 170. Despite the significant differences between the four model versions, the curves of the optimal orifice sizes are quite similar, mainly increasing in the first 3 stages and then decreasing further on in both the cold and average channels. The smallest size is required in the cold channel of stage 7. A nearly constant 10 mm difference is required between the two channels.

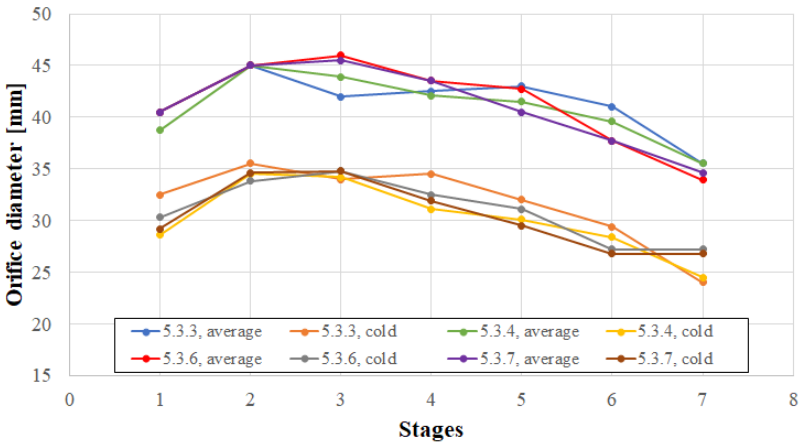

Figure 170: Comparison of the optimised orifice sizes in the investigated cases

From the Serpent calculations, in addition to the power profiles required for the Apros calculation, the k_{eff} values were also extracted and compiled into Table 12. As can be seen, the loading map used has the most significant effect, the values obtained with the UO_2 map are higher, i.e. it is expected to allow a longer burn-up cycle to be achieved. However, the MOX map is also able of achieve a cycle of at least 2 years, which is set as a minimum. The differences obtained between the 3-3 cases of a particular loading map are practically negligible, with the exception of the third case (alternative layout, MOX map), which provided an exceptionally low k_{eff}.

Model version	k_{eff}	±2σ
Orig. concept (MOX)	1.22489	0.00006
Concept with orifices (MOX)	1.22531	0.00006
Concept with orifices, alternative layout (MOX)	1.20766	0.00005
Orig. concept (UO_2)	1.24502	0.00006
Concept with orifices (UO_2)	1.24573	0.00006
Concept with orifices, alternative layout (UO_2)	1.24565	0.00006

Table 12: Effective multiplication factor result of the Serpent 2 calculations

On the basis of the above experience, it is recommended to continue the research activity primarily with the model versions investigated in chapter 5.3.3 (MOX) and 5.3.6 (UO2), but the possibility of testing further alternative layouts should not be completely excluded either. For the LTSBO transient study, the model version with the MOX map and optimised orifices (chapter 5.3.3) was selected as the BASE version.

5.4 Transient analyses for the LTSBO event with Apros

The SBO transient sequence for the Apros model was also developed on the basis of the WP3 joint discussions. The built controllers and protections perform the following actions after the activation of the SBO event:

- starts the trip of the condensate pump immediately;
- starts the trip of the feedwater pump immediately;
- starts the trip of the condenser cooling immediately;
- starts to open the turbine bypass line with 1 s delay and 3 s operating time;
- starts the closure of the turbine inlet shut-off valve, as well as the turbine outlet control valve with 2.5 s delay and 3 s operating time;
- stops the heating of the LP and HP pre-heaters, and the steam injection to the FW tank with 2 s delay;
- starts the reactor SCRAM with 2 s delay;
- opens the PHRS line valves with 50 s operating time and closes the containment isolation valves with 3 s operating time, when the RPV outlet pressure drops below 11.0 MPa;
- the check valves of the accumulator surge lines open automatically, when the system pressure drop below 4.8 MPa.

One part of the above sequence is intended to model the loss of functionality triggered by the initial event, while the other part is intended to model the response of the protection system to the initial event. The latter mainly involves a fast, controlled depressurisation, a change-over to natural circulation heat removal, and supplement of the coolant. The blow-down has two main purposes, firstly to maintain a controlled flow in the core, and secondly to reduce the system pressure sufficiently to activate the passive cooling circuit. Once the system pressure has been successfully reduced to 11 MPa, the passive cooling circuit is opened with a relatively long relaxation time of 50 s, while further blow-down is terminated by closing the containment isolation valves. Heat is then removed to the PHRS pools. Finally, coolant supplement is provided passively by the accumulators.

For the modelling of the reactor power, the same decay-heat curve has been used as in the RELAP model (see chapter 4.5.1). However, there are some differences in the assumptions made regarding the pump tripping. In the RELAP model, the feedwater injection was considered as a boundary condition and reduced to zero in 10 s, whereas in the Apros model, the condensate and

feedwater pumps were modelled. These pumps, especially the feedwater one, have to maintain a very high differential pressure in nominal operation, so in the event of a loss of electricity, even if they have a high inertia, the flow will stop quite quickly in the first phase of the coast-down and the check valves will close to prevent the backflow. In the performed Apros simulations, although assuming a pump coast-down time of 10 seconds, the flow stopped in less than 1.5 seconds. As a result, despite the bypass opening and the further delayed turbine closure, there is a period of time during which the core mass flow rate decreases and therefore the coolant, cladding and fuel temperatures increase. Such a behaviour is not observed in case of RELAP due to the assumptions applied. The above Apros assumption is of course more conservative, but which one is more realistic can only be determined later, when the details of the primary circuit concept is worked out more precisely and the pump characteristics are better defined. For now, this is important to evaluate the results of both models with this difference in mind.

Various calculations were run with the non-coupled Apros model in order to simulate the behaviour of the system as a consequence of this SBO event. The Base case was run up to the duration of 72 hours making use of the model version described in chapter 5.3.3 (maintaining the relative power profiles of Figure 118 throughout the transient), with MOX loading map and optimised orifices. The alternative versions were stopped however typically after 12 hours with some specific exceptions as described later.

Apros was able to perform these transient calculations at relatively high speeds, especially in the long-range subcritical pressure period. Only the transition from supercritical to subcritical pressure caused a significant decrease in the applied time step as this pressure wave moved through the entire system. However, in the numerous calculations performed, no computational stalls or non-convergence were experienced, meaning that the model and code were quite robust.

5.4.1 Base calculation case

In this Base case, the calculation was run for 72 hours, but for most parameters only the first 12 hours are plotted and presented, because no significant changes were observed later and with this timescale, the first, interesting phase is more visible and comparison with the RELAP results is easier. In some specific cases, an additional figure of the first few seconds is also provided.

Figure 171 to Figure 173 show the trend of pressure and mass flow rates in various regions of the vessel and primary system as obtained in the computations. The actuation of the depressurisation line is effective in bringing the reactor at subcritical pressure. The turbine bypass blow-down has a higher mass flow rate and therefore faster depressurisation in the Apros calculation compared to RELAP, so that the closure setpoint of 11 MPa is reached after about 10 seconds. This deviation is caused by the different assumptions used regarding the bypass line and its boundary condition.

Regarding the DC mass flow distribution, a similar behaviour and negative flow rate through the upper downcomer orifices have been observed as in RELAP, confirming the interesting feature of the transient and the vessel design that actually two main flow loops are combined:

1) a natural circulation loop including the downcomer, the lower plenum, the upward moderator flow path, the upper plenum and the downcomer orifices;
2) the loop that detaches from the previous one towards the moderator channel inlet plena, passes through the moderator boxes to the outlet plena, flows down to the double bottom structure and finally enters the sequence of the seven stages of the fuel coolant channels and is finally captured from the steam line by the Isolation Condenser to be returned to the downcomer.

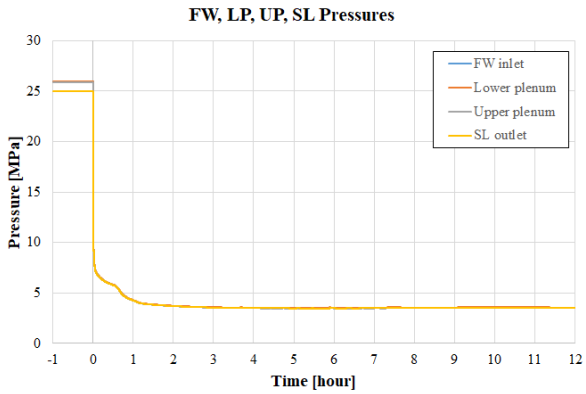

Figure 171: Pressure at various locations in the vessel

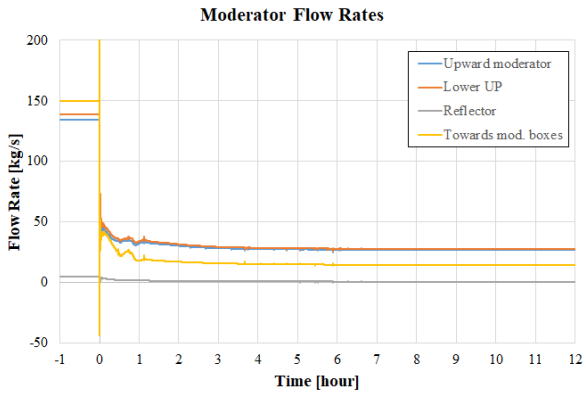

Figure 172: Moderator flow rates at various locations in the vessel

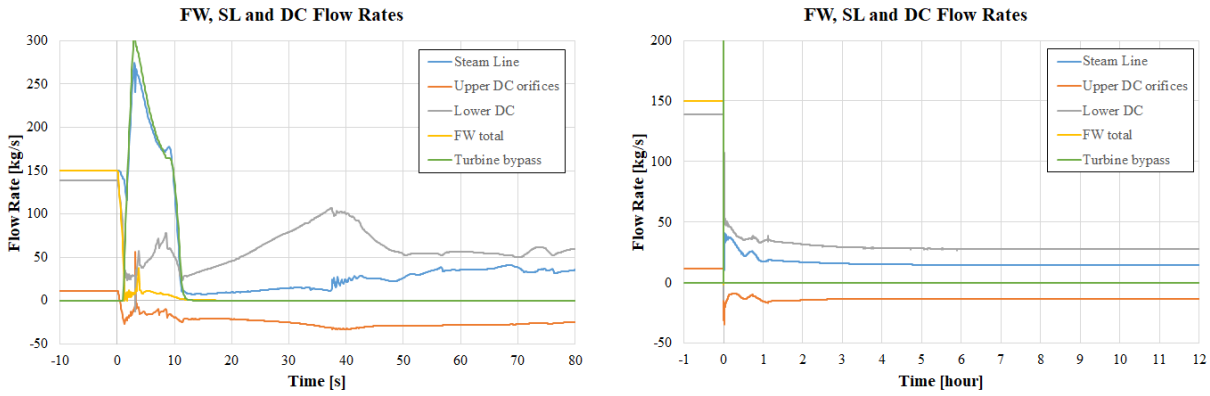

Figure 173: Flow rates at various locations of the primary system

The reversal of the flow direction in the 7th stage cold, average and hot moderator boxes is also confirmed by the Apros simulation as shown in Figure 174. At the other stages, the flow direction is normal, while its magnitude is mainly determined by the vertical position of the particular channel and the effect of the heating power, coming from the coolant channel, on the pressure drop. The coolant channel mass flow rates are shown in Figure 175. The flow distribution is mainly determined by the number of assemblies (relative number of cold and hot assemblies) per stage and the used orifice sizes.

A strong fluctuation is observed in all the presented mass flow rates in the first few seconds as a result of the pump stop, depressurisation and change-over to IC natural circulation. However, the flow rates are quickly stabilised after these actions, start to slowly decrease in the first hour according to the rate of the introduced decay heat and remain practically constant later on.

The time history of the coolant channel void fractions during the transient are shown in Figure 176. An important difference between the RELAP and Apros codes is that they define the void fraction differently for supercritical pressure media. Apros treats the medium as two-phase also in this pressure range and distinguishes water-like and gas-like water regions, between which it models a pseudo-phase change. The interpretation of the void fraction also follows this approach, i.e., a value of 0 for a water-like and 1 for a gas-like medium is provided. In the nominal operating state, the void fraction is therefore 0 in the first two stages, it has a transition along the stages 3-4 and a value of 1 is shown in the upper 5-7 stages.

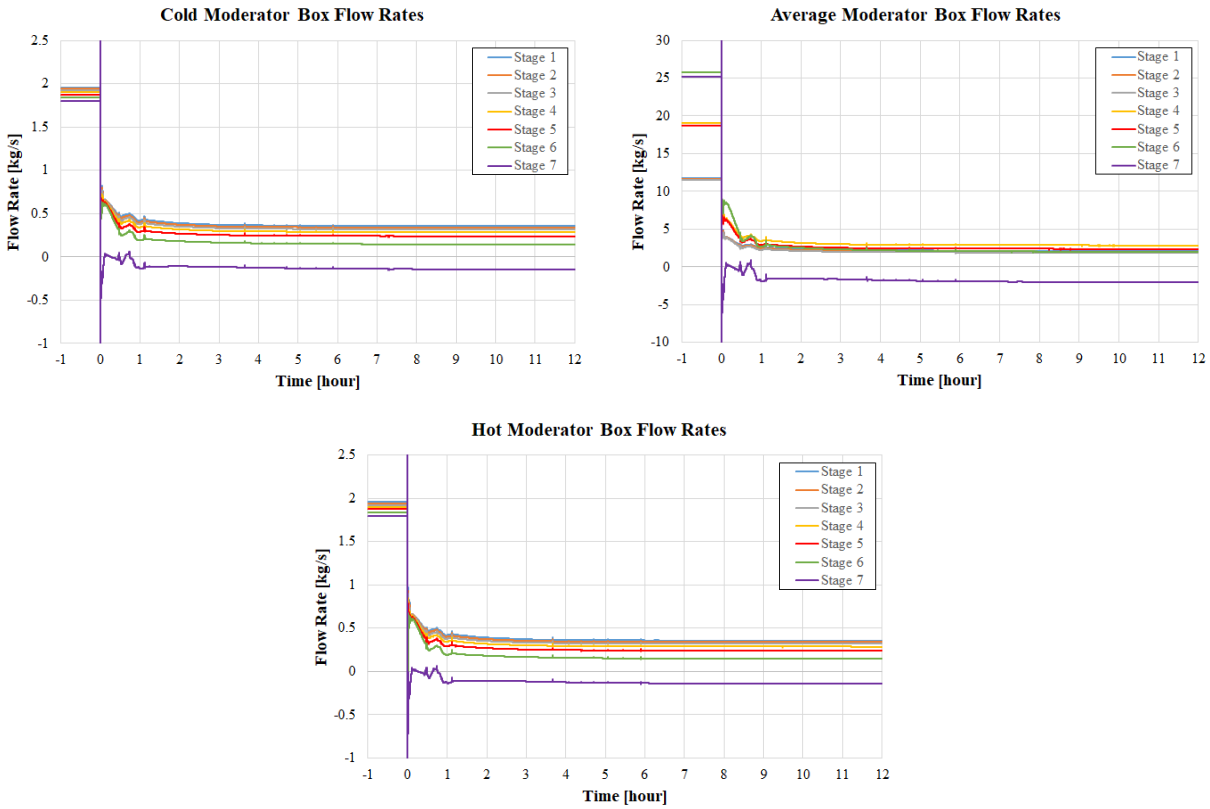

Figure 174: Moderator flows in the boxes

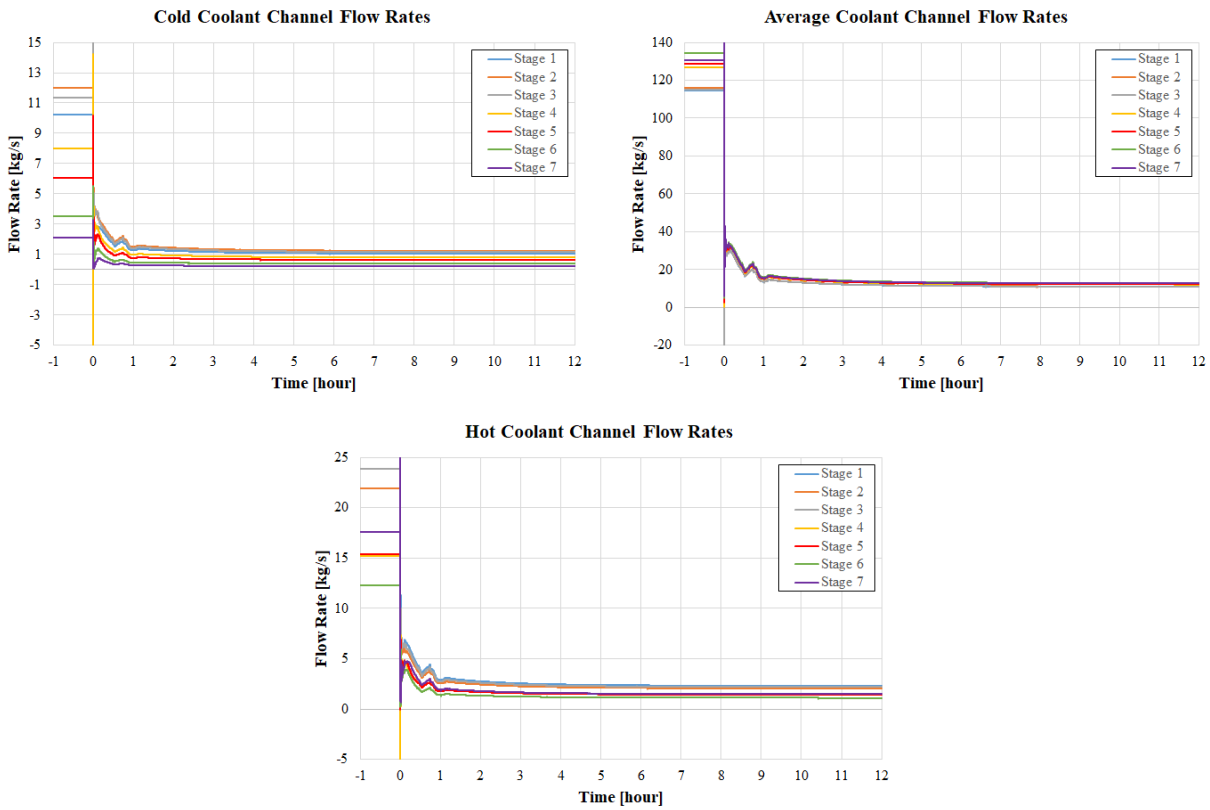

Figure 175: Mass flow rates in the coolant channels

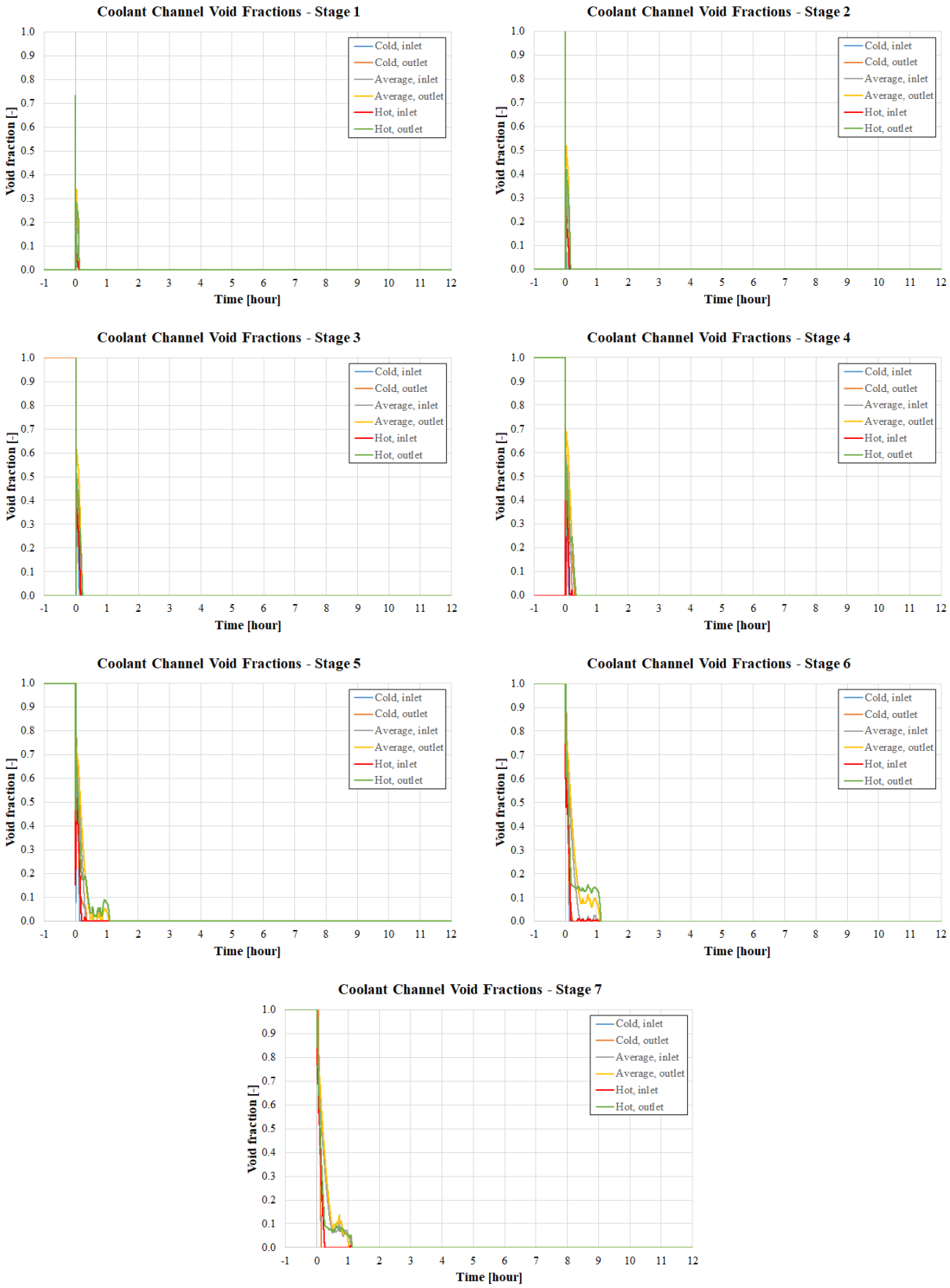

Figure 176: Void fraction in the coolant channels

In contrast, the interpretation used in RELAP gives a void fraction of 0 everywhere when the pressure is supercritical. Consequently, during the transient when the system enters subcritical pressure, a void fraction suddenly appears in RELAP, whereas it is already present in

Apros. Subsequently, both codes show a decrease in the void fraction as a result of the reflooding from the accumulators (see Figure 177) and, after the first hour or so, the core remains completely filled with water. In the accumulator injection, four main stages can be identified (Figure 177, Figure 178):

1) **0.8 – 4 hours**: a stable, high flow rate injection as a result of which the reactor vessel (with the exception of the UP) (Figure 176) and the passive cooling circuit (Figure 179) got completely refilled with water;
2) **4 – 10 hours**: small flow rate, fluctuating injection as the vessel UP starts to be refilled;
3) **10 – 45 hours**: stable, low flow rate injection, as a result of which the reactor vessel UP got completely refilled with water;
4) **45 – 72 hours**: really low flow rate injection to compensate for the temperature reduction and therefore density increase of the water.

At the end of the simulation, the accumulators still have a water level of over 2.3 m each (Figure 178), which means that a total amount of about 17 m^3 of water was injected. The above described behaviour also means that during this event the isolation condensers actually operate like a water-water heat-exchangers rather than condensers (Figure 179).

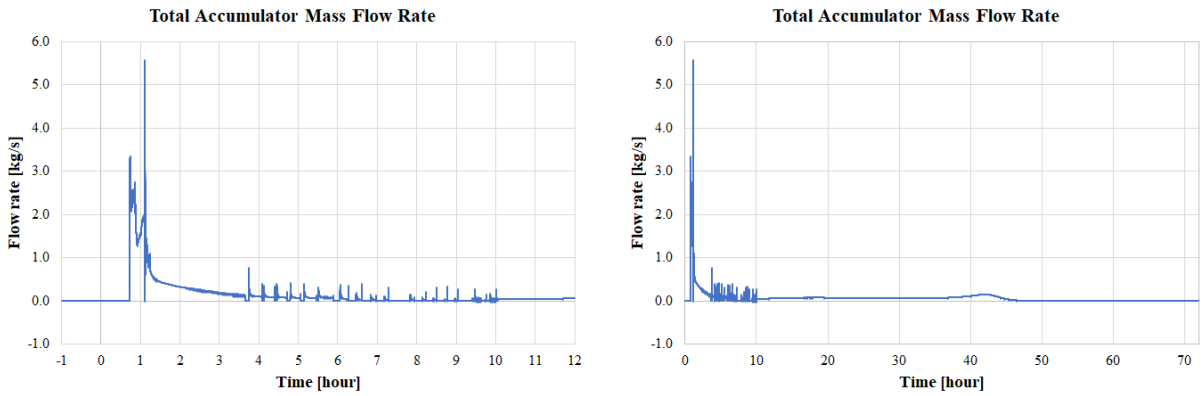

Figure 177: Total mass flow rates of the accumulators

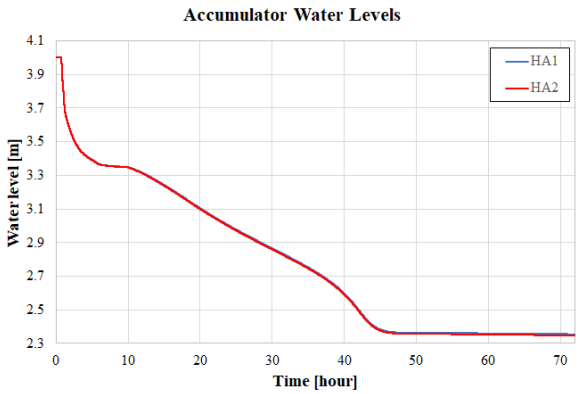

Figure 178: Water level of the accumulators

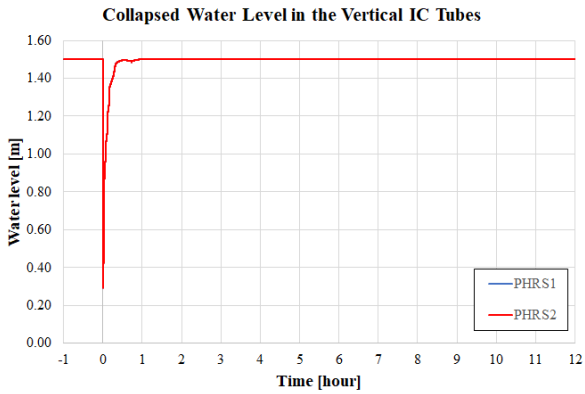

Figure 179: Collapsed water level in the IC tubes

While the accumulators take care of the system refilling, the IC system provides a permanent, passive mode of heat removal. Its mass flow rate (Figure 180), similar to the RPV mass flow rates previously discussed, stabilises rapidly after a short period of fluctuation following the system start-up and then remains practically constant after the first few hours. At the same

time, the remaining heat released in the reactor and the power transferred to the PHRS tanks reach an equilibrium (Figure 181), i.e., this passive safety system is fully able to perform its function.

As in other similar systems already in use, the PHRS tank first heats up (Figure 182) and the water level rises slightly (Figure 183), a process that takes approximately 9.5 hours for the given initial total water volume of 2x300 m^3 (at 30 °C). When the water in the tank reaches the saturation temperature, the boiling process begins and the water level starts to decrease steadily at an almost constant temperature. At the end of the 72 hours, the water level reaches about 2.3 m, i.e. the heat exchangers remain completely covered all the time.

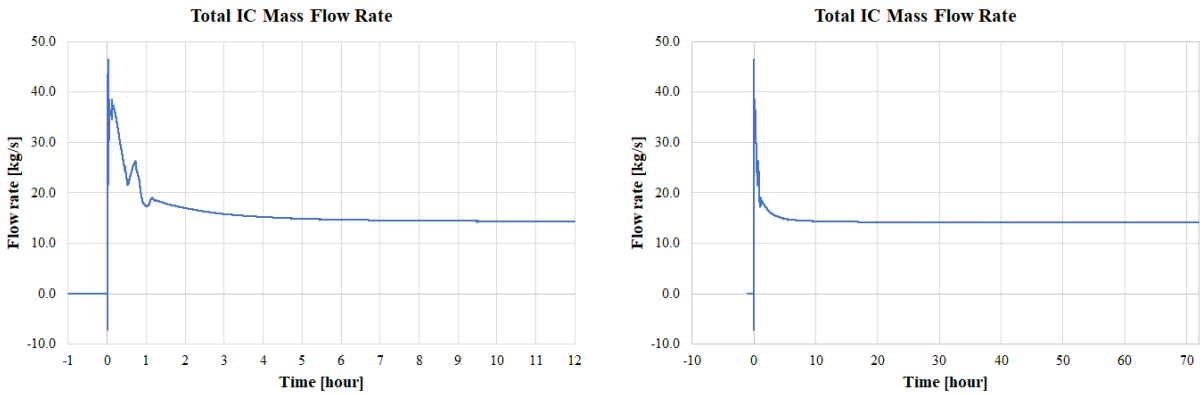

Figure 180: Total mass flow rates of the Isolation Condensers

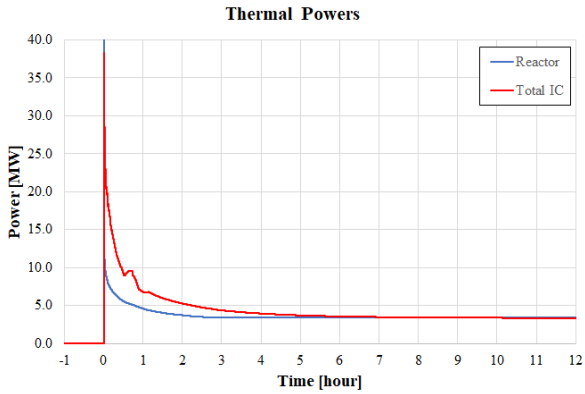

Figure 181: Thermal powers of the reactor and the IC system

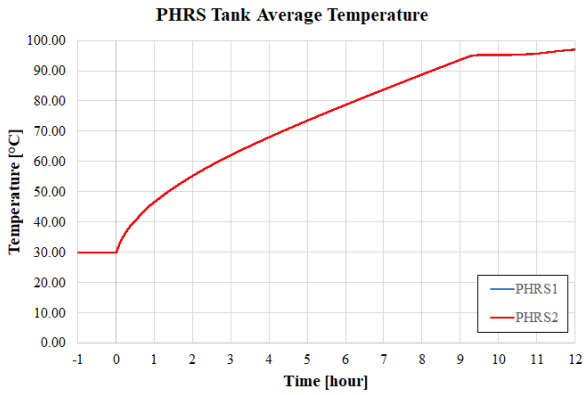

Figure 182: PHRS tank average temperature

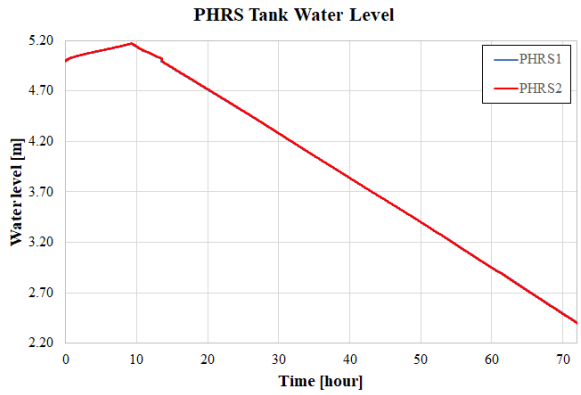

Figure 183: PHRS tank water level

As it can be noted, in Figure 184, Figure 185 and Figure 186, the fluid temperatures in the most important moderator and coolant channel regions steadily decrease with time, which is a sign of a general cooling process. A short, temporary increase of all of these temperatures can only be observed in the very beginning of the transient as a result of the quick stop of the feedwater injection, a difference between the RELAP and Apros model that has already been discussed above. The temperatures have a typical peak height of 10-20 °C, with the exception of the first stage, where it is slightly over 30 °C.

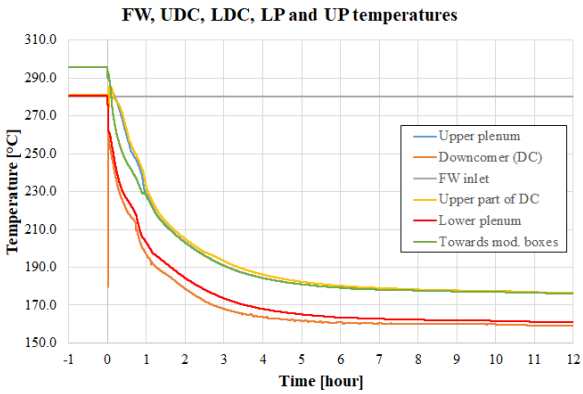

Figure 184: Fluid temperatures at various locations in the vessel

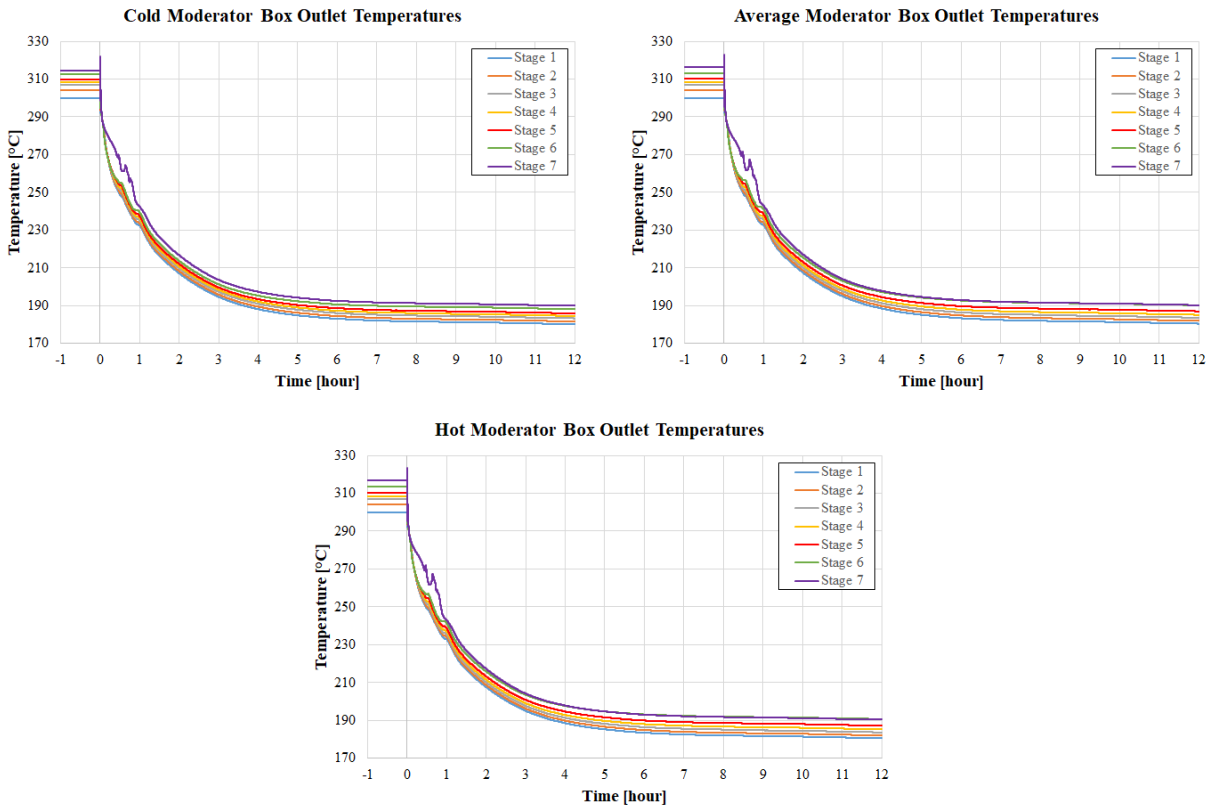

Figure 185: Moderator box fluid temperatures

The cladding temperatures (Figure 187, Figure 188) show similar characteristics, having a short temporary peak of 30-40 °C at the beginning and a continuous cooling later on. Most importantly, the cladding temperatures show no sign of deterioration or dry-out owing to the fast start of the depressurisation blow-down and the level of cooling maintained by the passive system

introduced. After 12 hours the temperatures of the fluid and of the cladding is steadily around 190-200 °C, which is a stable state, however, it is about 80 °C higher compared to the results obtained with RELAP.

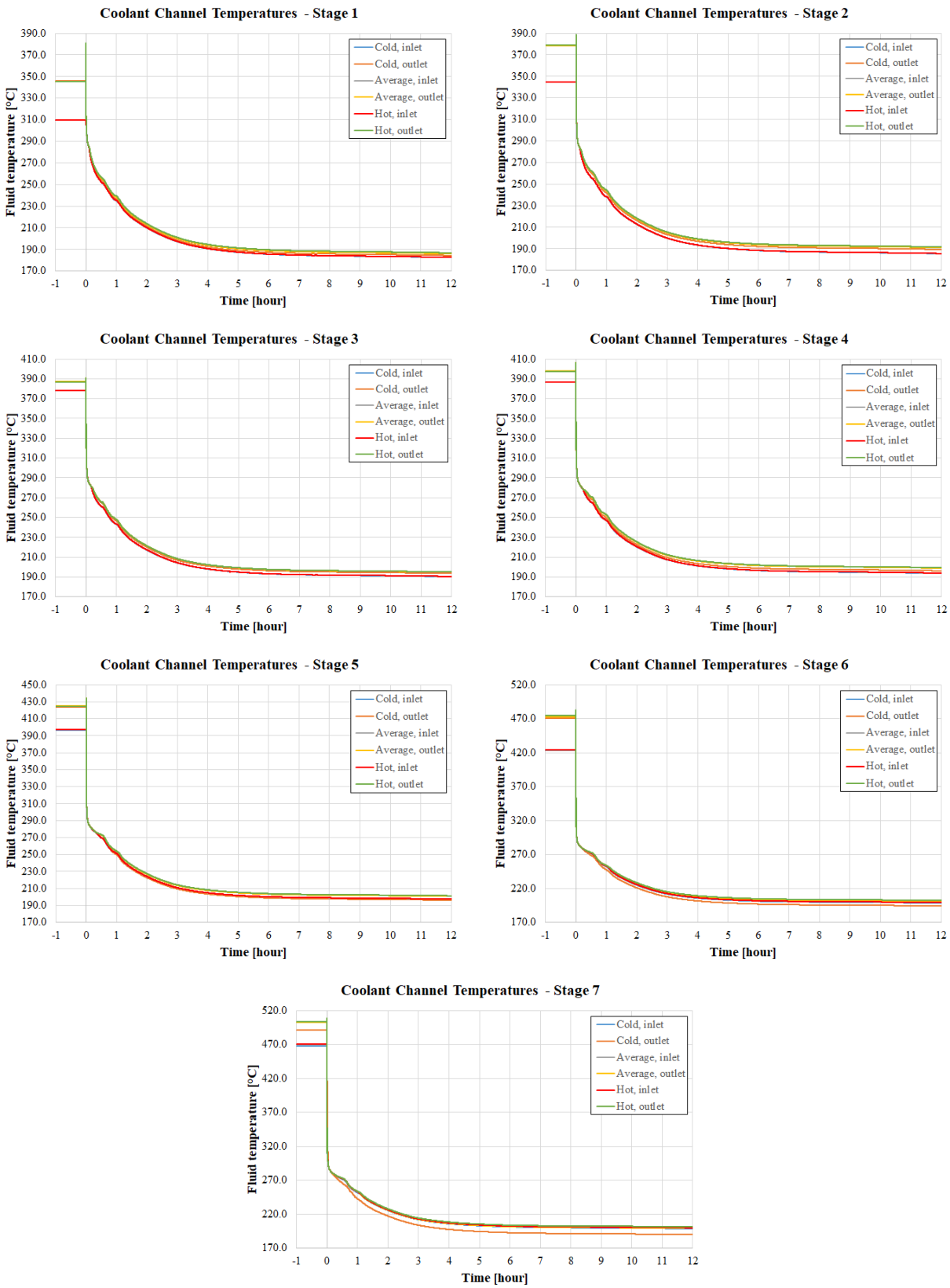

Figure 186: Coolant channel fluid temperatures

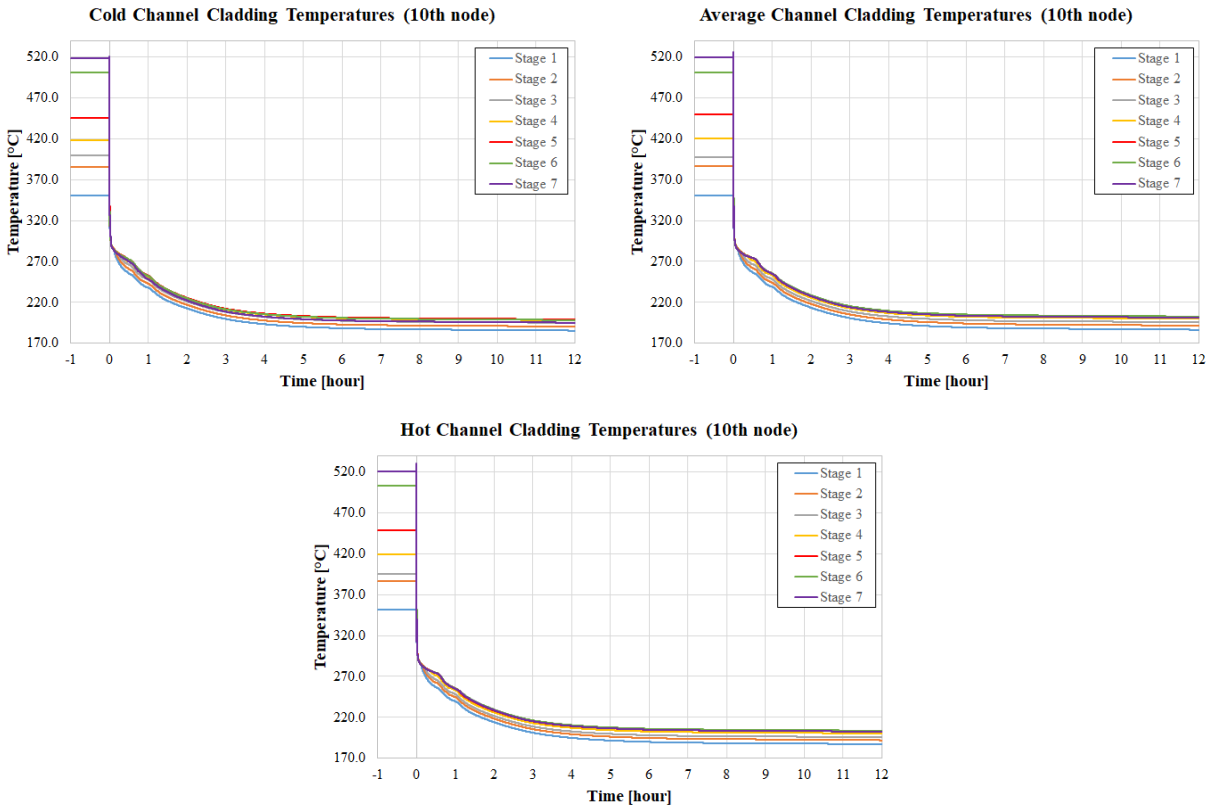

Figure 187: Cladding temperatures

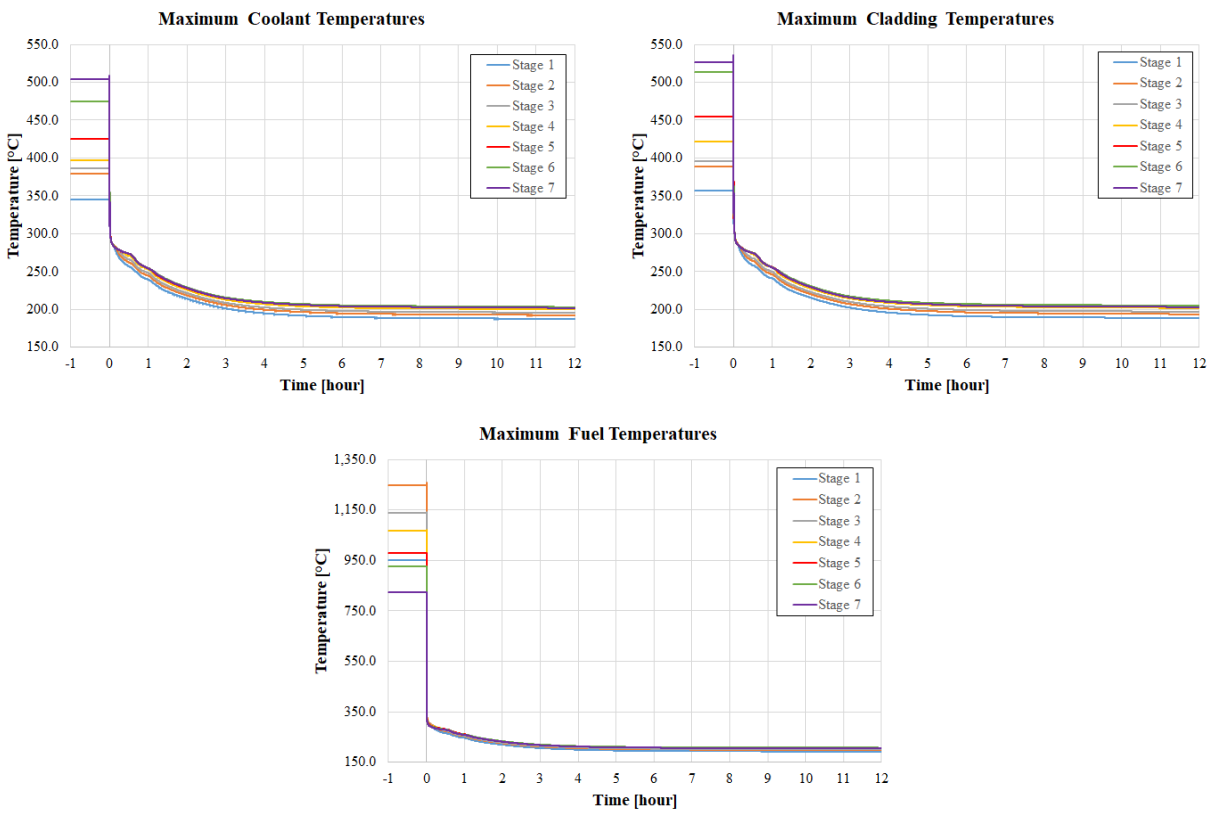

Figure 188: Maximum coolant, cladding and central fuel temperatures of the stages

The main reason for the observed difference is the modelling approach used in case of the isolation condensers. UNIPI assumed a boundary condition of a constant 30 °C temperature and 10,000 W/(m^{2}K) heat transfer coefficient on the IC heat exchangers. In case of Apros, the PHRS pools were modelled, the temperature of which increased up close to 100 °C (Figure 182), and also lower heat transfer coeffients were experienced. The different approches affected not only these temperatures, but the system pressures as well (Figure 171), which also remained higher in Apros. This behaviour will have great importance in other alternative SBO runs presented later.

On the basis of the calculation performed with Apros and presented above, similar final conclusions can be drawn as in chapter 4.5.1 based on the RELAP results. In summary:

- the modelling assumptions and the approximate sizing of the isolation condenser and of the accumulator systems appear to be sufficient to keep the reactor cooled for a long period of time, even exceeding the target grace period;
- within the limitations of the present study, no dangerous levels of cladding temperature is observed during the station black-out transient;
- the discharge of the accumulator tends to keep the reactor full of water, with pressure that decreases very slowly (it is still above 2.6 MPa at the end of the 72 hours);
- during the grace period, there is no need for a gravity driven injection system to intervene, so that it seems, once the on-site and/or off-site powers are recovered, it is possible to bring the reactor to cold shutdown conditions by active means.

Nevertheless, there are motivations for performing further sensitivity analyses, partly following the approches of UNIPI (see at the end of chapter 4.5.1), but adding some further cases as follows:

- Lowering the IC elevation;
- Excluding the accumulators from the simulation;
- Combining the previous two approaches;
- Using the original design concept without the inlet orifices (see chapter 5.3.2);
- Reducing the initial system pressure (see chapter 5.3.8.3);
- Using the Mokry HT correlation instead of Bishop (see chapter 5.3.8.5);
- Using the UO2 fuel map instead of the MOX one (see chapter 5.3.6).

The most important results and characteristics of the above sensitivity analyses are summarised in the following subchapters.

5.4.2 Lowered IC units

The only difference in the assumed plant configuration adopted for this calculation with respect to the Base case was the lowering of the IC units by 6.5 m, a length that was subtracted to both the rising and the return piping. The elevation of the PHRS pools was also accordingly reduced. This analysis follows the considerations of UNIPI and their RELAP analysis presented in chapter 4.5.2.

Figure 189 shows the differences obtained in the two cases for the IC flow rates. As it can be noted, the IC flow rate is correspondingly lower in the lower IC case, as a consequence of the reduced driving force developed by the fluid. This reduction is expectedly depending on the interplay between the smaller buoyancy force and the smaller friction along the riser and return pipes. Furthermore, the start-up of the system shows a stronger fluctuation and it requires a longer period of time to stabilise the natural circulation.

The behaviour of flows in the natural circulation flow paths is similar, as shown by Figure 191 and Figure 192. The inversion of flows in the moderator boxes at the 7th stage and the deviation of the flow rates in the other stages appears enhanced, probably due to higher temperature differences and then buoyancy forces driving the involved natural circulation flow paths. The flow rates in the moderator boxes and coolant channels are slightly reduced and have a stronger initial fluctuation just like in the whole natural circulation path.

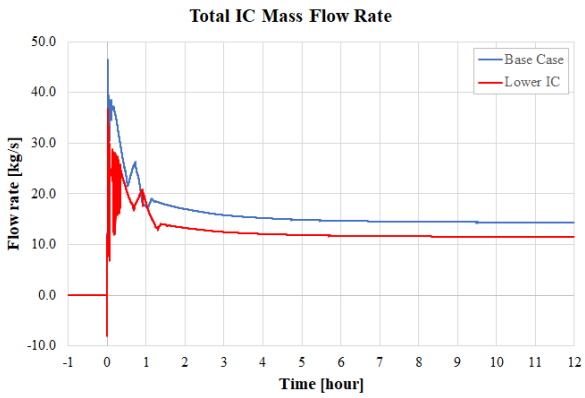

Figure 189: Total mass flow rates of the Isolation Condensers

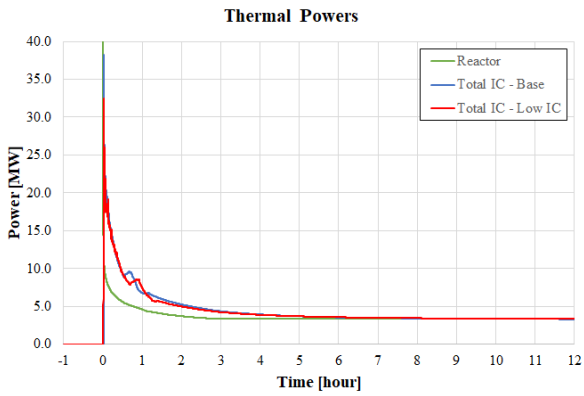

Figure 190: Thermal powers of the reactor and the IC system

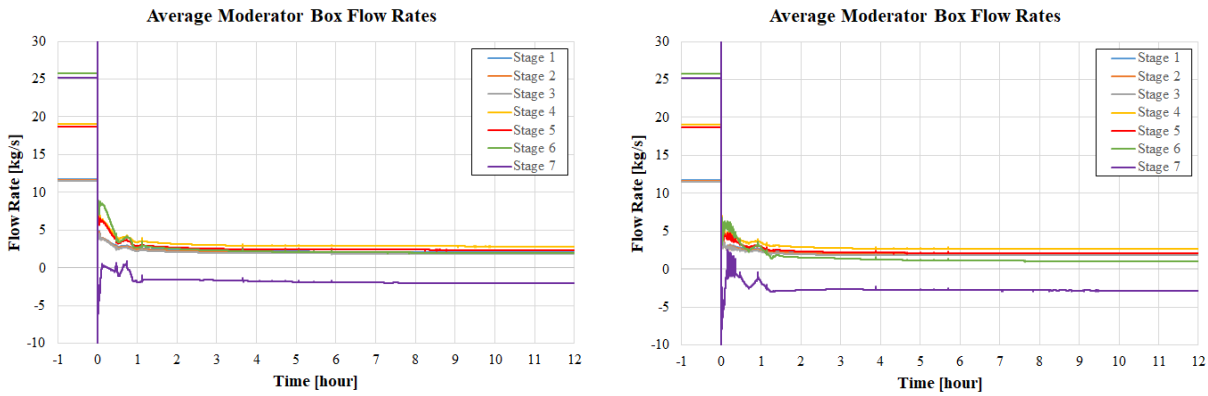

Figure 191: Moderator flows in the average boxes (Left – Base Case; Right – Lower IC)

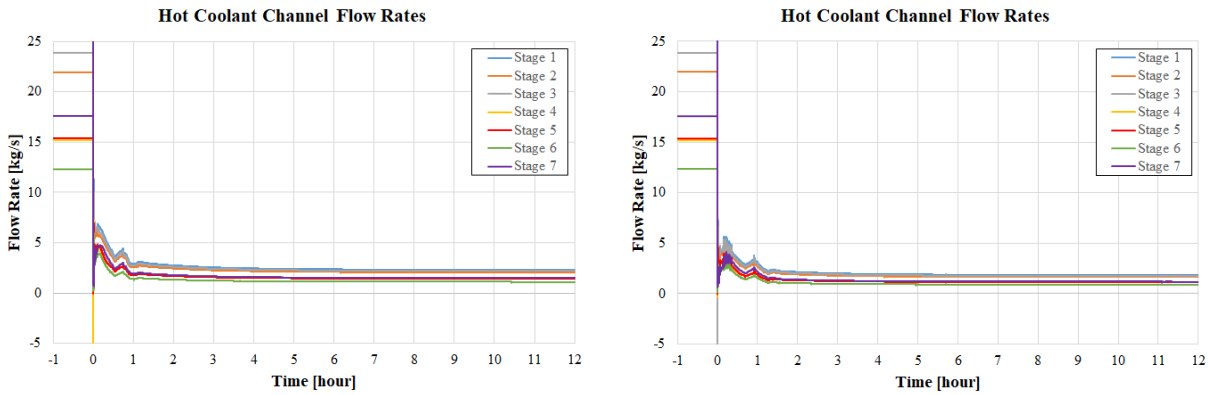

Figure 192: Mass flow rates in the hot coolant channels (Left – Base Case; Right – Lower IC)

As a consequence of the lower mass flow rates, the fluid, cladding and fuel temperatures are slightly higher (Figure 194), but the passive safety system is still able to provide adequate

cooling, as no signs of heat transfer deterioration or fuel dry-out are observed. This is also supported by the fact that the power released in the reactor and the power delivered to the PHRS pools reach equilibrium in a similar manner and at a similar rate (Figure 190).

The higher temperatures and slower cooling result in higher system pressures, therefore, the accumulator injection starts later and at a lower mass flow rate (Figure 193). Reflooding of the core is also delayed by about half an hour and preceded by a higher void fraction state (see Figure 195), but as it was noted, the heat removal is ensured by the two-phase flow.

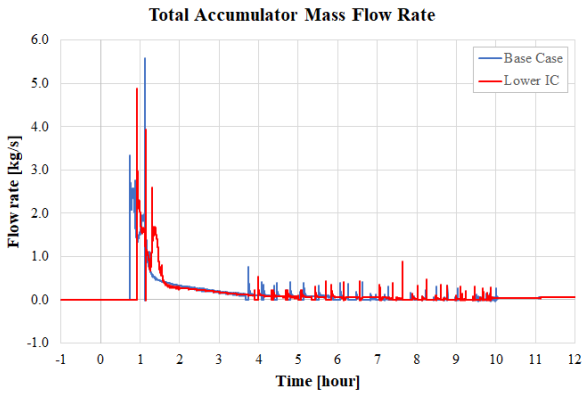

Figure 193: Total mass flow rates of the accumulators

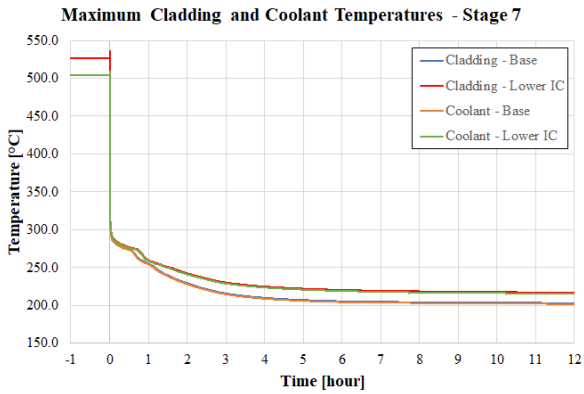

Figure 194: Maximum cladding and coolant temperatures at stage 7

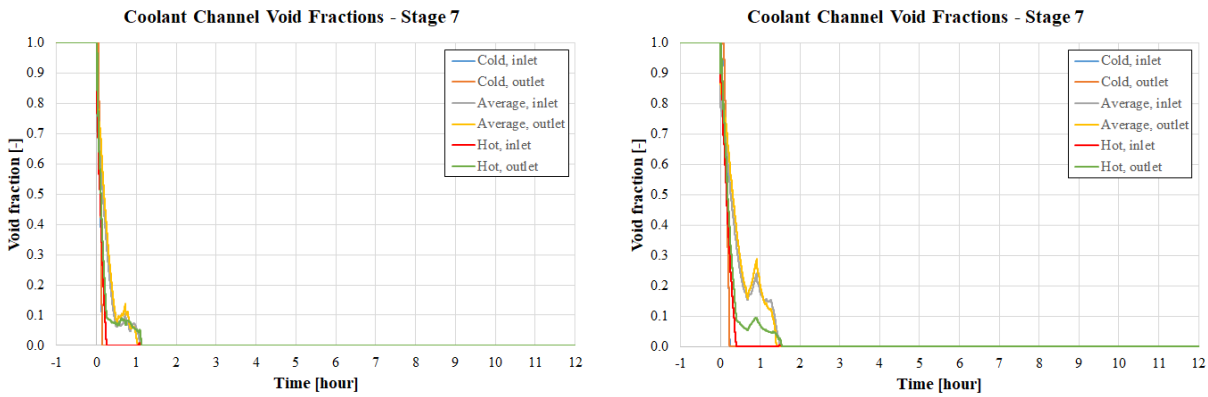

Figure 195: Void fraction in the 7th stage coolant channels
(Left - Base Case; Right - Lower IC)

All the above observations are in good accordance with those of the RELAP analysis. In summary, the lowering of the IC unit in height changes the observed transient behaviour quantitatively in a somehow expected way, without introducing qualitative changes in the observed phenomena. The residual mass of water in the accumulator system and in the PHRS pools at the end of the investigated 12 hours is sufficiently large and the residual discharge flow rate is sufficiently low to suggest that the presented scenario will remain qualitatively unchanged during the depressurization of the system for a sufficiently long grace period.

5.4.3 Sequence without the accumulator system

Similarly to the approach of UNIPI (as presented in chapter 4.5.4), this transient was run for assessing the consequences of the introduction of the accumulator system discharge in the sequence of events, more than to postulate a possible failure to activate such a well-assessed

passive system. In previous analyses, in fact, it was noted that the final level of pressure in the coolant system is mainly driven by the partial discharge of the accumulators (and the provided rate of heat removal in the ICs), filling with liquid all the vessel and thus becoming a sort of gas filled pressuriser for the rest of the transient. In the Base calculation case, in particular at the end of the considered 72 hours of transient, the pressure is still above 2.6 MPa (above 3.5 MPa at 12 hours), mainly due to the pressurization action of nitrogen in the accumulators. While this situation does not represent a real problem for a system to be designed for probably a maximum pressure equal to or exceeding 30 MPa, depressurising further the system would need to exclude the accumulator and possibly opening again a depressurisation valve, something that could be made also manually after a so long transient as a final provision to bring the reactor in depressurized and relatively cold conditions.

So, the scenario presented here differs from that of the Base calculation case for the absence of the accumulator system. In the RELAP calculation (in chapter 4.5.4), a Gravity Driven Coolant injection System (GDCS) was introduced with two liquid pools of 600 m^3 each, placed at an elevation of 3 m above the legs of the reactor and kept at a pressure of 0.12 MPa to account for a mild containment pressurisation. In case of Apros, the primary system pressure remains much higher mainly because of the differences in the modelling of the Isolation Condensers, as already discussed for the Base case in chapter 5.4.1. This is also true in this case where the accumulators are not available, therefore the pressure in the Apros calculation remains far too high to allow injection from such a gravity driven system (GDCS). For this reason, the GDCS was not even modelled in Apros and the initial event was simulated with a complete absence of injection.

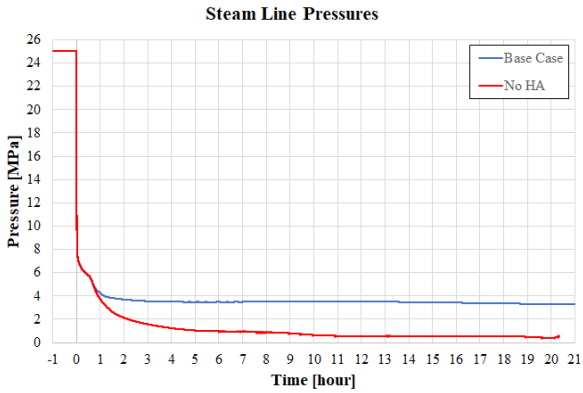

Figure 196: Steam line pressures

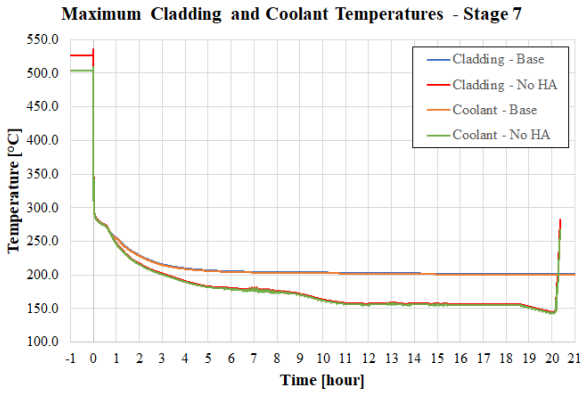

Figure 197: Maximum cladding and coolant temperatures at stage 7

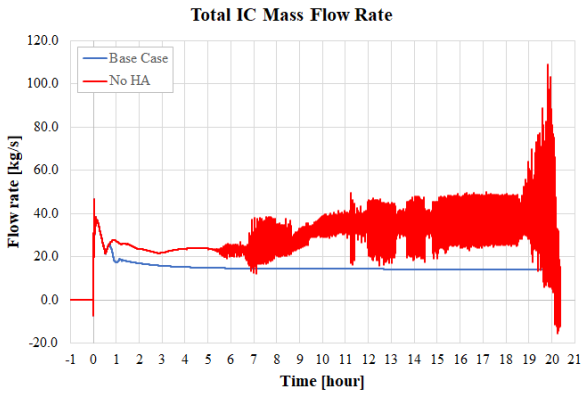

Figure 198 Total mass flow rates of the Isolation Condensers

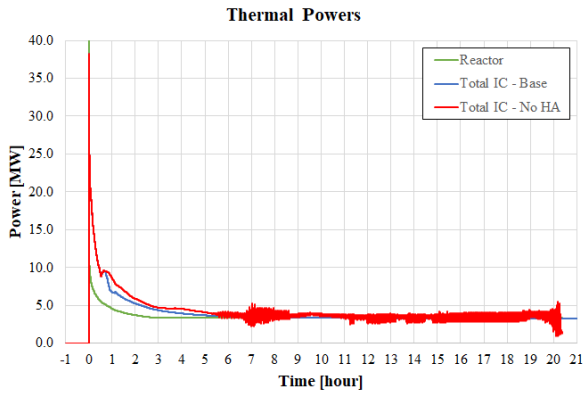

Figure 199 Thermal powers of the reactor and the IC system

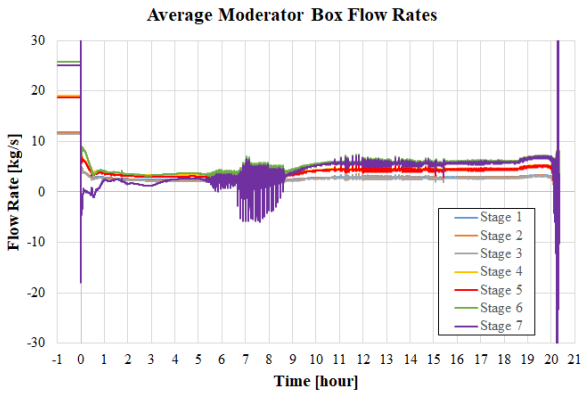

Figure 200: Moderator flows in the average boxes

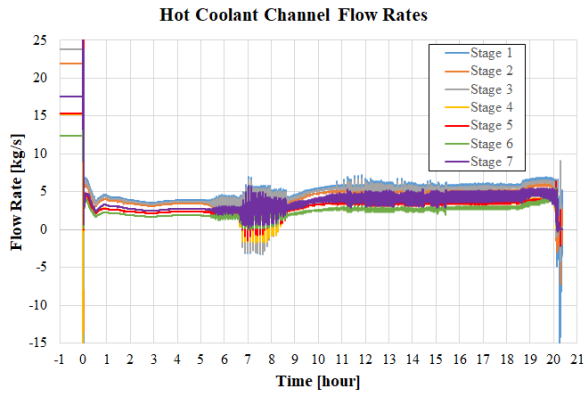

Figure 201: Mass flow rates in the hot coolant channels

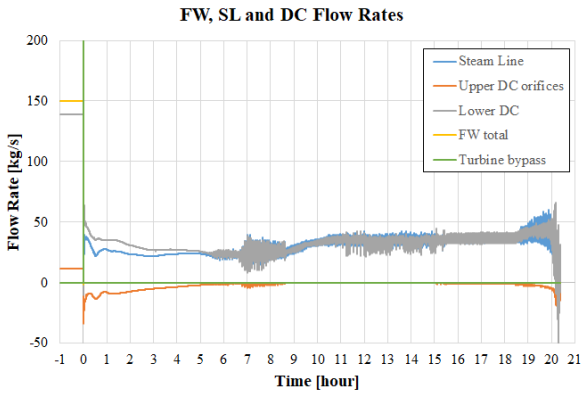

Figure 202: Flow rates at various locations of the primary system

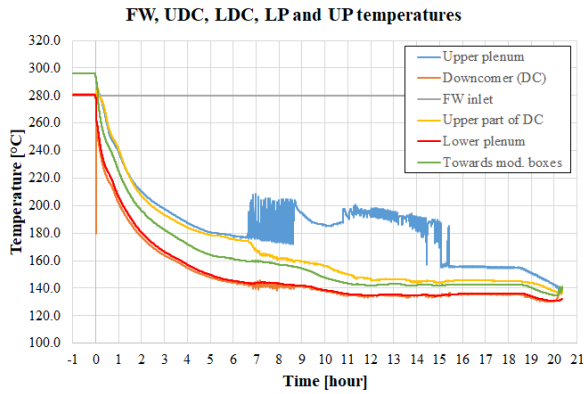

Figure 203: Main fluid temperatures in vessel

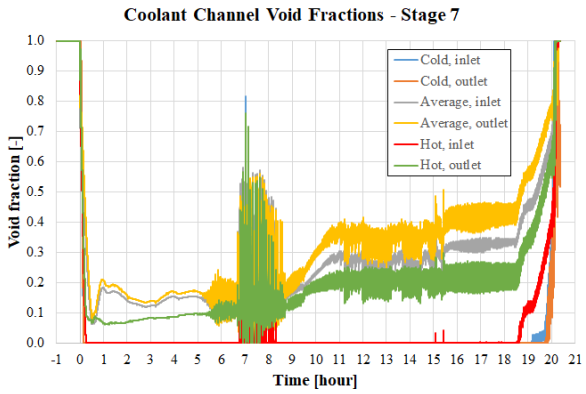

Figure 204: Void fraction in the 7th stage coolant channels

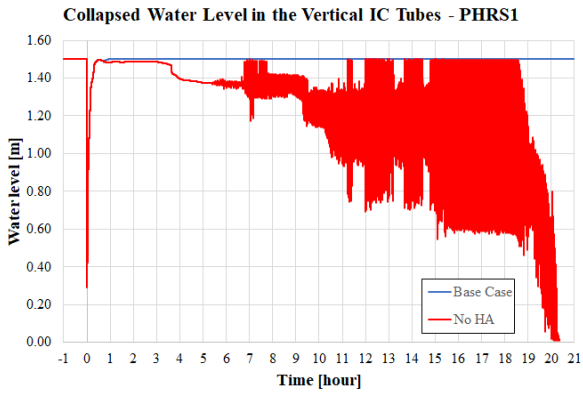

Figure 205: Collapsed water level in the IC tubes

In contrast to what has been observed so far, this scenario shows significant qualitative differences in Apros compared to RELAP, mainly due to the different IC heat removal assumptions and the complete absence of injection in Apros as already noted.

Figure 196 shows the evolution of the steam line pressure. It can be noted that, in the absence of the accumulator, pressure reaches much lower levels, but it still remains above 0.5 MPa after 20 hours preventing any GDCS injection. The IC and RPV flow rates (Figure 198, Figure 200, Figure 201, Figure 202) have actually an initial behaviour similar to that of the Base case, but with slightly higher stabilised rates after the first hour. This is caused by the continuous presence of voiding in the higher locations of the natural circulation loop (Figure 204, Figure 205), in the lack of injection and thus the higher buoyancy forces developed in the IC pipelines, which drive the flow. Due to the higher mass flow rate and presence of steam condensation in the ICs, their power is also higher (Figure 199), resulting in a faster cooling of the system (Figure 197, Figure 203).

After about 6 hours, when the vessel UP starts to get completely emptied and therefore the DC orifices are getting uncovered (see orange curve in Figure 202), a similar phase of huge oscillations starts like in RELAP, but the amplitude of the studied parameters remains smaller. This behaviour probably has a mixed physical and numerical origin. The strong oscillation phase stops after about 9 hours, when the uncovering of the DC orifices is completed, but the mass flow rates, the void fractions (Figure 204) and the IC collapsed level (Figure 205) remain subject to further, smaller oscillations in the absence of safety injection.

In the period of 9 - 18.5 hours, the system seems to operate in a relatively stable state, with the exception of the IC pipelines, where an even stronger oscillation than before can be observed approx. starting after 11 hours (Figure 198, Figure 205). Adequate heat removal is still provided, but such strong and permanent oscillations may compromise the integrity of the system.

From 18.5 hours onwards, the water level in the IC tubes can no longer be maintained, and is starts to steadily decrease (Figure 205), while the void fraction in the core is also rising (Figure 204). At the same time, the mass flow oscillations are amplified again (Figure 198) and the IC power decreases (Figure 199). After about 20 hours, the IC tubes are completely drained, the dissipated power drops significantly and the upper part of the core starts to dry out (Figure 197). The simulation was stopped at this point, because this process can not be avoided in the absence of safety injection.

In summary, with the consideration of the PHRS pool temperature rise and with the lower IC heat transfer coefficient modelled in Apros, the passive system is not able to reduce the pressure to the extent that a gravity-driven injection system could perform its role, and without

this, it cannot provide sufficient heat removal after a certain time (being about 20 hours based on the calculations), so that the core may become uncovered and dry out. However, it is important to emphasise the following:

- for the above result, a complete failure of the passive accumulator system had to be assumed for more than 20 hours;
- no other way of injection was assumed either for 20 hours;
- the proposed IC sizing is preliminary: upscaling could extend this time period or even prevent the core from drying out, but further studies are needed to verify this speculation.

5.4.4 Sequence without the accumulator system and with lowered IC units

Although the previous case already showed a core dry-out after about 20 hours, a further, more serious variant was also studied, as by UNIPI in chapter 4.5.5, where the absence of the accumulators is combined with the lower IC elevation. The main objective of this analysis was to investigate the effect of the lower IC, and therefore lower driving force, on the time available until the dry-out, and the preceding processes.

As can be seen in Figure 207, in this case the dry-out starts after less than 8 hours, i.e. the natural circulation and thus the heat removal can be maintained for a much shorter time. The processes are very similar in the first 2 hours (see Figure 206 - Figure 211), but the oscillation phase shows more significant differences. It starts much earlier (2.5 hours instead of 6 hours), and the trend of the behaviour is also different (Figure 208). The oscillation is similarly weak at the beginning (2-4 hours), but then it starts to become stronger and stronger, as if skipping the states observed in the previous case between 7-18.5 hours. Meanwhile, the water level of the IC tubes is continuously decreasing (Figure 211), while also strongly oscillating, until it empties completely at about 7.5 hours. As a result, the flow slows down considerably leading to dry-out in a short time.

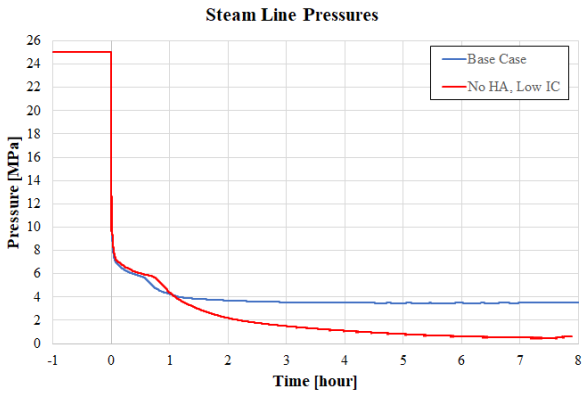

Figure 206: Steam line pressures

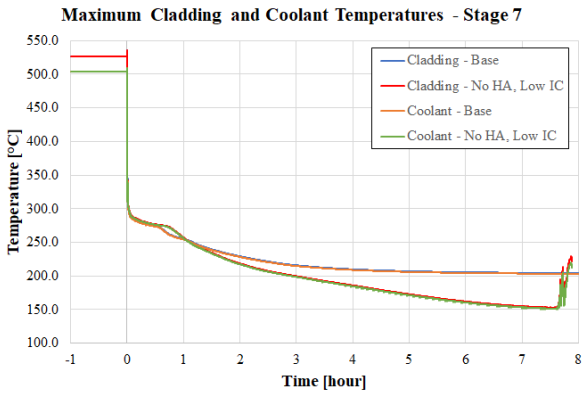

Figure 207: Maximum cladding and coolant temperatures at stage 7

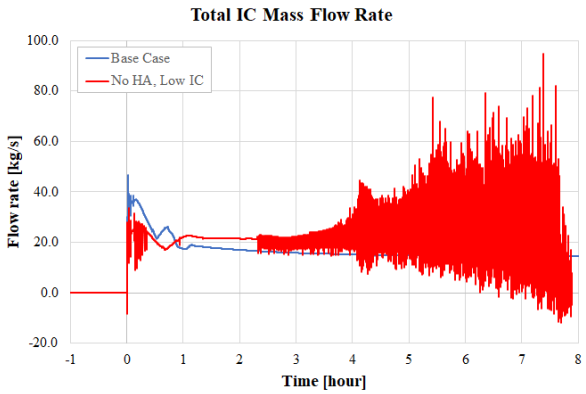

Figure 208: Total mass flow rates of the Isolation Condensers

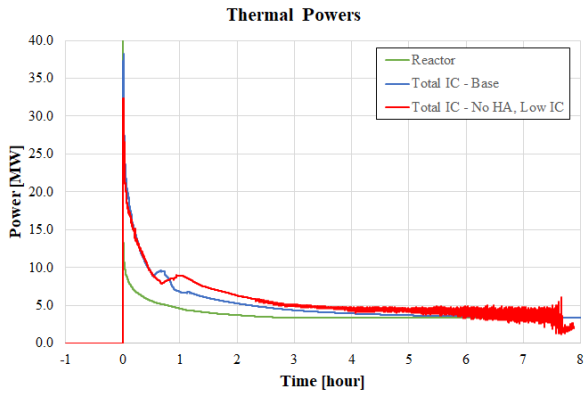

Figure 209: Thermal powers of the reactor and the IC system

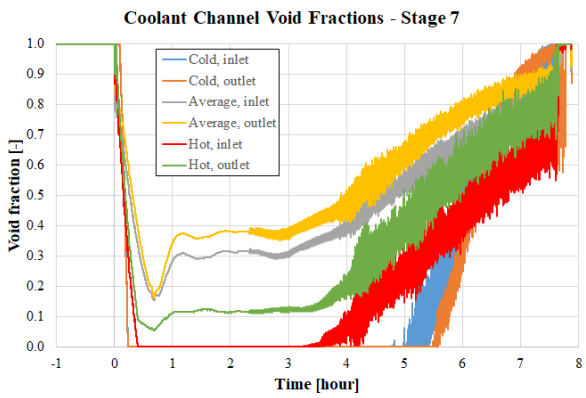

Figure 210: Void fraction in the 7th stage coolant channels

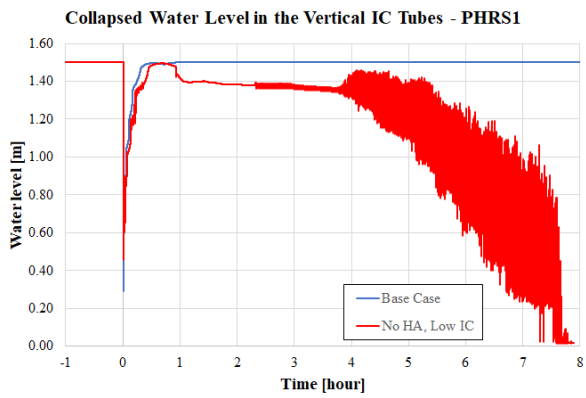

Figure 211: Collapsed water level in the IC tubes

5.4.5 Effect of the operating pressure

The previous SBO analyses have been conducted imposing a pressure of 25 MPa at the RPV outlet. This indeed results in a higher pressure in the reactor, also depending on the core pressure drops providing an additional burden for the reactor vessel design. The effects of the pressure on the steady-state has already been investigated as part of the sensitivity analysis presented in chapter 5.3.8.3, while the effect of the lowered nominal pressure on the transient behaviour is studied here.

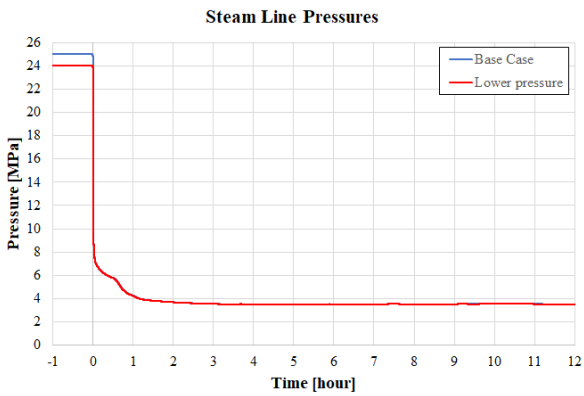

Figure 212: Steam line pressures

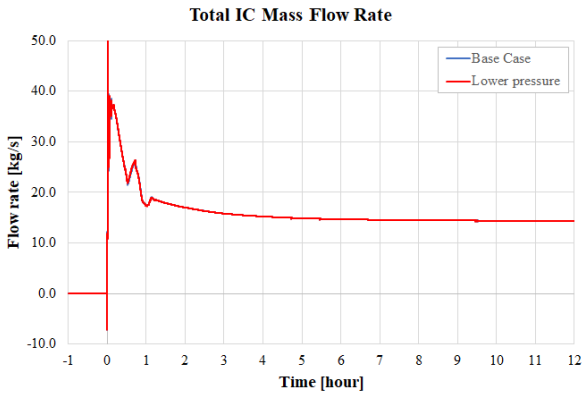

Figure 213: Total mass flow rates of the Isolation Condensers

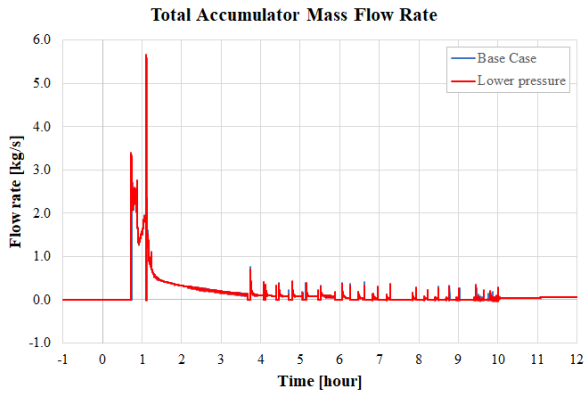

Figure 214: Total mass flow rates of the accumulators

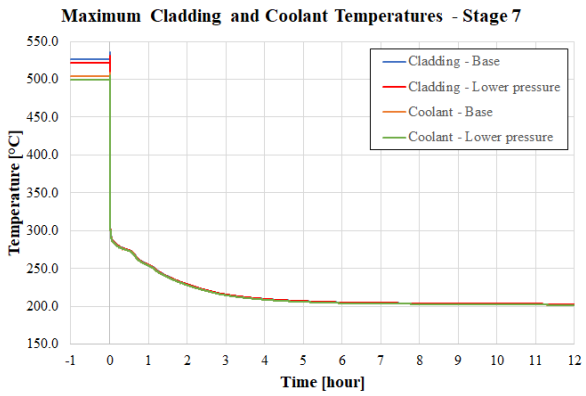

Figure 215: Maximum cladding and coolant temperatures at stage 7

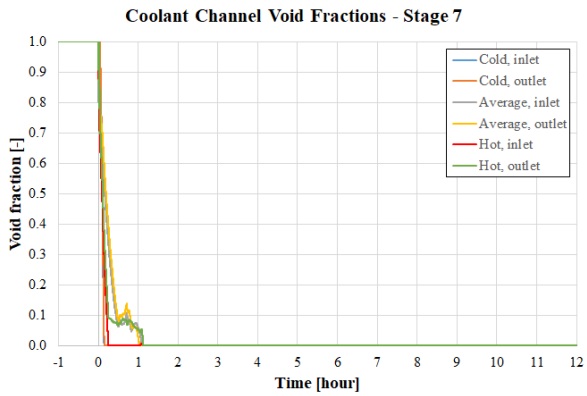

Figure 216: Void fraction in the 7th stage coolant channels

The initial differences in the system pressure (Figure 212) and temperatures (Figure 215) quickly disappear during the controlled depressurisation phase and the transient phenomena later show negligible differences (see Figure 212 - Figure 216), since the long term SBO mostly encompasses conditions at subcritical pressures that are weakly influenced by the difference in the initial steady-state conditions. In summary, it can be assumed that the previous conclusions of the Base case also apply to the present one.

5.4.6 Effect of the orifices

In the steady-state analyses, the use of inhomogeneous inlet orifices proved to be a successful method for reducing the cladding temperatures, and the model version with this feature (see chapter 5.3.3) was selected as the Base model for the SBO transient studies. As seen so far, despite the increased core pressure drop due to the orifices, the natural circulation can be quickly and stably established and the removal of the decay heat is ensured if reflooding of the RPV from the accumulators (or other sources) is feasible. However, the orifice sizes used there are not yet universally optimised and will certainly change as the design evolvs. For this reason, it is important to investigate the effect of the orifices on the transient behaviour; so, the SBO analysis was repeated with the model version implementing the original design (see chapter 5.3.2) without orifices.

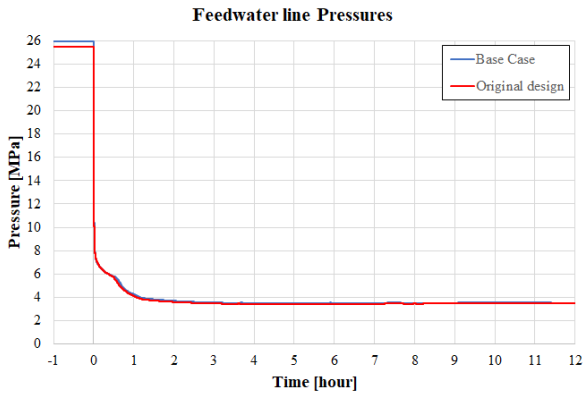

Figure 217: Feddwater line pressures

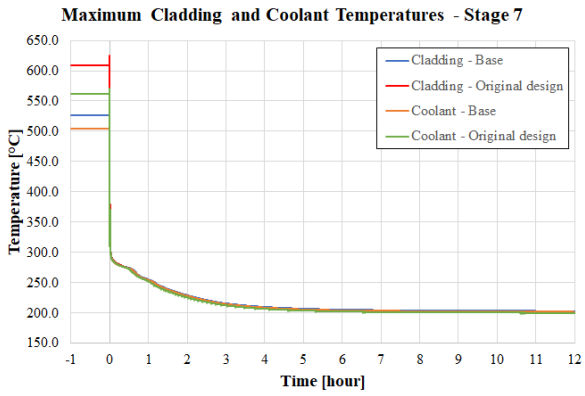

Figure 218: Maximum cladding and coolant temperatures at stage 7

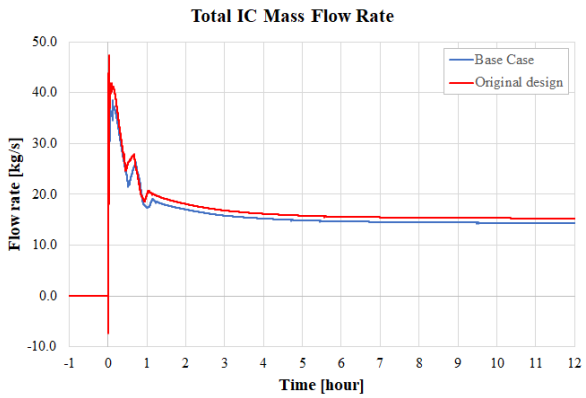

Figure 219: Total mass flow rates of the Isolation Condensers

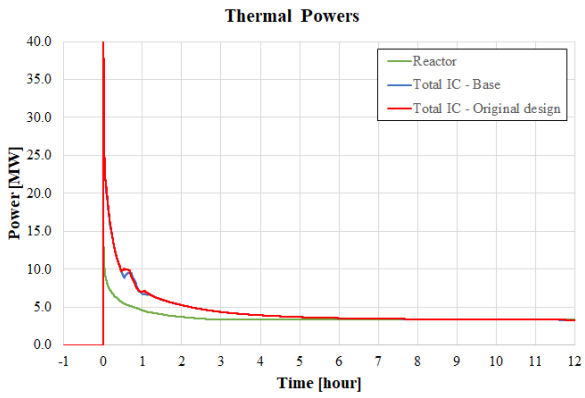

Figure 220: Thermal powers of the reactor and the IC system

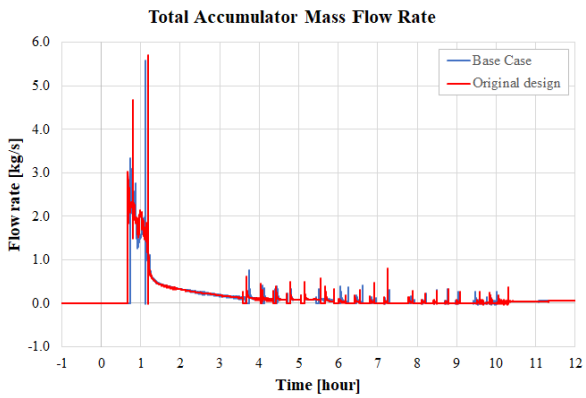

Figure 221: Total mass flow rates of the accumulators

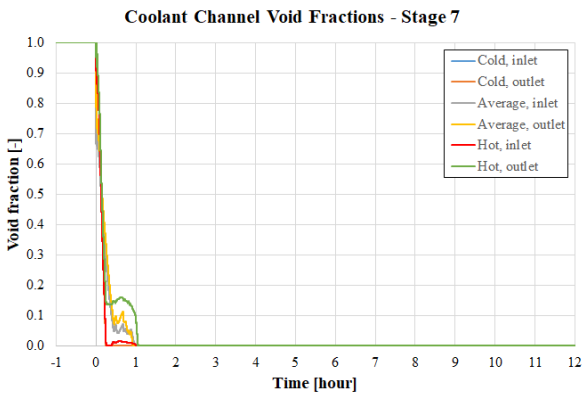

Figure 222: Void fraction in the 7th stage coolant channels

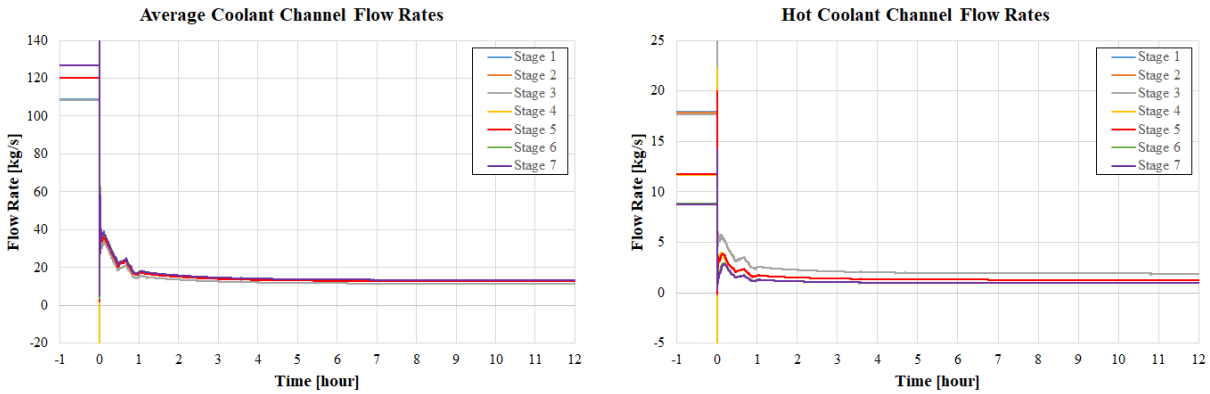

Figure 223: Mass flow rates in the coolant channels

The most significant differences in the results are observed in the initial state, and as the hot channel cladding temperatures are much higher in the original design, the initial transient peak is also higher (Figure 218). There are only minor differences in the main transient processes (see Figure 217 - Figure 223). Due to the higher stored heat and the lower mass flow rate in the hot channel compared to the Base case, its void fraction remains higher in the first hour (Figure 222), but no HT deterioration or core dry-out is seen. Of course, due to the lower pressure drop across the core, a slightly higher mass flow can develop (Figure 219), but the power dissipated (Figure 220) and hence the trend of cooling (Figure 218) and system pressure (Figure 217) are similar. Finally, due to the homogeneous inlet flow areas of the assemblies, the mass flow rates (Figure 223) are less scattered and the visible differences in the curves are practically only due to the difference in the total number of assemblies per stage (see Table 4).

5.4.7 Effect of the heat transfer correlation

The Mokry correlation was found to be the most conservative, among the correlations available in Apros in the benchmarking performed previously (see Deliverable D3.2) and also in the sensitivity analysis (chapter 5.3.8.5) of the steady-state. Therefore, the SBO transient has also been repeated using the Mokry correlation instead of the Bishop.

As can be seen, this has practically no effect on the transient phenomena (Figure 224 - Figure 227) similar to the case with a reduced initial pressure (chapter 5.4.5), and only slightly shifts the nominal cladding (Figure 226) and fuel temperatures, and their peaks at the very beginning of the transient. However, these differences are almost negligible, and there is no sign of heat transfer deterioration or core dry-out.

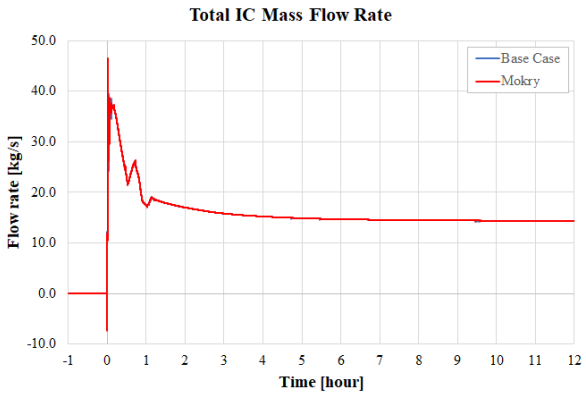

Figure 224: Total mass flow rates of the Isolation Condensers

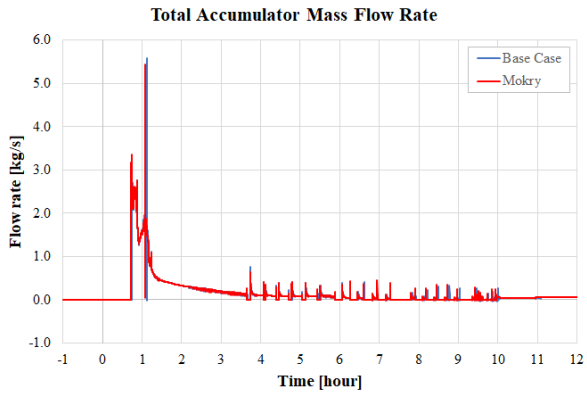

Figure 225: Total mass flow rates of the accumulators

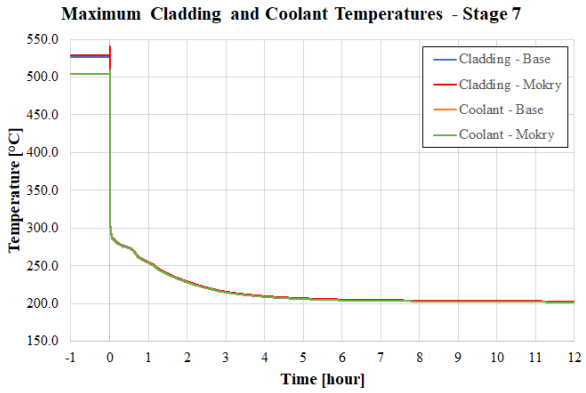

Figure 226: Maximum cladding and coolant temperatures at stage 7

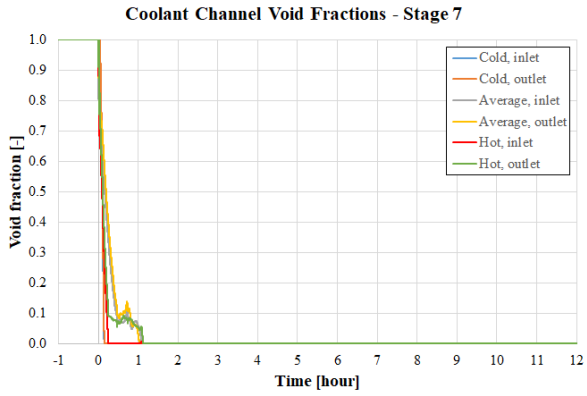

Figure 227: Void fraction in the 7th stage coolant channels

5.4.8 Effect of the loading map

All the previous SBO analyses have been conducted using the MOX core loading map (Figure 109), but another map with UO_2 fuel only has also been developed, the steady-state of which is investigated in chapters 5.3.5, 5.3.6 and 5.3.7. The transient behaviour of the model version with optimised orifices, original core layout and UO_2 map (see chapter 5.3.6) is studied here.

As in the cases with reduced pressure (chapter 5.4.5) and with the Mokry heat transfer correlation (chapter 5.4.7), the differences are practically negligible (see Figure 228 - Figure 231), while the initial temperatures (Figure 230) and hence their early peak are slightly shifted. Here, however, the void fraction remain a bit higher in the first hour (Figure 231), probably due to the different power profiles and orifices sizes (see Figure 170). Core cooling and the main processes are minimally affected by these differences.

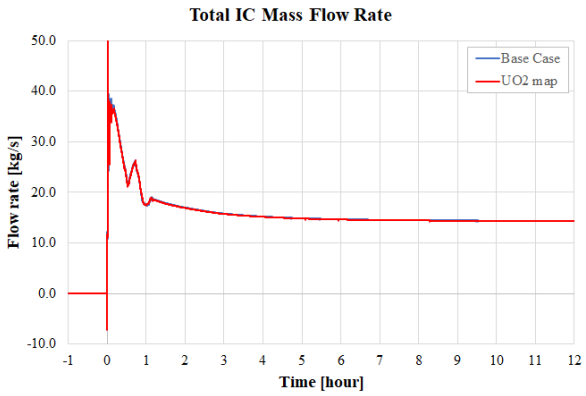

Figure 228: Total mass flow rates of the Isolation Condensers

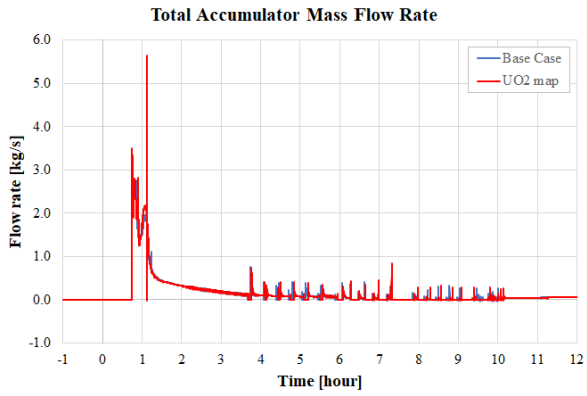

Figure 229: Total mass flow rates of the accumulators

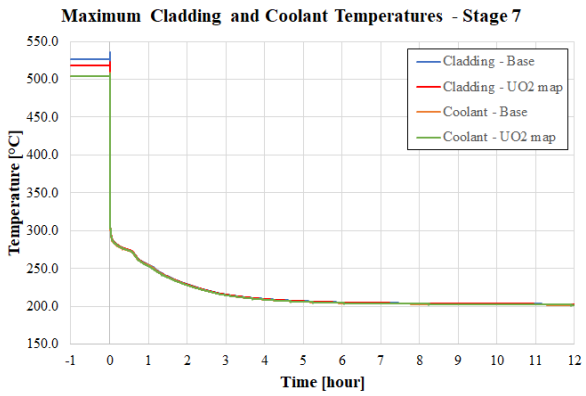

Figure 230: Maximum cladding and coolant temperatures at stage 7

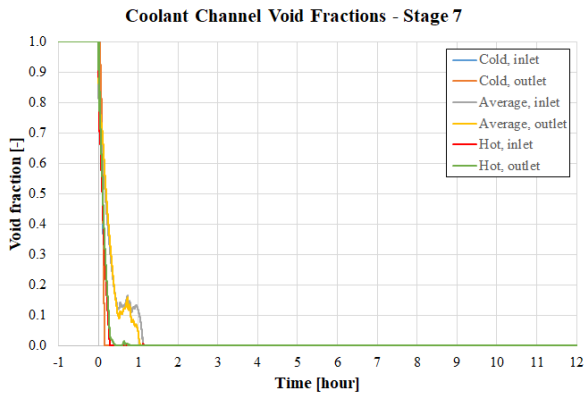

Figure 231: Void fraction in the 7th stage coolant channels

5.5 Steady-state calculations with the Apros – SPNDYN code system

This section is based on a MSc thesis project (Bertesina et al., 2023) and the conference paper prepared and submitted for the ISSCWR-11 symposium (Varju et al., 2024). In the research presented here, SPNDYN, an in-house reactor physics code developed at BME NTI (Babcsány, 2021), was coupled to Apros and used to simulate the reactor physics and thermal-hydraulics equilibrium state of the SCW-SMR core. For this purpose, the steady-state continuous Galerkin finite element module of SPNDYN was applied and run in diffusion mode to verify the applicability of this coupled code system for SCW-SMR design purposes.

5.5.1 The Gmsh model

The geometric model (see Figure 232) of the SCW-SMR core and the finite element meshes were created in Gmsh, code version 4.9.5 (Geuzaine et al., 2009). Only half of the SCW-SMR geometry was considered to take advantage of the vertical symmetry of the core. Two-group diffusion approximation and assembly-wise homogenisation was applied in the core. The reflector region was modelled with homogeneous material regions surrounding the core differentiated by their temperatures and densities. On the outer surface of the reflector, zero flux boundary condition was defined, while on the symmetry plane, the normal flux derivative was set to zero as the corresponding boundary condition. Unstructured meshes were generated using first-order (4-node) tetrahedral elements with first-order (3-node) triangular boundary elements. Before

selecting the appropriate mesh for the coupled reactor physics and thermal-hydraulics simulations, a mesh sensitivity analysis was performed.

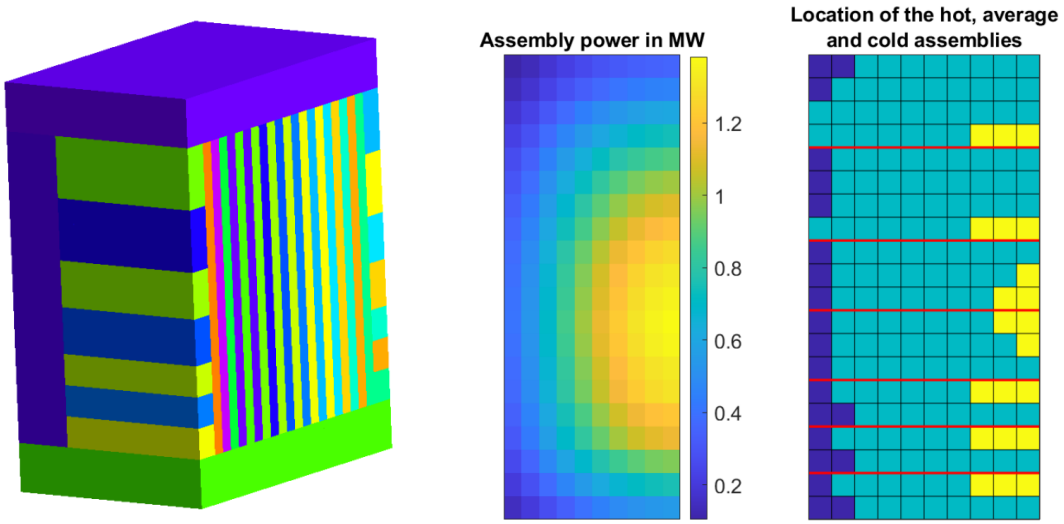

Figure 232: The Gmsh model of the core (left), the assembly power distribution (centre) and the positioning of the hot (yellow), cold (dark blue) and average (aquamarine) fuel assemblies (right) in the SCW-SMR SPNDYN model. The symmetry plane is on the right side of the model. (Bertesina et al., 2023; Varju et al., 2024)

5.5.2 Group constant database generation with Serpent 2 and group constant parametrisation

Group constant databases were generated using the Serpent 2 Monte Carlo transport code, version 2.1.31 and the ENDF/B-VII.1 nuclear data library. Databases were developed separately for the core and reflector regions.

In the preliminary core concept, homogeneously enriched UO_2 fuel (5 wt%) was considered; therefore, the group constant generation performed for the core region was based on a detailed, two-dimensional (axially homogeneous), 5 wt% enriched fuel assembly model. Here, infinite flux spectra were used for homogenisation and collapsing, and no critical spectrum correction was applied. The intermediate multi-group and final few-group structures were the default, 70-group and two-group structures of Serpent 2 (defaultmg and default2). To parameterise the group constant functions (here denoted by y) within the core, the function given in Equation (2) was applied, depending on the coolant temperature (T_{cool}) and density (ρ_{cool}), the fuel temperature (T_{fuel}) and the temperatures of the moderator flowing in the moderator boxes (T_{modbox}) and between the fuel assemblies (T_{outmod}).

$$y = a + b \cdot T_{fuel} + c \cdot T_{fuel}^2 + d \cdot T_{cool} + f \cdot T_{modbox} + g \cdot T_{outmod} + h \cdot \rho_{cool} \quad (2)$$

The Serpent 2 model used to generate the database for the reflector region is a simplified version of the SCW-SMR core. It consists of a semi-infinite lattice of fuel assemblies surrounded by a 20 cm thick layer of water with vacuum boundary condition defined at the outer surface. The function given in Equation (3) was applied to parameterise the group constant functions (here denoted by y) within the reflector, which depend on the reflector temperature (T_{ref}) and density values (ρ_{ref}).

$$y = a + b \cdot T_{ref} + c \cdot T_{ref}^2 + d \cdot \rho_{ref} + e \cdot \rho_{ref}^2 \quad (3)$$

In total, 59 different fuel assembly states and five different reflector states were modelled, and two-group constants for diffusion calculations were generated, which formed the basis for the non-linear least squares data fitting performed in MATLAB using the lsqcurvefit function of the Optimization Toolbox. The coefficients of the fitted curves are provided in (Varju et al., 2024).

5.5.3 Corresponding Apros and SPNDYN regions

The Apros model of the SCW-SMR core requires three axial power profiles in each stage to start the calculation: the average axial power profile of the five hottest, the five coldest and the remaining fuel assemblies within a stage. Hence, the power calculation module of SPNDYN has been extended to include a function to find, calculate and normalise the required power profiles for each heat-up stage. Since SPNDYN applies the same axial nodalisation to the fuel assemblies as defined in the Apros model, the correspondence between the heated channels and the provided power profiles is straightforward. In the current version of the SPNDYN model, the positions of the hot, cold and average assemblies were determined a priori as a result of a non-coupled, steady-state SPNDYN calculation and were fixed throughout a coupled calculation process, as shown in Figure 232. The fixing of the positions is supported by previously performed SCW-SMR coupled computations, which show insignificant changes in their positions (Mészáros et al., 2023).

As the reflector model of SPNDYN is simplified compared to the Apros model, an approximate correspondence was taken into account in this case. The temperatures of the upper and lower reflector regions in SPNDYN were approximated by the temperature of the moderator flowing between the fuel assemblies in the first and seventh stages, respectively. The reflector positioned at the side of the reactor was assigned the parameters of the fifth stage inter-assembly moderator, while for the reflector regions at the foot and head of the fuel assemblies, the temperature and density of the unheated part of the average coolant channels at each heat-up stage were taken into account. Two approximations are introduced using these correspondences, one resulting from neglecting the distinction between the three different channel types and the other from neglecting the structural components of the head and foot parts of the fuel assemblies and the moderator box located there.

5.5.4 Coupling methodology of the models

The coupling between Apros and SPNDYN was realised by developing a Transmission Control Protocol/Internet Protocol (TCP/IP) based communication module in each code. The socket and pickle libraries were used in SPNDYN, which is originally written in Python. SPNDYN is the server programme during data communication, while Apros is the client. The two programs do not necessarily have to be installed on the same computer, but this was the case in this study. In Apros, a plugin for Python integration is available since code version 6.09. The TPC/IP-based communication module was also written in Apros using the Simantics Constraint Language (SCL) module.

The coupled simulation is started in SPNDYN as the server program, then the Apros run should also be started. SPNDYN waits to receive the temperature and density distributions returned by Apros in the form of Python arrays at the end of its first simulation using a first guess for the axial power distributions. SPNDYN then recalculates the group constants based on the received data and using the parameterised group constant functions, and then performs a steady-state diffusion calculation. The axial power distributions of the hot, cold and average assemblies

are derived from the two-group flux distribution, normalised and returned as Python arrays to Apros, the client, which receives the data, overwrites the power profiles of the hot, cold and average channels using an SCL script and starts the next thermal-hydraulics simulation. SPNDYN waits for Apros to finish the simulation and receives the temperature and density distributions returned by Apros, and so on.

SPNDYN and Apros should perform steady-state calculations at each iteration step during the coupled simulations. Unfortunately, Apros can only perform dynamic (transient) calculations. To overcome this problem, the coupling is structured so that no communication occurs until the Apros transient simulation reaches a specific stopping condition, which was set to be a particular simulation time (called Apros runtime) that elapsed since the last successful communication between the codes. It must be stressed that this condition is based on the simulation time, which describes the length of the transient simulated by Apros and not the actual running time of the code.

5.5.5 Coupled, steady-state simulations

5.5.5.1 Sensitivity analyses

The coupled calculations were first started with some sensitivity analyses focusing on two main parameters: the Apros runtime mentioned above and the number of finite elements used in the Gmsh model.

Each time Apros receives a new power profile, a new transient is initiated, and, depending on the variation of the profile, the effects on the system may be more or less pronounced. Then, depending on the length of the simulated transient (runtime), the system may or may not reach a steady state during the iteration step. If the stopping condition is not set correctly, the data sent to SPNDYN will not be related to the steady-state condition of the reactor. Therefore, the reactor physics calculation will start with group constants calculated from the temperatures of a transient state of the system. This will probably not prevent the coupled calculation from converging, but it will require more iteration steps and a longer time. On the other hand, longer transients unnecessarily increase the computational demand of Apros. Finding the right setting for the parameter runtime is essential to optimise the coupled computation. Based on the analyses performed, Apros needs to simulate at least 320 s between two steps of the reactor physics calculation to reach a good equilibrium state. As expected, the fuel temperature was the fastest parameter to converge, as it directly depends on the power distribution. Due to the heat transfer from the fuel rods, the coolant temperatures take longer to converge. The moderator box temperature was the slowest parameter to converge because several heat conduction and transfer processes delay the effect of the new power profile.

The mesh sensitivity analysis aimed to optimise the discretisation error of the finite element solution, along with the computational cost of the simulations. For this purpose, four unstructured tetra meshes with different element sizes were created. Based on the results and the available computational resources, it was decided to use a 4.99×10^5 element mesh to perform the final simulations. This mesh guarantees a relatively fast SPNDYN calculation with low memory consumption and introduces a discretisation error of no more than 5-6 %.

5.5.5.2 Comparative analysis of the final simulation results

With the coupled code system Apros-SPNDYN, finalised based on the results of the sensitivity analyses, a steady-state simulation was performed until the whole system reached equilibrium. The results obtained are compared in Figure 233 to Figure 240 with a reference coupled simulation performed with Apros and Serpent 2. For the Apros and Serpent 2 simulations used as reference in the present study, a modified Serpent 2 model was developed. This Serpent 2 core model consists of uniform, 5% enriched UO_2 fuel assemblies, of which only the active length is modelled and surrounded by water reflector regions, as in the SPNDYN model. The reason for these simplifying modifications to the Serpent 2 model was to obtain as similar geometric models as possible for code verification purposes. However, differences between the models remained. On the one hand, in the Serpent 2 model, the temperature and density distributions between the fuel assemblies are interpolated based on the power distribution of the previous iteration step, whereas SPNDYN only considers the three different types of assemblies (hot, cold, average) in each heat-up stage. On the other hand, SPNDYN was run with zero flux boundary condition, while in Serpent 2, vacuum boundary condition is applied.

As can be seen, the usual cosine-like power profile is formed both axially within each stage and in the vertical direction thanks to the homogeneous 5% enrichment used in this simulation (Figure 233). However, the cosine curves are slightly shifted in both directions, horizontally towards the inlet side and vertically downwards, which can be explained by the temperatures of the moderator and the coolant, which are lower in these directions; hence, these regions can provide better moderation.

The two calculations show very good agreement. The effective multiplication factor obtained with Serpent 2 was 1.16720 ± 4 pcm, while that obtained with SPNDYN was 1.17442. The largest absolute deviation is observed in the hot channels of heat-up stages two to four, while the largest relative error is typically observed at the edges of the active core, i.e. in the cold channels of heat-up stages one and seven (Figure 234). The latter remains mostly below ±8%, but even the maximum does not exceed ±21%. The observed differences can be attributed to several possible sources, namely the accuracy of the transport approximation used (diffusion) compared to the Monte Carlo simulation, the differences between the boundary conditions, differences in the way the temperature and density distributions are taken into account in the SPNDYN (three-channel) and Serpent 2 models (interpolation), and, finally, the fixing of the position of the hot and cold assemblies in the SPNDYN model.

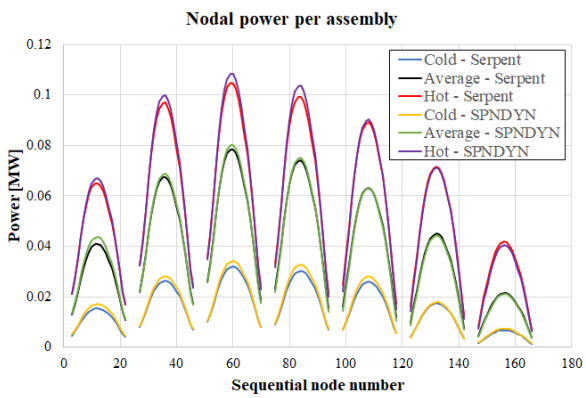

Figure 233: Nodal power distribution

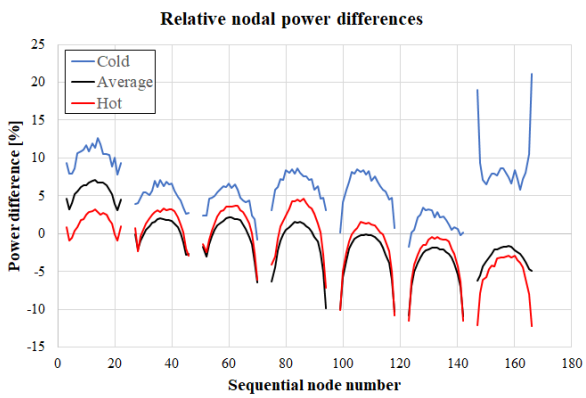

Figure 234: Differences of the nodal power distribution

As a result of the axially cosinusoidal power distribution, the rise in the coolant temperature describes successive S-shaped curves (Figure 235), which flatten out around heat-up stages two to four due to the supercritical transition (Figure 236). At the design power of 290 MW and an inlet mass flow rate of 145 kg/s, an outlet temperature of about 520 °C was achieved, similar to the cases presented in section 5.3.2 and 5.3.5. A significant temperature difference of over 50 °C is observed between the three channels, particularly in the upper stages. The design concept has already undergone several improvements during the project to reduce this high temperature peak, as presented in section 5.3. However, this analysis had a different focus, so the original concept was used. The comparison of the two models shows that the temperatures are in good agreement with the power profiles, and significant deviations are only found in the middle stages. The most considerable temperature difference is about 5 °C at the outlet of the hot channel of the fourth stage.

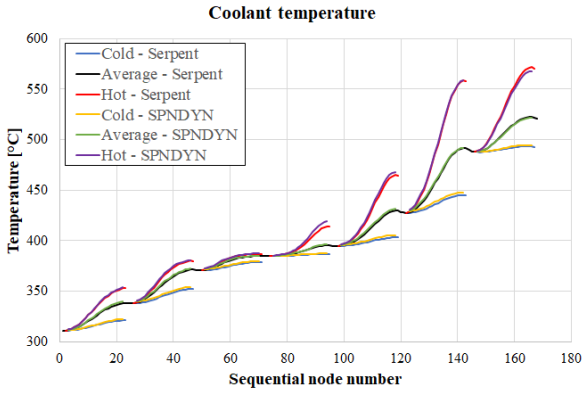

Figure 235: Temperature profile of the coolant channels

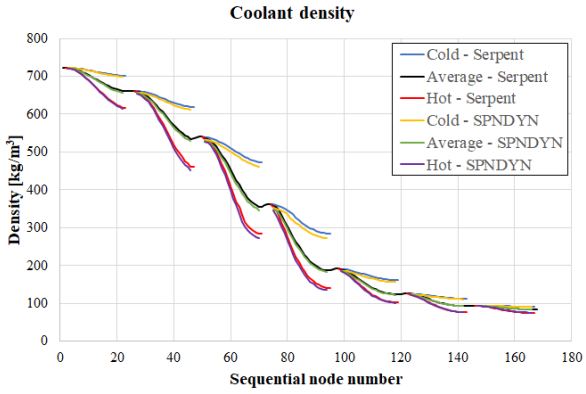

Figure 236: Density profile of the coolant channels

The moderator regions are heated by the coolant through the walls. The slight deviation of the coolant temperature results in a practically negligible variation of the temperature of both the moderator flowing in the upward moderator channel (Figure 238) and in the moderator boxes (Figure 237). In the upward channel, due to the higher upper coolant temperatures and the increasing number of assemblies per stage, the moderator temperature rises progressively as it moves upwards, reaching a temperature of over 296 °C at the outlet. The flow in the moderator boxes is parallel, i.e. the inlet temperature is almost the same for all the 400 boxes (Figure 237). First, a high temperature jump, which increases upwards, is observed on the profiles. This is a result of the significant heat transfer along the inlet section of the box, which is not yet inside the active core, especially in the cylindrical part of the box where the wall does not have an internal insulating layer. The temperature of the coolant surrounding the box is higher in the upper stages, resulting in higher moderator temperature rises in both the inlet and active sections. The maximum outlet temperature observed is approximately 320 °C.

The radially averaged fuel temperature (Figure 239) and the cladding temperature (Figure 240) are essentially determined by the combined effects of the power profiles and the continuously increasing coolant temperature. Again, significant differences between the models are only observed in the hot channels of heat-up stages two to four, with a global maximum of 49 °C and 18 °C in stage four. As a result of the quite uneven power distribution of the three channel types, the cladding temperature has a strong variation, ultimately leading to a maximum of over 650 °C.

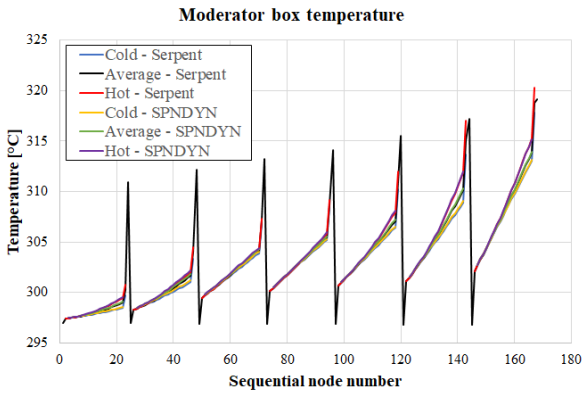

Figure 237: Temperature profile of the moderator boxes

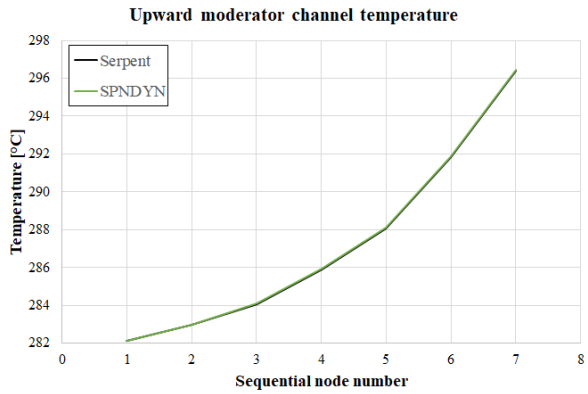

Figure 238: Temperature profile in theupward moderator channel

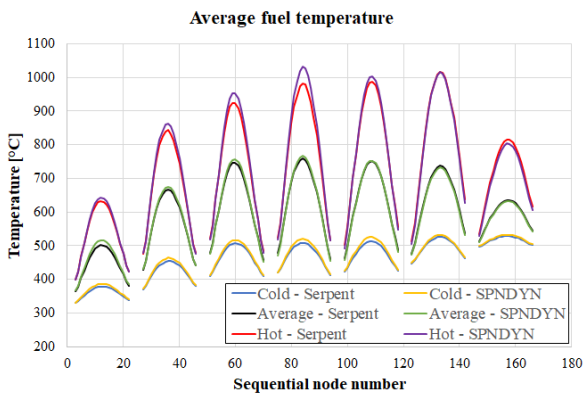

Figure 239: Radially averaged fuel temperature profiles

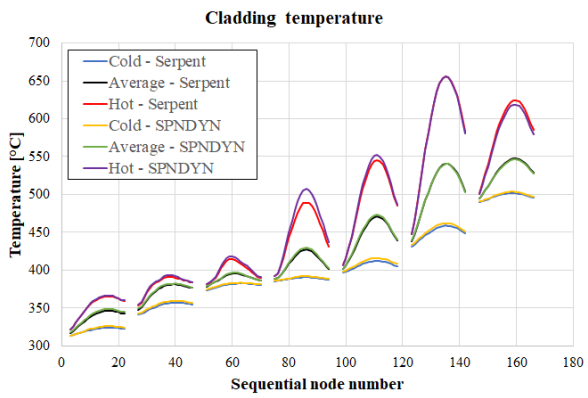

Figure 240: Cladding temperature profiles

Based on the above positive experience, we plan to develop the coupled system further in two main directions. For the steady-state analysis, we would like to refine the models in the future, particularly by modelling the reflector regions more precisely and we would also like to take into account the improvements made to the concept in the meantime. In addition, we would also like to be able to perform transient calculations of the SCW-SMR concept with the coupled system. In principle, both Apros and SPNDYN are already able to perform transient calculations, but further improvements are still needed to be able to perform such an analysis of the concept (e.g. the generation and parametrisation of additional group constants for transient reactor physics calculations).

5.6 Steady-state calculations with adapted subchannel codes

One of the most important components in a nuclear reactor is the fuel assembly (FA) as it contains the fuel rods and thus the nuclear fuel. The nuclear fuel and the cladding constitute the first barrier according to the concept of multiple barriers to the release of radioactive material, strictly linked to the defence in depth (DiD) one. However, designing a fuel-assembly concept is a multi-objective and multi-constrained task where different disciplines such as thermalhydraulics, reactor physics, materials, chemistry, and many others are inter-related having different constraints (see Figure *241*). Thereby an iterative approach is needed to define a feasible concept (or space solution). While the neutronic optimization is being carried out separately, this study focuses on

a preliminary thermalhydraulics subchannel assessment. Once completed, further development would require linking to operational and safety constraints and requirements, such as maximum burnup, maximum linear power and higher-reliability or reduced operational and maintenance costs.

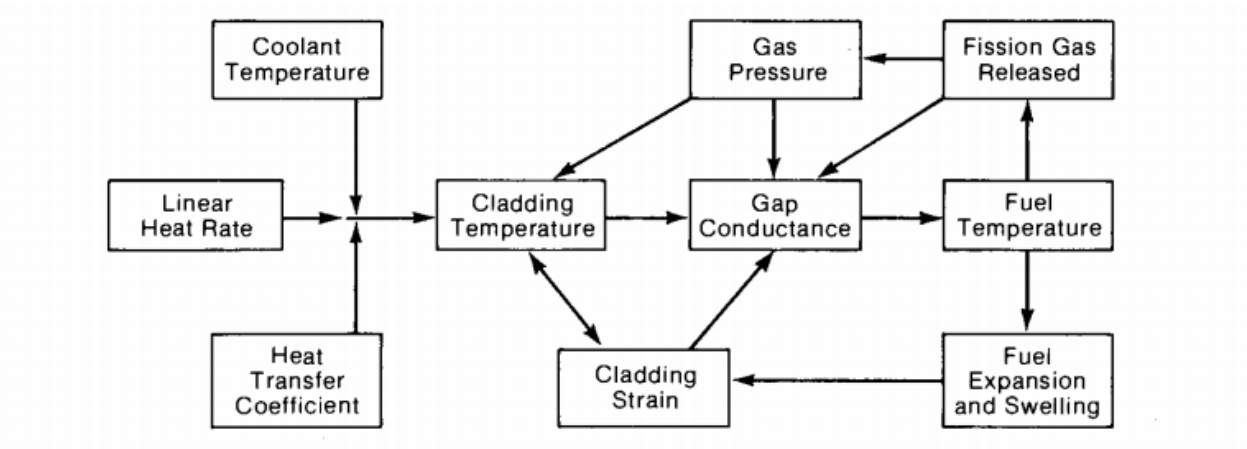

Figure 241: Disciplines involved in the design of a fuel rod and fuel assembly (Rao et al., 2014)

The optimization of the SCW-SMR fuel assembly utilizes the knowledge gained from the development of previous SCWR concepts, such as the Canadian SCWR fuel bundle (Nava-Dominguez et al. 2016), the High Performance Light Water Reactor (Schulenberg and Starflinger, 2012), and the CSR-1000 (see at Section 2.1). It considers geometrical features (such as heated perimeter, flow area and pitch) to minimize the Maximum Cladding Temperature (MCT). As the SCW-SMR is under development and not all the requirements have been identified, the assessment of the fuel bundle design is focused on the nominal operating conditions, i.e., the following study does not cover accident or transient conditions.

The conditions were selected based on the limits and operational experience of available materials and/or components. More specific requirements for the SCW-SMR are shown below in Table 13.

Parameter	European SCW-SMR	Canadian SCW-SMR
Reactor Power:	300 MW_e	300 MW_e
System pressure:	25 MPa	25 MPa
Inlet coolant temperature:	280 °C	290 °C
Outlet coolant temperature:	500-550 °C	450-500 °C
Maximum Cladding Temperature (overall):	550-600 °C	500-550 °C
Fuel assembly orientation	Horizontal	Vertical
Number of passes	7	1

Table 13: The proposed operating conditions of European and Canadian SCW-SMR

5.6.1 Thermalhydraulic Modelling

Two subchannel codes were used in the frame of ECC-SMART project to assess the thermal-hydraulic performance of the fuel assembly of European SCW-SMR concept. The subchannel codes ASSERT-PV SC (Nava-Dominguez et al., 2016) and STAFAS (Cheng et al., 2003) were used for modelling the SCW-SMR fuel assembly for the fuel bundle region. The walls of moderator

box (MBW) and fuel assembly box (FABW) were modelled as adiabatic surface boundaries assuming perfect insulation (i.e., no heat transport to the coolant inside the moderator box and gaps between FAs).

The analysis were performed using the Jackson and Bishop heat transfer correlations (Pioro and Duffey, 2007) for supercritical flows.

Table 14 and Table *15* summarize the main model options, correlations and operating conditions used in ASSERT-PV SC and STAFAS codes for the base-case model for the assessment of the European SCW-SMR.

Model	**Description**
Fluid	Water at supercritical pressure conditions
Gravity term	Include gravity terms
Wall friction	Colebrook-White (Nava-Dominguez et al., 2016) formula for frictional pressure loss.
Cross-flow mixing	Rogers and Tahir correlations (Nava-Dominguez et al., 2016) for inter-subchannel turbulent mixing multiplied by 2.0 (for tight-lattice rod arrays)
Rod-to-coolant heat transfer	Jackson correlation (Pioro and Duffey, 2007) for supercritical pressure conditions.
Appendages/Spacers	Bare bundle, no appendages or wire wrap modeled.

Table 14: Model options, correlations and operating conditions used in ASSERT-PV SC code

Model	**Description**
Fluid	Water at supercritical pressure conditions (at 25 MPa)
Gravity term	Exclude gravity terms
Wall friction	Modified Blasius equation (Waata, 2006) for frictional pressure loss.
Cross-flow mixing	Cheng and Müller correlation (Cheng and Müller, 1998) for inter-subchannel turbulent mixing
Rod-to-coolant heat transfer	Bishop correlation (Waata, 2006) for supercritical pressure conditions.
Appendages/Spacers	Grid spacers without additional mixing vanes (Waata, 2006).

Table 15: Model options, correlations and operating conditions used in STAFAS code

5.6.2 Subchannel Analysis and Codes

The subchannel approach consists in subdividing the cross-sectional flow area of a nuclear fuel bundle into simple parallel and interconnected cells called “subchannels”. Each subchannel is

bounded by solid walls of the fuel rods and/or pressure tube and by imaginary boundaries connecting rod centres. Subchannel codes solve the one-dimensional (1D) conservation equations of mass momentum and energy for each interconnected subchannel. The exchanges of mass, momentum and energy between interconnected subchannels are modelled as semi-empirical source terms to the 1D equations (Waata, 2006).

ASSERT-PV is the Canadian subchannel code developed and qualified for predictions of subchannel flow, enthalpy and phase distributions, heat transfer and fuel cladding temperatures in horizontal PHWR fuel channels (Nava-Dominguez et al., 2016). The code has been designed to be general enough to accommodate other geometries and orientations. These include simple geometry of a few subchannels and bundles or assemblies relevant to PHWR, PWR and BWR designs, in both vertical and horizontal orientations. As well, the code can accommodate a range of fluids, including single- and two-phase heavy water, light water, various Freons, and two-phase air-water.

ASSERT-PV (Rao et al., 2014, Nava-Dominguez et al., 2016) is based on ASSERT IV (Carver et al., 1990), which in turn originated from the COBRA IV (Wheeler et al., 1976, Stewart et al., 1977) computer program; ASSERT-PV has been enhanced to meet the specific requirements for the thermal-hydraulic analysis of two-phase flow in the horizontally oriented PHWR fuel channels. The ASSERT-PV version for SCWR analysis is V3R1m2 (also referred to as ASSERT-PV SC) developed to model flow and heat transfer in subchannels of fuel bundles under supercritical pressure conditions. This interim version can handle the supercritical flows, but not the transition between supercritical and subcritical flows when the system pressure varies across the critical point during a transient. This is judged to be sufficient, since phase transition and transients are not required in a subchannel analysis at this stage of concept development.

The STAFAS code (Sub-channel Thermal-hydraulics Analysis of Fuel Assembly under Supercritical conditions) was originally created at the Karlsruhe Institute of Technology (KIT) by Prof. Xu Cheng (Cheng et al., 2003) and developed further by the Author and his research team (mainly his PhD student C. L. Waata (Waata, 2006)). The objective of the STAFAS development was to create a coupled algorithm with a neutronics and thermal-hydraulics (the STAFAS subchannel) codes. The coupled algorithm was intended to be used for detailed design and thermal hydraulic analysis of rod bundles and fuel assemblies, where the density variation in the subchannels and the power distribution in the fuel rods are highly variable. The foreseen typical application was the HPLWR concept (Schulenberg and Starflinger, 2012) operating under supercritical pressure conditions. Regarding the needed neutronics code, the Monte Carlo code MCNP (see the related MCNP website) has been selected for coupling with the subchannel code STAFAS. The Monte Carlo code MCNP is an internationally recognised code for nuclear reactor applications while the STAFAS code is capable of modelling the supercritical water flow not only in the FA but in the moderator box as well. The STAFAS code was based on the well-known thermohydraulics or rather subchannel code COBRA (Rowe, 1967). Both STAFAS and MCNP are able to model complex geometries like rod bundels or FAs. The variable distributions which are exchanged during the coupling are: power distribution from the neutronics (MCNP) code on one side, water density distribution, water temperature distribution and fuel temperature distribution from the thermal hydraulics (STAFAS) code on the other side (Waata, 2006). The coupled algorithm uses a serial integration coupling approach during the run. The STAFAS code has been written in FORTRAN 90 language. During the later development stage, it was modified in order to accept the power distribution calculated by the neutronics code (Waata, 2006). The coupled algorithm uses an external data exchange approach, which means that the codes run separately one after the other exchanging data after each run via a dedicated so-called “batch“ file.

5.6.3 Subchannel models

The ASSERT-PV SC and STAFAS discretizations for the European SCW-SMR fuel assembly is presented in Figure *242* and Figure *243*. The subchannel dimensional data and boundary conditions are listed in Table 16 and Table 17 for ASSERT-PV SC and in Table 16 and Table 18 for STAFAS, respectively. The model options used for the ASSERT-PV SC and STAFAS analysis are presented previously in Table 14 and Table 15.

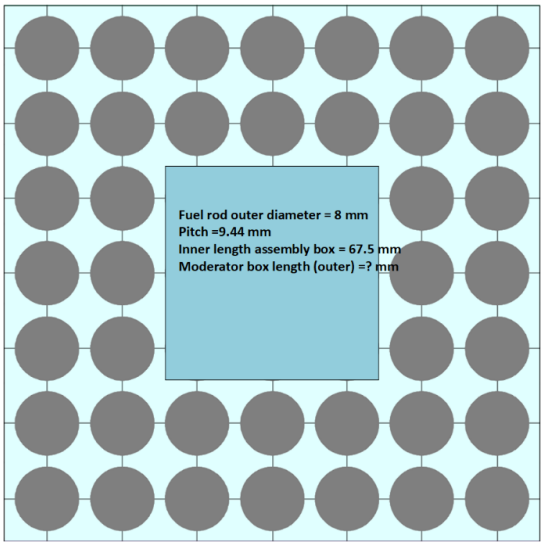

Figure 242: ASSERT-PV SC ("full") discretization for the SCW-SMR fuel assembly

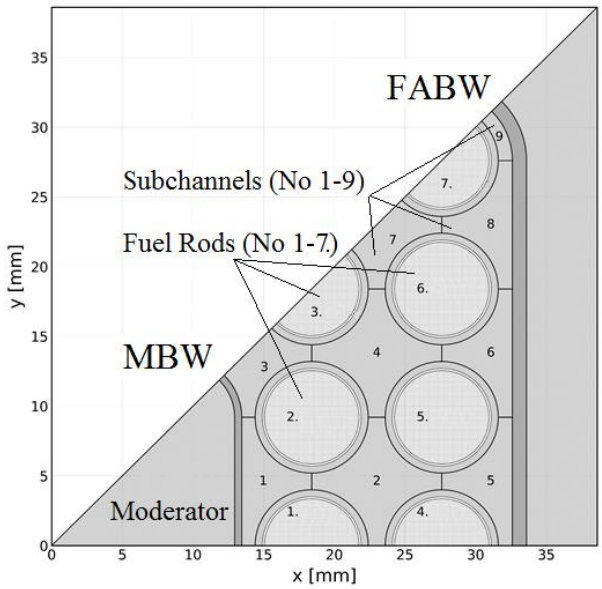

Figure 243: STAFAS ("1/8") discretization for the SCW-SMR fuel assembly with the numbering of modelled subchannels (SC 1-9) and fuel rods (FR 1-7)

Subchannel type	Flow area [cm^2]	Wetted perimeter [cm]	Heated perimeter [cm]
Corner	0.1692	1.7143	0.6283
Side	0.2613	2.2006	1.2566
Center	0.3885	2.5133	2.5133
Center-corner	0.4561	2.3670	1.8850
Center-side	0.4123	2.2006	1.2566

Table 16: Subchannel dimensional data for the models of both codes

Pass No.	P [MPa]	Inlet coolant Temperature [°C]	G [kg/m^{2}s]	Q (assembly) [kW]	q'' [kW/m^2]
1	25.39	312.3	2.4149	810.4	479.9810
2	25.342	348.5	2.4149	1183.2	700.7818
3	25.267	379.8	2.4149	1097.6	650.0829
4	25.217	386.5	1.61	955.2	565.7427
5	25.14	400.2	1.61	780.8	462.4497
6	25.077	433.7	1.207	556	329.3059
7	25.003	487.2	1.207	297.6	176.2615

Table 17: Applied boundary conditions for ASSERT-PV SC model

Pass No.	P [MPa]	Inlet coolant Temperature [°C]	MFR [kg/s]	Q (assembly) [kW]	q'' [kW/m^2]
1	25.421	312.3	0.453	810.4	479.9810
2	25.368	348.5	0.453	1183.2	700.7818
3	25.327	379.8	0.453	1097.6	650.0829
4	25.264	386.5	0.302	955.2	565.7427
5	25.204	400.2	0.302	776	459.6307
6	25.129	433.7	0.227	552	326.6330
7	25.062	487.2	0.227	297.6	176.2615

Table 18: Applied boundary conditions for STAFAS model

To complete the modelling of the fuel assembly concept, the following simplifications and assumptions are made at both subchannel models:

1. the non-fuel components of the fuel bundle, such as displacer rods, do not produce heat, that is, gamma heating is not considered;
2. the fuel channel modelling is based on bare fuel bundles, that is, there is no appendages or devices attached to the rods, such as spacer pads, bearing pads and others;

3. the bottom-peak power distributions (shown below in Figure 244) are considered for the stages to ensure conservative results (cladding and fuel temperatures);
4. for ASSERT-PV SC model the same phenomenological models and correlations are used to model all fuel assembly concepts; for STAFAS, three different fuel assembly power levels are used: the cold, the average and the hot;
5. for ASSERT-PV SC model no coupled iterations between physics and thermal-hydraulics are performed; that is, no feedback effects are considered; for STAFAS, coupled iterations between MCNP (reactor physics) and thermal-hydraulics (STAFAS) are performed; that is, some feedback effects are considered.

Three different FA models were developed in the STAFAS subchannel analysis regarding the applied power level: cold, average and hot FA models. Figure 244 shows the meaning of different power levels.

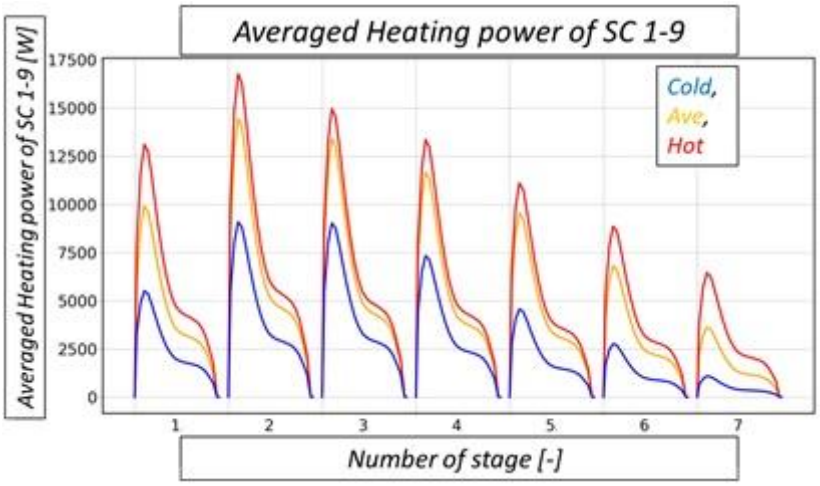

Figure 244: The cold, average and hot power levels for STAFAS subchannel analysis.

Three different calculation series were performed with the STAFAS subchannel (cold, average and hot FA) models, in which the applied boundary conditions differed a little bit from each other with the following details. At “Version 1” or “v01” calculation series: the previous stage outlet parameters were set as the input parameters of the next stage model. At “Version 2” or “v02” calculation series: the input parameters of each stage were specified by the results of (BME) APROS system code model. At “Version 3” or “v03” calculation series: identically to “v02”, the input parameters of each stage were specified by the results of (BME) APROS system code model and additionally the mass flow rates were reduced in the Gap between FAs and in the moderator box (MB).

5.6.4 Results

The subchannel analysis with the two subchannel codes was conducted for the European SCW-SMR fuel assembly concept. The subchannel analysis for the Canadian SCW-SMR (Nava-Dominguez et al., 2016) and Chinese CSR-150 (see at Section 2.1) are documented elsewhere.

The detailed description of the reactor core and coolant flow path is described in the previous Sections. The European SCW-SMR pre-conceptual design uses seven passes to minimize the possibility of hotspots. For that reason, the simulation was performed using seven cases, each one representing a pass through the core.

These values were used in the ASSERT-PV SC and STAFAS modelling. The MCT was used as the key-parameter for the code-to-code comparison. Figure 245 to Figure 248 present

the comparison between the calculated MCT provided by the subchannel codes ASSERT-PV SC and STAFAS.

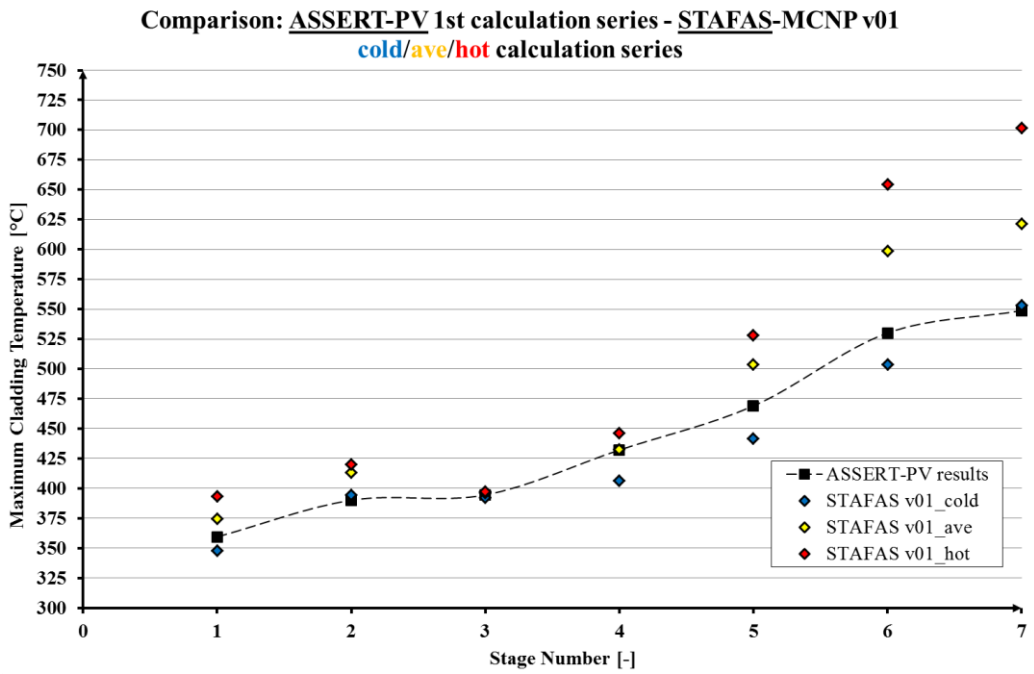

Figure 245: Comparison of MCTs calculated with ASSERT-PV SC and STAFAS v01 cold/ave/hot subchannel models

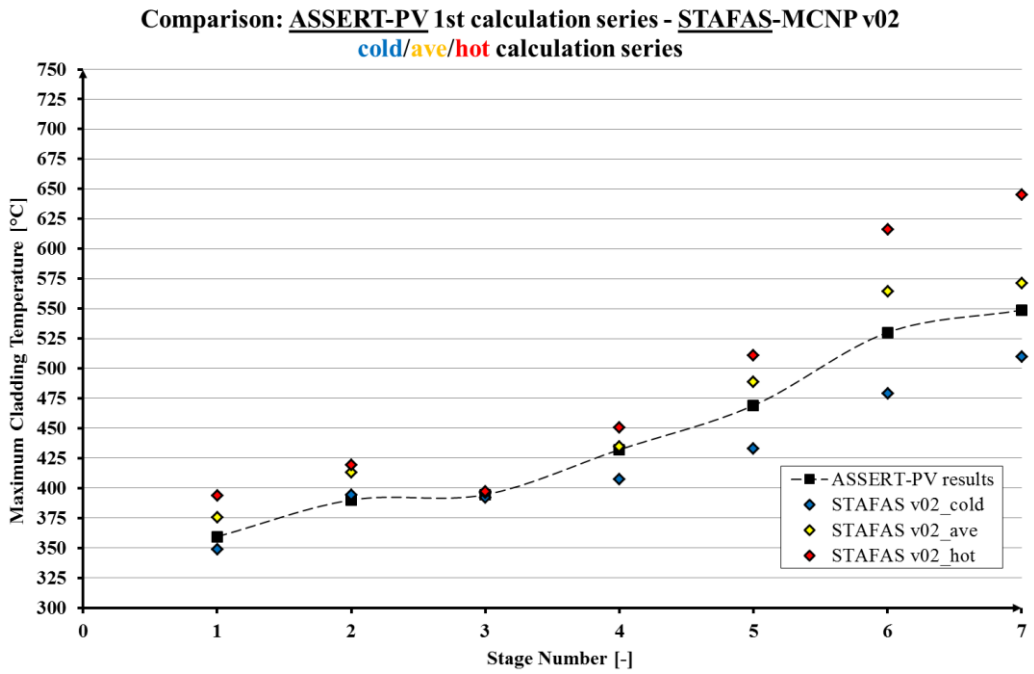

Figure 246: Comparison of MCTs calculated with ASSERT-PV SC and STAFAS v02 cold/ave/hot subchannel models

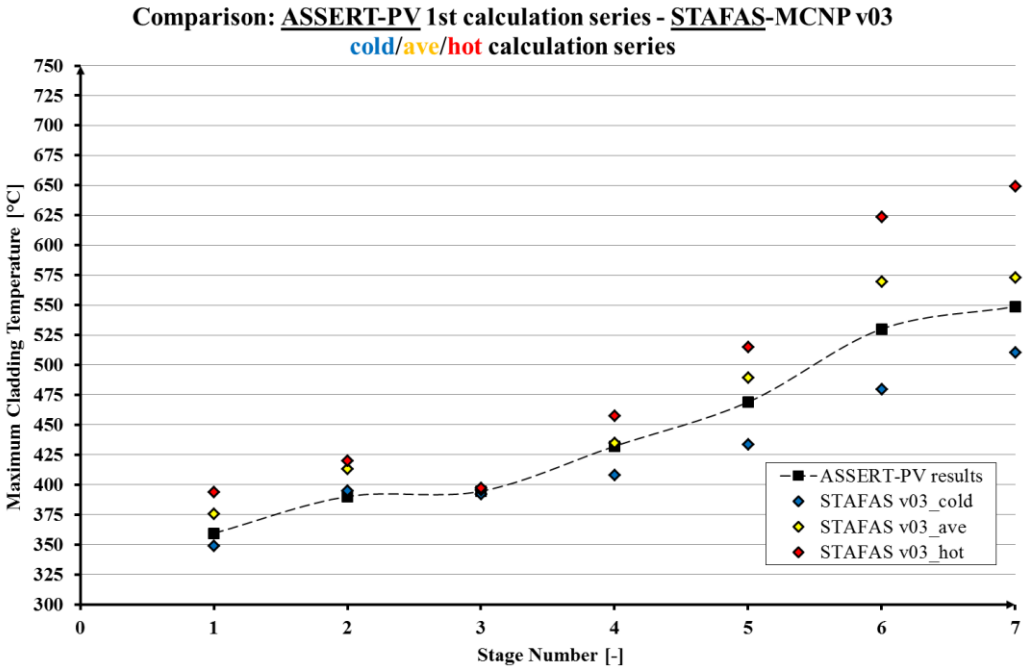

Figure 247: Comparison of MCTs calculated with ASSERT-PV SC and STAFAS v03 cold/ave/hot subchannel models

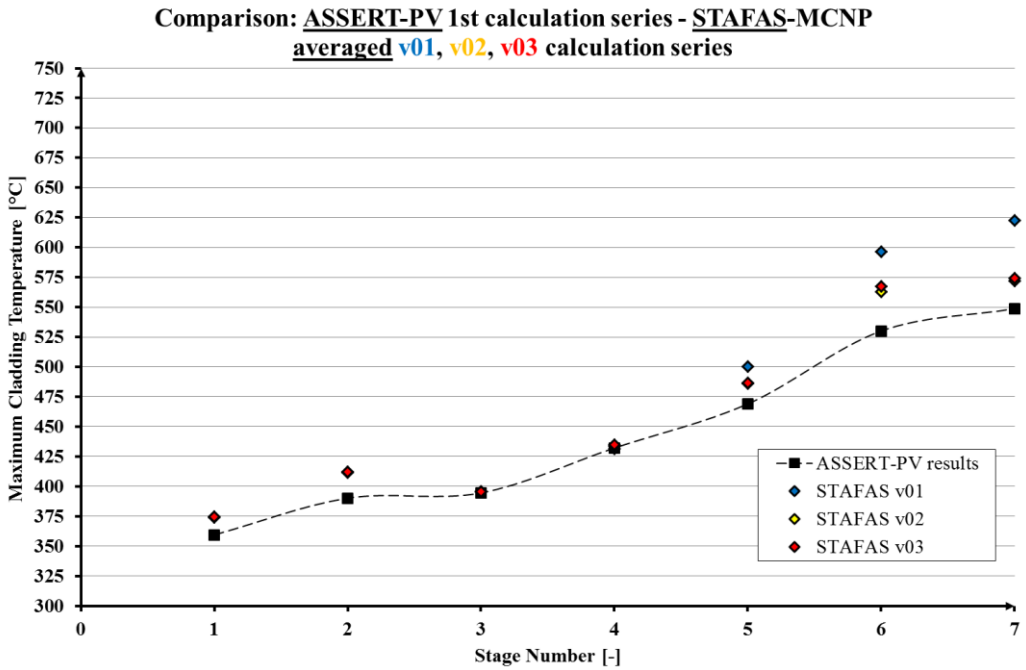

Figure 248: Comparison of MCTs calculated with ASSERT-PV SC and STAFAS (averaged v01, v02 and v03 calculation series) subchannel models

As it can be observed, both codes give similar results. This increases the level of confidence of the analysis. However, none of the subchannel codes have a correlation to take into account the flow stratification due to the buoyancy caused by the density gradient across the subchannel in a horizontal section. Although ASSERT-PV SC is developed for CANDU type reactors, where the fuel channels are horizontal, the model that takes into account this stratification is based on the void fraction and not on the density. As the fluid is under supercritical conditions, the concept of void faction is no longer used and only one phase is used in the code. This approximation is

no longer valid for horizontal flows. To compensate for that, new heat transfer correlations for supercritical fluids in horizontal flows are being studied. For that reason, it is expected that the MCT from the half-bottom section of the fuel assembly to be lower than the half top of the fuel assembly.

In conclusion, both subchannel codes give similar results, however, the effect of the flow stratification still needs to be evaluated more carefully. However, these preliminary results show that the design of the fuel assembly is suitable for the design of a SCW-SMR.

5.7 Significance of the work and final remarks

The research work carried out by BME in relation to the Apros system code can be divided into two main parts: a model development and an analysis part. First, a detailed Apros RPV model was developed in spring 2022, using the CAD model data already available at that time and the previous RELAP model development experience shared by project partners from UNIPI. This Apros model was later extended with models of the primary and safety systems and the RPV model itself was also further developed and refined several times based on the experience of the calculations performed in the meantime. The final model version is presented in detail in chapter 5.2.

In addition to Apros, several other models of the SCW-SMR concept have been developed at BME in the frame of WP3 and WP4 activities, such as a detailed Ansys CFX model, several Serpent model versions and an SPNDYN model. During these developments, a quite important goal was to also make it possible to perform various coupled calculations (Apros-Serpent, Apros-SPNDYN and Ansys CFX-Serpent) with these models. After the first model versions were completed, the coupling methods and various Matlab and Python scripts implementing them were developed. The main purpose of the Apros-Serpent and Ansys CFX-Serpent coupled calculations was to investigate in detail the steady-state characteristics of the concept and to further develop and optimise the design (chapter 5.3). In addition, these calculations provided a suitable initial state for the SBO transient investigations (chapter 5.4) and input data for the Apros-SPNDYN calculations. This latter coupled code system has so far only been used for steady-state analyses (chapter 5.5), but the future aim is to extend its use to detailed transient analyses as well.

From the above description, it can be seen that a significant part of the work has focused on the development of various TH and reactor physics models and their coupling, which can be used in the future for further development of the concept or even for the analysis of other similar designs after minor specific modifications.

In the second part of the work, a comprehensive analysis of the SCW-SMR concept was performed. The coupled code systems were used to investigate in detail the steady-state characteristics: the flows in the reactor vessel and their distribution between the main and bypass paths, the various temperature and power profiles, the in-vessel heat transfer processes that strongly influence the flow distributions, and the sensitivity of the system to changes in the main parameters (chapter 5.3). Possibilities for improvements of the concept have also been partly explored, where the use of inhomogeneous inlet orifices proved to be beneficial, while the investigated alternative core layout had more disadvantages. Obviously, there is still a long process of development ahead in this direction before the concept can be finalised and the primary aim of the analyses carried out so far was only to understand the qualitative effects and the system behaviour.

The other major part of the analyses carried out with Apros focused on the transient analysis of the LTSBO event and the possibility for natural circulation and passive heat removal. Based on the lessons learned from the analyses presented in chapter 5.4, with a controlled

depressurisation, followed by the activation of the passive heat removal loops and the injection from the passive accumulators, this initial event can be managed, natural circulation can be developed and the decay heat released can be removed for a long period of time despite the complex flow path. However, it has also been shown that reflooding the vessel from the accumulators or other sources is necessary, as there is a risk of core dry-out after a few hours in the complete absence of injection.

The results of the steady-state and SBO transient analyses confirmed the conceptual approach of reducing hot spots and allowing passive heat removal by natural circulation in the emergency situation by using seven heat-up stages and a horizontal core layout. The main future development objectives include refinement of the models both in terms of RPV nodalisation, the range of safety systems considered and the control/protection sequences; extension of the range of transients considered; further development of the Apros-SPNDYN code system for transient studies; and, based on the experience gained, further development and refinement of the design concept.

Regarding the joint BME-CNL subchannel benchmark, it can be stated that both subchannel codes give similar results, however, the effect of the flow stratification still needs to be evaluated more carefully. Nevertheless, these preliminary results obteined with two subchannel codes show that the design of the fuel assembly seem adequate in view of the results which could be obtained by the analyses.

6 Safety and design analysis of the SCW-SMR concept (by IPP)

Safety analysis of a nuclear reactor is an important stage of development work. Reaching such an objective is valuable and significant for promising next-generation nuclear reactors, especially for those innovative from the design point of view. The accumulated experience for the light-water reactors (LWR) (IAEA, 2016) defines approaches to ensure fundamental safety functions (IAEA, 2019a) that are mostly applicable for the present discussion.

International research is being conducted to understand better the characteristics of important thermophysical and thermal-hydraulic phenomena for supercritical (SC) coolant. For some of them, prediction methods have been proposed (IAEA, 2020a) and solutions have been formulated to support the development of technology for supercritical coolant usage (Schulenberg, 2014).

In general, the implementation approach of the safety systems is the same as for the traditional LWRs. The emergency core cooling systems consist of high-pressure and low-pressure injection subsystems, for which some concepts propose passive solutions. The automatic pressure depressurisation system inherent in such designs makes it possible to reduce the impact of pressure on the fuel channel boundary at the initial stage of the transient. In the majority of projects, the reactor vessel is located in an enclosed compartment (concrete cavity) with an internal overpressure safety system.

Some papers (Zhao et al., 2023; Novog et al., 2012; Wu and Ren, 2022; Liu et al., 2019) present the research results of the above mentioned safety systems for the actual SCWR concepts and related experimental loops. Their performance is evaluated using both system codes and coupled CFD methods. Despite the successful use of nodal codes by extending the range of the coolant thermophysical properties functions for the supercritical pressure region, it is still too early to declare a sufficient assessment. However, a good example in this field is the application of the modified ATHLET code (Cao et al., 2016) for the computational analysis of the Loss Of Coolant Accident (LOCA) scenarios, where large LOCA transients "with" and "without" the safety systems actuation are postulated. In the latter case, a rapid decrease of the loop pressure, reactor coolant starvation and core dry-out are predicted.

In the SCW-SMR pre-conceptual design, the related phenomenology has its own specifics. The main one is a very significant length of the fuel channel flow paths from the inlet to the reactor outlet. The time component of the overpressure force effect is objectively larger than for a typical LWR with single-pass vertical arrangement. Therefore, the study of the LB LOCA dynamics, in view of the possible vulnerability of the SCW-SMR reactor pressure vessel design, became the subject of the research to be performed by the IPP-CENTRE.

6.1 Applicability of the severe accident analysis codes for the SCW-SMR concept

Predicting the timing of reactor pressure vessel (RPV) rupture contains many uncertainties due to different variants of the core degradation process. The existing base of data related to the simulation of severe accident (SA) scenarios for nuclear reactors with horizontal arrangement of fuel assemblies (FA) is objectively small. Moreover, those existing results are difficult to interpret regarding SCW-SMR because of the specifics of the core internals design. Nevertheless, the loads that the RPV metal must withstand are clear. Among the main ones are the weight of corium accumulating on the bottom and thermal loads due to the high temperature of molten core materials.

According to (IAEA, 2019b and IAEA, 2013), estimating degraded core conditions can be tackled by available calculation tools for SA analysis. These codes have the capabilities of fast

running prediction of transient processes involved in the circulation loop thermal hydraulics, related phenomena occurring during the core degradation, RPV behaviour under thermal and mechanical loading, and containment response. Presently available codes include: ATHLET-CD, ASTEC, MAAP, MELCOR, RELAP/SCDAP, SOCRAT.

With the existing variety of SA codes, the features of the spatial representation of the investigated reactor type internals, at the stage of specifying the core volume and the lower plenum (LP), is considered only by those based on MAAP (IAEA, 2008). For example, MAAP-CANDU has been successfully applied to perform computational analyses in the framework of a Level 2 probabilistic safety assessment project (Brown, 2018 and Brown and Petoukhov, 2015).

Based on the description by Sandia National Laboratories (2014), certain possibilities for the horizontal fuel channels representation were also provided by the MELCOR code family. However, the direct application of the ACR reactor type for code version 1.8.6 encountered the problem of the computational grid designation for the required core region nodalization; it may be caused by incomplete software implementation of the required solution procedures. On the other hand, in later versions of the code (Sandia National Laboratories, 2017) the necessary details of the application are not documented.

So, the application of available SA codes, in particular MELCOR, to the analysis of severe accident progression for the considered pre-conceptual design of the proposed SCW SMR encounters two issues that do not allow their use in a standard fashion:

- the horizontal layout of the SCW SMR core fuel assemblies;
- the need to model depressurization from a supercritical state when considering a large break (LB) LOCA as a representative initial event.

However, it seems possible to apply the MELCOR code to determine the melt mass and temperature characteristics in the in-vessel stage of the SA with the approach of equivalent volume approximation. Thus, it is possible to estimate the melt characteristics of reactor internal materials and the main timing, if the problem of transition from supercritical to subcritical state is solved. In this case the late stage of melt propagation dynamics in RPV should be solved separately.

Hence, in the framework of the Safety and Design analysis of the SCW-SMR concept, a 3-stage consideration of the severe accident progression caused by a LB LOCA as the initial event is proposed:

- **Stage 1 - CFD calculation of the initial dynamics of the transient caused by the LOCA event** (cold leg, CL, rupture). Computational analysis of the pressure wave propagation caused by the LB LOCA, allowing preliminary estimation of the dynamic forces on the reactor internals. Also, simulation of depressurization and transition from supercritical to subcritical state is used to generate pressure and temperature fields for the 2nd stage.
- **Stage 2 - Obtaining the main characteristics of the corium and analysis of its formation timings by the MELCOR code** application to the SCW-SMR concept with horizontal core layout in the equivalent approximation.
- **Stage 3 - Calculation of the late phase of the severe accident, based on complete structural elements molten materials characteristics** (temperatures and component composition) **obtained in Stage 2.** Parametric analysis of the minimum time to RPV failure depending on the external cooling conditions.

Thus, using the proposed method, it is possible to estimate the load-bearing capacity of the reactor vessel in the event of a bounding case with a complete or partial/complete meltdown of the fuel and of the pressure vessel internals, respectively, considering different patterns for the corium stratification.

6.2 Stage 1. CFD modelling of the LB LOCA initial dynamics

The LB LOCA analysis for reactors with supercritical coolant parameters (Dang et al., 2021) has certain features associated with the transition through the critical point. Not all one-dimensional codes can correctly handle the transition from supercritical (single-phase) to subcritical (two-phase) state, especially considering the critical flow. For this purpose, it is necessary to introduce special relationships for thermophysical properties, which allow us to consider the supercritical flow in a two-component approximation with pseudo-boiling (Wang et al. 2021 and Nasuti and Pizzaruti, 2021). This approach allows one-dimensional calculation codes to be used for supercritical parameters without changing the code structure.

The estimation of the initial dynamics of the decompression shock wave propagation requires accounting spatial distributions along three coordinates in the general case. Based on the obtained instantaneous pressure and velocity fields, the loads on the structural elements could be assessed, which could provide with the first conclusions regarding the strength behaviour of SCW SMR internal structural elements under dynamic loads caused by LB LOCA. Also, the subcritical state in SCW-SMR after decompression could be formulated and used for subsequent severe accident analysis.

Additional conditions and assumptions are required to assess the initial dynamics of decompression of a promising IV generation reactor with supercritical parameters due to the peculiarities of the phase state of the coolant. During rapid decompression, the state of the coolant changes from a single-phase supercritical one to a two-phase fluid. In this case, the level of dynamic loads is determined by the minimum impact pressure, which depends on the pressure established at the rupture site (Dubyk Y., Filonov V. et al., 2018 and Ishchenko O., Filonov V. et al., 2021). The level of steady-state pressure is determined by the presence of a critical flow, whose prediction in the general case requires a heterogeneous formulation both in temperature and in velocity. Commercial CFD codes do not provide the ability to couple single-phase and two-phase setups functionally. It means that in the computational domain, depending on the state parameters, either a single-phase or a heterogeneous two-phase formulation is applied zonally. Such mathematical models would solve the problem of introducing abstract pseudo-boiling (two-phase formulation in the supercritical region), which is widely used in system codes (Dang G. et al., 2021 and S.W. Fu et al., 2012).

The second difficulty in analysing the initial dynamics, which applies to all types of reactors, is the need for detailed geometrical modelling of the reactor flows, especially in those places where the flow is split (for example, at a baffle, at various partitions) for a correct assessment of pressure drops during decompression wave propagation. In this case, it is important to correctly calculate the hydraulic resistance of the flow, since this will determine both the dynamic component (braking speed on the wall) and the dynamics of the shock wave. Physically, the first few milliseconds of the negative pressure wave propagation are determined exclusively by the acoustic properties of the medium, by analogy with a water hammer. Negative pressure causes the flow to accelerate and can even change direction (for example, when a cold circulation loop breaks). At Mach numbers close to the limit at which considering the medium's compressibility is necessary (M>0.3), in the acoustic formulation it is necessary to account for the transport velocity. In addition, due to the phase transition, the density of the fluid begins to change as a function of pressure and temperature; thus, hydrodynamic equations should be considered. In this case, the speed of sound is a complex function of a two-phase medium flow structure and flow regime (Lund and Flåtten, 2010) and can be significantly lower than in the liquid and gas phases (Figure 249).

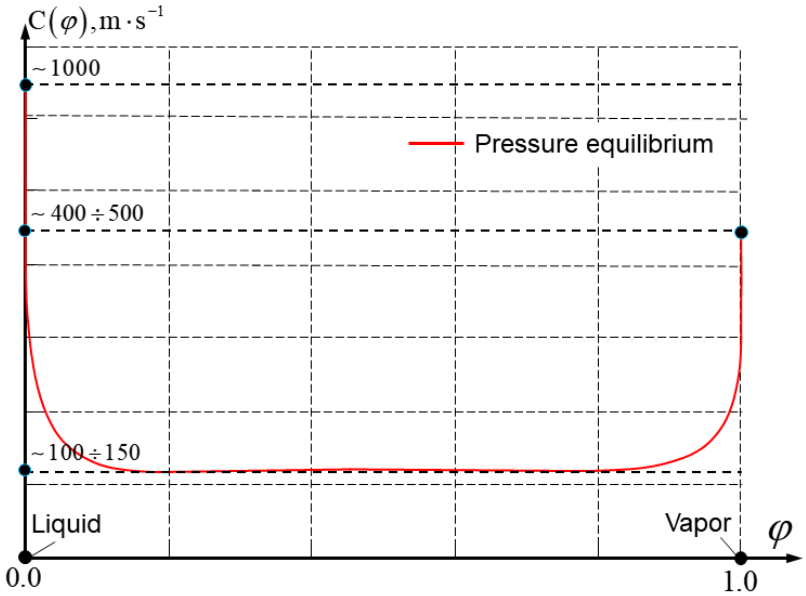

Figure 249: Dependence of the sound velocity of the mixture on the vapor content

The above-listed features require a full-scale reactor CFD model with the most resource-intensive two-phase setup (Filonov et al., 2024). For engineering purposes, there is a “simplification” method that allows to display the main features of the propagation of a decompression shock wave in a three-dimensional setting in a reasonable amount of time (see section 6.2.1).

6.2.1 The concept of representative CFD modelling

From an engineering point of view, the most rational way of thermal-hydraulic calculations is using methods that accurately consider spatial features. In this case, the heat transfer and the intensity of flow energy dissipation are calculated based on experimental correlations. At the same time, the methods must be fast enough to allow multivariate parametric analysis to be performed in an acceptable time.

The modelling method proposed here is intermediate between sub-channel approximation and CFD on a coarse grid. This approach is called “representative” modelling (Diaz-Pescador et al. 2022), which is a compromise between speed and efficiency of calculations of complex elements (sub-channel) using simple formulations for the heat transfer and a fairly accurate description of coolant transport in each direction.

For example, ATHLET (Baikov et al., 2016) is one of the most well-known specialized codes that allow for the three-dimensionality of flow to be taken into account. Figure 250 shows an example of the typical discretization of calculation models of the VVER reactor primary circuit under various approaches. A distinctive feature of each approach is the mesh discretization, which is primarily determined by the presence of subgrid empirical models. Thus, the more complex the processes being calculated within one control volume (ATHLET), the smaller the number of such control volumes can be used (Volkov et al., 2019).

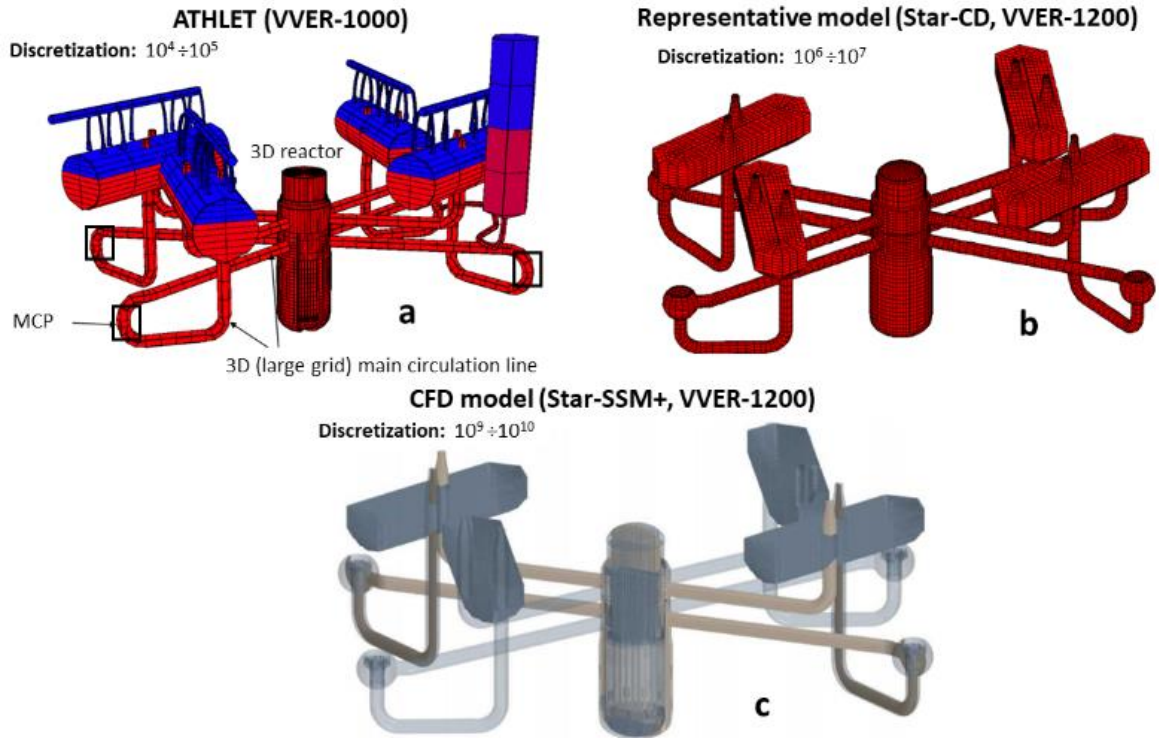

Figure 250: Calculation models of the reactor primary circuit of a VVER type (a – sub-channel, system code, b – representative approach, c – detailed CFD model).

Numerical algorithms limit the allowable detail, although in modern versions of the codes this problem is less important. The representative model (b) (Volkov et al., 2019) is based on universal approaches that use local formulations for physical processes, but only for coolant transport. Herewith, the relatively low discretization density, which generally does not allow modelling processes associated with turbulence (both heat transfer and hydraulic resistance), is compensated by explicit and implicit sub-grid mathematical formulations for heat transfer and hydraulic resistance based on relation (1). This approach makes it possible to simulate physical processes with acceptable accuracy, obtaining a fairly high-quality spatial distribution of fields.

For instance, in the formulations

$$\begin{cases} \nabla \cdot \left(\left(\mu + \mu_t \right) \left[\nabla \vec{U} + \left(\nabla \vec{U} \right)^T \right] \right) \Big|_{\{x,y,z\} \in wall} \approx \underbrace{\xi(\mathrm{Re})}_{PLF \cdot H_{ref}} \rho \dfrac{U_z^2}{2} \\ \nabla \cdot \left(\left[\dfrac{\mu}{\mathrm{Pr}} + \dfrac{\mu_t}{\mathrm{Pr}_t} \right] h \right)_{\{x,y,z\} \in wall} \approx q_v(x,y,z) \end{cases} \quad (1)$$

ξ (Re) is an empirical function of hydraulic resistance and q_v (x, y, z) is a volumetric energy release function.

The most complete approach from the CFD point of view is one that, in addition to detailed geometry, does not use for calculations any additional empirical information regarding the modelled processes and basic flow scalars are calculated by local formulations. Heat transfer processes are calculated using a turbulence model and sources of thermal energy are specified in the fuel core (the most complete case), which makes it possible to simulate the distribution of thermal load, as well as, in special cases, critical heat flux. Sometimes, for simplification, assigned

surface heat fluxes are used. Basically, approaches (a) and (b) are aimed at analysing transient processes, while (c) is used primarily to confirm design values, for example, such as: temperatures in the loops and mass flow rates, uneven velocity fields at the core inlet, the hydraulic resistance of the reactor or of the installation as a whole, etc.

In fact, "representative" modelling involves using a CFD core, introducing special models to account for heat transfer and hydraulic resistance, and formulas for calculating transverse moments of force. Often such approaches require the use of similarity numbers, which are determined by the mass-average (non-local) flow parameters.

6.2.2 Generalization of heterogeneous two-phase formulation for supercritical coolant state

To describe the supercritical state of the coolant with the possibility of transition to a two-phase region, the concept of pseudo-boiling is used (Wang et al., 2021 and Nasuti and Pizzaruti, 2021). The essence of this approach is that a supercritical medium is generally described by a two-phase state with an assumed boiling point in the supercritical region. There are different methods (Figure 251) for determining the continuation of the saturation temperature curve (Widom-line) (Fu et al., 2012 and Banuti, 2021), which are based on different thermodynamic properties of the medium.

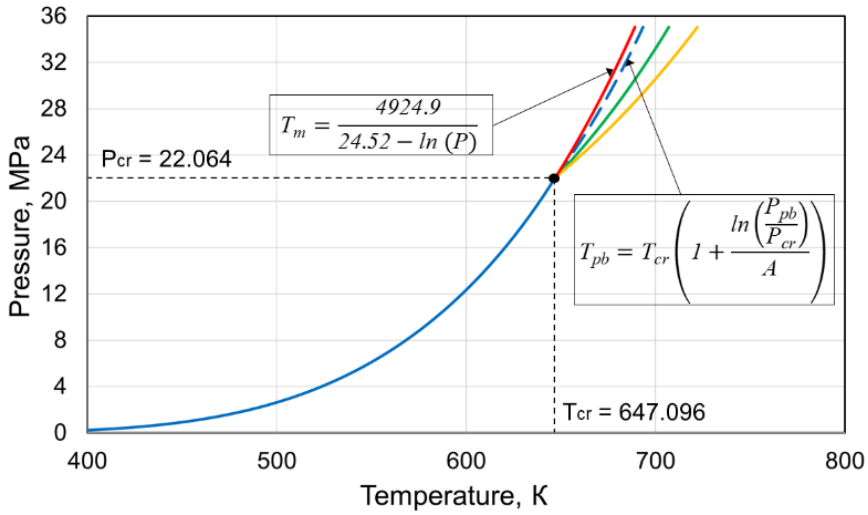

Figure 251: Saturation line with the consideration of supercritical region

The intensity of the non-equilibrium phase transition is determined by dependence expressed in Eq. (2), where the following parameters remain undefined for the supercritical state:

- heat of vaporization (HR);
- characteristic morphological size of interfacial interaction (D_{ref});
- method for determining the intensity of heat transfer between phases (in general, HTC_l and HTC_v).

$$MFT = \left(\frac{6vf}{D}\right) \cdot \frac{HTC_l \cdot (T_s - T_l) + HTC_v \cdot (T_s - T_v)}{HR} \quad (2)$$

Each of these issues requires special attention since there is no reliable evidence for the existence of pseudo-boiling regions and the data on how to describe the supercritical state is still controversial.

By analogy with boiling (in terms of temperature change), during a pseudophase transition the temperature changes quite smoothly (Figure 252).

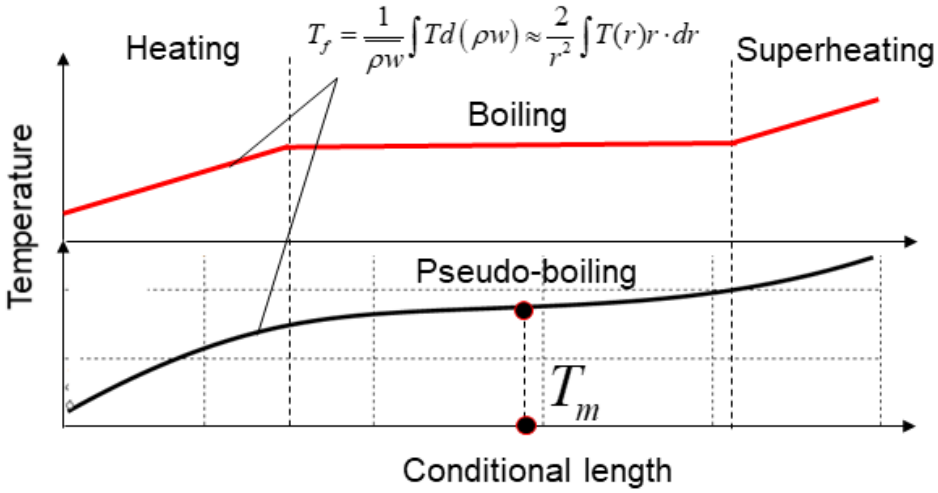

Figure 252: Analogy of boiling and pseudo-phase transition

As a first approximation, we limit ourselves to the question of determining the heat of vaporization HR based on theoretical analysis. To determine the limits at which a pseudophase transition occurs, consider the specific work of expansion forces, which can be estimated as (3).

$$E_q = \left(\frac{p\Delta V}{E}\right) = -\frac{p}{\rho^2 C_p}\left(\frac{\partial \rho}{\partial T}\right)_p \tag{3}$$

Here *E* is the energy supplied to the system [J].

If the flow temperature is $T<T_m$, then the value of the specific work of expansion forces E_q is not large and is of the order of $10^{-3} \div 10^{-2}$, which corresponds to a low-compressibility liquid. For gas media, the value of E_q is in the range of 10^{-1} to $5 \cdot 10^{-1}$. This means that by setting the upper and lower limits of the specific work of the expansion forces, it is possible to determine the lower and upper values of the enthalpy of pseudo-phase transition. The difference of these values will be the heat of vaporization during pseudo-boiling. We assume that the beginning of the phase transition corresponds to E_q=0.04, and the end to E_q=0.2 (see Figure 253).

In spite of its simplicity and theoretical justification, the proposed method, strictly speaking, does not work around the critical point, since the upper and lower values of E_q are not defined. The saturation temperature at pseudo-boiling is assumed to be equal to the pseudo-phase transition temperature T_m [K], and is determined by the approximation dependence (4) (Kurganov et al., 2018).

$$T_m = \frac{4924.9229}{24.5204 - \ln(p)} \text{ [K]} \tag{4}$$

For further calculations in the non-equilibrium model, the following parameters were used. The heat transfer coefficients from the vapor and liquid phases are calculated based on a constant value of the Nusselt number, which for vapor phase is taken equal to 0.0. For the liquid side, the HTC is calculated using the Ranz-Marshall correlation (Ranz and Marshall, 1952) with a characteristic size equal to 1.0 mm. The interfacial surface area is estimated assuming that the

vapor phase morphology is mono-sized bubbles. The interfacial friction coefficient is assumed to be constant and equal to 0.44.

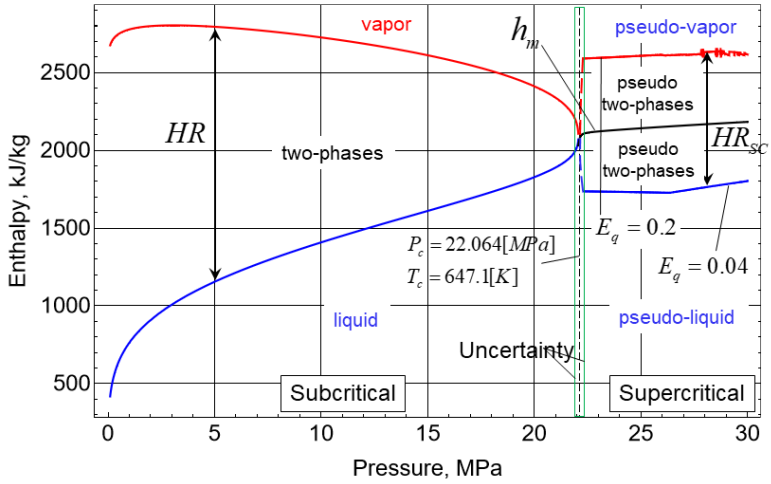

Figure 253: Determination of the specific heat of phase transition

To assess the efficiency of the “expansion” of the non-equilibrium two-phase approach, the classic Edwards test (Edwards and O’Brien, 1970) is considered, which was also calculated at a supercritical initial pressure. To a first approximation, this analysis is correct, since the initial temperature largely determines the established choking pressure. Figure 254 shows the corresponding test results. In this case, the Edwards test only demonstrates the capabilities of predicting decompression at supercritical parameters. The key point of its test was to demonstrate the applicability of the proposed approximation for describing a supercritical medium in a two-component formulation.

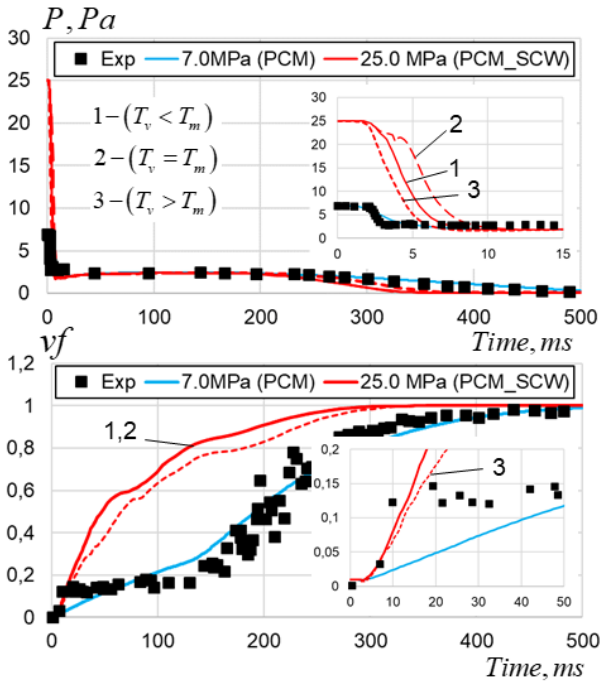

Figure 254: Results of depressurization assessment from supercritical pressure depending on the initial temperature of the vapor phase

Although the Edwards test is strictly speaking inappropriate for supercritical parameters, some important conclusions can be formulated for the initial dynamics. Firstly, the established critical pressure depends little on the initial state, which is quite good from the point of view of assessing loading factors. The second is the intensity of the phase transition which, although fundamentally different in dynamics from the subcritical state, still occurs over relatively prolonged intervals (after 300-400 ms) and also weakly depends on the initial state. All these features are acceptable for the first approximation of assessing the dynamic impacts on the structural elements of a promising reactor and for obtaining sub-critical pressure and temperature fields for subsequent system analysis using MELCOR.

6.2.3 Representative CFD model of the SCW-SMR concept

This section describes the developed representative CFD model of ECC-SMART SCW-SMR concept, the flow part of which is constructed quite accurately (Figure 255a). The reactor core contains 400 fuel assemblies (20×20) and is conventionally divided into 7 levels (Figure 255b) with different numbers of fuel assemblies. The coolant flows through every group sequentially.

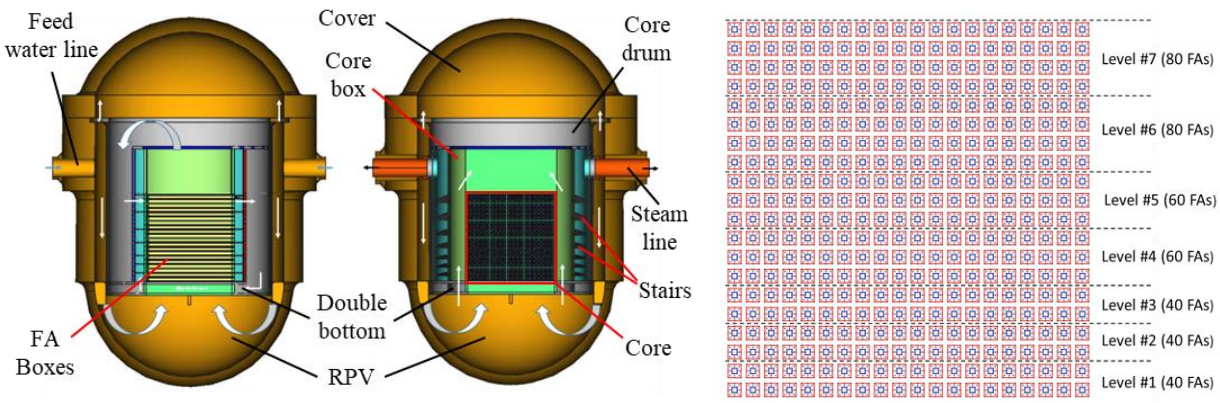

a) b)

Figure 255: The SCW-SMR concept (a) and the core cross-section (b) general view

In the analyses, the cross-section of a fuel assembly was represented in two ways. In the first case, the cross-section is represented accurately: fuel rods are considered, the total number of which is 40 as in Figure 256a. In the second case, the fuel assembly cross-section is simplified as a porous body, only to compensate for the reduced cross-section (see Figure 256b).

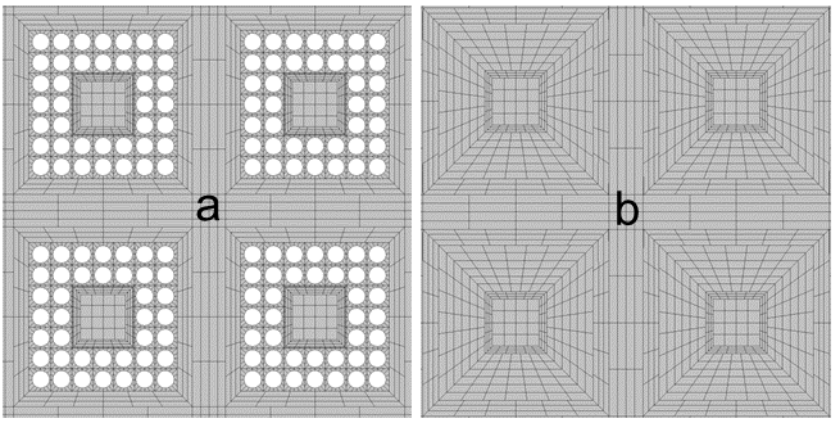

Figure 256: Cross section of the FAs model

The discretization of the computational model is performed according to the approach of "representativeness". The total number of control volumes is $30x10^6$ for the first core variant (Figure 256a), and ~$12x10^6$ for the second one (Figure 256 b). At the same time, the discretization of the rest of the flow path remains unchanged. A general view of the computational mesh for the reactor flow path is shown in Figure 257.

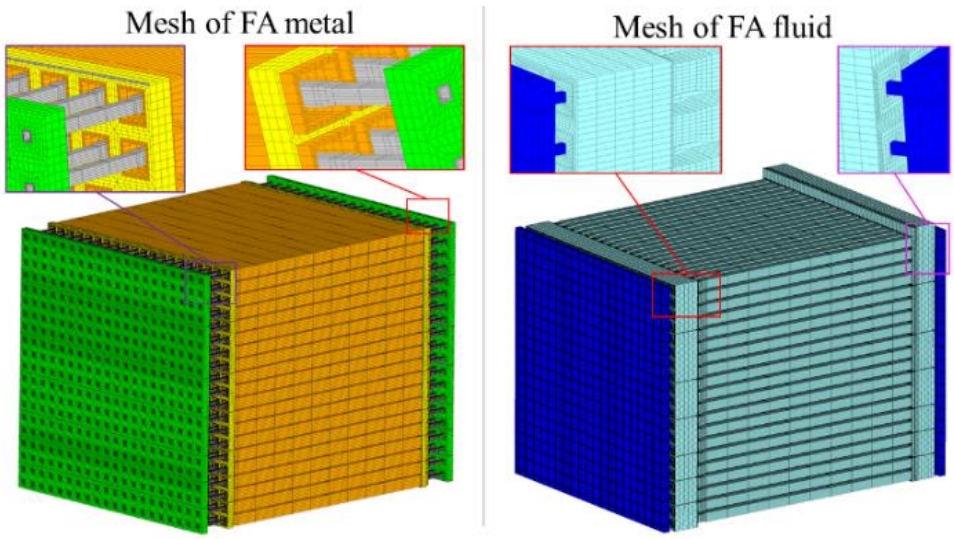

Figure 257: General view of the calculation mesh constructed for the flow part and metal structures of the core

An additional longitudinal momentum term was introduced into the core calculation model, which allows to set the hydraulic resistance of the fuel assembly. The pressure loss factor (PLF) is assumed to be equal to 20 m^{-1}. The energy release in the core was specified as a uniform volumetric source with an integral power of 290 MW. Calculations were performed using ANSYS CFX18. The formulation of equations for a non-isothermal two-phase medium is heterogeneous in speed and temperature. The Euler-Eulerian approximation is used to describe the phases. The boundary conditions for the steady state are shown in Figure 258. The reference pressure is 25 MPa.

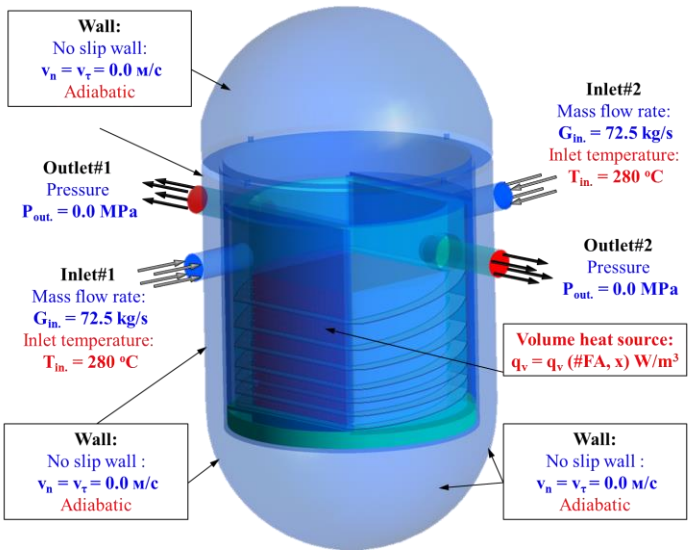

Figure 258: General view of the calculation model and boundary conditions specification applied for the steady state regime

The steady state was calculated for the nominal power operation parameters, as well as for the initial state of the “hot zero power” regime. Figure 259 shows the main parameters of the nominal power operation (290 MW) with the uniform heat generation field.

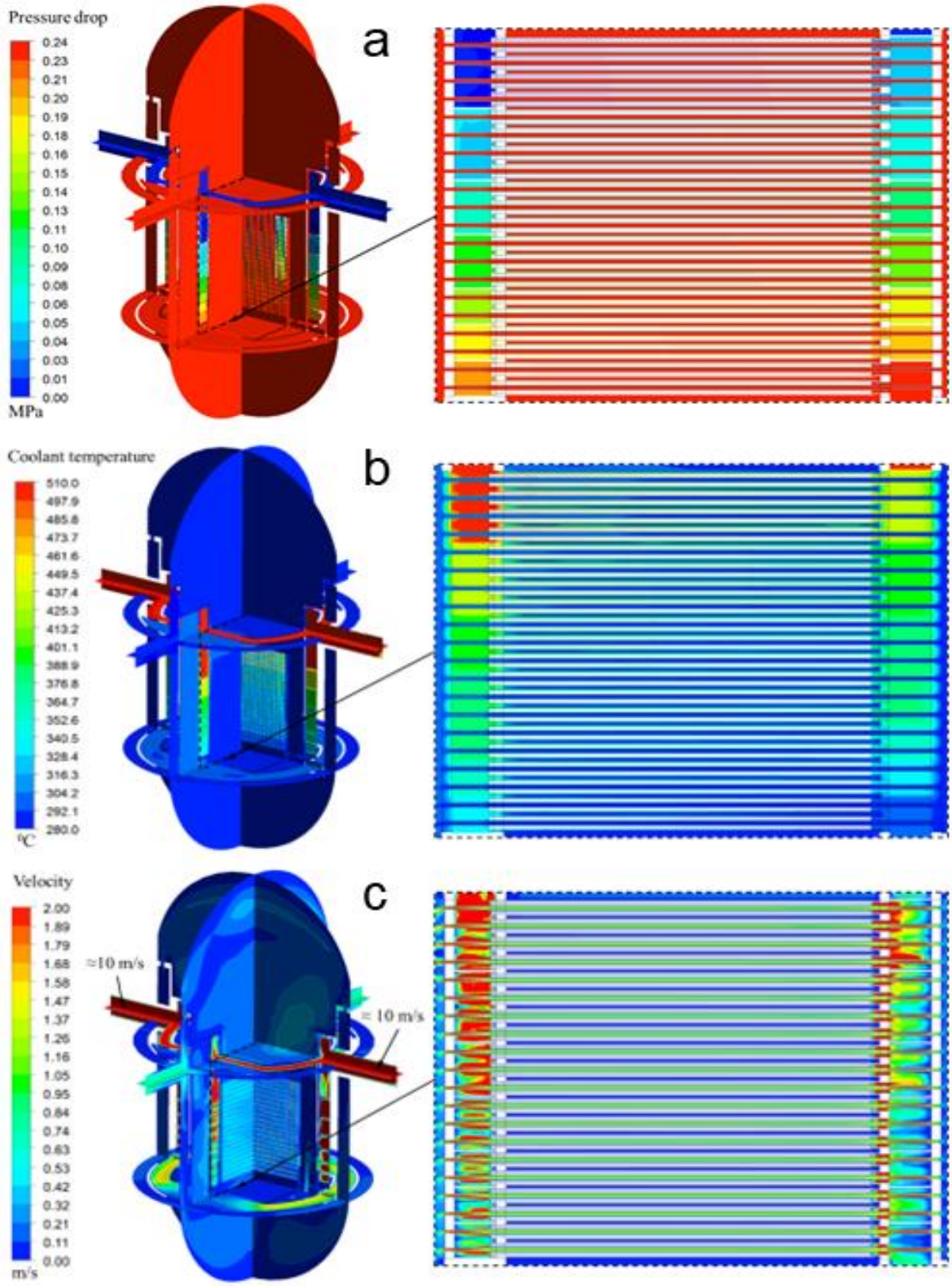

Figure 259: Steady state conditions for operation at the nominal power
(a – pressure drop, b – coolant temperature, c – velocity)

6.2.4 CFD calculations of the decompression wave propagation during LB LOCA initial dynamics and assessment of corresponding dynamic loads

To perform the calculations of the initial dynamics of LB LOCA, an instantaneous break of a cold leg is considered (Inlet#1, see Figure 258) for three options:

- Option #1 – single-phase formulation for the entire range of pressure changes, with initial conditions of “hot zero power”;
- Option #2 – two-phase formulation with generalization to the supercritical state (approach described in section 6.2.2), with initial conditions of “hot zero power”;
- Option #3 (test) – single-phase setting for the entire range of pressure changes, with initial “Nominal power” conditions.

The IAPWS-IF97 library, which is built into ANSYS CFX, is used to calculate thermophysical properties.

A duration of 0.250 seconds of transient decompression sequence was considered, with a time integration step having a minimum of 10^{-5} s and a maximum of 10^{-3} s, using a first order approximation of the time derivative (implicit scheme). The boundary conditions at the break (Inlet#1, see Figure 258) are replaced with “soft” far-field conditions (of “Opening” type), with a reference pressure of 0.1 MPa and temperature of 100 °C.

The practice of performing a similar analysis for the subcritical reactor VVER-1000 (Dang et al., 2021 and Wang et al., 2021) shows that the estimated loads in this case are maximum due to the absence of choking pressure and the higher average coolant density.

Calculation options #1 and #2 are considered to directly assess dynamic forces with subsequent strength analysis. The third calculation (option #3), taking into account the energy release in the core, still requires analysis and testing, especially for two-phase formulation with pseudo-boiling. The problem here is the rather large internal energy of the coolant which, with a sharp drop in pressure, leads to rapid coolant expansion, which causes backpressure and, based on the preliminary results of testing in a two-phase formulation, to explosive behavior of the phase transition.

However, the calculation from the initial state (Figure 259) of operation at the nominal power level (Option #3) was considered and the obtained result in terms of sub-critical pressure and temperature distributions were used for subsequent analysis in MELCOR (see section 6.3). In this case, the influence of changes in density (primarily the moderator) on the integral power in the core was assessed by a simple relation, which, to a first approximation, is presented in the form of Eq. (5) and estimated based on the neutronic characteristics of the fuel assembly.

$$Q(t) = Q_0 \cdot 2.3^{0.0145\left[\vec{\rho}(t)-\vec{\rho}_0\right]} \tag{5}$$

where Q_0 and ρ_0 are the initial integral thermal power and average coolant density in the core.

The dynamics of pressure changes for the selected calculation options is shown in Figure 260. The obtained results show that for the initial state of “hot zero power, " the decompression wave generally moves unhindered to the reactor outlet boundary. Herewith, the change in pressure in the core occurs when the pressure in the coolant of the moderator and reflector has already dropped significantly, which can cause significant shock loads. This is primarily due to the complexity (multi-level) of the flow part of the proposed concept, which is probably its significant drawback compared to direct-flow supercritical pressure reactors.

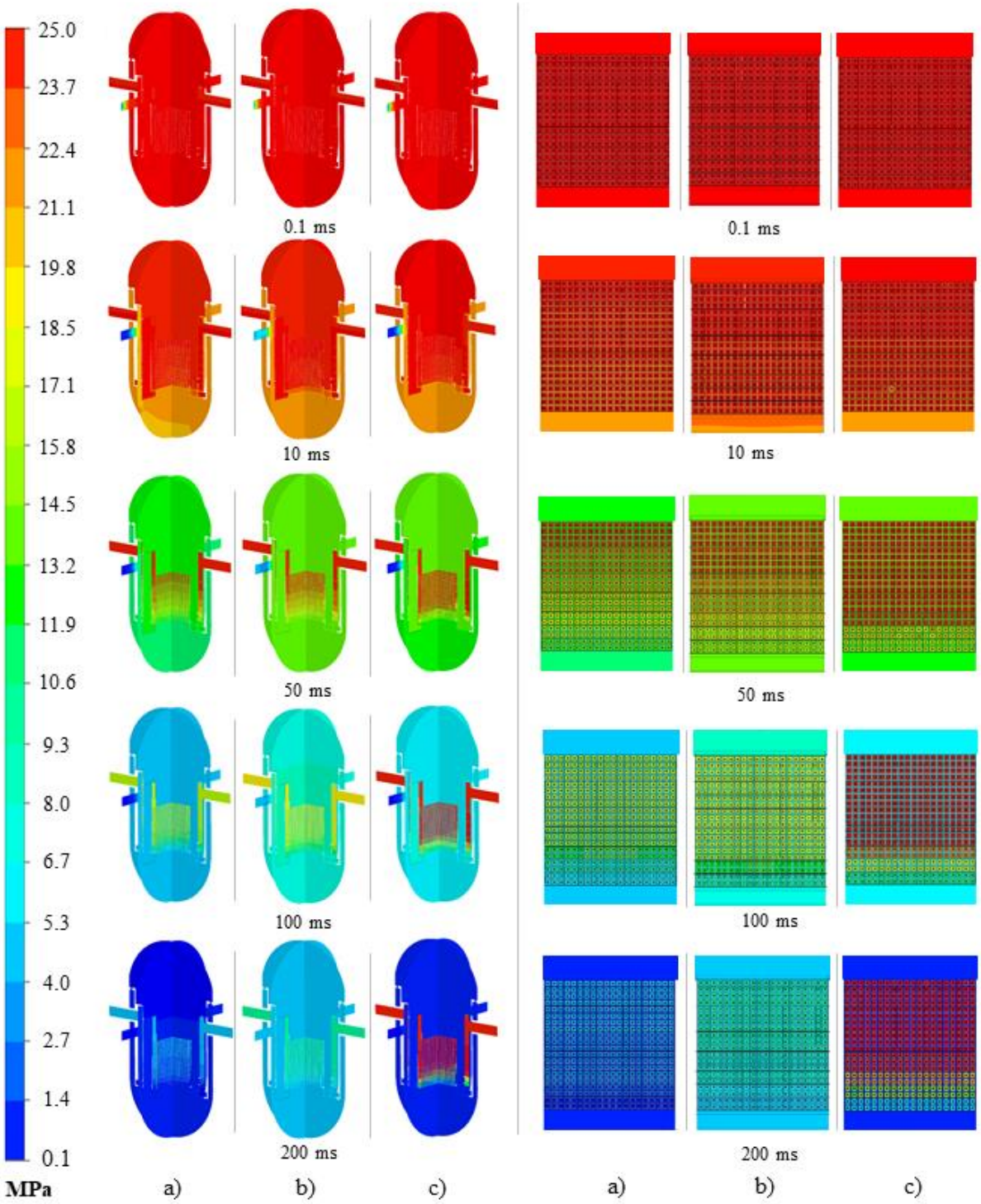

Figure 260: Dynamics of the pressure field change (a – Option #1, b – Option #2, c – Option #3)

Estimation of the decompression wave propagation in the presence of energy release in the core (Option #3) leads to the fact that pressure rise occurs due to expansion of the coolant, which will generally lead to higher peak loads. In addition, due to the expected presence of a fairly strong dependence of power on coolant density, fluctuations in thermohydraulic parameters may also be observed. It is also important to note the fact that after the disturbance reaches the boundary at the reactor outlet, calculations of the dynamics of the decompression wave behaviour

can be significantly distorted. Generally, it will require additional boundary conditions, which can be formulated based on a preliminary system analysis.

The forces on selected reactor structural elements that divide the coolant flow (stairs between core levels, moderator tube and fuel assembly box) were estimated based on the total pressure drop. Figure 261 shows the dynamics of changes in the maximum pressure drop along the length of the fuel assembly, as well as for different FA levels (stairs).

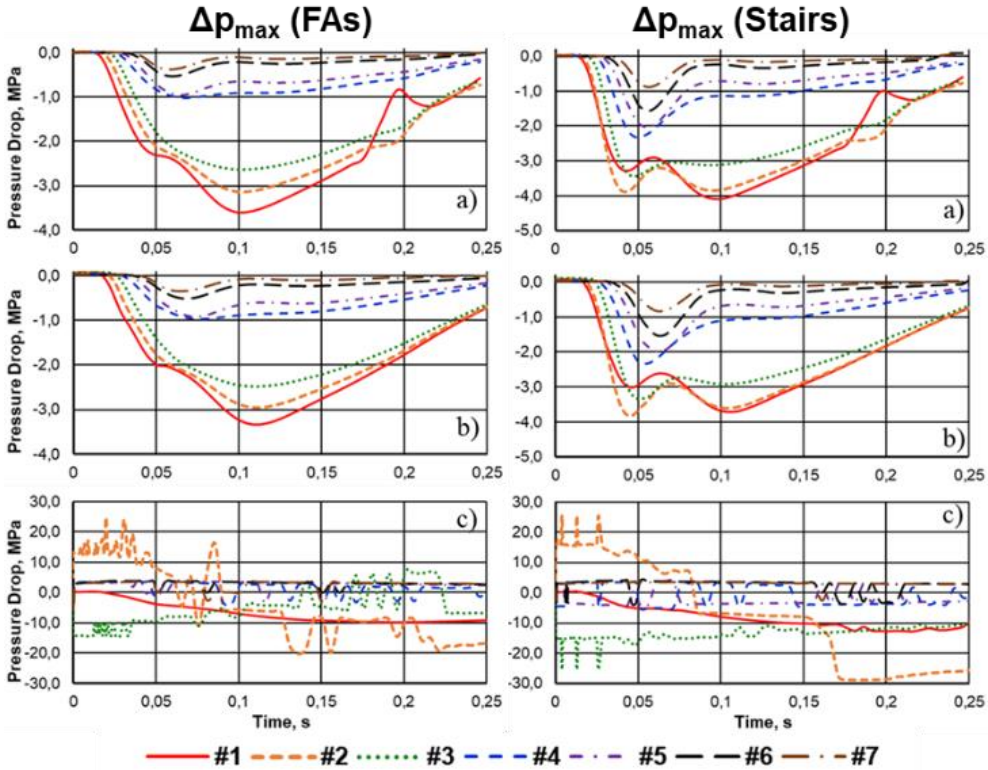

Figure 261: Dynamics of changes in the maximum total pressure difference along the length of the assembly and stairs for each of the levels (a – Option #1, b – Option #2, c – Option #3)

Figure 262 shows the dynamics of the maximum pressure difference between the medium in the fuel assembly and the reflector, as well as between the fuel assembly and the moderator. It can be seen that for Option #3 there are fluctuations in parameters, including a local increase in pressure in the fuel assembly due to expansion of the coolant.

Based on the obtained dynamic parameters of decompression, it is appropriate to evaluate the structural strength of the fuel assembly box. Although a single failure will most likely not lead to a critical loss of the core box's load-bearing capacity, the fuel assembly potential destruction is a subject for discussion and optimization of the chosen concept.

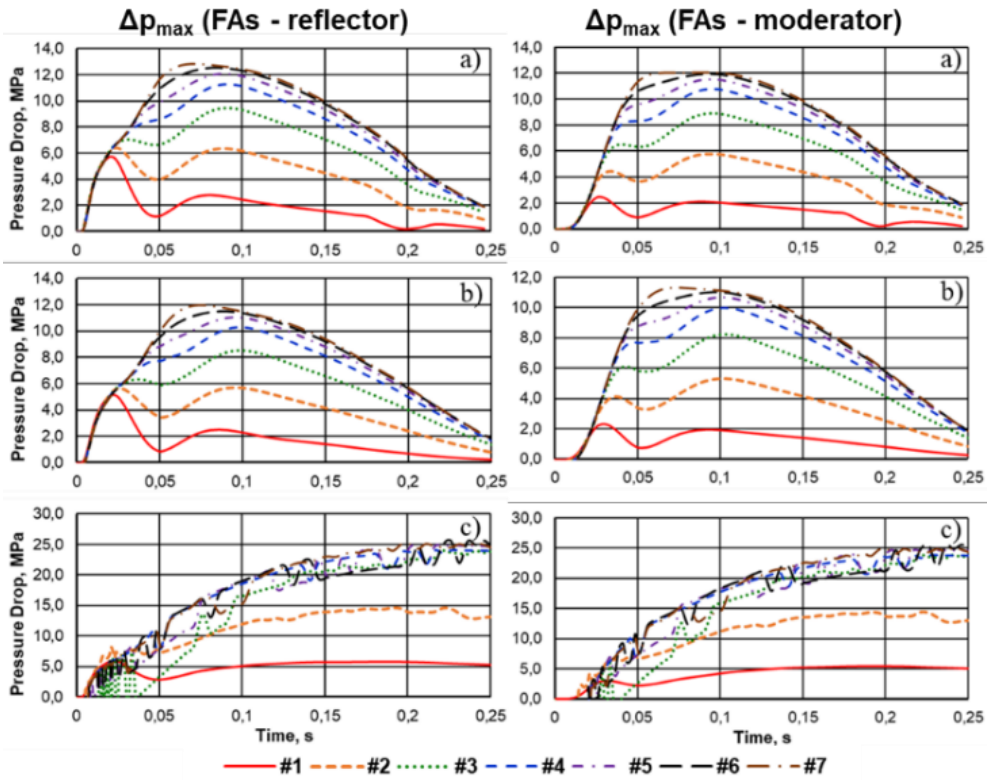

Figure 262: Dynamics of changes in the maximum total pressure difference between FAs and the reflector/moderator for each of the levels (a – Option #1, b – Option #2, c – Option #3)

The stress assessment of fuel assembly box was performed for two calculation options - Option #1 and #2 (Filonov et al., 2024). For this purpose, a simple but robust linear 2D FE model with a generalized plain strain option was created, consisting of 4351 Nodes and 1260 Elements. The model includes all the layers made from stainless steel, Zircalloy, and Zirconia. Only a quarter part of the assembly box was created, the cut parts are replaced by the corresponding BC (frictionless support). Estimation calculations performed using ANSYS Mechanical. The results of the FE analysis are presented in Figure 263.

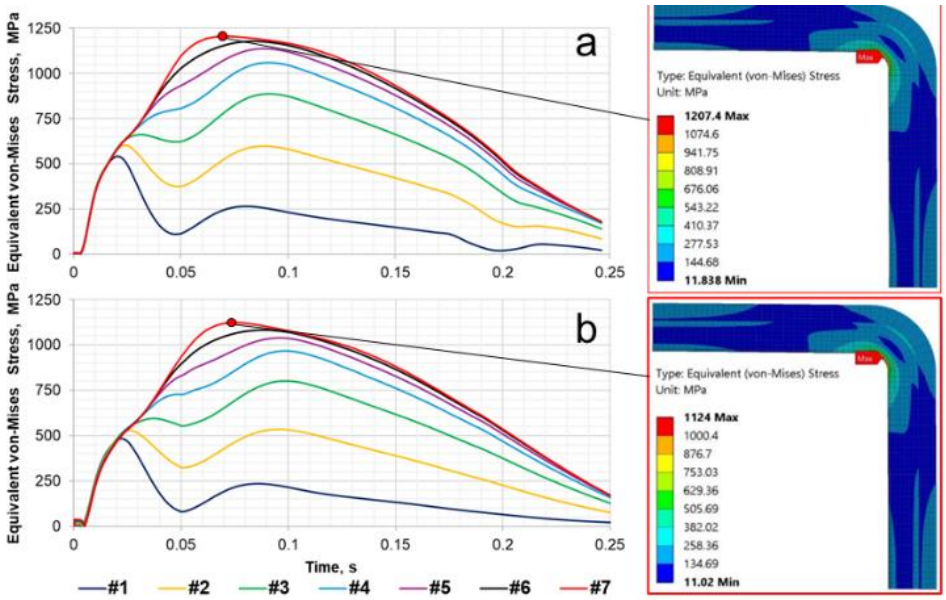

Figure 263: Maximum equivalent von Mises stress (a – Option #1, b – Option #2)

A non-linear model was also adopted to clarify the results of the analysis. In this case geometrical (large deflections) and contact (frictional with coefficient 0.1) non-linearities are included in the model. Physical non-linearities, i.e. plasticity effects are disregarded, since due to the neutron irradiation assembly box materials become very brittle and the ultimate strength is almost equivalent to yield strength. Calculations are done only for the Level #7, as the most loaded one. The new results for Option #1 and #2 are shown in Figure 264.

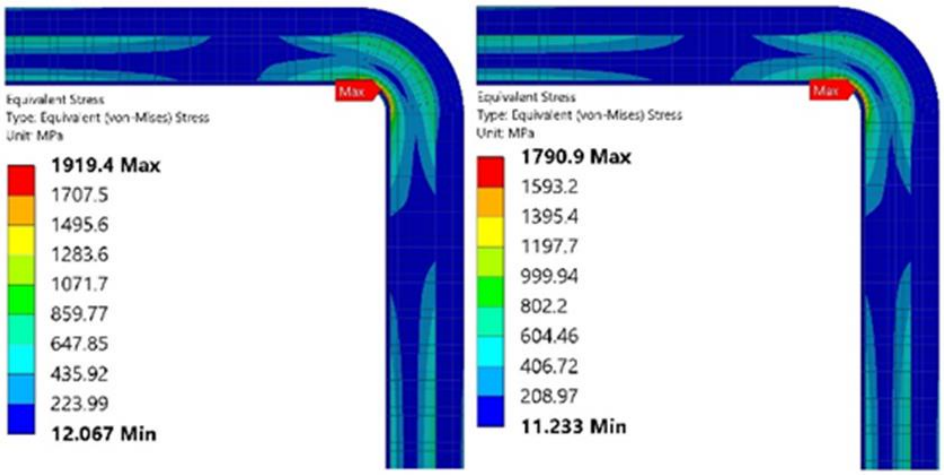

Figure 264: Maximum equivalent von Mises stress (left – Option #1, right – Option #2) non-linear case, level #7

A comparison of Figure 263 and Figure 264 shows some stress redistribution and an increase in stress values for the non-linear case, but the maximum stresses are still observed on the same time step as for linear analysis. Nevertheless, the same conclusion can be drawn for non-linear analysis: obtained lower stresses for Option#2 (lower pressure drop), but still stresses are too high, thus structural integrity is not maintained. It is most likely that Assembly Box will collapse, due to the high dynamic loading. It should be noted that the elastic (linear) analysis is quite sufficient for such kind of problem, as fast and robust results are provided, which is very important on the design stage.

6.3 Stage 2. MELCOR code application for SCW-SMR core degradation analysis

As mentioned in chapter 6.1, the basis for this approach is the fact that the code represents the actual reactor internals region in the core modelling domain (COR package), in the form of an axisymmetric cylinder. This cylinder is divided into concentric radial rings and axial levels by height (see Figure 265). Thus, in terms of SA progression under postulated core dry-out conditions, it makes sense to try using the tool in an equivalent approximation of the mass distribution. Moreover, the conceptual SCW-SMR lower plenum design is similar to a typical PWR.

For horizontally located SCW-SMR fuel channels, the grid space division in the radial direction is maximised (limited by the code to a maximum of 9 rings), and the option of the BWR reactor type is used to consider the fuel assembly boxes design.

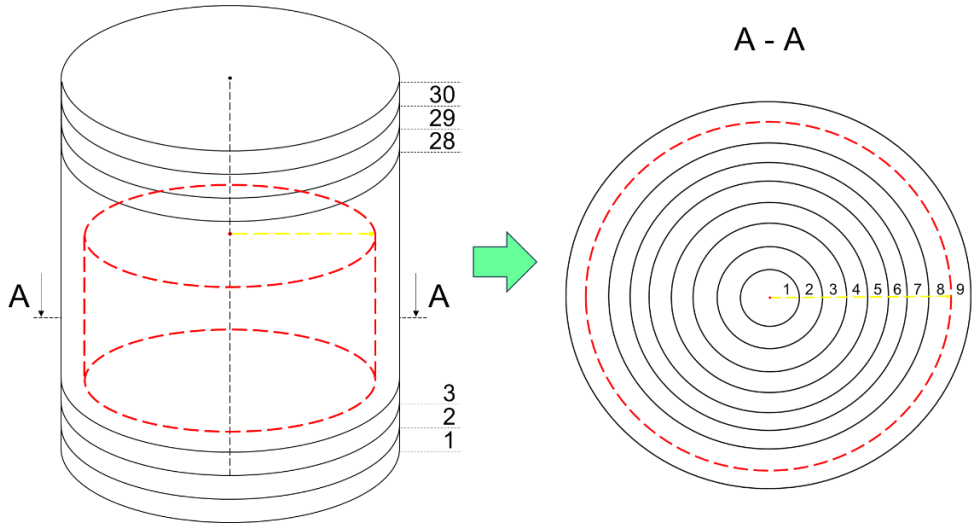

Figure 265: Representation of the modelled SCW SMR internal region in MELCOR

The evaluation of the formed melt in the reactor core and lower plenum is performed for the following thermodynamic initial conditions:

- "dry, at the saturation line" LP region, without flooding of the RPV cavity;
- "dry, at the saturation line" LP region, with flooding of the RPV cavity;
- "wet, at the saturation line" LP region, without flooding of the RPV cavity;
- "wet, at the saturation line" LP region, with flooding of the RPV cavity.

The "dry" LP region is understood as the state when the coolant has boiled off and there is a minimal amount of water in the liquid phase. "Wet" is interpreted as the presence of most of the coolant in the liquid phase in the LP volume, by the time of the end of depressurization process. The argument for postulating that condition is a design feature of the SCW-SMR concept, which determines a complex hydraulic characteristic of the core flow.

In fact, these bounding computational scenarios help to fulfil the objectives of the stage task, taking into account important physical phenomena occurring during the in-vessel SA late phase:

- melt candling, spreading and forming the local pool at LP;
- its rapid cooling ("quenching") during submersion in LP medium;
- convection and heat transfer in the melting pool.

Moreover, the proposed approach allows to obtain the estimated mass characteristic of the melt in the LP, reference temperatures and time characteristic of the emergency procedure "with" and "without" actions of the reactor concrete cavity flooding.

All selected scenarios in the absence of cooling water supply to the reactor vessel will predictably lead to core damage, degradation, and formation of a liquid "corium" pool in the LP lower part, that will inevitably end by heating and further melting of the reactor vessel metal, and its potentially early rupture.

6.3.1 SCW-SMR core input general description for MELCOR code

The inner reactor vessel volume, including the upper, lower plenum, core, upward and downward peripheral regions, is divided into 30 axial segments in height and 9 rings in the radial direction. The first 8 rings are assigned to the reactor core. The inner core hull side plates, as well as other outside metal structures and elements, are defined by boundary heat structures. The nodalization scheme of the core volume space included in the modeling region, is presented in Figure 266.

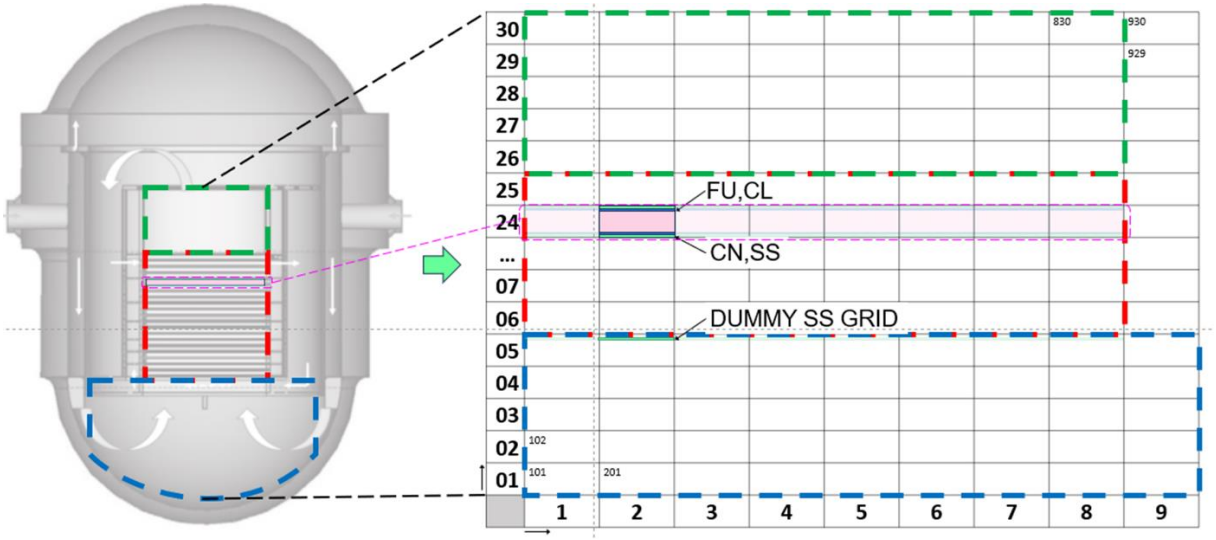

Figure 266: SCW SMR core nodalization scheme in MELCOR

The first five axial segments represent the volume of the lower plenum. The last one consists in the bottom dummy “grid” of the reactor core box in the part of the large square window for the coolant flow into the inter-box space. The reactor core, made of a system of parallel horizontal fuel assemblies, is uniformly divided into 20 levels (from level 6 to 25). The height of one level is taken to be 0.1 m so that geometrically it would correspond to the size of one fuel assembly. The upper plenum volume is allocated in the last 5 levels. The axial and radial power density profiles are applied uniformly to a first approximation. This assumption is acceptable for the first stages of the safety analysis of the pre-conceptual design and should be clarified in the course of further work. From the centre to the periphery, the core is divided in such a way that in the radial rings the mass characteristics of structural components of fuel, materials of cladding and fuel assembly boxes are distributed uniformly (see Figure 267).

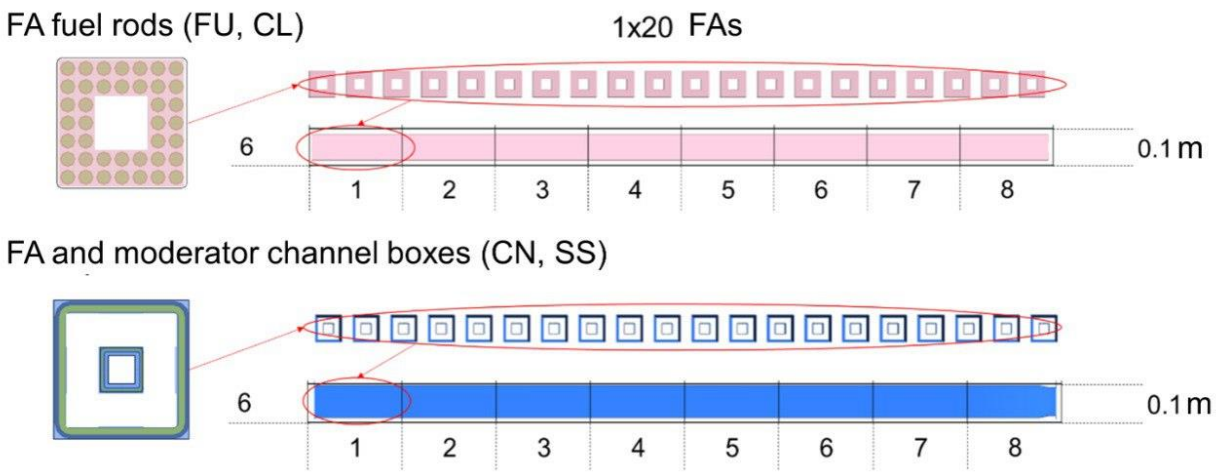

Figure 267: General approach to mass distribution of core structural components

To emphasize the FA boxes “holding” ability, to limit the movement of the melt in the axial direction, their mass is taken into account by the structural component of the “SS” type. Also, from an engineering point of view, the space of the square opening at the 5th axial level contains a mass of the dummy “support grid”. This allows to avoid early movement of molten materials from the upper axial levels into the lower plenum. In fact, this can also be attributed to the influencing

factor of the “early” melt reactor vessel body contact time during SA for the current pre-conceptual design of the SCW-SMR nuclear reactor.

The core boundary is determined by its internal location in the nuclear reactor. Radially, it is adjacent to the casing plates, which are defined as radial thermal structures, divided along the height into individual heat structures (see Figure 268) and axially at the top core limited by the upper plate of the reactor drum.

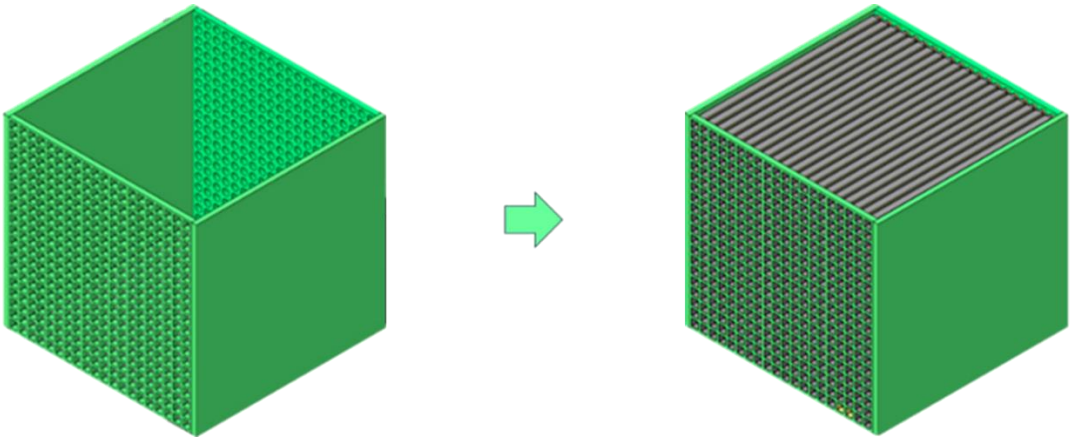

Figure 268: Core internal radial boundary structures

In the MELCOR calculation code, the specified thermal power is formed as the sum of the fission power and the residual energy release caused by decay heat. In this case, only the first component was set when operating at 100% power, which corresponds to the value of 290 MW. It is assumed that the calculation starts from 0.0 s, already after the SCRAM signal, so the residual heat power curve is determined by the calculation code in accordance with the ANS 5.1 standard (American Nuclear Society, 1994) and graphically illustrated in Figure 269; in the figure, the metal oxidation reactions rates for all calculation scenarios are added for magnitude comparison.

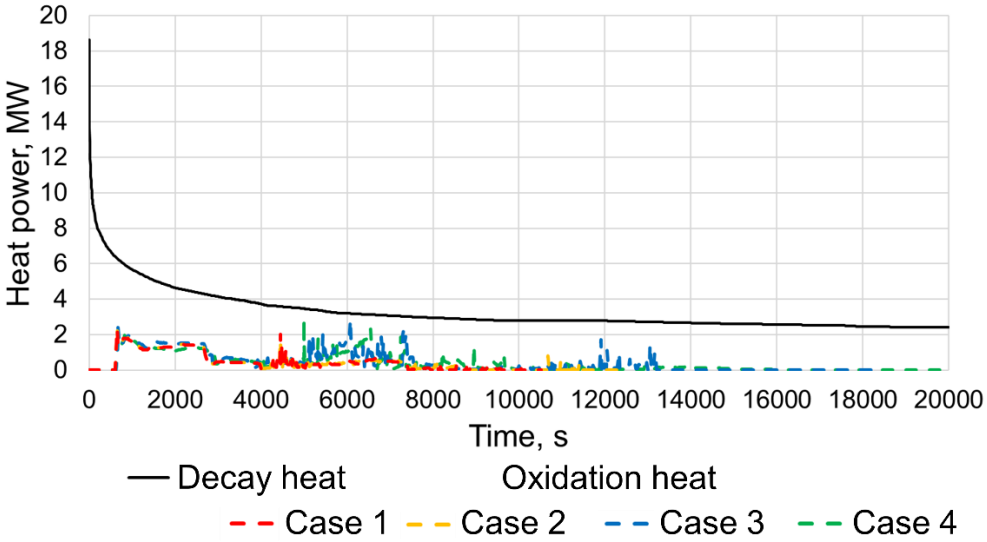

Figure 269: Heat generation sources rates in the core

It should be noted that the additional heat by the metal oxidation reaction (dominantly is the oxidation of Zircaloy by steam reaction) reaches high values. Fuel radionuclides masses, as well as the corresponding residual energy release functions by their classes, are not specified in the input deck.Molten materials characteristics and core state assessment during SA

This subsection describes the computational analysis of four representative scenarios performed using the developed MELCOR model. A large break LOCA is set as the initial event of the accident, which leads to a rapid pressure decrease in the nuclear reactor to the sub-critical level. The initial thermodynamic state of the SCW-SMR for analysing the early in-vessel stage of a severe accident is taken according to the results of the CFD calculation carried out at Stage 1. As for ex-vessel parameters in the sub-reactor compartment, in order to obtain a greater heat transfer from the RPV bottom surface, it is conservatively assumed that the initial water is subcooled with respect to saturation temperature of 10 degrees only.

The initial conditions applied for all four calculation cases are described in Table 19.

Parameter	Case 1	Case 2	Case 3	Case 4
Initial decay heat power	18.6 MW	18.6 MW	18.6 MW	18.6 MW
Reactor coolant pressure	6.4 MPa	6.4 MPa	6.4 MPa	6.4 MPa
Reactor coolant temperature	280 ^{o}C	280 ^{o}C	280 ^{o}C	280 ^{o}C
Initial reactor LP coolant level	-	-	2.8m	2.8m
IVMR system water temperature	-	90 ^{o}C	-	90 ^{o}C
Reactor cavity pressure	0.1 MPa	0.1 MPa	0.1 MPa	0.1 MPa
Reactor cavity water level	-	3 m	-	3 m

Table 19. MELCOR initial conditions for the SCW-SMR SA progression analysis

It is postulated that the reactor concrete cavity compartment is already flooded at the time of 0.0 s of calculation run to the level of 3 m, which is maintained during the transient. The schematic view of the thermal hydraulic nodalization for in-vessel and ex-vessel reactor volumes is shown in Figure 270.

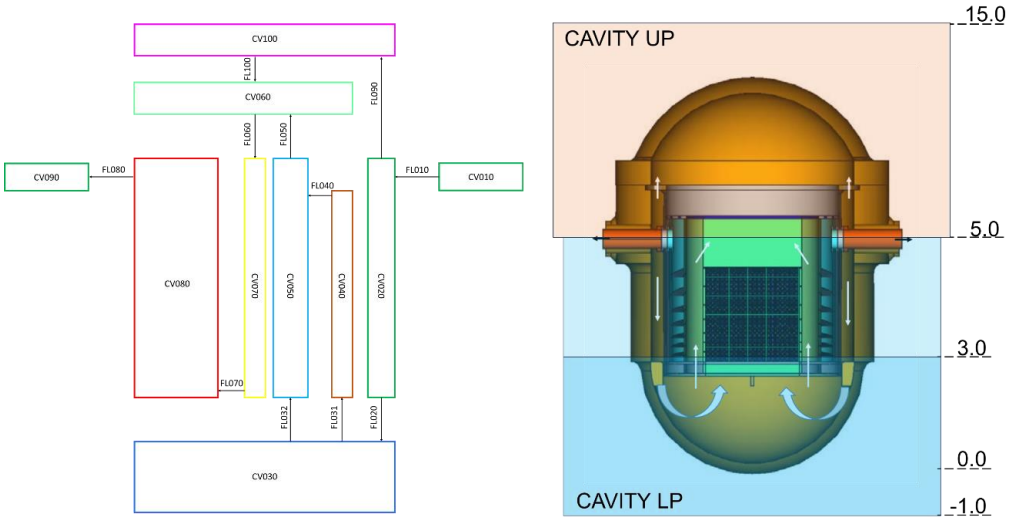

Figure 270: Reactor in-vessel TH scheme and cavity schematic view

Rapid boiling off and irreversible loss of coolant leads to a quick decrease in the core level and its early drying. The fast core dry-out at a sufficiently high residual power density level determines the beginning of its heating and further overheating. The temperature of fuel rod cladding quickly increases, causing oxidation reactions and melting processes.

From this moment, the calculation scenarios can be divided into two subgroups depending on the presence of liquid water in the reactor's lower plenum.

For the first two scenarios with a “dry” LP, the sequence of events is as follows. As the core temperature increases, many rod cladding areas begin to melt. Considering the peculiarity of the location of fuel channels and the presence of FA boxes, the logical condition for the potential movement of liquid metal and not melted fragments is imposed. Namely, movement along the downward axis is “allowed” only when 90% of the material mass of the multilayer fuel assembly boxes is melted. This leads to more accurate modelling of the predicted behaviour of the SCW-SMR internals during its degradation. The candling physical model is not turned off; therefore, the movement of the melt is accompanied by its periodic solidification and melting. This primary stage of the sequential FA failure along the height of the core, until the accumulation of a liquid metal pool and debris (fragments) on the “dummy” support structure, takes about two hours. Further, under the influence of temperature, the melt begins to flow downward into the LP after the support grid structure failure. The increase of thermal loading on the inner surface of the reactor vessel bottom happens right after. Since that time, it begins to consequently heat up. An hour later, after reaching the “plastic uncertainty” condition of the steel, the integrity of the reactor vessel is lost. Concrete reactor cavity flooding allows to shift the time of reactor vessel failure (RFV) by an hour; however, the arrest of the melt does not occur.

For the calculated scenarios of the second subgroup, where the LP is “wet”, the initial sequence of reactor core degradation is similar to the first one, but the presence of water in the liquid phase significantly influences the late phase of SA. The contribution to the total energy release of exothermic oxidation reactions almost doubles. The portion of reacted zirconium and the liquid phase fraction of this metal in the metal pool increases. A high hydrogen mole fraction in the degraded core volume and an average gas temperature are noted. As for the time sequence characteristics, the boiling of LP water allows more intensive heat removal of the residual energy that particularly accumulated in FA fragments and ensures corium cooling. The external flooding of the concrete cavity further shifts the reactor vessel failure time. However, it is still not possible to maintain its integrity.

A summary of the SA chronology for all scenarios is shown in Figure 271 to Figure 274, while the overall characteristics of the LP molten materials for the quasi-stationary state (close to the end of run time), are summarized in Table 20, where their masses and distribution in LP are illustrated by diagrams and graphs in Figure 275 to Figure 276.

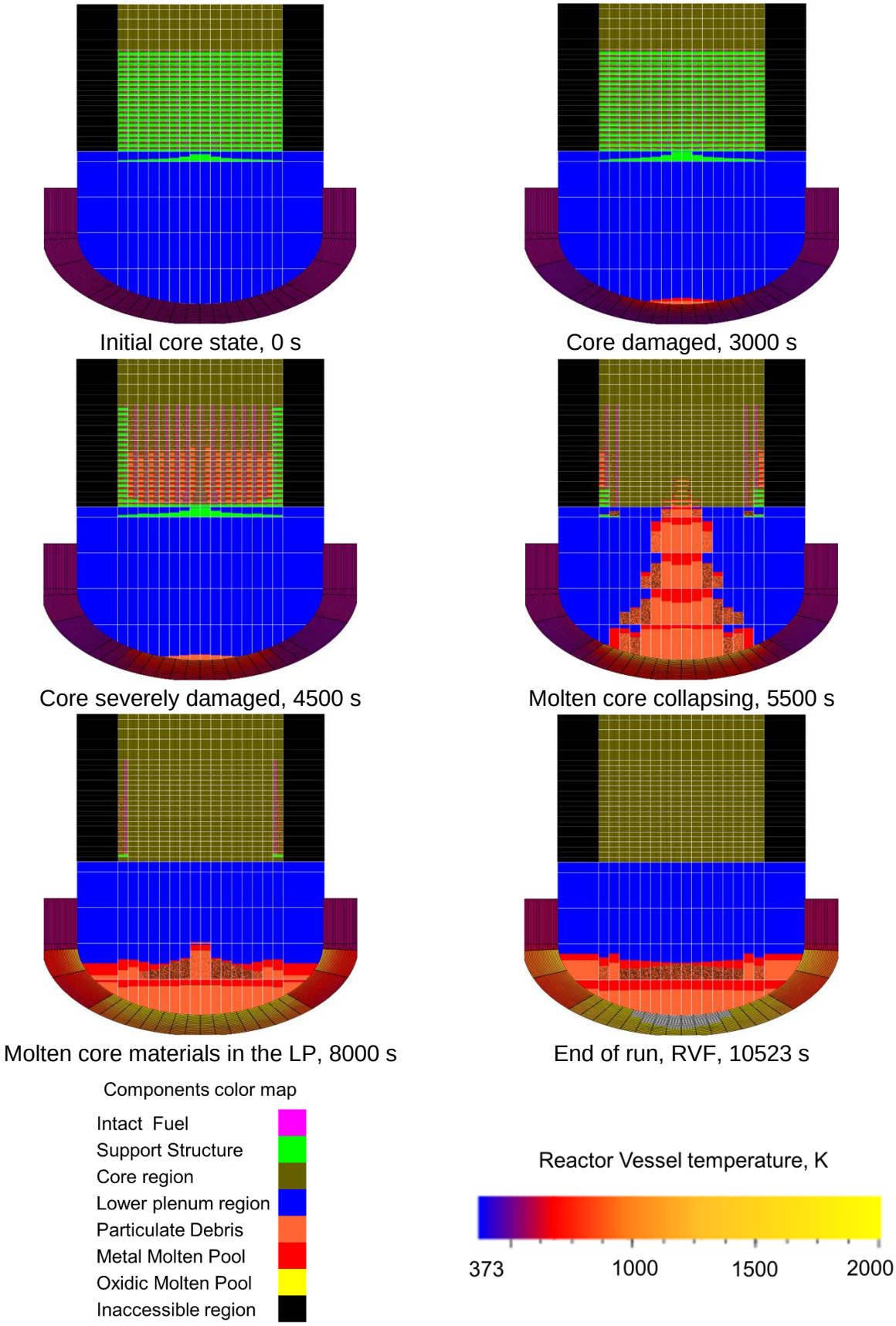

Figure 271: Case #1. SA chronology

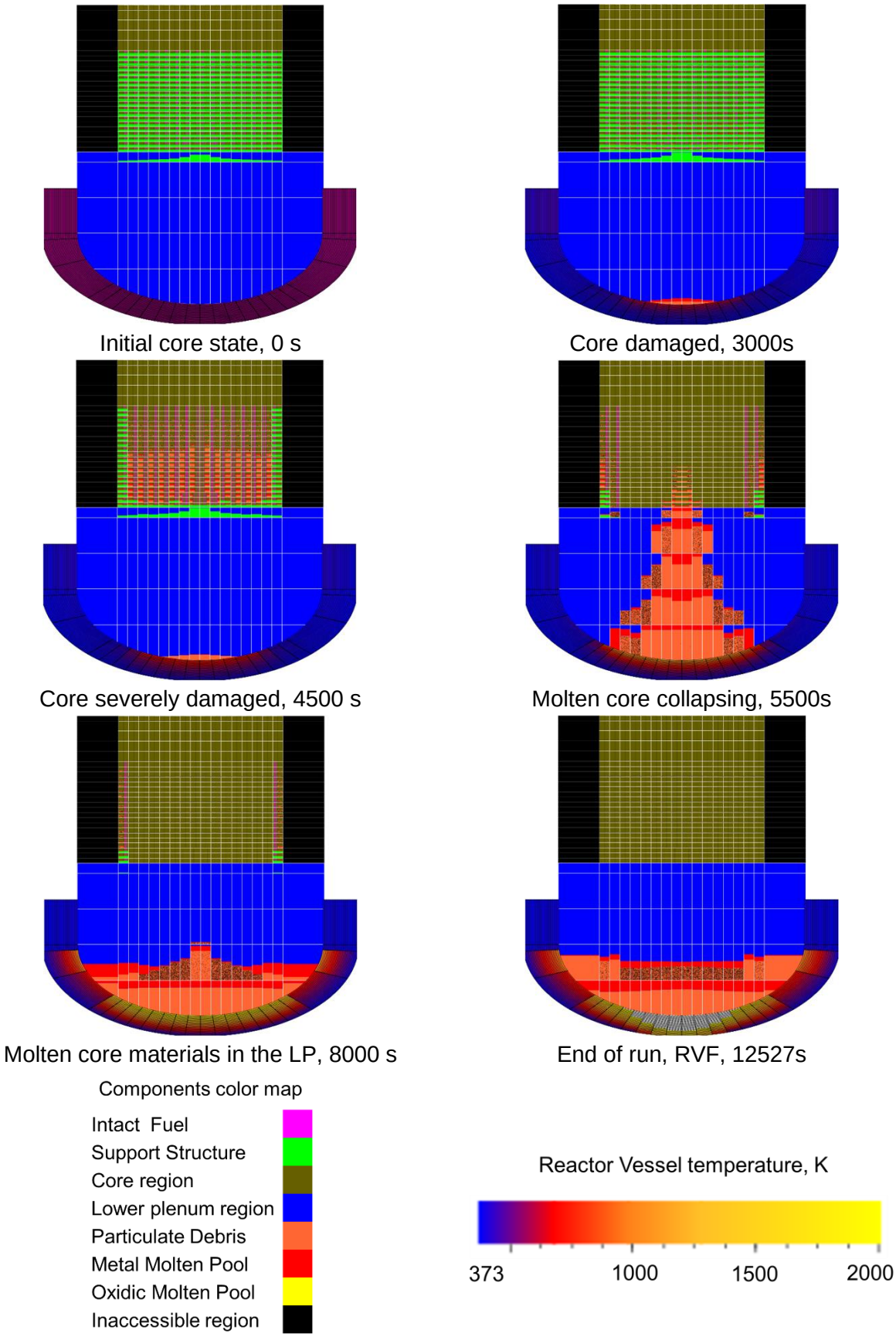

Figure 272: Case #2. SA chronology

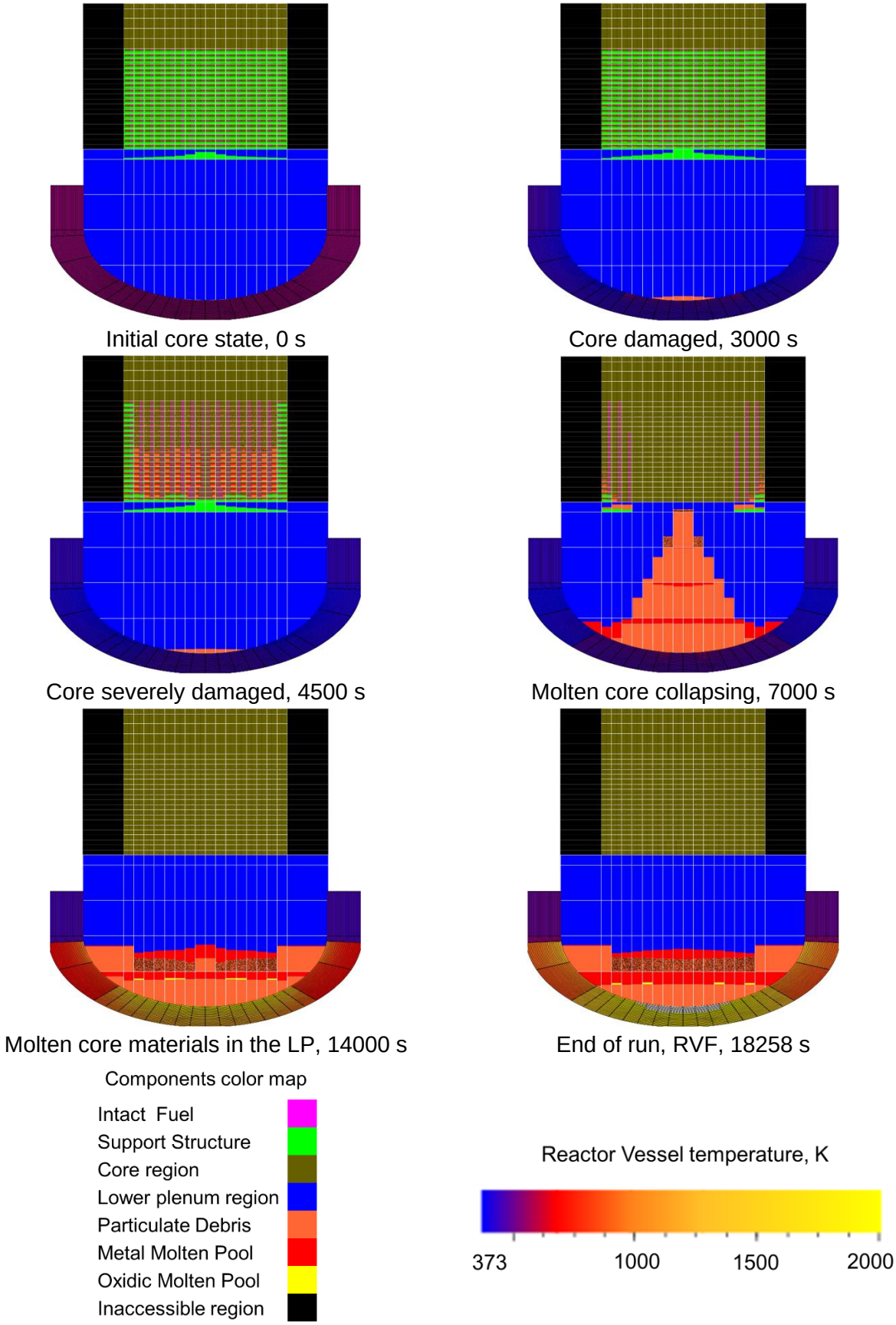

Figure 273: Case #3. SA chronology

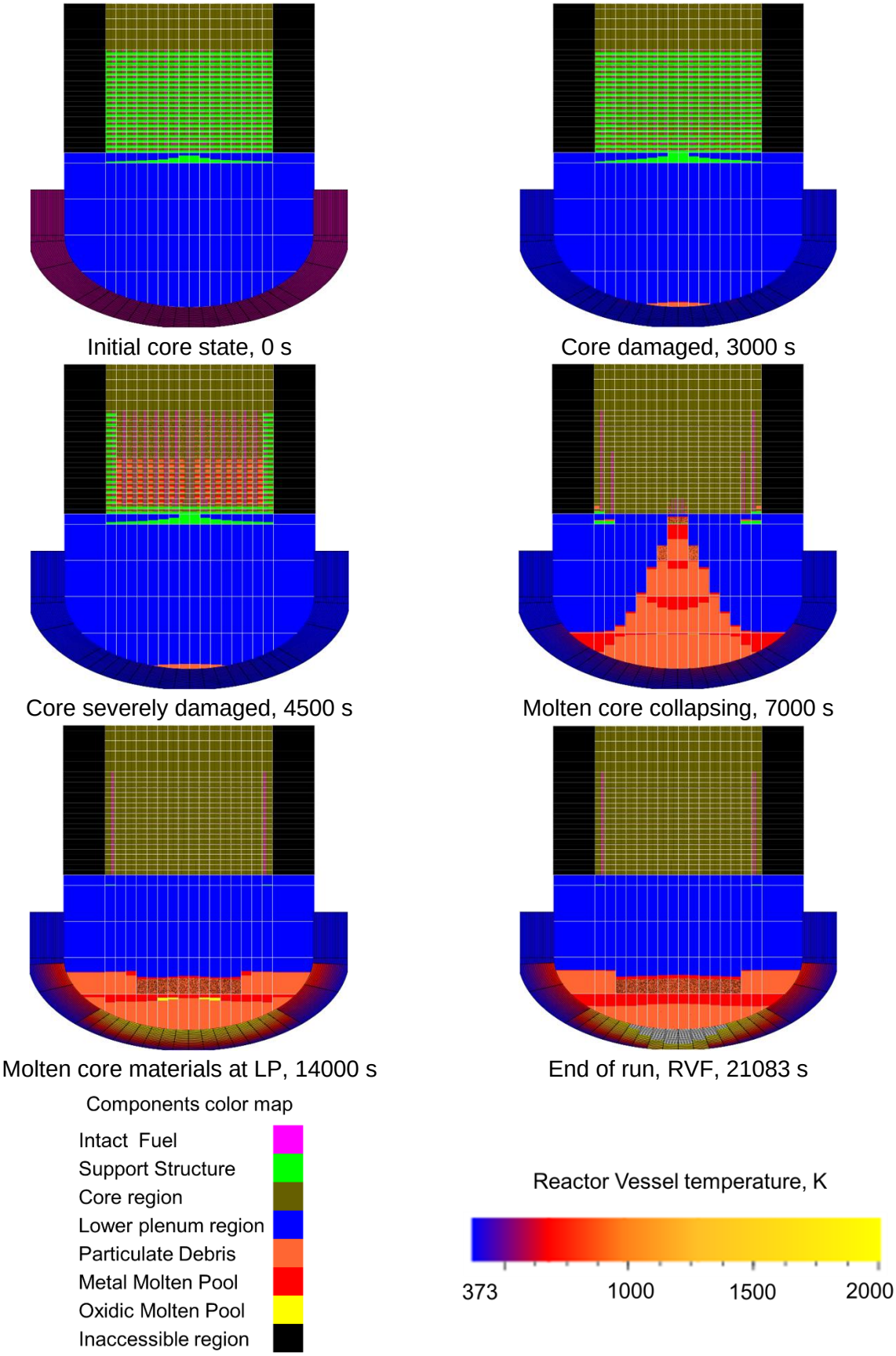

Figure 274: Case #4. SA chronology

Parameter	Case 1	Case 2	Case 3	Case 4
Reference time for Stage 3 input data	10000 s	12000 s	18000 s	20000 s
Total material mass in lower plenum	37363 kg	37375 kg	37230 kg	35459 kg
Oxidic melt fraction temperature	2400 K	2400 K	2100 K	2500 K
Metal melt fraction temperature	2100 K	2250 K	2100 K	2140 K
Ex-vessel heat transfer coefficient	10 W/(m^2·K)	~20 kW/(m^{2}K)	10 W/(m^2·K)	~20 kW/(m^{2}K)
Reacted Zirconium fraction	6.5%	6.8%	10.4%	11.3%
Degraded core gas temperature	1200 K	1200 K	1700 K	1700 K
Reactor cavity temperature	726 K	373 K	738 K	373 K
Mass flow rate to RC upper part	0 kg/s	1.05 kg/s	0kg/s	0.9 kg/s
Reactor vessel failure time*	10523 s	12527 s	18258s	21083 s
Reactor vessel failure delay	-	+0.5 h	+2.1 h	+3.0 h

*- by mechanical loading (1D mechanical model calculates the thermal and plastic strain)

Table 20. Main events and calculation output summary from MELCOR runs

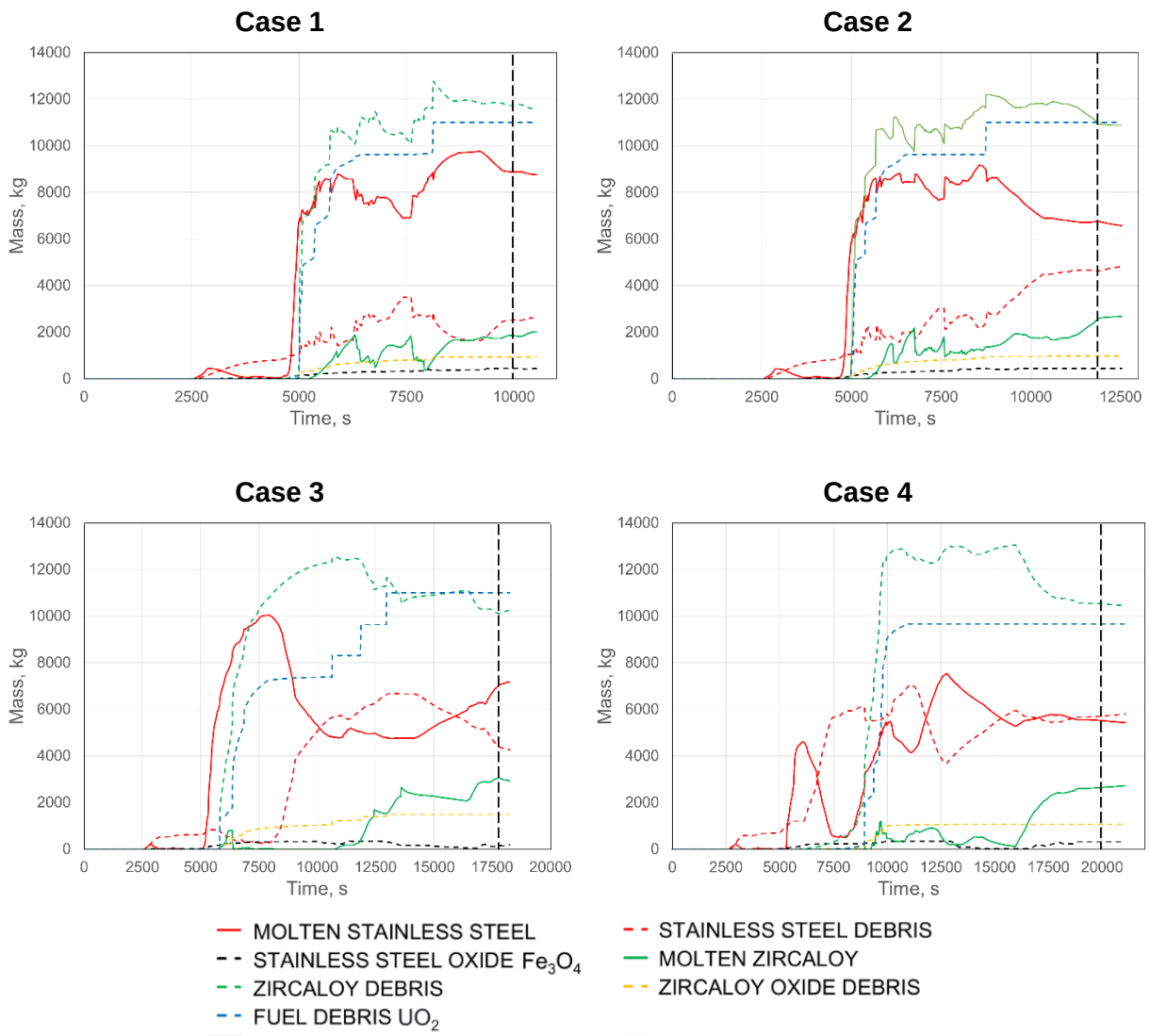

Figure 275: Mass characteristics of the molten materials in lower plenum

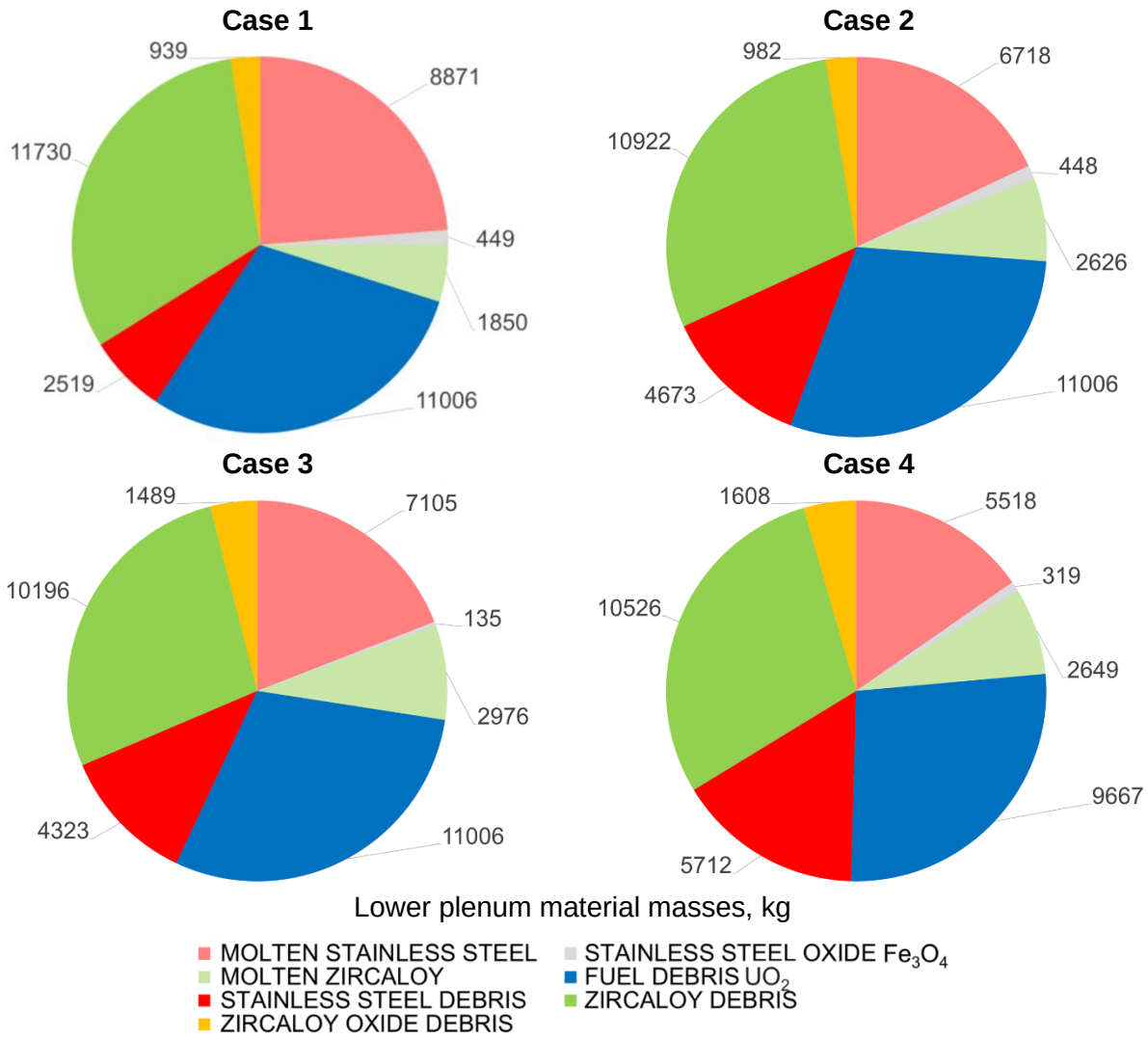

Figure 276: Molten materials distribution in LP

As seen, the reactor concrete cavity flooding action is not successful in preventing the reactor vessel failure. Detailed reactor core sensitivity analyses as, for example, the adjustment of the heat transfer coefficients during candling process, was not performed. However, it was noted that doubling the heat transfer coefficient values for Case 4 scenario leads to delay in RPV failure noticeably and the amount of molten Zircaloy at lower plenum decreases.

6.4 Stage 3. Analysis of the late phase of severe accident in SCW-SMR

Finally, the reactor vessel bottom rupture of the pre-conceptual SCW-SMR is analysed. The following state of the degraded reactor core is considered, when the coolant is boiled off, the core is dried out, all fuel assemblies have oxidized and collapsed. A pool of liquid “corium” (a mixture of fuel and core structural materials) is formed in the reactor lower plenum and the process of heating the reactor vessel elliptical bottom is then started; this happens in the absence of core cooling, and inevitably leads to the reactor wall failure.

The Stage 2 of the proposed analysis of SCW-SMR pressure vessel failure showed that the margin for operational actions before the start of the ex-vessel SA stage ranges from 3 to 7 hours. It was assumed that the RPV failure mechanism is realized by the loss of the material load-

bearing capacity (assessment performed using the standard MELCOR toolset). The objective of the current Stage 3 is to evaluate the most heat-loaded reactor vessel zone, where maximum thinning is achieved due to melting processes and mass transfer between the vessel and the corium.

The analysis is performed in a 2D axisymmetric formulation, which considers the presence of the RPV, corium and a simplified gaseous medium above the melt pool. Configuring the calculation procedure allows to set different compositions of the “heavy” and “light” fractions and to individually adjust the energy release, including considering the oxidation reaction. The procedure also allows for a stationary configuration of normal and “abnormal” stratification (Zvonarev et al., 2017) or the use of a dynamic model with calculation of the component slip rate.

In the base case, corium is considered as a two-component medium with individual thermophysical properties, which are determined based on a binary mixture. Thus, the melt components that are obtained in Stage 2 are pre-grouped. The main features of the calculation procedure in comparison with MELCOR and effective thermal conductivity models (Tran and Dinh, 2009 and Palagin et al., 2012) include the direct calculation of the velocity and pressure field in natural variables (U, V, P), as well as the turbulent viscosity field (special one-parameter RNG-1eq) and the concentration field of the “light” fraction taking into account mass transfer from the reactor vessel wall. The governing equations for corium transport have been supplemented with terms that characterize the presence of a “solid” fraction, which acts as additional volume resistance. Thus, both heat transfer and mass transfer are considered at the corium-RPV interface. This corresponds not only to the temperature mechanism of vessel destruction due to melting, but also to the so-called volumetric destruction, which leads to the presence of material "looseness" and directly affects its mechanical properties (Dolgov and Kashcheev, 1996). This effect is taken into account only in mass transfer (adding the rate of melting front change in the Stefan problem), since mechanical deformation of the vessel is not considered.

Both components of the melt are formed by grouping the components obtained on Stage 2. The conditionally “heavy” (oxide) fraction includes: UO_2, Zr, ZrO_2 - in which all integral energy release is concentrated, including heat release due to oxide reactions. The “light” (metallic) component includes steel and iron oxide.

Two options are provided for determining the thermophysical properties. The first and simple one is to consider the melt as a binary mixture, where the thermophysical properties are calculated as a sum for each component based on their mass fractions. As for the second option, it essentially assumes that the reciprocal thermal conductivity of the mixture is equal to the sum of the reciprocal thermal conductivities of each component multiplied by their mass fractions. In the first case, the thermal conductivity and viscosity of the component (oxide and metal layer) will be higher, while in the second case they tend to the minimum of each fraction, which leads in general to higher values of temperature in the energy-releasing layer, but to a much lower value of interface heat transfer if we talk about time-averaged values. Also, the choice of a particular method of determining the thermophysical properties depends on the choice of melt configuration with regard to stratification. The most frequently considered calculation variants are analysed: homogeneous, normal and abnormal (light phase is at the bottom) stratification. The dynamic stratification variant due to the homogeneous time unequilibrated state is also considered, which is obtained in Stage 2. The analysed melt configurations are shown in Figure 277.

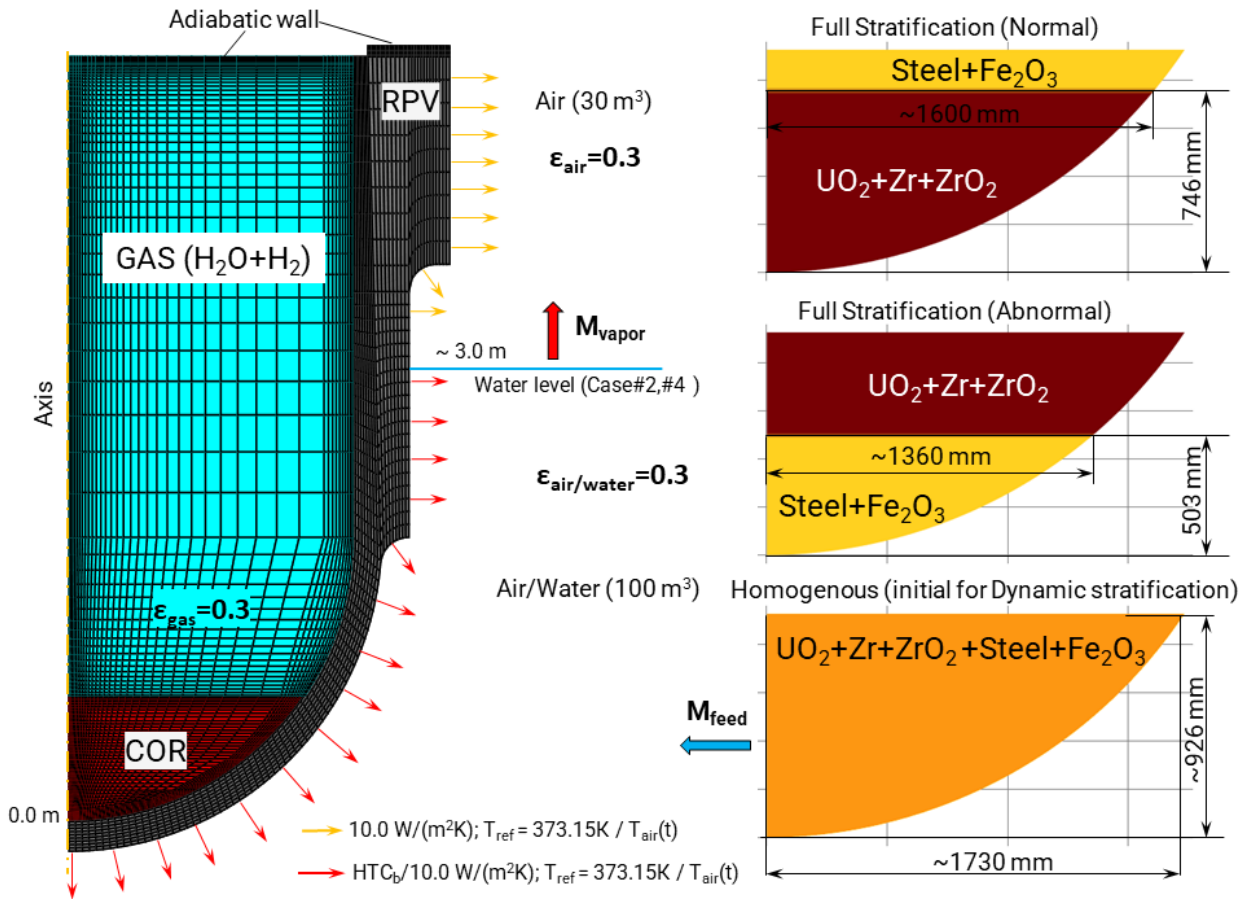

Figure 277: Calculation model general view, boundary conditions and melt configuration

In the calculation variants Case#1 and Case#3 (see Table 20 and Figure 276 of Stage 2), the external reference temperature of air is estimated as an enthalpy averaged value, taking into account that the active volume of the concrete reactor cavity is 130 m^3. The convective heat transfer coefficient is constant, equal to 10 W/(m^{2}K). For Case#2 and Case#4 we consider the option of partial flooding of the concrete reactor cavity up to the level ~ 3.2 m from the bottom of the reactor vessel (the origin corresponds to the lowest point of the inner surface at the initial time). The flooding volume is 100 m^3. The boiling heat transfer coefficient is calculated as a function of the wall temperature and the average flooded volume water temperature. It is assumed that for the initial time of Stage 3 the flooding water with a temperature of 350 K and mass flow similar to the evaporation rate occur. Above the flooded level, the HTC is assumed to be 10 W/(m^{2}K) and a reference temperature is 373.15 K. In each calculation variant, the degree of blackness is assumed to be 0.3 for both the external and internal environments. The interface value of the heat transfer coefficient between the corium and the RPV is calculated excluding the angular correction. By angular correction the additional terms in the correlation for the Nusselt number are meant, which are implemented in the code but were not used in the calculations.

The initial condition of each variant is formed based on the values given in Table 20 as follows. Initial melt circulation velocities are assumed to be zero. The initial corium temperature is assumed to be equal to the maximum temperature between the oxide and metal layers. This approach is motivated by the results of Stage 2, which show that stratification has not yet occurred; the assumed maximum temperatures represent a conservative option. The temperature of the gas medium above the melt pool is accepted to be uniform. In the considered cases, the heat energy released by the oxide reactions is negligibly small compared to the decay heat energy

generation (see Figure 269). In this case, the bulk energy release function is calculated on the basis of Eq. (6) below, where the integral thermal power corresponds to the MELCOR data:

$$q_v(r,z) = Q_\Sigma(t)\frac{1-\varphi(r,z)}{2\pi\int_{V_{COR}} r\left[1-\varphi(r,z)\right]dV} \tag{6}$$

where $Q_\Sigma(t)$ is the integral decay heat, $\varphi(r,z)$ is the volume fraction of «light» component.

The criterion for loss of bearing capacity of the reactor vessel is evaluated by the simple expression in Eq. (7); the maximum pressure corresponds to the lowest point of the vessel inner surface

$$\delta(t) \le \frac{p_{\max} R_{t=0}}{2R_m\left(T_{RPV}^{\max}\right)} \tag{7}$$

where $p_{\max}$ is the maximum relative pressure (actually the difference between the absolute internal and external pressure), R_m is the ultimate strength (Figure 278), $R_{t=0}$ is the radius of curvature of the undeformed vessel body.

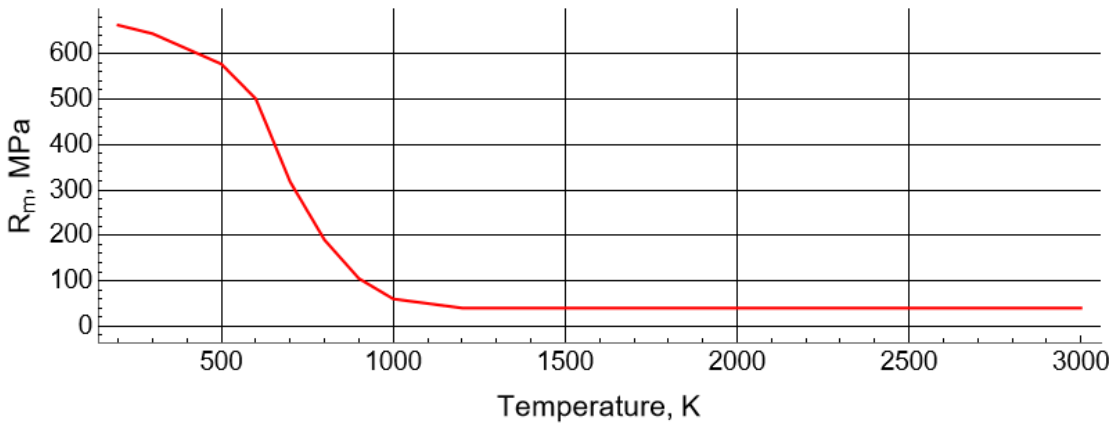

Figure 278: Functional dependence of ultimate strength on temperature (Holmström et al. (re-edition), 2017)

A preliminary analysis (see Figure 279) shows that the reactor vessel temperature initialization at the minimum value causes the reactor vessel failure by the melting mechanism more than 5000 seconds later in the case of external air cooling and more than 7500 seconds later in the case of reactor cavity flooding. The evaluation is performed with Case#1 initial conditions, considering the corium dynamic stratification model. Thus, the whole reactor vessel metal temperature is conservatively assumed to be equal to the average value, which will provide the smallest estimated margin for the time of RPV failure by the melting mechanism in further analysis.

Figure 280 shows the reactor vessel state estimated for a similar initial condition (Case#1) where the heat transfer is calculated according to the assumption of additivity of heat fluxes of each fraction only. This leads to the fact that the thermal conductivity coefficient of the “heavy” component (UO_2) tends to a minimum value.

Despite the higher corium temperatures, failure by the melting mechanism is obtained ~3000 s later, even at the lower thermal conductivity of the mixture. This is primarily due to the lower interface HTC at the corium-vessel interface. The thermal conductivity coefficient is calculated assuming an ideal mixture.

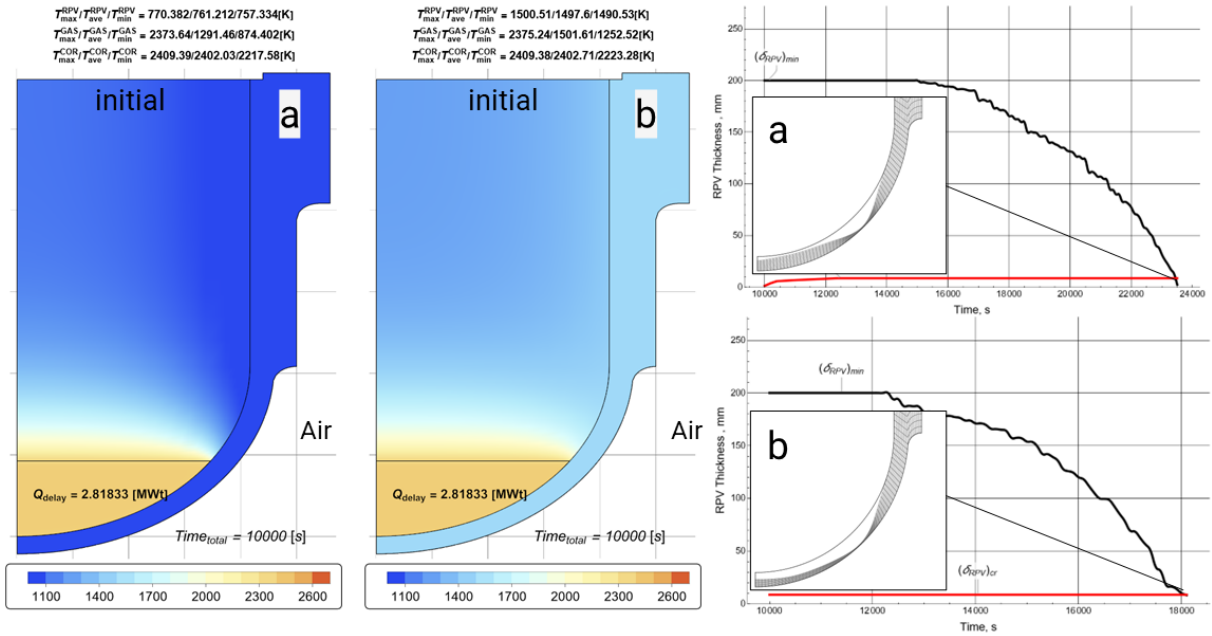

Figure 279: Comparative analysis of the reactor vessel initial temperature influence (a - initialization at minimum temperature, b - initialization at average temperature)

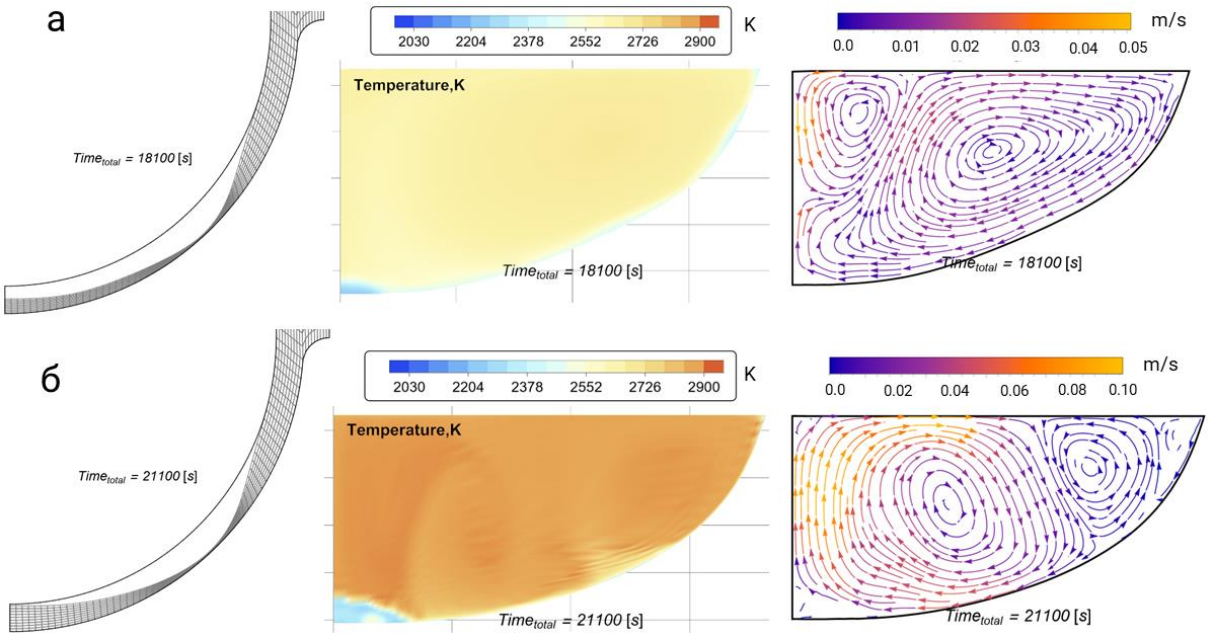

Figure 280: Comparative analysis of the influence of the method of determining the corium thermal conductivity (a - ideal mixture, b - assumption of additivity of the heat flux of i-fraction)

In the case of reactor cavity flooding, the way of determining the boiling heat transfer rate as well as mechanisms to account for the critical heat flux plays a special role. The analysis of similar scenarios for PWR-type light water reactors (VVER-440/1000/1200) (NRC “Kurchatov Institute” and Matejovic et al., 2017) shows that there is a significant uncertainty in the efficiency of external flooding systems.

For this purpose, a preliminary analysis was performed using three different heat transfer correlations, reported in Eqs. (8). Each of them assumes that boiling takes place in a large volume and is dominant over convection:

$$HTC_{boiling} = \begin{bmatrix} \left(T_w - T_{ref}\right) < 23.4, 34.5 p^{0.25} \left(T_w - T_{ref}\right)^{1.523} \\ \left(T_w - T_{ref}\right) \geq 23.4, 1.41 \cdot 10^7 p^{0.25} \left(T_w - T_{ref}\right)^{-2.575} \end{bmatrix} \quad (8a)$$

$$HTC_{boiling} = 4.34 \cdot \left[\left(\frac{p}{10^5} \right)^{0.14} + 0.0137 \left(\frac{p}{10^5} \right)^2 \right] q^{0.7} \quad (8b)$$

$$HTC_{boiling} = \frac{3.44 \left(\frac{p}{10^5} \right)^{0.14}}{1 - 0.045 \left(\frac{p}{10^5} \right)} q^{\frac{2}{3}} \quad (8c)$$

In the above formulations, p is the flooded volume pressure (assumed to be equal to 1 atm.), q [W/m^2] is the value of wall heat flux, that is recommended to be estimated as an average over the surface. In our case wall heat flux it is taken as a local value.

The impact of applying one of the correlations in Eqs. (8) for Case#2 is presented in Figure 281. The reactor vessel initial temperature is assumed to be equal to the average value obtained at Stage 3.

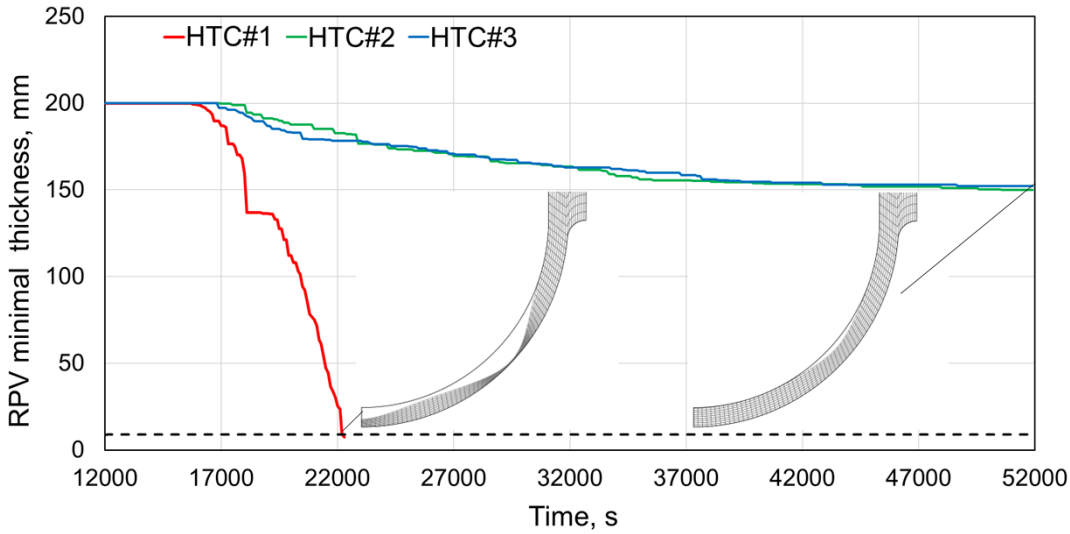

Figure 281: Effect of the choice of boiling correlation for the reactor vessel outer surface (HTC#1 - eq. 3a, HTC#1 - eq. 3b, HTC#3 - eq. 3c)

Correlation (8a) for Case#3 and Case#4 will be applied in further analysis. It should be noted that correlation (8a) for bubble and film boiling is available in MELCOR and was used during the Stage 2 analysis.

For each of the calculated Case#1- Case#4 runs, 4 variants of melt configuration are considered: homogeneous (HOM), normally stratified (NORMAL), abnormally stratified (ABNORMAL, “heavy” component on top), and dynamic stratification (DYN, Figure 279). For the dynamic stratification model, the maximum characteristic size of the steel and iron oxide fraction is assumed to be d_{max}=5.0 mm. The characteristic one-group size of the light fraction is calculated using dependence in Eq. (9) for the characteristic size:

$$d_{ref} = \int_0^{d_{max}} l^3 \left(4 l^2 e^{-2l}\right) dl \Big/ \int_0^{d_{max}} l^2 \left(4 l^2 e^{-2l}\right) dl \quad (9)$$

Here the expression in parentheses is the distribution function of the size of structural units. The distribution function is assumed to be constant over time.

So, the configuration of calculations is such that the shortest time to reactor vessel failure by the melting mechanism is obtained in each of the calculated variants. The convergence criteria are as follows: the discrepancy in temperature, velocity and pressure fields, as well as the “light” component mass concentration is assumed to be no more than 1.0%, in turbulent viscosity up to 5%. The calculation time step varies and does not exceed 100 seconds (for some calculation variants no more than 50 seconds). The velocity and pressure fields are solved in a fully coupled formulation, temperature and concentration, as well as turbulent viscosity are solved segregated from the force equations. The discrepancy in the system total mass at the level of 1-2% is allowed. Performed sensitivity study of time step and space discretization (with focus on RPV wall), shown that RPV failure time decreases with time step increasing, since the averaged in time melting rate of reactor vessel rises. If the discretization is insufficient for the reactor vessel, difficulties arise in recovering the melting front by solving the Stefan problem with a mass transfer component. The parameters of the computational time step and spatial discretization are chosen to minimize the sensitivity of the results and guarantee a convergent solution. The computational model also includes a special melting interface control procedure that performs a shape smoothing function. Without its use, the melting front is significantly non-uniform, which might be a more realistic option for some cases but requires significantly more computational resources. The concentration transfer equations were solved when the dynamic stratification model was applied only and in this case a correction for diffusion into the main volume of the reactor vessel inner surface was also considered.

Figure 282 and Figure 283 show the basic characteristics of temperature, dimensionless velocity,and the shape of the spherical part of the reactor vessel for Case#1. Figure 284 and Figure 285 show the basic characteristics of temperature, dimensionless velocity and the shape of the spherical part of the reactor vessel for Case#2. Figure 286 and Figure 287 show the basic characteristics of temperature, dimensionless velocity, and shape of the spherical part of the reactor vessel for Case#3. Figure 288 and Figure 289 show the basic characteristics of temperature, dimensionless velocity, and the shape of the spherical part of the reactor vessel for Case#4.

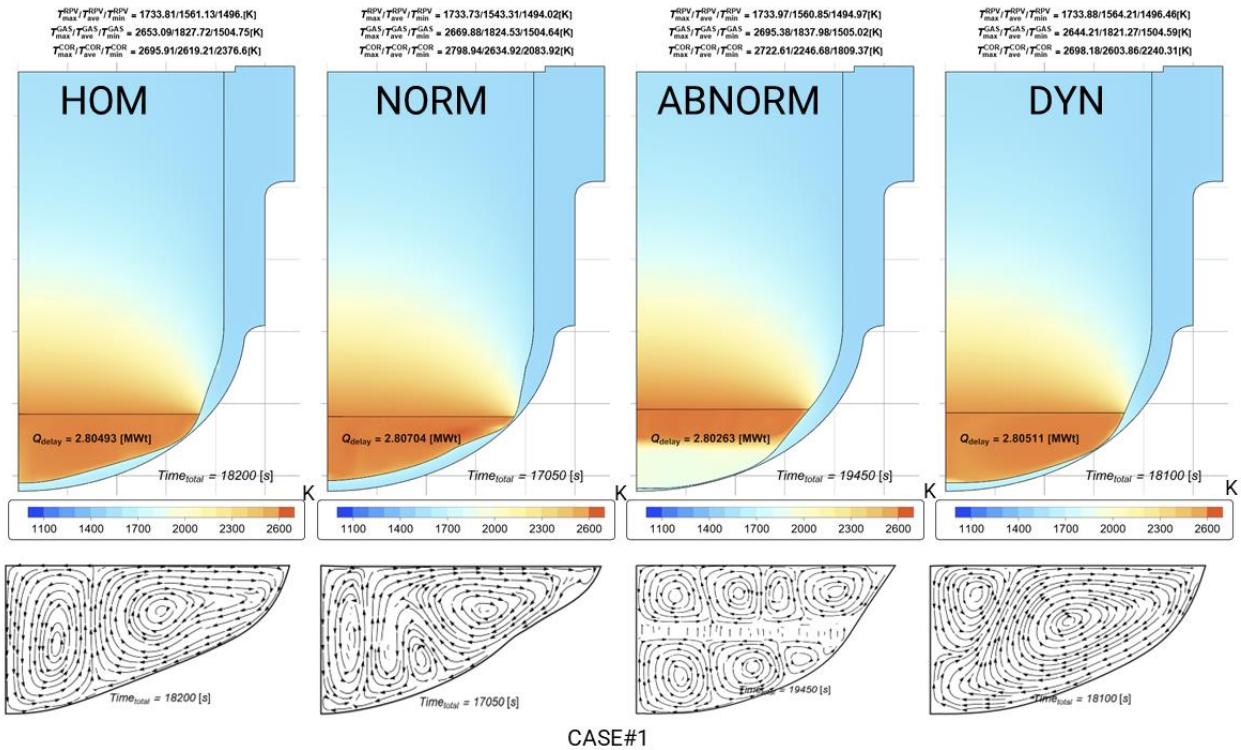

Figure 282: Temperature and dimensionless velocity fields at the reactor vessel failure time for Case#1 as a function of corium configuration

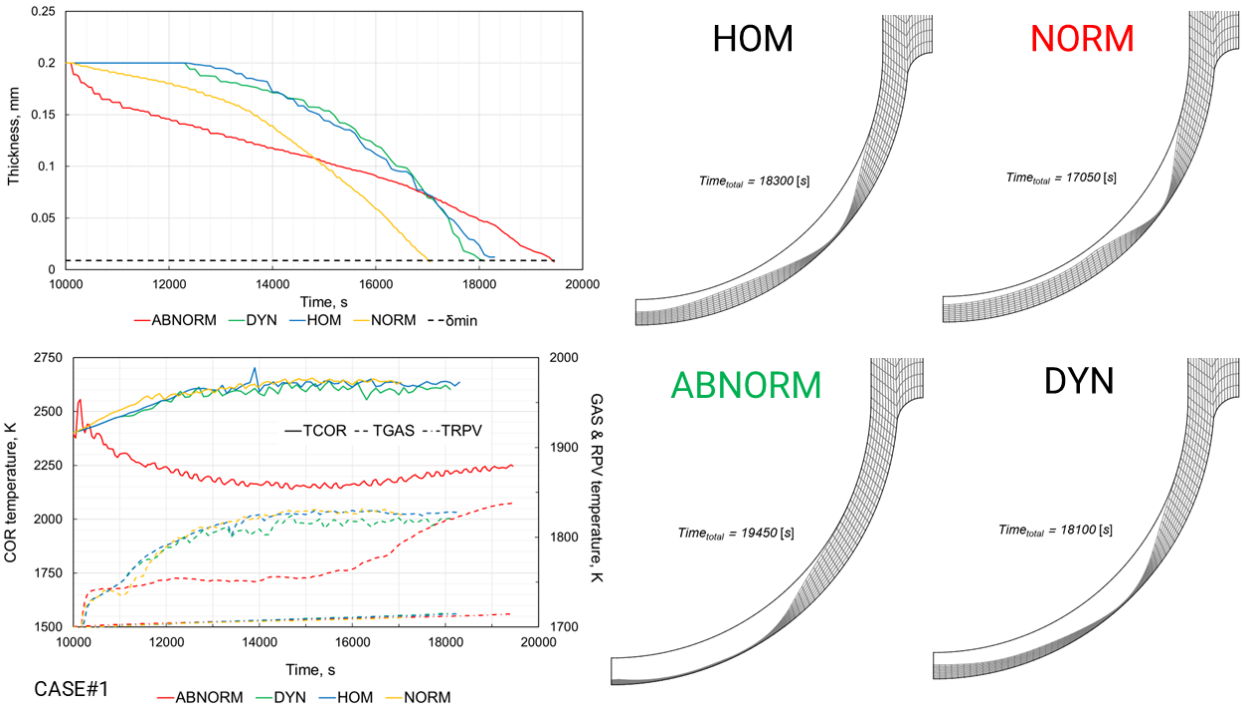

Figure 283: Dynamics of thickness and temperature change and shape at the reactor vessel failure time for Case#1

For Case#1 loss of RPV wall load bearing capacity by melting occurs at ~17000 seconds (corium configuration normally stratified).

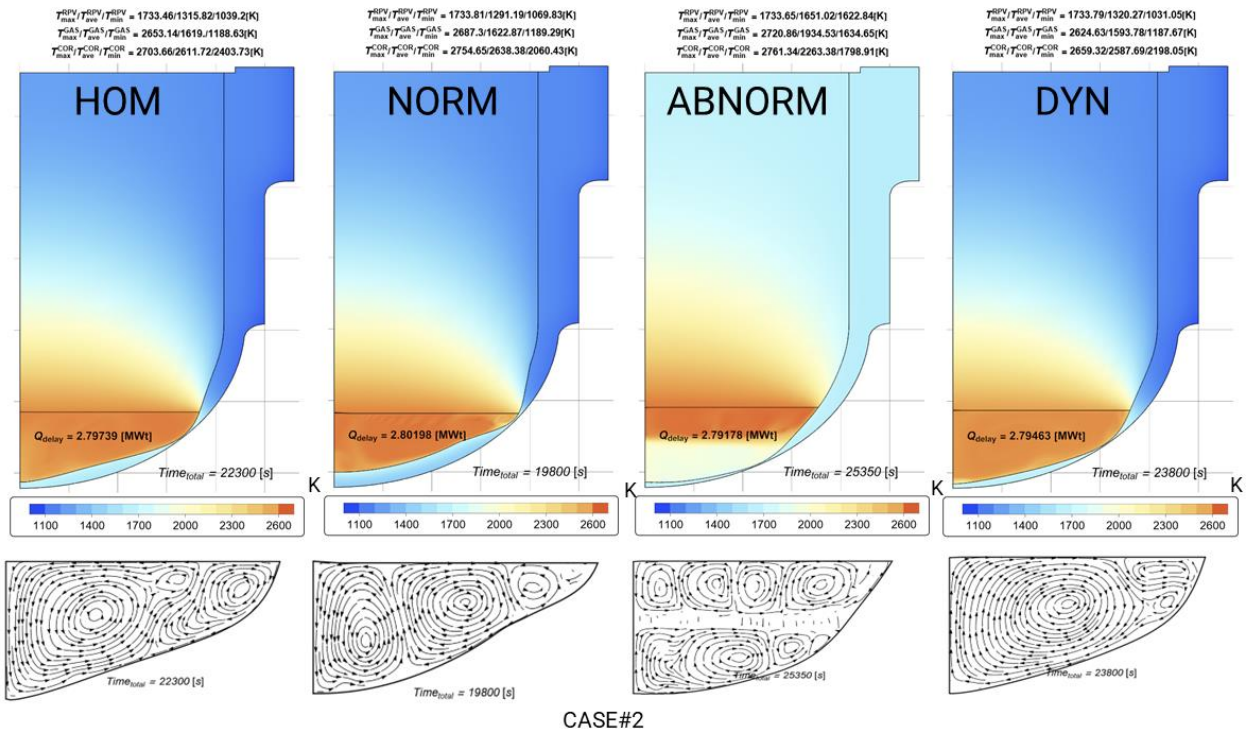

Figure 284: Temperature and dimensionless velocity fields at the reactor vessel failure time for Case#2 as a function of corium configuration

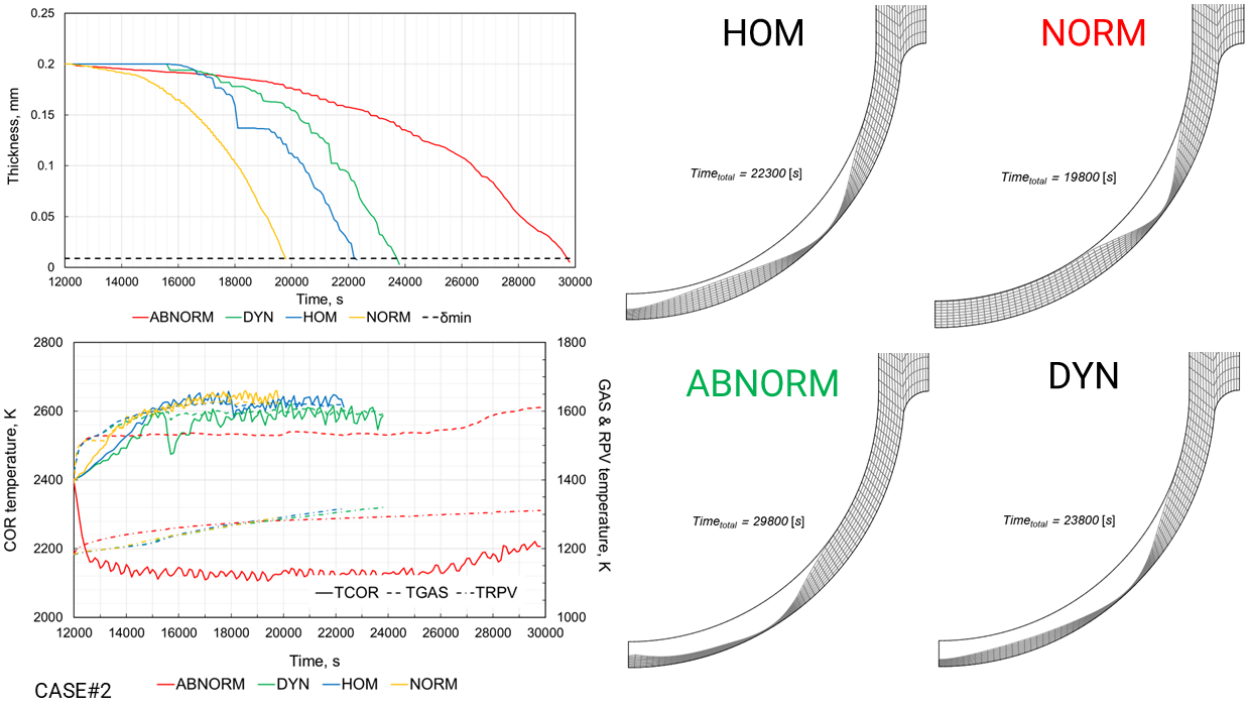

Figure 285: Dynamics of thickness and temperature change and shape at the reactor vessel failure time for Case#2

For Case#2 loss of RPV wall load bearing capacity by melting occurs at ~19800 seconds (corium configuration normally stratified).

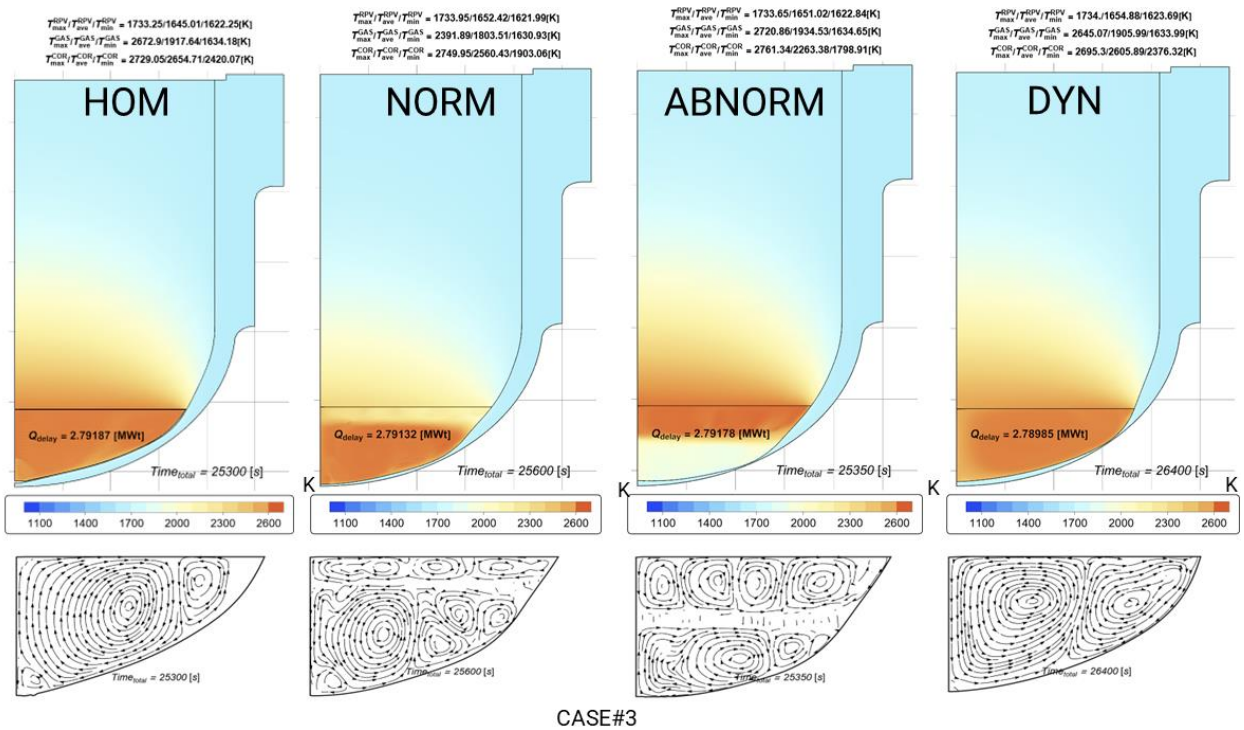

Figure 286: Temperature and dimensionless velocity fields at the reactor vessel failure time for Case#3 as a function of corium configuration

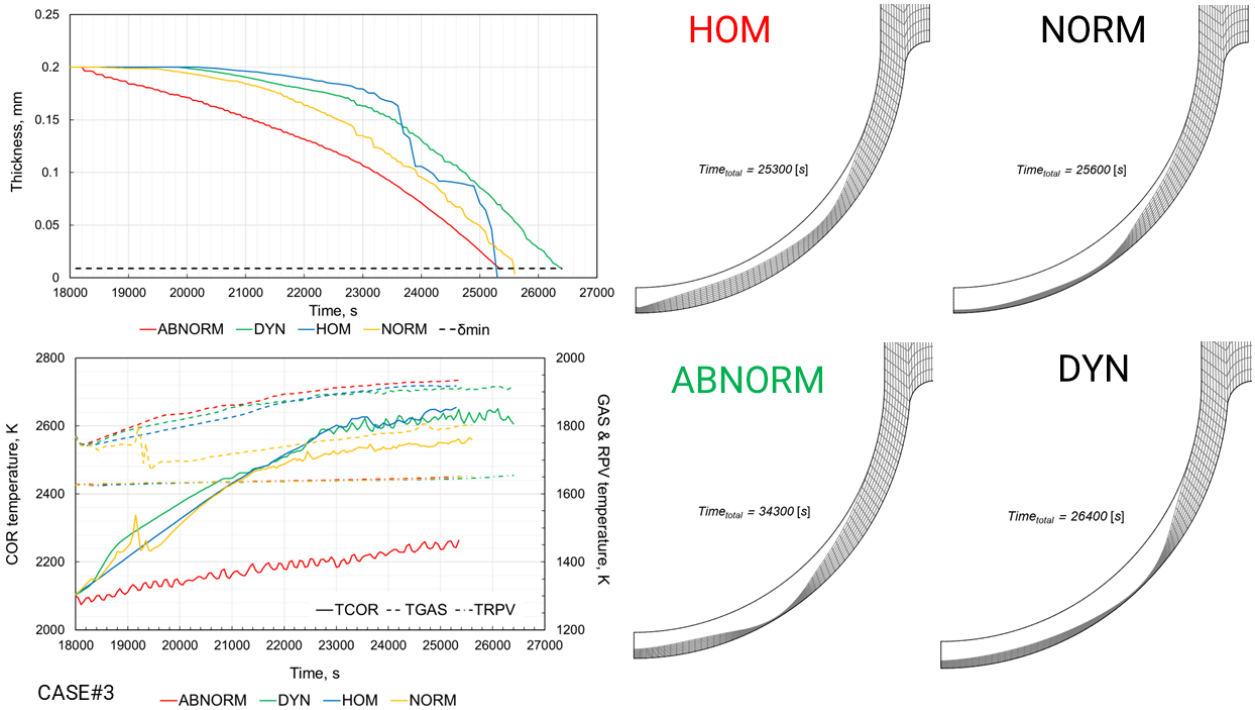

Figure 287: Dynamics of thickness and temperature change and shape at the reactor vessel failure time for Case#3

For Case#3 loss of RPV wall load bearing capacity by melting occurs at ~25300 seconds (corium configuration homogenous). Although the results between normal-stratified are very close to each other.

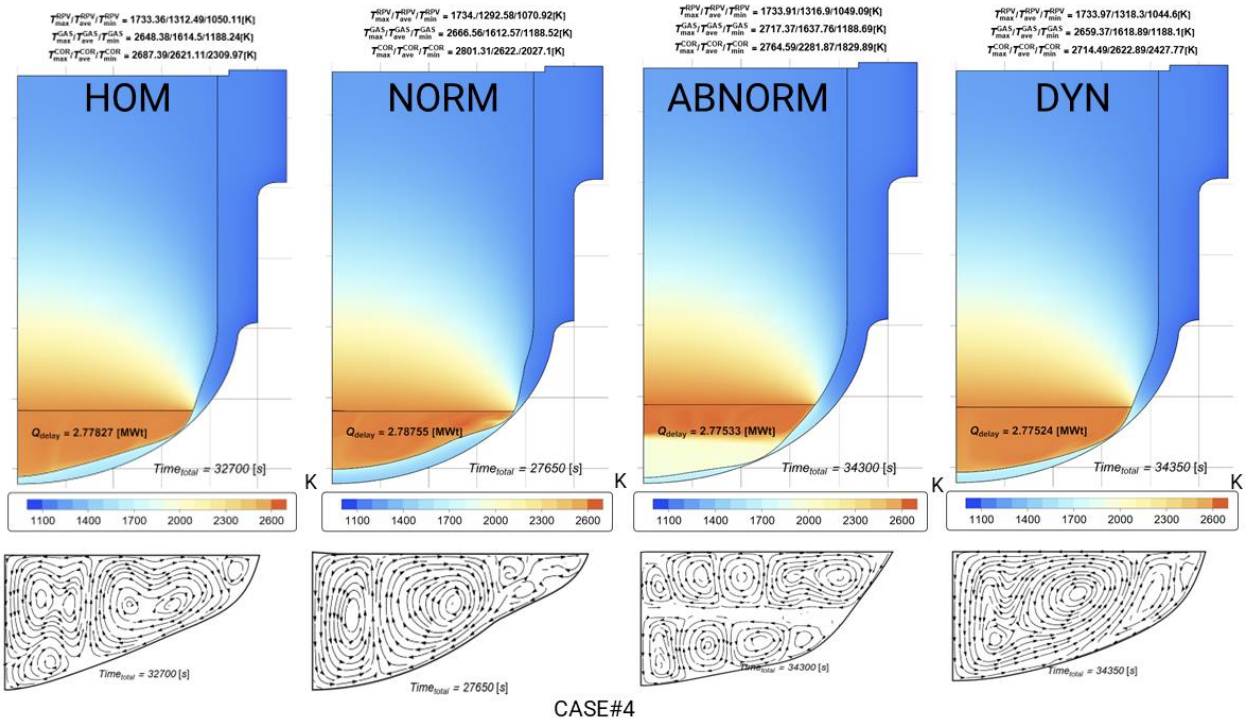

Figure 288: Temperature and dimensionless velocity fields at the reactor vessel failure time for Case#4 as a function of corium configuration

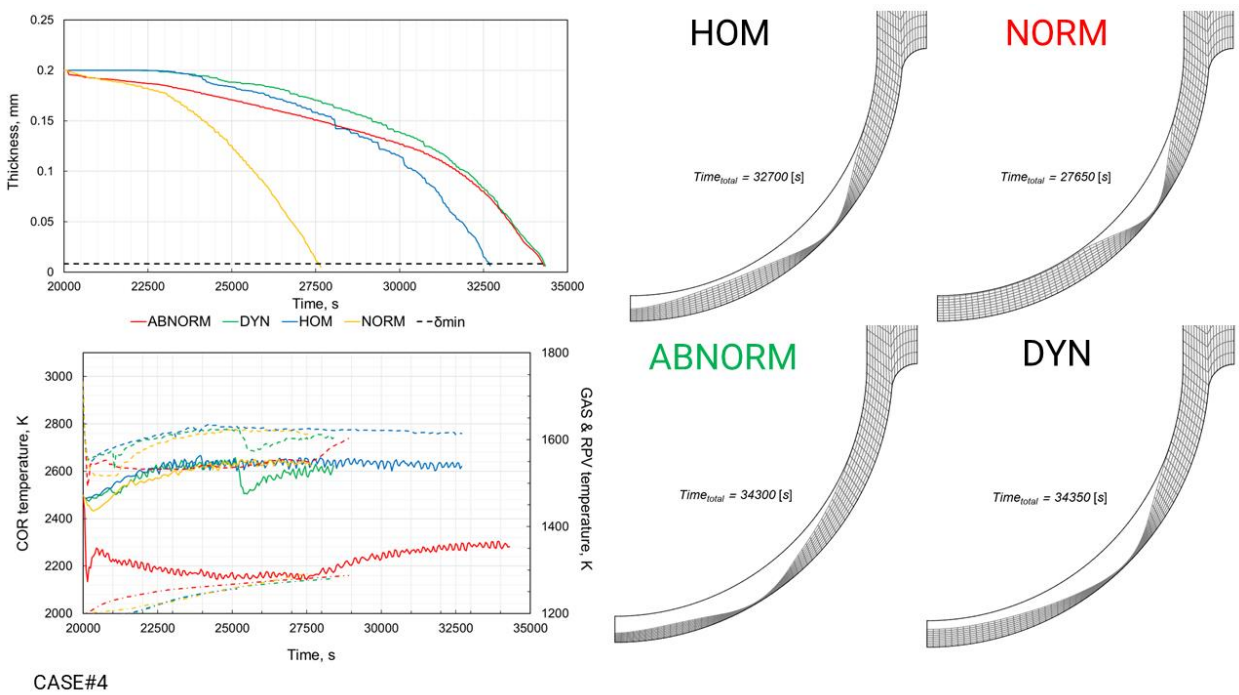

Figure 289: Dynamics of thickness and temperature change and shape at the reactor vessel failure time for Case#4

For Case#4 loss of RPV wall load bearing capacity by melting occurs at ~27650 seconds (corium configuration normally stratified).

In general, the presence of stratification leads to forming a zone mainly composed of steel and iron oxide fractions with higher thermal conductivity, resulting in more intense heat and mass

transfer at the internal interface between the vessel and the corium. With the application of the dynamic stratification model, which is based on a single-velocity mixture model and concentration transfer of the “light” component, full steady-state stratification is not achieved (Figure 290). Hence this leads to forming zones with higher thermal conductivity and lower energy release.

However, according to the results of the analysis, everything depends on the reactor ex-vessel cooling conditions.

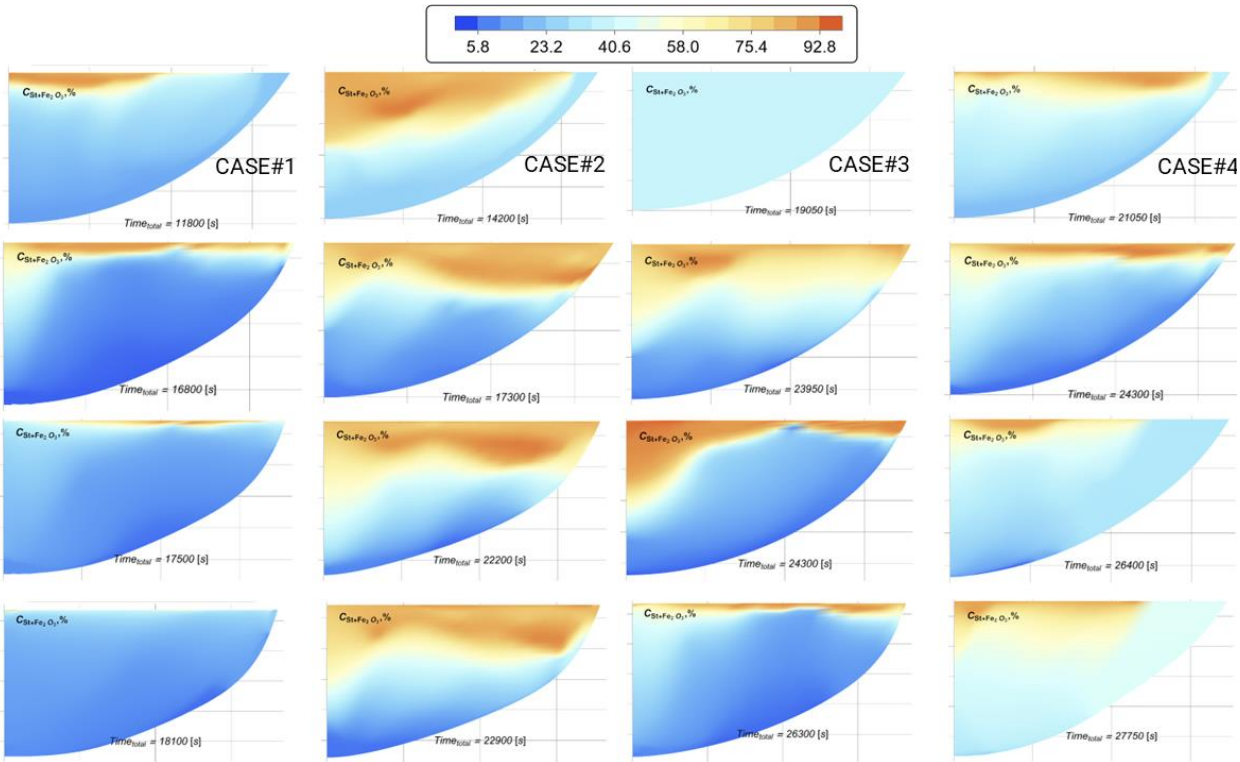

Figure 290: Change in the concentration field of the “light” component under dynamic stratification

To summarize the obtained results, which are conservative due to the high initial value of the reactor vessel temperature, as well as for the choice of correlation for the estimate of the boiling heat transfer, the following can be stated.

The concept of external flooding, especially considering the parametric analysis whose results are summarised in Figure 291, can be considered as a severe accident mitigation strategy. In view of the analytical evaluation, it is necessary to establish realistic heat transfer conditions in the case of external flooding and to formulate a more reliable temperature distribution in the reactor vessel.

As it was shown, based on the performed parametric study, the RPV failure by melting mechanism is obtained in all cases. Thus, it is necessary to analyze the possibility of using core catcher systems, i.e. ex-vessel melt retention strategy. Another option is to include systems to obtain a forced circulation in the concrete cavity.

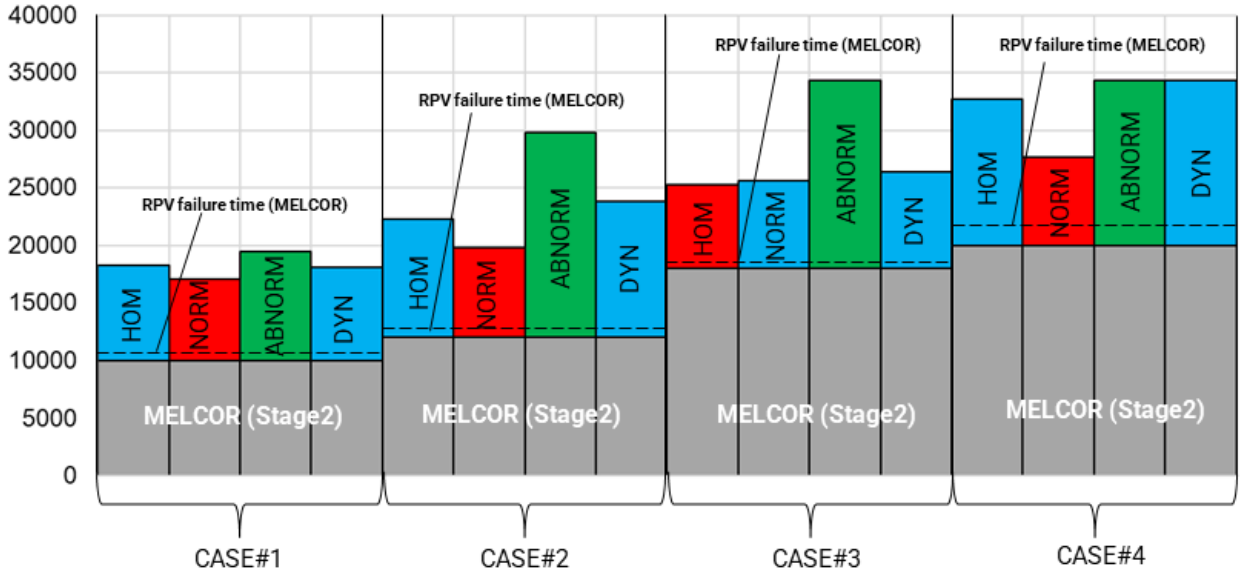

Figure 291: Summary results of parametric analysis for the calculated cases

6.5 Significance of the work and final remarks

The severe accident analysis of a supercritical reactor is generally similar to that of a PWR/BWR except for some key features. The first one is the supercritical state and the peculiarities of decompression with regard to phase transitions. The second feature in the present particular case is the horizontal arrangement of fuel assemblies, which is not typical for Europe.

In general terms, as a consequence of the initial supercritical pressure initial state, no main differences in the phenomenology of the in-vessel stage of a severe accident were found. The main differences are instead related to the horizontal arrangement of fuel assemblies, especially regarding the downward relocation of metal and oxide components.

A wide range of computational tools are currently available for modelling reactor core degradation and melt behavior. All of them cover the main related phenomena, processes and complex interactions during the SA in-vessel stage. However, the task of representing a non-standard pre-conceptual SCW-SMR design with a horizontal core layout represented a clear challenge in the direct application of existing models. In this situation, an unconventional equivalent model interpretation was proposed using the MELCOR code, using the guillotine rupture of the cold leg as initiation event.

In particular, the task to be performed in this work was divided into three stages, where the **Stage 1** addressed the analysis of the initial dynamics, aimed at evaluating the integrity of the core under the shock loads experienced during depressurisation. In order to evaluate the spatial distribution of decompression forces, a representative model of the considered pre-conceptual reactor design was developed, where the supercritical and two-phase coolant is considered in the two-component approximation over the entire pressure range. For this purpose, special user functions were introduced in ANSYS CFX 18, which allowed for the estimation of decompression and phase transitions. In this first approximation, it was also possible to estimate the critical flow parameters, which are very important both for dynamic forces and for the formation of a quasi-steady thermodynamic state for Stage 2.

Then, **Stage 2** presented a first attempt to evaluate the formation of the lower plenum melt pool and the thermodynamic parameters of each material fraction.

Finally, the main objective of **Stage 3** has been a detailed evaluation of the reactor vessel melting dynamics depending on the reactor ex-vessel cooling conditions.

The following conclusions can be formulated from the preliminary results of the initial dynamics estimation. The presence of a rather complex fuel cooling section (which is more than 12 m along the coolant path) leads to the fact that the pressure drop acting on relatively thin FA boxes may result critical for their resistance. Probably, this can cause loss of bearing capacity and a change of the initial core geometry. Crucial also may be an effect of fast over pressurization due to the substantial enthalpy at the upper core level caused by rapid expansion of the coolant during the transition to a two-phase state (vapour) in the presence of heat generation. Even if the heat transfer coefficient from the fuel rod decreases significantly during decompression and some of the thermal energy from the initial dynamics leads to a rise in fuel/cladding temperature, the local enthalpy will still be large enough to lead to a significant expansion of the coolant and resulting pressure rise in the FA boxes. This means that the loads acting outward will be more significant. Therefore, based on the Stage 1 results, a core design revision is recommended, for further development of the proposed SCW-SMR concept.

Based on the Stage 1 results, a non-typical ECC-SMART core model was developed using the MELCOR 1.8.6 code. Despite the lack of direct support from this integrated code to represent the specific spatial orientation of the fuel channels, a fast core model of the conceptual reactor was prepared. The approach of a volume/mass equivalent approximation was used as a basis, since the code essentially operates with the masses and enthalpies of the components. Furthermore, the conceptual SCW-SMR lower plenum design is similar to the one of a typical PWR. The results of the calculation scenarios allowed us to form a general picture of the core degradation course of SA in-vessel early phase for different initial conditions and to evaluate the characteristics of the accumulated in LP corium at the late phase.

As part of Stage 3, a parametric evaluation of reactor vessel failure due to wall melting was performed depending on the external cooling conditions. The calculations are conservative in terms of the initial vessel temperature and the minimization of external heat transfer during boiling. Reactor vessel failure was obtained in each of the parametric cases, regardless of the cooling conditions. According to the analysis the marginal time for operational action to activate compensating system is no more then 10 hours. The obtained results represent first approximations, which should be clarified at the stage of further development of the concept of a small modular reactor with supercritical operating conditions, emphasizing the reliability of estimation of the external heat transfer intensity in case of reactor cavity flooding. However, based on the results presented, it could be recommended to further evaluate the necessity of considering a core catcher system.

7 Conclusions

This report summarised the activities performed in the frame of the ECC-SMART Project, in relation to Task 3.4, Study of a pre-conceptual core layout and passive safety concept for SCW-SMR.

After the description of the general layout and safety characteristics of the Canadian and Chinese reactor concepts, the reference SCW-SMR proposed by Schulenberg and Otic (2021) and taken as a reference in the project has been described. Then, contributions to the safety analyses of this pre-conceptual design have been proposed in an early analysis by the University of Pisa, in a more refined work by BME and in a severe accident tool application by IPP.

In short summary, the work performed by the University of Pisa and BME, performed by the use of system codes, allowed to characterise the steady-state and natural circulation behaviour of the new proposed concept, showing that preliminary choices for the configuration of safety systems may be effective in protecting the reactor during a long-term station black-out. Though a single accident scenario was considered, something that does not allow to declare that the proposed concept is sufficiently safe, the work had the worth to show that even such a complex seven core passage configuration can be considered as a passive safety concept, whose integrity can be assured during a LTSBO sequence by ordinary means proposed for several other subcritical light water or even advanced generation IV reactors. A further work by BME and CNL on the application of subchannel codes to the proposed rod bundle configurations, though coping with the difficulty to simulate horizontal bundle systems, was able to provide preliminary information of the maximum cladding temperatures that can be achieved in rated conditions.

For both the analyses performed by the University of Pisa and by BME on the LTSBO, it must be mentioned that in the future a greater refinement in the vertical discretisation of the core could be needed, e.g, in representing each one of the 20 levels of fuel channels proposed in the concept. While this complication, due to the presence of horizontal channels, was not considered necessary at the present stage of preliminary analyses, such a more detailed description might be needed to assure that the present common feature of the RELAP and Apros models of using only seven levels of discretisation (one per each stage) may not hide some relevant phenomena occurring during postulated accidents, e.g., related to the creation of water levels feeding only part of the stacked fuel channels facing common inlet and outlet plena.

Finally, the work by IPP represents a smart attempt to circumvent the basic difficulty of the lack of validated codes for the analysis of severe accidents for such horizontal core bundle configuration in the condition of a guillotine break LB-LOCA without intervention of the ECCS systems. In particular, an existing CFD code was adapted to evaluate the dynamic phase of depressurization from supercritical pressure of the reactor vessel system, assessing the internal forces generated by the passing depressurisation wave; then, the progression of the molten corium towards the lower plenum and the phases of attack of the lower plenum shell, with and without external cavity flooding, were addressed. In this case, the results of the analyses for such a very low probability sequence are less encouraging, suggesting the need for further and more refined analyses and, probably, a reconsideration of the core and internal vessel structures to make them less prone to the effects of a fast depressurisation.

The overall work reported herein fulfilled the goal of the Task 3.4 of investigating the passive aspects of the proposed pre-conceptual reactor configuration and involved the customisation of existing codes and models that were upgraded and variously shaken down for performing the presented studies. The nice cooperation established between the Partners, also favoured by the innumerable meetings held weekly or bi-weekly to exchange ideas and monitor the progress of the work, created a solid group of experienced researchers of different ages,

which will result a key asset for a cooperation in future European projects aimed at studying the promising features of Supercritical Water Reactors for proposing them as a reliable design of Generation IV LWRs.

8 References

Allison, C. M., and Hohorst, J. K., 2010, Role of RELAP/SCDAPSIM in Nuclear Safety, Hindawi Publishing Corporation, Science and Technology of Nuclear Installations, Volume 2010, Article ID 425658, 17 pages, doi:10.1155/2010/425658.

Ambrosini, W., Pucciarelli, A., Kassem, S., 2022, Benchmarking of system thermal-hydraulic codes on the basis of rod bundle data, Università di Pisa, Dipartimento di Ingegneria Civile e Industriale, Pisa, May 27th, 2022, RL 306(2022).

American Nuclear Society, 1994. ANSI/ANS-5.1-1994, Decay Heat Power in Light Water Reactors, August 23, 1994.

Andreani, M., Bittermann, D., Marsault, Ph., Antoni, O., Keresztúri, A., Schlagenhaufer, M., Manera, A., Seppäla, M., Kurki, J., 2012. Evaluation of a preliminary safety concept for the HPLWR, Progress in Nuclear Energy, Volume 55, 2012, Pages 68-77

Babcsány, B., 2021. Development of a finite-element-based neutron physics code system for the solution of the simplified P3 approximation to the neutron transport equation, PhD thesis, BME, Budapest, 2021

Baikov A.V., Kotsarev A.V., Tsyganov S.V., 2016. The process of asymmetric boron dilution in the VVER-1000 reactor during testing of the fast boron injection system at the Kudankulam NPP. Results of process modeling / National Research Center "Kurchatov Institute", Moscow, Russia. (In Russian)

Banuti, DT., 2021. Supercritical Pseudo Boiling in Cubic Equations of State, Proceedings of the ASME Turbo Expo 2021: Turbomachinery Technical Conference and Exposition. Volume 10: Supercritical CO2. Virtual, Online. June 7–11, 2021. ASME. https://doi.org/10.1115/GT2021-58788

Bertesina, Z., Varju, T., Babcsány, B., 2023. Coupled thermal hydraulics and neutron physics analysis of an SCW-SMR reactor concept, MSc thesis, BME, Budapest

Bishop A.A., Sandberg R.O., Tong L.S., 1965, Forced convection heat transfer to water near critical temperatures and super-critical pressures. A.I.Ch.E.-I.Chem.E. Symposium Series. 1965, Vol. 2, S.77- 85.

Brown M., 2018. Improved core collapse model for CANDU severe accident modelling (MAAP-CANDU v500). International severe accident management conference (ISAMC), Canada: CNSC

Brown M.J., and Petoukhov S.M., 2015. Severe accident analysis of a station blackout accident using MAAP-CANDU for the Point Lepreau Station Refurbishment Project Level 2 PSA. Canada.

Cao, Z., Liu, X., and Cheng, X., 2016. Accident Analysis on Supercritical Water-Cooled Reactor during Design Basis and beyond Design-Basis Condition. Journal of Nuclear Science and Technology 53, no. 8 (2016): 1120–33. doi:10.1080/00223131.2015.1095658

Carver, M.B., Tahir, A., Kiteley, J.C., Banas, A.O., Rowe, D.S., Midvidy W.I., 1990. Simulation of flow and phase distribution in vertical and horizontal bundles using the ASSERT-4 subchannel code. Nucl. Eng. Des., Vol. 122, 1990, pp. 413-424.

Chaaraoui, O., 2024, Thermal-hydraulic analyses in support to the development of an innovative reactor concept at supercritical pressure, Università di Pisa, Dipartimento di Ingegneria Civile e Industriale, Laurea Magistrale in Ingegneria Nucleare, Academic Year 2022/2023.

Cheng, X., Müller, W., 1998, Turbulent mixing and critical heat flux in tight 7-rod bundles, Int. J. Multiphase Flow, Vol. 24, pp. 1245-1263, 1998.

Cheng, X., Schulenberg, T., Bittermann, D., Rau, P., 2003, Design Analysis of Core Assemblies for Supercritical Pressure Condition, Nuclear Engineering and Design, 223, 279-294, 2003.

Dang G., Li, Q., Liu, Yu., Song, D., Zhu, D., 2021. Large-break LOCA analysis of CSR1000, Annals of Nuclear Energy,Volume 161, 2021. https://doi.org/10.1016/j.anucene.2021.108444.

Diaz-Pescador, F. Schafer, S. Kliem, 2022. On the validation of ATHLET 3-D features for the simulation of multidimensional flows in horizontal geometries under single-phase subcooled

conditions, Nuclear Engineering and Technology, 2022, 3567-3579. https://doi.org/10.1016/j.net.2022.04.017

Dolgov V.V., Kashcheev M. V., 1996. Modeling of the thermal destruction of the reactor body during a severe accident at a nuclear power plant with reactors of the water-water power reactor (VVER) type, TVT, 1996, vol 34(5), 770–779 (in Russian).

Dubyk Y., Filonov V. et al., 2018. Dynamic Assessment of the Core Barrel During Loss of Coolant Accident, American Society of Mechanical Engineers. https://doi.org/10.1115/PVP2018-84762

Edwards, A.R., O'Brien T.P., 1970. Studies of phenomena connected with the depressurization of water reactors, Journal of the British Nuclear Energy Society 9 (1970) 125-135

Filonov V., Dubyk Y., Kovalenko O., Filonova Y., Fedorov D., 2024. Evaluation of three-dimensional initial dynamics of the decompression wave at LB LOCA in the advanced supercritical reactor ECC-SMART, ICONE31-136271, Proceedings of the 2024 31st International Conference on Nuclear Engineering ICONE31 August 4-8, 2024, Prague, Czech Republic.

Fu, S.W., Liu, X.J., Zhou, C., Xu, Z.H., Yang, Y.H., Cheng, X.,2012. Modification and application of the system analysis code ATHLET to trans-critical simulations, Annals of Nuclear Energy,Volume44, 2012, Pages 40-49,https://doi.org/10.1016/j.anucene.2012.02.005

GE Hitachi Nuclear Energy, 2011, ESBWR Plant General Description,(6.1.2011), https://www.gevernova.com/content/dam/gevernova-nuclear/global/en_us/documents/large-modular-boiling-water-reactors/ESBWR-General-Description-Book.pdf

Geuzaine, C., Remacle, J.-F., 2009. Gmsh: a three-dimensional finite element mesh generator with built-in pre- and post-processing facilities. International Journal for Numerical Methods in Engineering, Vol. 79, No. 11, pp. 1309-1331.

Hassan, H., Pucciarelli, A., Ambrosini, W., 2022, Check on CAD data in support of system code modelling of the ECC-SMART proposed supercritical water SMR, Università di Pisa, Dipartimento di Ingegneria Civile e Industriale, Pisa, September 20th, 2022, RL 311(2022).

Holmström, S. et al (re-edition), 2017. Determination of high temperature material properties of 15-15Ti steel by small specimen techniques, EUR 28746 EN, Publications Office of the European Union, Luxembourg, 2017, ISBN 978-92-79-72278-3, doi:10.2760/259065, JRC105589.

IAEA, 2008. Analysis of Severe Accidents in Pressurized Heavy Water Reactors, IAEA-TECDOC-1594, IAEA, Vienna (2008)

IAEA, 2013. Benchmarking Severe Accident Computer Codes for Heavy Water Reactor Applications, IAEA-TECDOC-1727, IAEA, Vienna (2013)

IAEA, 2014. Heat Transfer Behaviour and Thermohydraulics Code Testing for Supercritical Water Cooled Reactors (SCWRs), IAEA-TECDOC-1746, IAEA, Vienna (2014).

IAEA, 2016. Safety of Nuclear Power Plants: Design, IAEA Safety Standards Series No. SSR-2/1 (Rev. 1), IAEA, Vienna (2016)

IAEA, 2019a. Status of Research and Technology Development for Supercritical Water Cooled Reactors, IAEA-TECDOC-1869, IAEA, Vienna (2019)

IAEA, 2019b. Status and Evaluation of Severe Accident Simulation Codes for Water Cooled Reactors, IAEA-TECDOC-1872, IAEA, Vienna (2019)

IAEA, 2020a, Understanding and Prediction of Thermohydraulic Phenomena Relevant to Supercritical Water Cooled Reactors (SCWRs), IAEA-TECDOC-1900, IAEA, Vienna (2020).

IAEA 2020b, Advances in Small Modular Reactor Technology Developments, A Supplement to: IAEA Advanced Reactors Information System (ARIS), 2020 Edition, Printed by the IAEA in Austria, September 2020.

Idel'chik, I. E., 1960. Handbook of Hydraulic Resistance, Coefficients of Local Resistance and of Friction

Ishchenko O., Filonov V., Dubyk Y., 2021. Dynamic model of the VVER-1000 reactor for seismic and LB LOCA evaluation, Proceedings of ASME 2021: 28th International Conference on Nuclear Engineering, ICONE 28. – August 4–6, 2021. – Virtual, Online. – C. 9. DOI: 10.1115/ICONE28-65756

Jackson, J., Hall, W., 1979. Forced convection heat transfer to fluids at supercritical pressure, Turbulent forced convection in channels and bundles, Vol 2, edited by S. Kakaç and D. Spalding

Kurganov V.A., Zejgarnik Yu. A., Jan'kov G. G. and Maslakova I. V., 2018. Heat transfer and resistance in pipes at supercritical pressures of the coolant: results of scientific research and practical recommendations, Moscow: Printing salon chance LLC, 2018, 304 p. ISBN 978-5-9500112-7-6

Kurki, J., 2008, Simulation of thermal hydraulic at supercritical pressures with APROS. IYNC 2008. Interlaken, Switzerland, 20–26 September 2008, paper no. 145, https://www.apros.fi/wp-content/uploads/sites/27/2020/09/58-IYNC_supercritical_paper_2008.pdf

Kurki J., Seppälä M., 2009, Thermal Hydraulic Transient Analysis of the High Performance Light Water Reactor Using APROS and SMABRE, 20th International Conference on Structural Mechanics in Reactor Technology (SMiRT 20), August 9-14, 2009

Leppänen, J., Pusa, M., Viitanen, T., Valtavirta, V. and Kaltiaisenaho, T., 2015, "The Serpent Monte Carlo code: Status, development and applications in 2013." Ann. Nucl. Energy, 82 (2015) 142-150.

Liu X, Yang T, 2019. Preliminary safety analysis for the SCWR-FQT facility. Int J Energy Res. 2019;1–10. https://doi.org/10.1002/er.5032

Lund, H., Flåtten, T., 2010. Equilibrium conditions and sound velocities in two-phase flows/ SIAM Annual Meeting (AN10), July 12-16 2010

Matejovic, P., Barnak, M., Bachraty, M., Vranka, L., Berky, R., 2017. Adoption of in-vessel retention concept for VVER-440/V213 reactors in Central European Countries, Nuclear Engineering and Design, Volume 314, 2017, Pages 93-109,https://doi.org/10.1016/j.nucengdes.2017.01.015.

MCNP Code website, https://mcnp.lanl.gov/

Mészáros, P., Babcsány, B., Varju, T., 2023. Reactor physics and thermal hydraulics analysis of the SCW-SMR conceptual design with the Serpent 2 and Apros codes, MSc thesis, BME, Budapest, 2023

Mokry, S., Pioro, I., Farah, A., King, K., Gupta, S., Peiman, W., and Kirillov, P. (2011). Development of supercritical water heat-transfer correlation for vertical bare tubes. Nucl. Eng. Des., 241(4) :1126–1136.Dittus, F.W. and Boelter, L.M.K., 1930, Heat Transfer in Automobile Radiators of the Tubular Type. University of California Press, Berkeley, University of California Publications in Engineering, Vol. 2, 443-461.

Nasuti., F., Pizzaruti, N. 2021. Pseudo-boiling and heat transfer deterioration while heating supercritical liquid rocket engine propellants, The Journal of Supercritical Fluids, Volume168. https://doi.org/10.1016/j.supflu.2020.105066

Nava Dominguez, A., Onder, N., Rao, Y. , and Leung, L., 2016, Evolution of the Canadian SCWR fuel-assembly concept and assessment of the 64-element assembly for thermalhydraulic performance, CNL Nuclear Review 5 (2016): 221–238. https://doi.org/10.12943/CNR.2015.00057 .

Novog, D., G. McGee, et al., 2012. Safety concepts and systems of the Canadian SCWR, The 3rd China-Canada Joint Workshop on Supercritical Water-Cooled Reactors, Xi'an, Shaanxi, China.

NRC "Kurchatov Institute" Technical report. In-vessel retention of corium by external water cooling of the reactor vessel: feasibility assessment for VVER-1000.

Oka, Y., Koshizuka, S., Ishiwatari, Y., Yamaji, A., 2010. Super Light Water Reactors and Super Fast Reactors: Supercritical-Pressure Light Water Cooled Reactors. Springer.

Page of SCWR on the Generation IV International Forum website https://www.gen-4.org/gif/jcms/c_9360/scwr

Palagin A., Miassoedov A., Gaus-Liu, Xiaoyang, Buck, Tran, Chi-Thanh, Kudinov P., Carenini L., Koellein C., Luther W., Chudanov V., 2012. Analysis and interpretation of the LIVE-L6 experiment.

Pioro, I.L., Duffey, R.B., 2007. Heat Transfer and Hydraulic Resistance at Supercritical Pressure in Power Engineering Applications. ASME Press, New York.

Pomogaev, A., 2022. BWRX-300 Isolation Condenser System analysis. Master's thesis, Lappeenranta–Lahti University of Technology LUT, LUT School of Energy Systems. https://lutpub.lut.fi/handle/10024/164715

Ranz, W. and Marshall, W., 1952. Evaporation from Drops. Chemical Engineering Progress, 48, 141-146

Rao, Y.F., Cheng, Z., Waddington, G.M., Nava-Dominguez, A., 2014. ASSERT-PV 3.2: Advanced subchannel thermalhydraulics code for CANDU fuel bundles, Nuclear Engineering and Design, Vol. 275, 2014, pp 69-79, ISSN 0029-5493, https://doi.org/10.1016/j.nucengdes.2014.04.016.

Razumovskiy, V.G., Pis'mennyi, Eu. N., Koloskov, A.E., and Pioro, I.L., 2009, Heat transfer to supercritical water in vertical 7-rod bundle", Proceedings of the ICONE-16, 2009, pp. 963-969.

Razumovskiy, V.G., Pis'mennyi, Eu. N., Sidawi, Kh., Pioro, I. L., Koloskov, A. Eu., 2016, Experimental heat transfer in an annular channel and 3-rod bundle Cooled with upward flow of supercritical water, JNERS, Vol. 2, Iss.1, 2016, pp 1-8.

RELAP5 Code Development Team, 2001, "RELAP5/MOD 3.3 Code Manual, Vol 1–8," NUREG/CR-5535/Rev1, 2001.

Rowe, D. S., 1967, Cross-Flow mixing between parallel flow channels during boiling Part-I COBRA-Computer program for coolant boiling in rod arrays, BNWL-371-Pt-I., 1967.

SANDIA NATIONAL LABORATORIES, 2014. MELCOR Computer Code Manuals, MELCOR Code Revisions. Users' Guide, Version 1.8.5 RL, Rev.4, SNL, (2004)

SANDIA NATIONAL LABORATORIES, 2017. MELCOR Computer Code Manuals, Vol. 1: Primer and Users' Guide, Version 2.2.9541, SAND 2017-0455 O, SNL, (2017)

SCDAP/RELAP5 Development Team, 1998, "SCDAP/RELAP5/MOD3.2 Code Manual, Vol. 1–5," NUREG/CR-6150, INEL-96/0422, July 1998.

Schlagenhaufer, M., Schulenberg, T., Starflinger, J., Bittermann, D., Andreani, M., 2010. Design proposal and parametric study of the HPLWR safety system, International Congress on Advances in Nuclear Power Plants 2010, ICAPP 2010. 1. 106-118.

Schulenberg, T., et al., 2014. Review of R&D for supercritical water cooled reactors, Progress in Nuclear Energy, http://dx.doi.org/10.1016/j.pnucene.2014.02.021

Schulenberg, T., Starflinger, J., 2012. High Performance Light Water Reactor: Design and Analyses. KIT Scientific Publishing.

Schulenberg, T., and Otic, I., 2021, Suggestion for design of a small modular SCWR, 10th International Symposium on SCWRs (ISSCWR-10), Prague, the Czech Republic, March 15-19, 2021.

SCIENTECH Inc., 1999. RELAP5/Mod3 Code Manual. Code Structure, System Models and Solution Methods, vol. I. The Thermal Hydraulics Group, Idaho.

Stewart, C.W. et al., 1977. COBRA-IV: The model and the method, Battelle Pacific Northwest Laboratories Report, BNWL-2214.

Todreas, N.E., Kazimi, M., 2012, Nuclear Systems, Volume I, Thermal-hydraulic Fundamentals, Second Edition, CRC Press, Taylor & Francis,

Tran, C-T., Dinh, T-N., 2009. The effective convectivity model for simulation of melt pool heat transfer in a light water reactor pressure vessel lower head. Part I: Physical processes, modeling and model implementation, Progress in Nuclear Energy,Volume 51, Issue 8, 2009, Pages 849-859. https://doi.org/10.1016/j.pnucene.2009.06.007.

Varju, T., Bertesina, Z., Babcsány, B., 2024. Coupling of Apros and SPNDYN to analyse the SCW-SMR concept within ECC-SMART, 11th International Symposium on SCWRs (ISSCWR-11), Pisa, Italy, February 3-5, 2025 (submitted)

Varju, T., Csige, A., Kiss, A., Filonov, V., Filonova, Y., Fedorov, D., Pucciarelli, A., Kassem, S., Ambrosini, 2024, Discussion and perspectives for improvements of heat transfer correlation capabilities for fluids at supercritical pressures, Nuclear Engineering and Design, Volume 421, May 2024, 113085.

Volkov V.Yu., Golibrodo L.A., Krutikov A.A. et al., 2019. Application of the results of CFD calculation of the VVER primary circuit to obtain the initial data of thermal-hydraulic calculations, OKB "GIDROPRESS", Podolsk, Russia, 2019. (In Russian)

Volkov V.Yu., Golibrodo L.A., Krutikov A.A. et al., 2017. Development of a CFD model of the VVER reactor of the AES-2006 project, OKB "GIDROPRESS", Podolsk, Russia, 2017. (In Russian)

Waata, C. L., 2006. Coupled neutronics/thermal-hydraulics analysis of a high-performance light-water reactor fuel assembly (FZKA-7233), Karlsruhe, 2006, https://elib.uni-stuttgart.de/handle/11682/1712

Wang, Q., Ma, X., Xu, J., 2021. The three-regime-model for pseudo-boiling in supercritical pressure, International Journal of Heat and Mass Transfer,Volume 181, 2021, https://doi.org/10.1016/j.ijheatmasstransfer.2021.121875

Wheeler, C.L., et al., 1976. COBRA-IV-I: an interim version of COBRA for thermal-hydraulic analysis of rod-bundle nuclear fuel elements and cores, Battelle Pacific Northwest Laboratories Report, BNWL-1962.

Wu, P., Ren, Y., 2022. A review of existing Super Critical Water reactor concepts, safety analysis codes and safety characteristics, Progress in Nuclear Energy, Volume 153, 2022, https://doi.org/10.1016/j.pnucene.2022.104409.

Yetisir, M., Gaudet, M., Pencer, J., Mcdonald, M., Rhodes, D., Hamilton, H. and Leung, L., 2012, Canadian supercritical water-cooled reactor core concept and safety features, CNL Nuclear Review 5 (2012): 189–202. https://doi.org/10.12943/CNR.2016.00042 .

Zvonarev, Yu., Melnikov, I., Smelkov, Yu., 2017. Simulation of corium pool on the bottom of the VVER-1000 vessel in the conditions of a severe accident with core fuel melting, OKB GP, 2017 (in Russian).

Zhao, X., and contributors, 2023, Report on the results of the benchmark exercise, ECC-SMART PROJECT, Deliverable D3.2, April 2023.

Zhao X., Huang Y. and Zang J., 2023. Research and Development on Thermal Hydraulic and Safety of Supercritical Water-cooled Reactor[J]. Nuclear Power Engineering, 2023, 44(5): 223-231. doi: 10.13832/j.jnpe.2023.05.0223